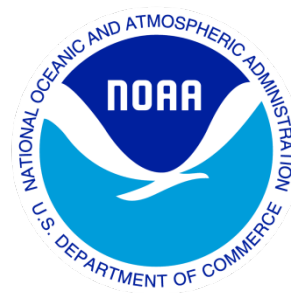# Climate Data Record (CDR) Program

Climate Algorithm Theoretical Basis Document (C-ATBD)

AVHRR Cloud Properties - NASA

A Consistent Long-Term Cloud and Clear-Sky Radiation Property Dataset from the Advanced Very High Resolution Radiometer (AVHRR)

CDR Program Document Number: CDRP-ATBD-0826
Configuration Item Number: 01B-30b
Revision 1 / September 19, 2016

REVISION HISTORY

Rev.	Author	DSR No.	Description	Date
1	Patrick Minnis and Kristopher Bedka, NASA LaRC. Qing Trepte, Christopher R. Yost, Sarah T. Bedka, Benjamin A. Scarino, Konstantin Khlopenkov, and Mandana M. Khaiyer, SSAI	DSR-1051	Initial Submission to the CDR Program	9/19/2016

TABLE of CONTENTS

LIST of FIGURES

Figure 1: Equatorial crossing times during ascending branch of NOAA POES and IJPS orbits, illustrating the precession of orbits with time. Each line represents a different NOAA (NX) or MetOp (MX) satellite, where X corresponds to the satellite number, e.g. N14=NOAA-14, M1=MetOp-A, M2=MetOp-B.   Taken from: http://www.star.nesdis.noaa.gov/smcd/emb/vci/VH/vh_avhrr_ect.php.

Figure 2: Schematic showing relationship between full (LAC or HRPT, in blue) and reduced resolution (GAC, in blue with black border) data. From Figure 4.1 at: http://oiswww.eumetsat.org/WEBOPS/eps-pg/AVHRR/AVHRR-PG-4ProdOverview.htm

Figure 3: Processing outline of the SatCORPS-A.

Figure 4: Spectral response functions for selected for the TRMM VIRS, Terra MODIS, and selected AVHRR (N*XX*) SIR channels. *XX* denotes the NOAA satellite number. Gray lines denote wavelength sub-interval boundaries for computing atmospheric attenuation.

Figure 5: Cloud mask selection process.

Figure 6: Schematic overview of daytime scene identification algorithm.

Figure 7: Daytime thin cirrus tests for SatCORPS-A1.

Figure 8: C1 test over land for SatCORPS-A1/3.

Figure 9: Same as Figure 6, except for night.

Figure 10: Schematic of nighttime E3 test for SatCORPS-A1/2.

Figure 11. Same as Figure 9, except for terminator conditions, 82° < SZA $\leq$ 88.5°, SatCORPS-A1 only.

Figure 12: VIS reflectance parameters for (a) NOAA-18 AVHRR image, 2331 UTC, 1 October 2012. (b) observed reflectance, (c) standard deviation of clear-sky reflectance, and (d) predicted clear-sky reflectance.

Figure 13. Same as Figure 12, except for IRW and SIR channels.(a) observed T_4, (b) Predicted T_{cs4}, (c) standard deviation of predicted T_{cs4}, (d) observed BTD_{34}, (e) predicted clear-sky BTD_{34}, (f) standard deviation of predicted BTD_{cs34}.

Figure 14. Cloud mask for NOAA-18 AVHRR image, 2331 UTC, 1 October 2008.

Figure 15: Schematic of VISST/VINT iterative processing. Smiling and frowning faces denote favorable and unfavorable termination of iteration, respectively.

Figure 16: Flow diagram of phase determination process for VISST and VINT.

Figure 17: LBTM sub-algorithm flowchart for phase determination.

Figure 18: Flowcharts for phase determination. (a) Thin cirrus test sub-algorithm, (b) marine stratocumulus edge pixel test applied to ice cloud pixels.

Figure 19: Theoretical variation of BTD_{34} and BTD_{45} with T_4 for ice (left) and liquid water (right) clouds in a tropical atmosphere. T_c = 230 K and 255 K for the ice and water clouds, respectively.

Figure 20: Schematic diagram of SIST procedure.

Figure 21: NOAA-18 1° gridded monthly-averaged clear-sky skin temperature retrieval for October 2008 fromSatCORPS-A1.

Figure 22: (left) NOAA-9 visible reflectance imagery over the Congo overlaid with the overshooting convective cloud top pixel detection mask (blue). (right) NOAA-9 color-enhanced IRW BT imagery for the same scene.

Figure 23: (a) Number of OT pixel detections per 0.25° grid box using 18 years of half-hourly GOES data. (b) 10-year Vaisala cloud-to-ground lightning flash density database over eastern U.S. Image, cropped to approximate domain in (a). (c) Number of OT detections per 0.5°region using 7 years of 15-min MSG

SEVIRI data. Note that only the coldest pixel in an OT is counted here versus the GOES analysis in (a) where all pixels in an OT are counted. (d) Number of OT pixels per year per 1° grid box using 17 years of AVHRR GAC data with observations between 0100 and 0300 AM/PM LT.

Fig. 24: Regression of global SW AVHRR α_{SWA} versus Aqua CERES α_{SWE}, for the ocean scene type during January 2008. The NB-BB conversion coefficients, a_i, are listed at lower right.

Fig. 25: As in Figure 24, but for LW AVHRR M_4 and Aqua CERES M_{LWE} during (a) daytime and (b) nighttime. The NB-BB conversion coefficients, b_i, are listed in lower right corner.

Fig. 26: Demonstration of third order adjustment applied to daytime January 2008 AVHRR-derived M'_{LWA} plotted against CERES $Aqua$ M_{LWE} for ocean scenes. Unadjusted data (gray points) in the biased range are averaged into 10 Wm^{-2} bins (blue dots). Final mean values, M_{LWA}, after adjustment are in green.

Figure 27: Clear-sky VIS overhead-sun albedos for January.

Figure 28: Mean clear-sky VIS albedo variation with SZA for major surface-type categories.

Figure 29: October 2008 day + night cloud fraction. Regional means from (a) N18 SatCORPS-A1, (b) CERES Aqua Ed 4, (c) Aqua MAST C6, (d) PATMOS-X N18, (e) ISSCP D2, (f) CLARA-A1 N18, and (g) CALIPSO. (h) Zonal means. Resolution is 1°, except for ISCCP (2.5°) and CALIPSO (5°).

Figure 30: Same as Figure 29, except for mean cloud top pressure. (a) N18 SatCORPS-A1, (b) CERES Aqua Ed 4, (c) MAST Aqua C6, (d) PATMOS-X N18, (e) ISSCP D, (f) CLARA-A1 N18. (g) Zonal means.

Figure 31: Same as Figure 29, except daytime, 1° regional mean liquid (a-c) and ice (d-f) cloud fractions from (a) SatCORPS-A1 N18, (b) CERES Aqua MODIS Ed4, (c) MAST Collection 5, and (d) PATMOS-X N18. Zonal averages for (e) liquid and (f) ice cloud fraction.

Figure 32: October 2008 daytime zonal mean cloud optical depths from SatCORPS-A1 N18, CERES Aqua MODIS Ed 4, MAST C6, and PATMOS-X N18. (a) liquid and (b) ice clouds.

Figure 33: October 2008 zonal mean cloud particle effective radius from SatCORPS-A1 N18, CERES Aqua MODIS Ed 4, PATMOS-X N18, and MAST C6 3.7-μm retrieval. (a) water droplets and (b) ice crystals.

Figure 34. Classification of CALIPSO-determined mixed-phase cloudy pixels by SatCORPS-A1 during October 2008 using N18 data. (a) frequency of mixed-phase pixels as a function of T_c from SatCORPS-A1. (b) Percentage of mixed-phase pixels classified as liquid water by SatCORPS-A1 as a function T_c.

Figure 35: JAJO 2008 matched SatCORPS-A1 N18 and CALIPSO single-phase liquid water cloud top heights.

Figure 36. Same as Figure 35, except for ice clouds over nonpolar water surfaces.

Figure 37. JAJO 2008 matched SatCORPS-A1 N18 and CALIPSO single-phase liquid water cloud base heights over nonpolar water surfaces.

Figure 38. Same as Figure 37, except for ice cloud base heights.

Figure 39: JAJO 2008 matched SatCORPS-A1 N18 and CALIPSO ice COD for CALIPSO non-opaque clouds over ice-free water surfaces. (day), (b) night.

Figure 40: JAJO 2008 matched SatCORPS-A1 N18 AVHRR and Aqua AMSR-E LWP over ice-free water surfaces during daytime. (a) nonpolar, (b) polar waters.

Figure 41: Same as Figure 39, except for IWP. (day), (b) night.

Figure 42: Comparison of April 2010 CloudSat Radar only and CERES Ed4 Aqua IWP over CONUS for CERES COD between (a) 10 and 20, and (b) 80 and 149. *Courtesy of William R. Smith, Jr., NASA.*

Figure 43: Mean July 2008 (a) AVHRR SST, (b) NOAA ESRL Optimum Interpolation SST, and (c) their differences with 1° land mask applied. (d) The scatterplot of instantaneous 0.25° regional values, where the color scale indicates the number of points.

Figure 44: AVHRR Land Surface Temperature compared to matched ARM SGP IRT temperatures, January-December 2008.

Figure 45: AVHRR Land Surface Temperature compared to SURFRAD (a) Desert Rock, NV and (b) Sioux Falls, SD PIR measurements, January-December 2008.

Figure 46: Scatterplots of CERES Aqua and NOAA-18 AVHRR measurements of (a) OLR and (b) reflected SW flux for all scenes and times of day during October 2007.

Figure 47: Example of RGB composites for two NOAA-18 AVHRR scenes using VIS reflectance for the red channel, BTD_{34} for the green channel, and T_4 for the blue channel. AVHRR observed RGBs and predicted clear-sky RGB images over the (a, b) Middle East and (c,d) southern North America and simulated clear-sky RGB right panels use simulated clear-sky reflectance and BTs.

Figure 48: AVHRR BTD_{34} (y-axis) as a function of T_4 for October 1986 NOAA-9 (blue) and October 2008 NOAA-18 (red) data over southern Africa.

Figure 49: Comparison of nighttime retrievals using 3-channel SIST and 2-channel SIRT (no SWC channel) of a) COD and b) CET for 6 scenes from NOAA-9 (~1.7 million pixels).

Figure 50: Mean water droplet effective radius from NPP VIIRS data (July 2013) using (a) 1.6 μm and (b) 3.7 μm.

Figure B.1: Schematic demonstrating impact of errors in sensor attitude angles on satellite image navigation.

Figure B.2: Example of 0.86-μm clear-sky reference map derived from MODIS 250-m data during August 2005-2007 over the North American domain used in the SAPS navigation correction module.

Figure B.3: Multispectral NOAA-18 AVHRR scene overlaid with the ground control points (yellow boxes) used in navigation correction.

Figure B.4: Distribution of AVHRR navigation error for various ground control point matches along satellite scan direction for a selected AVHRR orbit. X-axis: AVHRR HRPT pixel position within the scan line. Y-axis: magnitude of navigation error oriented along the scan line (i.e. crossing the satellite track). Navigation error oriented along the satellite track is not shown. Improvements in navigation with each iteration of the correction routine are shown the panels. 0th-order correction: satellite roll angle adjustment. 1st-order correction: accounts for errors in satellite altitude and/or angular scan range (i.e., yaw angle). 2nd-order correction: accounts for pitch angle errors, which are equivalent to a time delay that results in a clock difference between the scan line timing & the Earth rotation. Note, change in y-axis scales from "before correction" to "after correction" panels.

Figure B.5: Images highlighting AVHRR Level 1B data problems addressed by AVHRR pre-processing software. Color-enhanced NOAA-18 AVHRR 10.8-µm BT imagery over southeast Asia (a) before and (b) after navigation correction. The BT gradient in this scene associated with land/ocean temperature differences should align with the coastlines (white lines). Color-enhanced NOAA-9 AVHRR 3.74-µm imagery over Antarctica (c) before and (d) after noise filtering. Color-enhanced NOAA-9 AVHRR 12.0-µm imagery over Central Asia (e) before and (f) after bad scan line detection.

Figure C.1. Schematic of Sat-CORPS-A1 C2 tests.

Figure C.2. Schematic of SatCORPS-A1/3 C3 tests over land.

Figure C.3. Schematic of SatCORPS-A1/3 C3 tests over ocean.

Figure C.4. Schematic of SatCORPS-A1/3 C4 tests.

Figure C.5. Schematic of SatCORPS-A1/3 C5 tests.

Figure C.6. Schematic of SatCORPS-A1/3 C6 tests over land.

Figure C.7. Schematic of SatCORPS-A1/3 C6 tests over ocean.

Figure. C.8. Schematic of SatCORPS-A1 E1 tests.

Figure C.9. Schematic of SatCORPS-A1/2 E2 tests.

Figure C.10. Schematic of SatCORPS-A1/2 E4 tests.

Figure C.11. Schematic of SatCORPS-A1/2 E5 tests.

LIST of TABLES

Table 1: Historical and currently operational AVHRR instrument launch dates, service start/end dates, local daytime ECT at satellite launch, and GAC Level 1B filename satellite identification string. This table combines information from http://en.wikipedia.org/wiki/Advanced_Very_High_Resolution_Radiometer, http://www.star.nesdis.noaa.gov/smcd/emb/vci/VH/vh_avhrr_ect.php, and Ignatov et al. (2004).

Table 2: Spectral channels observed by the AVHRR series. Channels are referred to by their central wavelength or acronym in the text.

Table 3. IGBP surface types (general type used for model selections).

Table 4. Selection of C and E tests based on B/D test results.

Table 5. Criteria for setting special regional flags.

Table 6. Transition pressure levels P1 and P2 for each of the three latitude zones (tropics, midlatitudes, and polar regions) over three different snow-free surfaces (land, coast, and water). The lapse rates are used to rebuild temperature profiles at altitudes below the height of pressure P1. Between P1 and P2, the temperature profile is a blend of the lapse rate and model values. For lower pressures, only the model values are used.

Table 7. Albedo RMS errors (unitless, and also expressed as percent) for 2008 monthly SW NOAA-18 AVHRR vs CERES *Aqua* NB-BB fits by scene type.

Table 8. RMS errors in Wm^{-2} (%) for 2008 monthly NOAA-18 AVHRR vs CERES *Aqua* NB IRW-BB LW fits for three scene types.

Table 9. Angular nodes, optical depths and particle sizes used for cloud reflectance LUTs.

Table 10: Coefficients and constants used for thick ice cloud thickness estimates.

Table 11: Parameters provided in the AVHRR Cloud TCDR NetCDF-4 output files. A brief description of each parameter and its unit, the data type of the parameter in the NetCDF file, the valid data range, and the dimensions of each array are provided. The variable *nlines* corresponds to the number of scan lines in an AVHRR GAC orbit. The number of pixels is always 409 for GAC files. CDR-quality parameters are indicated in bold.

Table 12. Error budget for SatCORPS-A1 global cloud fraction and phase based on differences between N18 and CALIPSO data, January, April, July, and October 2008. SF – snow/ice free, SI – Snow or ice covered surfaces.

Table 13. Error budget for single-layer liquid cloud-top height from N18-CALIPSO differences from January, April, July, and October 2008. SF – snow/ice free, SI – Snow or ice covered surfaces.

Table 14. Error budget for COD, LWP, and IWP for single-phase clouds from differences between N18 and reference datasets. SF – snow/ice free, SI – Snow or ice covered surfaces. NP – non-polar, P – polar.

1.   Introduction

1.1   Purpose

This Climate Algorithm Theoretical Basis Document (C-ATBD) documents the algorithms and theoretical basis of the Satellite ClOud and Radiative Property retrieval System - AVHRR (SatCORPS-A) used to create the *Consistent Long-Term Cloud and Clear-Sky Radiation Property Dataset from the Advanced Very High Resolution Radiometer (AVHRR)* Thematic Climate Data Record (TCDR) for the National Climate Data Center. The actual algorithms are defined by the computer program (code), which accompanies this document, and thus the intent here is to provide a guide to understanding that algorithm, from a scientific perspective and in order to assist a software engineer or end-user performing an evaluation of the code.

1.2   Definitions

Following is a summary of the symbols used to define the algorithm.

Spectral and directional parameters:

$$B_\lambda(T) = Planck\ function\ evaluated\ at\ \lambda\ for\ temperature\ T \qquad (1.01)$$

$$B_\lambda^{-1}(L) = inverse\ Planck\ function\ evaluated\ at\ \lambda\ for\ radiance\ L \qquad (1.02)$$

$$BTD_{i1,i2} = brightness\ temperature\ difference\ between\ channels\ i1\ and\ i2 \qquad (1.03)$$

$$BT_i = brightness\ temperature\ for\ channels\ i \qquad (1.04)$$

$$d_o = normalized\ Earth\text{-}sun\ distance \qquad (1.05)$$

$$E_\lambda = solar\ constant \qquad (1.06)$$

$$\lambda = wavelength\ (\mu m) \qquad (1.07)$$

$$\theta,\ \theta_o = viewing,\ solar\ zenith\ angle\ (°) \qquad (1.08)$$

$$\mu,\ \mu_o = cos(\theta),\ cos(\theta_o) \qquad (1.09)$$

$$\phi = relative\ azimuth\ angle,\ backscatter\ is\ 180° \qquad (1.10)$$

$$B_\lambda(T) = Planck\ function\ evaluated\ at\ \lambda\ for\ temperature\ T \qquad (1.11)$$

$$B_\lambda^{-1}(L) = inverse\ Planck\ function\ evaluated\ at\ \lambda\ for\ radiance\ L \qquad (1.12)$$

Surface and clear-sky parameters:

$$\alpha_{cs} = VIS\ surface\ albedo \qquad (1.13)$$

α_{csd} = NIR diffuse surface albedo *(1.14)*

α_s = NIR surface albedo *(1.15)*

α_{sd} = NIR diffuse surface albedo *(1.16)*

χ_N = NIR surface normalized BRDFs *(1.17)*

χ_v = VIS clear-sky normalized BRDFs *(1.18)*

δ_s = NIR normalized surface directional albedos *(1.19)*

δ_{cs} = VIS normalized clear-sky directional albedos *(1.20)*

ε_{si} = surface effective emissivity for channel i *(1.21)*

K = IGBP surface type *(1.22)*

L = radiance (Wm^{-2}sr^{-1}) *(1.23)*

T_b = effective temperature of upwelling radiance reaching cloud base (K) *(1.24)*

T_s = surface skin temperature (K) *(1.25)*

z_o = surface elevation (km) *(1.26)*

Cloud parameters:

α_{cd} = cloud VIS diffuse albedo *(1.27)*

α_c = cloud VIS directional albedo *(1.28)*

α_{cs} = VIS surface albedo *(1.29)*

ΔT_{sc} = temperature difference between background and cloud (K) *(1.30)*

ε_i = cloud effective emissivity for channel i *(1.31)*

ε_{ti} = cloud top emissivity for channel i *(1.32)*

ε_{ai} = cloud beam emissivity without scattering for channel i *(1.33)*

ε_{adi} = cloud diffuse emissivity without scattering for channel i *(1.34)*

d =cloud emittance parameterization coefficients *(1.35)*

$n(r)$ = number of particles of radius r *(1.36)*

N = cloud particle number density (m^{-3}) *(1.37)*

r = particle radius (µm) *(1.38)*

r_e = particle effective radius (µm) *(1.39)*

τ = VIS cloud optical depth   (1.40)

τ_a = IR cloud absorption optical depth   (1.41)

ϖ = single-scattering albedo   (1.42)

α_{cd} = cloud VIS diffuse albedo   (1.43)

α_{cd} = cloud VIS diffuse albedo   (1.44)

Atmospheric parameters:

Γ = apparent lapse rate (K km^{-1})   (1.45)

p = pressure   (1.46)

T = temperature (K)   (1.47)

T_p = tropopause temperature (K)   (1.48)

τ_{ij} = gaseous absorption optical depth for channel i and layer j   (1.49)

τ_R = layer Rayleigh scattering optical depth   (1.50)

τ_{Na1} = above cloud NIR absorption optical depth   (1.51)

τ_{Na2} = below cloud NIR absorption optical depth   (1.52)

z = altitude (km)   (1.53)

Polynomial representations:

$\varepsilon(\zeta, \mu, \xi)$ $= \sum_{i=0}^{2} \sum_{j=0}^{4} \sum_{k=0}^{1} d_{ijk}\, \zeta^i \mu^j \xi^k$ = cloud emittance parameterization   (1.54)

$\xi = 1/ln(T_b)$ (1.55)

$\zeta = 1/ln(\Delta T_{sc})$ (1.56)

1.3   Referencing this Document

This document should be referenced as follows:

A Consistent Long-Term Cloud and Clear-Sky Radiation Property Dataset from the Advanced Very High Resolution Radiometer (AVHRR)- Climate Algorithm Theoretical Basis Document, NOAA Climate Data Record Program CDRP-ATBD-0826 Rev. 1 (2016). Available at http://www.ncdc.noaa.gov/cdr/operationalcdrs.html

1.4   Document Maintenance

This document describes the initial submission, version 1.0, of the processing algorithm and resulting data. The version number will be incremented for any subsequent enhancements or revisions and these changes will be coordinated with the CDR Program office.

2.   Observing Systems Overview

2.1   Products Generated

The products generated by the AVHRR Cloud and Clear-Sky Radiation TCDR are listed below:

1) Calibrated 0.63, 0.86, 1.61-μm reflectances

2) Cloud mask

3) Clear-sky land and ocean surface skin temperatures

4) Cloud optical depth

5) Cloud thermodynamic phase

6) Ice crystal and water droplet effective radius

7) Cloud effective, top, and base pressures

8) Cloud effective, top, and base heights

9) Cloud effective and top temperatures

10) Overshooting convective cloud top pixel detection flag

11) Broadband shortwave albedo and outgoing longwave radiation

12) Quality control flags for the cloud mask and land/ocean surface skin temperature

2.2   Instrument and Dataset Characteristics

The AVHRR is a broadband scanning radiometer sensing in the visible, near-infrared, and thermal infrared portions of the electromagnetic spectrum. AVHRR has been carried on the NOAA Polar-orbiting Operational Environmental Satellites (POES) since TIROS-N in 1978 and continues through to NOAA-19 at the present time. AVHRR is also one of many instruments aboard the MetOp-A and -B satellites in the EUMETSAT/NOAA Initial Joint Polar System (IJPS). Table 1 provides a list of historical and currently operational AVHRR instruments with their launch date, service start/end dates, and local daytime equator crossing times (ECTs) at satellite launch. NOAA POES were historically configured to fly in pairs, one morning and one afternoon satellite, nominally at 07:30 and 14:30 ECTs, respectively. The polar-orbiter configuration was changed when NOAA-17 was moved to a 10:00 ECT orbit. The NOAA POES are nominally in fixed orbits, but because the orbits are not maintained by a propulsion system, their ECTs change slowly due to drag. The MetOps are maintained in their nominal orbital configuration (0930 ECT) as shown in Figure 1, which illustrates the change in ECTs of the ascending branch of NOAA POES and IJPS MetOp orbits throughout the lifetime of each satellite. The TIROS-N and NOAA-6 satellites, not shown in Figure 1, were launched in 1978 into 1430 and 0730 ECTs, respectively. The

individual NOAA and MetOp satellites are also referred to as NX and MX, respectively, where X indicates the satellite's identification number or letter. For example, NOAA-14 would be N14.

From its nadir view, a given AVHRR observes the Earth at a 1.1-km spatial resolution in 4 to 6 of the spectral channels listed in Table 2. This 1.1-km dataset is known as HRPT or LAC data and are only available over regional domains at NOAA CLASS. This Cloud TCDR uses the AVHRR GAC dataset since it provides global coverage throughout the entire lifetime of each satellite. GAC data are created from HRPT/LAC data by sub-setting every third scan line and averaging four pixels along the scan line to create a single pixel observation that is recorded in the GAC dataset (see Figure 2). Every 5th pixel along a scan line is skipped in the creation of the GAC data yielding a nominal effective resolution

Table 3: Historical and currently operational AVHRR instrument launch dates, service start/end dates, local daytime ECT at satellite launch, and GAC Level 1B filename satellite identification string. This table combines information from http://en.wikipedia.org/wiki/Advanced_Very_High_Resolution_Radiometer**,** http://www.star.nesdis.noaa.gov/smcd/emb/vci/VH/vh_avhrr_ect.php**, and Ignatov et al. (2004).**

Satellite Name	Launch Date	Service Start	Service End	Approxmate Daytime Equatorial Crossing Time at Satellite Launch	GAC Filename Satellite ID String
TIROS-N	13 Oct 1978	19 Oct 1978	30 Jan 1980	0300 PM	TN
NOAA-6	27 Jun 1979	27 Jun 1979	16 Nov 1986	0730 AM	NA
NOAA-7	23 Jun 1981	24 Aug 1981	7 Jun 1986	0230 PM	NC
NOAA-8	28 Mar 1983	3 May 1983	31 Oct 1985	0730 AM	NE
NOAA-9	12 Dec 1984	25 Feb 1985	11 May 1994	0230 PM	NF
NOAA-10	17 Sep 1986	17 Nov 1986	17 Sep 1991	0730 AM	NG
NOAA-11	24 Sep 1988	8 Nov 1988	13 Sep 1994	0200 PM	NH
NOAA-12	13 May 1991	14 May 1991	15 Dec 1994	0730 AM	NI
NOAA-14	30 Dec 1994	30 Dec 1994	23 May 2007	0130 PM	NJ
NOAA-15	13 May 1998	13 May 1998	Present	0730 AM	NK
NOAA-16	21 Sep 2000	21 Sep 2000	9 June 2014	0200 PM	NL
NOAA-17	24 Jun 2002	24 Jun 2002	10 Apr 2013	1000 AM	NM
NOAA-18	20 May 2005	30 Aug 2005	Present	0200 PM	NN
NOAA-19	6 Feb 2009	2 Jun 2009	Present	0200 PM	NP
MetOp-A	19 Oct 2006	20 Jun 2007	Present	0930 AM	M2
MetOp-B	17 Sep 2012	24 April 2013	Present	0930 AM	M1

of 3.3 km x 5.5 km, or ~4 km on average per pixel. The AVHRR scans the Earth out to a VZA of ~70°, where the pixel effective resolution is ~7 km. Table 2 shows that AVHRR channels 1, 2, 3B, and 4 are present on all NOAA POES and MetOp satellites. Since the launch of N15, the AVHRR/3 has the capability to switch between 3A during daytime and 3B during nighttime. However, several AVHRR/3s are operated using channel 3B at all times of day. Channel 5 (12.0 µm) is absent on the TIROS-N, NOAA-6, -8, and -10 AVHRRs.
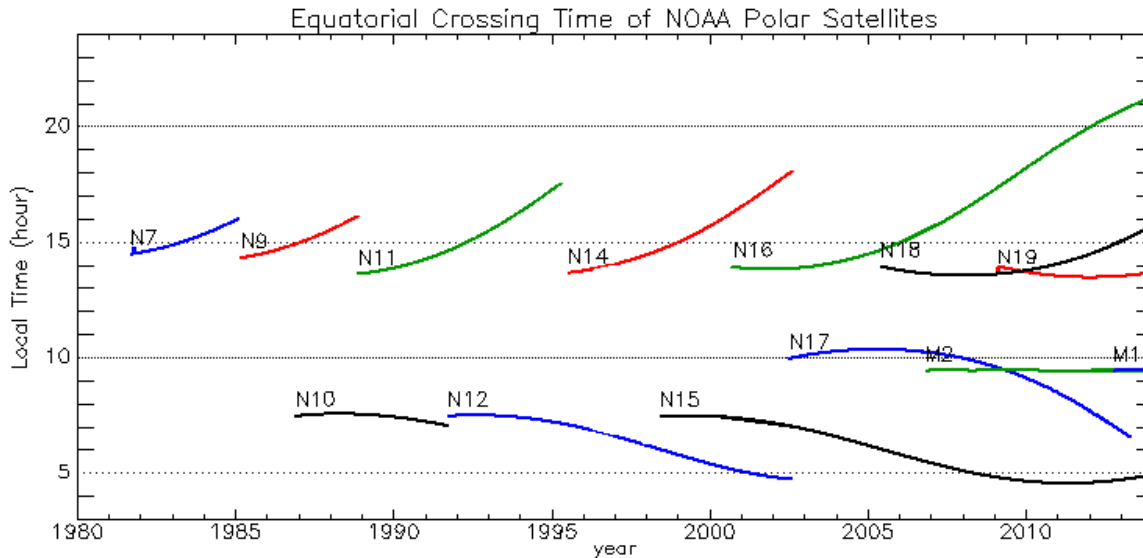
Figure 4: Equatorial crossing times during ascending branch of NOAA POES and IJPS orbits, illustrating the precession of orbits with time. Each line represents a different NOAA (NX) or MetOp (MX) satellite, where X corresponds to the satellite number, e.g. N14=NOAA-14, M1=MetOp-A, M2=MetOp-B. Taken from: http://www.star.nesdis.noaa.gov/smcd/emb/vci/VH/vh_avhrr_ect.php.

AVHRR data are recorded at a 10-bit resolution corresponding to a ΔL of 0.0028, 0.18, and 0.21 mW m^{-2} s^{-2} cm^{-1} for the SIR, IR, and SWI channels, or a ΔT of 6.06, 0.28, and 0.27 K at 220 K and 0.16, 0.12, and 0.13 K at 290 K (Mittaz and Harris 2011), respectively. These values correspond to AVHRRs on NOAA-15 through MetOp-B that are also referred to as the AVHRR/3 series. The nominal range in brightness temperature for each AVHRR is 180 – 335 K. The infrared channels are calibrated onboard using a blackbody calibration system, while the solar channels (1, 2, and 3A) are calibrated prior to launch and have no onboard calibration system. Thus, to account for degradation in the sensors, external methods are used to adjust the solar channel calibration coefficients (e.g., Brest et al. 1997; Rao and Chen, 1996). The nominal calibration process for the AVHRR on the satellites through NOAA-14 is given at http://www.ncdc.noaa.gov/oa/pod-guide/ncdc/docs/podug/html/c3/sec3-3.htm. A description of the AVHRR/3 instrument is given at http://www.ncdc.noaa.gov/oa/pod-guide/ncdc/docs/klm/html/c3/sec3-1.htm.

An AVHRR GAC data file typically covers an entire orbit (~90-120 min) with ~13,000 scan lines, on average, with 409 pixels in each scan line. The GAC files occasionally cover a shorter time period with some files containing observations for < 5 min in duration. This does not necessarily have any impact on the TCDR because all files are processed in the same manner. In addition, AVHRR data from the CLASS archive can also have temporal gaps that extend from 90 min to several days, especially in the era prior to NOAA-15. There are also approximately 5-6 min of overlap where identical data are recorded at the end of one orbit and the beginning of the following orbit. These overlaps are included in TCDR processing but they should be excluded in the creation of "Level 3" derived products.

Table 4: Spectral channels observed by the AVHRR series. Channels are referred to by their central wavelength or acronym in the text.

AVHRR Channel Number (Central Wavelength, Abbreviation)	Channel Wavelength Range (µm)	Satellites With This Channel
1 (0.63 µm, VIS)	0.58-0.68	All NOAA and MetOp satellites
2 (0.86 µm, VEG)	0.73–1.00	All NOAA and MetOp satellites
3A denoted as 6 (1.61 µm, NIR)	1.58-1.64	Daytime observations only for NOAA-15 during 1st month of operation, disabled for remainder of lifetime. Daytime only for NOAA-17, MetOp-A and -B
3B denoted as 3 (3.74 µm, SIR)	3.55-3.93	All NOAA and MetOp satellites. Nighttime observations only for NOAA-15 during 1st month of operation (day and night for remainder of lifetime). Nighttime observations only for NOAA-17, MetOp-A and -B
4 (10.8 µm, IRW)	10.30-11.30	All NOAA and MetOp satellites
5 (12.0 µm, SWI)	11.50-12.50	All NOAA and MetOp satellites except TIROS-N, NOAA-6, -8, and -10

The GAC filename indicates 1) the year and day of year at the time of the first observation recorded in the file, 2) a string to identify the NOAA or IJPS satellite carrying the particular AVHRR instrument (see Table 1, last column), 3) the start and end UTC time of the data in the file, 4) the processing block ID, and 5) the ground station that received the data. For example, the filename: NSS.GHRR.NN.D08274.S2336.E0127.B1733940.GC indicates that this is a NOAA-18 file from day 274 of year 2008, beginning at 2336 UTC on day 274 and ending at 0127 on day 275. The data were received at the Gilmore Creek, Alaska ground

station (GC). The processing block ID, beginning with the character B followed by a string of 7 numbers, is disregarded because it is not relevant to this TCDR.
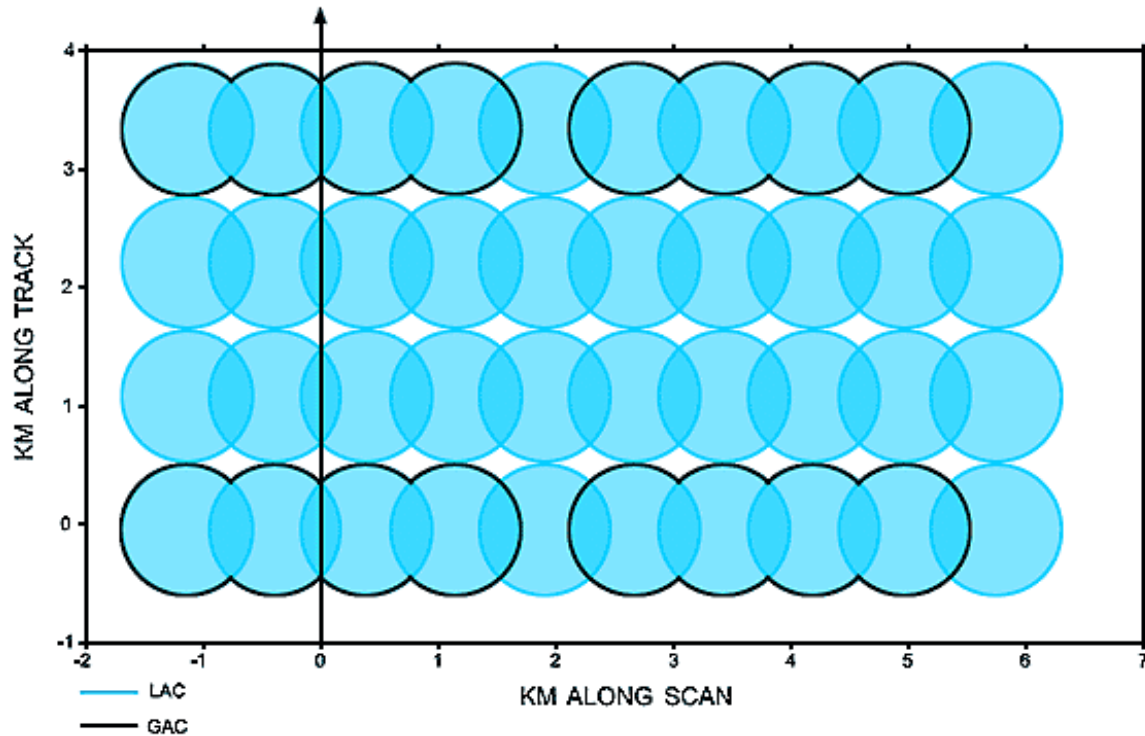
Figure 5: Schematic showing relationship between full (LAC or HRPT, in blue) and reduced resolution (GAC, in blue with black border) data. From Figure 4.1 at: http://oiswww.eumetsat.org/WEBOPS/eps-pg/AVHRR/AVHRR-PG-4ProdOverview.htm

3.   Algorithm Description

3.1   Algorithm Overview

The CERES Cloud Mask and Cloud Property Retrieval System (CCPRS), initially designed to use MODIS and VIIRS data, is adapted in this TCDR to utilize the 4-6 channel AVHRR 4-km GAC data. To make it more general, because forms of this set of algorithms are applicable to many different satellites, the basic algorithms based on the CCPRS are designated as the Satellite ClOud and Radiative Property retrieval System (SatCORPS). Versions of this algorithm that are designed specifically for application to various types of satellite imagers will be indicated with a hyphenated suffix index. For example, the primary AVHRR-based variant of SatCORPS will be indicated by the suffix A1. SatCORPS-A1 covers the algorithms that use channels 1, 2, 3B, 4, and 5 both day and night. SatCORPS-A2 uses channels 1, 2, 3A/3B, 4, and 5; A3 uses 1, 2, 3B, and 4 only. Subsequent variants, such as new versions or satellite-specific alterations, can be denoted with appropriate suffix indices separated by a decimal point. The suffixes are required only when referring to the specific form of the algorithms.

3.2   Processing Outline

A schematic overview of SatCORPS-A is presented in Figure 3. Processes or input/output are indicated with single-letter labels that are referenced in the following discussion.

(A) Two days of AVHRR orbits encompassing 28-30 GAC Level 1B files are simultaneously submitted for processing by the SatCORPS-A. (B) Each Level-1B orbit file is first navigation-corrected and noise-filtered by pre-processing software. The orbit is then broken into 1000 scan line segments, and the solar channel raw counts, thermal channel BTs, image navigation, pixel viewing, solar zenith, and relative azimuth angles (VZA, SZA, and RAA, respectively), and scan line date/time data are read into the SatCORPS-A. The 0.63, 0.86, and 1.61-µm (when available) channels are then calibrated using gains derived using the procedures described by Doelling et al. (2015). Application of these gains normalizes the AVHRR solar channel reflectances to the corresponding Aqua MODIS observations and accounts for differences in the channel responses. The process and resulting calibration coefficients are described by Doelling et al. (2015). Use of these MODIS-normalized reflectances within the SatCORPS-A minimizes the potential for instrument-induced trends in the TCDR products affected by such measurements and ensures that level-1 solar data are consistent with those used for the CERES cloud property data record that is based on MODIS data. Applying the SatCORPS-A to the normalized AVHRR data should yield a TCDR that is as consistent as possible with the CERES cloud CDR. It effectively extends the CERES cloud product back to 1979 from 2000, leading to an algorithmically consistent cloud property CDR for 1979 through, at least, 2014. No attempt is made to account for any thermal channel deviations from the nominal calibration (e.g., Trishchenko et al. 2002) in this version of SatCORPS-A. (C) Atmospheric temperature, specific humidity, pressure, and height profiles, in addition to surface skin temperature, 10-m temperature, and (E)

snow/ice cover are read from MERRA reanalysis files (Rienecker et al. 2011). The MERRA data are linearly interpolated to the time of the AVHRR observation.

(K) The AVHRR pixel data are then processed in small tiles having a dimension of 12 scan lines x 8 pixels. This tile size closely approximates the areal coverage of the tile used in CCPRS processing and is also close to the size of a CERES scanner FOV at nadir. The appropriate MERRA data and ancillary fields listed in Section 3.3.2 below are associated with the center coordinate of the tile. Atmospheric attenuation is then computed for every layer in the MERRA profile and parameterizations are employed to estimate the clear-sky TOA radiances (J) VIS reflectance and (I) various BTs in the tile for each AVHRR channel, except channel 2, based on the (G) surface albedo or skin temperature, (F) surface type, (E) snow conditions, (D) surface emissivity, and (H) atmospheric attenuation parameters.

(N) In the cloud mask, observed AVHRR TOA calibrated reflectances and BTs are matched with their corresponding clear-sky TOA values and numerous other ancillary inputs to discriminate between cloudy and clear pixels. (M) For clear-sky pixels, (Q) a method to retrieve land and ocean surface skin temperature is then applied. (L & O) For cloudy pixels, (P) one method from a set of three techniques (i.e., VISST, VINT, or SIST) is selected and applied to retrieve the cloud properties listed in Section 2.1. Selection of the method used to retrieve the cloud properties depends on the SZA and the available channels. For most satellites, the VISST is applied during daytime and the SIST is applied at night. Night is defined as times when the SZA > 82°. The VINT is used when channel 3B is unavailable during the day. For those cases, the retrieval of cloud effective particle size relies mainly on the NIR channel instead of the SIR channel. The retrievals require (R) a set of cloud reflectance and emissivity models to characterize the expected TOA reflectances and BTs expected for a given cloud phase, cloud effective radius (CER), cloud optical depth (COD), and cloud effective height (CEH) over the center of the tile at the SZA, VZA, and RAA of the observations. The cloud mask and the retrieval methods, VISST and SIST, are described by Minnis et al. (2008a and b) and Minnis et al. (2011a and b) and summarized in Section 3.4. VINT is the same as VISST except that it substitutes channel 3A reflectances for channel 3B BTs. (S) The cloud and clear-sky property retrievals and other relevant ancillary information are written to a NetCDF-4 format file for each of the 1000 scan-line segments comprising an AVHRR orbit segment. After all segments from an orbit are complete, the scan-line segment NetCDF files are merged into a single orbit file along with the necessary Climate and Forecast (CF) metadata describing each of the parameters and global file attributes.

```
┌─────────────┐  ┌──────┐   ┌──────────┐  ┌──────────┐  ┌──────────┐  ┌──────────┐
│      A      │  │   C  │   │    D     │  │    E     │  │    F     │  │    G     │
│ AVHRR GAC   │  │MERRA │   │ Surface  │  │  MERRA   │  │  IGBP    │  │Clear Sky │
│ Level 1B Solar│ └──────┘   │Emissivity│  │  Snow/   │  │ Surface  │  │Overhead  │
│ Channel Raw │            │   Map    │  │ Ice Map  │  │  Type    │  │ Albedo   │
│ Counts, IR  │            └──────────┘  └──────────┘  │   Map    │  │   Map    │
│ Brightness  │                                        └──────────┘  └──────────┘
│Temperatures │
│Default Image│
│ Navigation, │
│Viewing/Solar│
│  Geometry   │
│and Scan Time│
└─────────────┘
```
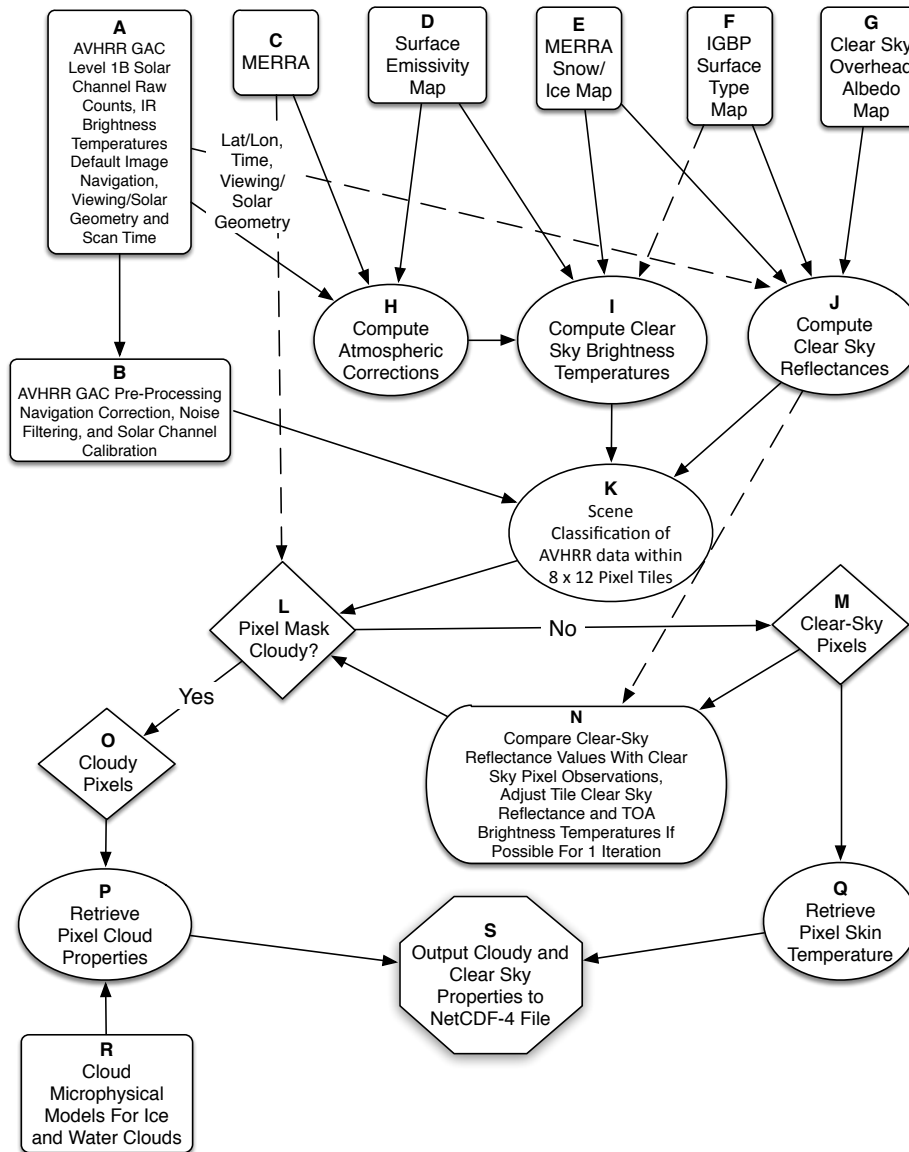
Figure 6: Processing outline of the SatCORPS-A.

3.3   Algorithm Input

This section describes the various input data needed to process the AVHRR GAC data using the SatCORPS-A.

3.3.1   Primary Sensor Data

AVHRR Level 1B GAC data are the primary sensor input for this TCDR. Level 1B data for the 1979-2014 time period were acquired from the NOAA Comprehensive Large Array-data Stewardship System (CLASS, http://www.nsof.class.noaa.gov).

3.3.2   Ancillary Data

The TCDR cloud and clear-sky property processing depends on the inputs below:

1) NASA MERRA 0.5° x 0.66° spatial resolution hourly 2-D fields
    a. Surface air temperature
    b. Surface specific humidity
    c. Surface pressure
    d. Surface geopotential height
    e. Surface skin temperature
    f. Surface ocean, lake, and land cover fraction
    g. Surface snow and ice cover fraction
    h. Tropopause pressure and temperature
2) NASA MERRA 0.5° x 0.66° spatial resolution 6-hourly 3-D profiles
    a. Air temperature
    b. Specific humidity
    c. Ozone
    d. Pressure
    e. Geopotential height
3) 10' spatial resolution, gridded land surface elevation Z_s from the GTOPO30 dataset used in the CCPRS (https://lta.cr.usgs.gov/GTOPO30)
4) 10' spatial resolution gridded condensed IGBP land surface cover type map from the CCPRS for the categories listed in Table 3
    (https://climatedataguide.ucar.edu/climate-data/ceres-igbp-land-classification)
5) 10' spatial resolution gridded water percentages WP, derived from the IGBP map and used in the CCPRS
6) 10' spatial resolution gridded surface spectral emissivities from the CCPRS (Chen et al. (2004), Minnis et al. 2008a and references therein)
7) 10' spatial resolution gridded and dynamically-generated clear-sky VIS reflectance maps based on clear-sky AVHRR observations
8) Directional and bi-directional reflectance distribution factors for snow/ice-free and snow/ice-covered land and water surfaces (Minnis et al. 2008a; Chen et al. 2010)
9) Cloud microphysical reflectance and albedo LUTs for spherical water droplets and roughened hexagonal column ice crystals (Yang et al. 2008a,b).

Table 3. IGBP surface types (general type used for model selections).

1. evergreen needleleaf (conifer)
2. evergreen broadleaf (conifer)
3. deciduous needleleaf (deciduous)
4. deciduous broadleaf (deciduous)
5. mixed forests (1/2 conifer + 1/2 deciduous)
6. closed shrublands (mosaic)
7. open shrubland (mosaic)
8. woody savannas (grass)
9. savannas (grass)
10. grasslands (grass)
11. permanent wetlands (1/2 grass + 1/2 water)
12. croplands = grass
13. urban
14. mosaic (1/2 grass + 1/2 mixed forest)
15. snow/ice
16. barren/sparsely vegetated (desert)
17. water
18. tundra (1/2 grass + 1/2 water)
19. coastline (10% to 90% water)

3.3.3   Data Navigation, Filtering, and Adjustment

As described in Section 3.1.1, AVHRR GAC Level 1B data acquired from the NOAA CLASS system is the primary sensor data used in this TCDR. Simpson and Yhann (1994) and references therein together with our practical experience reveal that the original Level 1B data exhibit a number of issues that render the data unsuitable for direct input into TCDR processing. These problems include:

1) Random bad scan lines throughout an orbit

2) Navigation errors up to 200 km in magnitude

3) Periodic striping in pre-NOAA-15 SIR data

4) Noise at very cold SIR BTs, most notably in pre-NOAA-15 data

5) Noise at very warm SWI BTs, noted in NOAA-9 data but possibly present in other satellites.

An AVHRR pre-processing software package (referred to as SAPS hereafter) has been developed to address these issues to the fullest possible extent. This software ingests a GAC Level 1B file, correctly navigates and noise filters the data, and writes out a NetCDF-4

file that includes all the parameters needed by the SatCORPS-A. SAPS processes a typical GAC file in approximately 75 seconds. Details of the SAPS are provided in Appendix B.

3.3.4   Forward Models

Forward models are used to compute the expected clear-sky VIS ρ_{cs1} and, when necessary, NIR ρ_{cs6} reflectances and expected TOA clear BTs for the SIR, IRW, and SWI channels, T_{cs3}, T_{cs4}, and T_{cs5}, respectively. They are also used to compute the atmospheric attenuation of the radiances in each layer of the atmosphere and to compute the TOA radiances for each channel for specified cloud conditions. These models employ LUTs and parameterizations that are discussed in Sections 3.3.5 and 3.3.6, respectively. The LUTs are based on calculations using adding-doubling (e.g., Minnis et al. 1998) and discrete ordinates (Stamnes et al. 1988) radiative transfer models. For each tile computation, the surface temperatures, vertical profiles of atmospheric temperature and humidity from the model values are linearly interpolated in time and space to the center of the analysis tile and time of observation.

All emission model calculations are computed at a specific VZA. For the sake of clarity and brevity; the µ dependence is not explicitly specified in the following sections. Likewise, all reflectances are computed as functions of the illumination and viewing angles, θ_o, θ, and ϕ. Again these dependencies are not included in the notation below for clarity and brevity.

3.3.4.1   TOA thermal channel brightness temperatures

Consider an atmosphere with J layers and the top layer is 1. The simple model of brightness temperature used here is that, for a cloud with effective particle radius r and optical depth τ_i at some layer j within the atmosphere, the observed radiance for channels i = 3 - 5 can be represented as:

$$B_i(T_i) = L_{UiJ1} - L_{UiJj-1} + t_{UiJ1}\{[1-\varepsilon_i(\tau_i,r;\mu)][(1 - \varepsilon_{si})(L_{Di1J} - L_{Di1j}) + \varepsilon_{si} B_i(T_s)]$$

$$+ \varepsilon_i(\tau_i,r;\mu) B_i(T_j) / t_{UiJj-1}\} \tag{1}$$

where T_i is the equivalent blackbody temperature, T_j is the cloud effective radiating temperature, B_i is the Planck function, ε_{si} is the surface emissivity, and the effective cloud emittance ε_i approaches unity as the cloud becomes optically thick. The first two terms represent the radiance contributed by the atmosphere above the cloud; L_{UiJ1} is the upwelling radiance from the surface to the TOA and L_{UiJj-1} is the upwelling radiance from the surface to the base of the cloud in layer j. The third term includes the radiances from the cloud and the surface attenuated by the atmosphere. The downwelling radiation from the cloud is neglected. The upwelling transmissivities from the surface to the TOA and the surface to the cloud base are t_{UiJ1} and t_{UiJj-1}, respectively. The downwelling radiance from the atmosphere reaching the surface is given by $L_{Di1J} - L_{Di1j}$, where the first and second terms are the downwelling radiances at the surface for the atmospheric column and at

cloud top, respectively. The downward transmittance of the cloud and surface reflectance are approximated as the quantities, $[1-\varepsilon_i(\tau_i,r;\mu)]$ and $[1 - \varepsilon_{si}]$, respectively.

The upwelling layer transmissivity is t_j,= $\exp(-\tau_{ag}/\mu)$, where $\tau_{ag} = \Sigma \tau_{gl}$ for l = 1, K and K is number of gaseous absorbers in the spectral interval. The downwelling transmissivities are computed in the same manner, except that μ = 0.6 because the radiances are from a diffuse source. The optical depths are computed from the average concentration of the particular gas using the correlated k-distribution technique described by Goody *et al.* (1989) and Kratz (1995). In this approach, the discrete version of the spectral-mean transmissivity $t_{\Delta\omega}(u,p,T)$ is:

$$t_{\Delta\omega}(u,p,T) \cong \sum_{i=1}^{n} w_i ex\, p[-k_i(p,T)u], \qquad (2)$$

Given the cumulative transmissivities and atmospheric radiances computed for a given tile, it is possible to quickly compute $B_i(T_i)$ for a model cloud placed at any height providing the means to iteratively solve for T_c as discussed in the next section. Note, the clear-sky brightness temperature T_{csi} is computed using Eq (1) with τ_i = 0. If scattering in the cloud is neglected

$$\varepsilon_{ai} = 1 - exp(-\tau_{ai}/\mu), \qquad (3)$$

where the absorption optical depth $\tau_{ai} = (1 - \varpi_o)\tau_i$ and ϖ_o is the single-scattering albedo. The value of T_s is taken either from MERRA or from the clear portion of the tile. The clear-sky brightness temperature T_{csi} is computed using Eq (1) with τ_i = 0.

As seen in Figure 4, the AVHRR SIR channel is considerably wider than its MODIS counterpart and somewhat broader than the TRMM VIRS channel 3. This width and the fact that the SIR includes both solar and terrestrial components, requires a different formulation. The atmospheric absorption varies significantly across the bandwidth $\Delta\lambda$, the band sits between the peaks of the Planck function curves for both radiance sources, and the Planck radiance from each source changes differently with wavelength across the band. For the solar source, the radiance at 3.5 µm is larger than at 4.0 µm, while the opposite is true for the terrestrial radiance. Thus, the radiative transfer through the atmosphere is broken into five wavelength intervals $\Delta\lambda$ (gray lines in Figure 4). The up- and downwelling radiances and transmissivities are computed separately for solar and terrestrial radiances for each sub-band. The sub-band radiances and transmissivities are combined from both sources are combined at the end of the calculations to single values for the up and downwelling transmissivities.
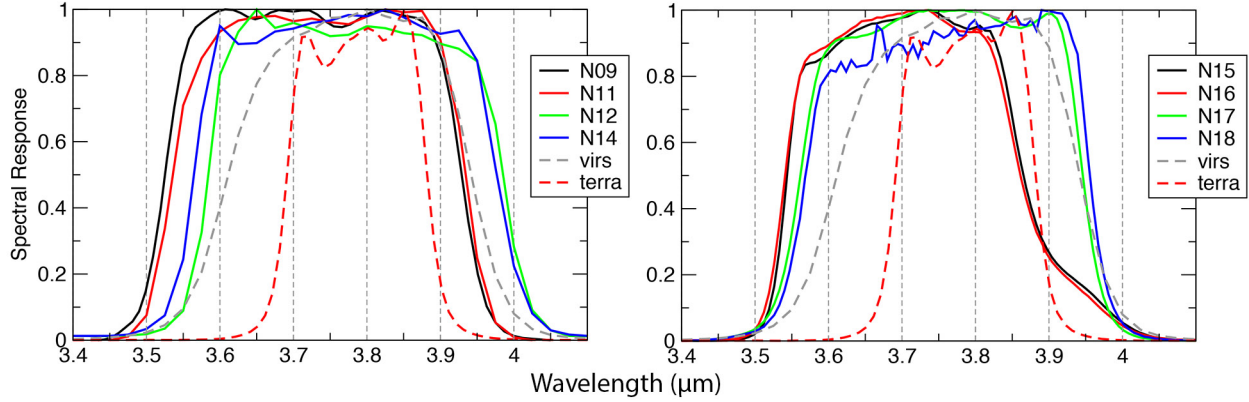
Figure 4: Spectral response functions for selected for the TRMM VIRS, Terra MODIS, and selected AVHRR (N*XX*) SIR channels. *XX* denotes the NOAA satellite number. Gray lines denote wavelength sub-interval boundaries for computing atmospheric attenuation.

Thus, for example, the upwelling emitted SIR radiance from the surface to an arbitrary layer (cloud base, in this instance) is

$$L_{3Uij-1} =$$
$$\sum_{m=1}^{5} \Delta\lambda_m \eta_m \{ L_{s3m} \prod_{k=j}^{j-1} t_{km} + (1 - t_{j-1m}) B_m(T_{j-1}) +$$
$$\sum_{k=j}^{j-2} (1 - t_{km}) B_m(T_k) \prod_{l=k-1}^{1} t_l) \} / \Delta\lambda, \tag{4}$$

where η is the normalized spectral response for subinterval *m* of channel 3B, B_m is the Planck function evaluated at the center wavelength of the sub-band, and the total radiance leaving the surface is

$$L_{s3m} = \varepsilon_{s3} B_m(T_s) + (1 - \varepsilon_{s3}) [L_{D31J} - L_{D31j}]. \tag{5}$$

Typically, $\Delta\lambda_m$ = 0.1 and η_m varies with each satellite sensor (see Figure 9). During daytime, the solar component of the SIR radiance must be taken into account. Thus, the observed radiance has an additional term:

$$B_3(T_3) = L_3' + \mu_o \, d_o \sum_{m=1}^{5} \Delta\lambda_m w_m \, \rho_{c3m} \, t_{U3mJ1} \, t_{D3mJ} / \Delta\lambda , \tag{6}$$

where L_3' is computed with Eq (1) after accounting for the sub-bands, d_o is the Earth-sun distance correction, the weight w_m is the product of η_m and the normalized solar constant for the sub-interval, and the combined surface and cloud reflected component is

$$\rho_{c3m} = [\rho_3(\tau, r; \mu_o, \mu, \phi) / t_{U3mJj-1}] + [t_{D3m1J} / t_{D3m1j}] [1 - \varepsilon_{a3} - \alpha_{c3}(\tau, r; \mu_o)] \rho_3', \tag{7}$$

where

$$\rho_3' = [1 - \varepsilon_{a3} - \alpha_{c3}(\tau, r; \mu_o)] \rho_{s3}(\mu_o, \mu, \phi) + [1 - \alpha_{cd3}(\tau, r) - \varepsilon_{ad}] \alpha_{cd3}(\tau) \alpha_{sd3}^2, \tag{8}$$

and α_{c3}, α_{cd3}, and ρ_3, from the channel-3 reflectance LUTs, represent the cloud albedo for a given incident angle, the diffuse cloud albedo, and the cloud bidirectional reflectance, respectively. The first term in Eq (7) accounts for the reflectance directly from the cloud, while the second term accounts for the contribution of the surface to the reflectance. It is approximated as a combination of primary and secondary surface reflectances. The primary assumes reflectance of the direct beam in the direction of the sensor and the secondary assumes that the second reflectance is diffuse and reflects the radiation originally reflected by the surface and scattered back by the cloud. Since the secondary term is usually very small relative to the first term, it and higher order reflectances are ignored.

These forward models are used to compute cloudy and clear-sky TOA BTs for a given scene and time at a specified viewing and illumination angle combination for both cloud phases over a range of CER, COD, and CEH values.

3.3.4.2   Solar channel reflectances

Over water surfaces, the VIS surface bidirectional reflectance ρ_{s1} and diffuse albedo α_{sd1} are computed as a function of wind speed using the model of Jin et al. (2006) with a sea-salt aerosol having an optical depth of 0.1. Over pure snow surfaces (IGBP type = 17), ρ_{s1} and α_{sd1} are interpolated from LUTs created from radiative transfer calculations. For snow-free land, the VIS bidirectional reflectance ρ_{s1} and diffuse albedo α_{sd1} are computed from the overhead sun clear-sky albedo of the 10' area closest to the center of the tile as discussed in Section 3.3.5.2. For non-permanent snow areas, estimates of snow-covered values of ρ_{cs1} and α_{csd1}, are based on a blending technique similar to that described by Chen et al. (2013). The values of the clear-sky parameters are computed in the following manner.

Surface albedo and reflectance are needed for cloud retrievals. Values for α_{sd1} and ρ_{s1} are estimated from the input clear-sky diffuse albedo α_{csd1} and the observed or estimated clear-sky reflectance ρ_{cs1}:

$$\alpha_{sd1} = 1.149\ \alpha_{csd1} - 0.0333 \tag{9}$$

$$\rho_{s1} = \rho_{s1}' - D\alpha_{sd1} / exp(-\tau_{R1J}/\mu_o), \tag{10}$$

where

$$\rho_{s1}' = [\rho_{cs1} / exp\ (-\tau_{g1J}(1/\mu + 1/\mu_o)) - \rho_{R1J}] / (1 - \alpha_{Rd1J}) \tag{11a}$$

$$D = (1+S)(1-\alpha_{R1J}-exp(-\tau_{R1J}/\mu_o)+S\ exp(-\tau_{R1J}/\mu_o) \tag{11b}$$

$$S = \alpha_{sd1}\ \alpha_{Rd1J} / (1 - \alpha_{sd1}\ \alpha_{Rd1J}) \tag{11c}$$

and τ_{g1J} is the total absorption optical depth for the gaseous absorbers, such as ozone, water vapor, and oxygen, for the particular VIS channel being used. It is computed using the correlated k-distribution technique. The diffuse albedo, directional, and bidirectional reflectance of the atmosphere due to Rayleigh scattering are given by α_{Rd1J}, α_{R1J}, and ρ_{R1J}, respectively. This formulation does not explicitly account for any aerosols, so that the

surface albedo and reflectance are actually more representative of the surface and aerosols combined. For a cloudy atmosphere, the TOA reflectance is approximated as

$$\rho_{TOA1} = (\rho_{acs} + \Delta R) \, exp(-\tau_{g1J}(1/\mu + 1/\mu_o)), \tag{12}$$

where ρ_{acs} is the combined reflectance from the cloud, atmosphere, and surface estimated using an adding parameterization, ΔR is a residual from the parameterization regression fit that depends on the scattering angle, and τ_{g1j} is the gaseous absorption optical depth above the cloud layer. The adding parameterization and regression fit for ΔR are given in detail by Minnis et al. (2011a).

The clear-sky NIR TOA reflectances are computed for cloud-free and cloudy skies in a similar manner. Assuming no scattering by the atmosphere and given the surface reflectance, ρ_{s6}, the clear-sky NIR reflectance is estimated as

$$\rho_{cs6} = t_{1N}(\mu_o)t_{1N}(\mu) \, \rho_{s6}, \tag{13}$$

where t_{1N} is the atmospheric transmissivity between the TOA and the surface. For cloudy conditions, the simulated TOA reflectance is approximated as

$$\rho_{TOA6} = t_{1M}(\mu_o)t_{1M}(\mu) \, \{\rho_{c6} + f_{dir} \, \rho_{dir} + (1-f_{dir}) \, \rho_{dif}\}, \tag{14}$$

where t_{1M} is atmospheric transmissivity between the bottom of the cloud layer, ρ_{c6} is the modeled NIR cloud reflectance, and the TOA and the fraction of direct radiation passing through the cloud is

$$f_{dir} = exp(-0.5 \, \tau_6/\mu_o) / (1 - \alpha_{c6}(\mu_o)], \tag{15}$$

where $\alpha_{c6}(\mu)$ is cloud albedo at μ. The reflectance due to the direct solar beam passing through the cloud, reflecting from the surface and passing back through the cloud in the direction of the sensor is

$$\rho_{dir} = t_{M1N}(\mu_o)t_{M1N}(\mu) \, \rho_{s6} \, exp[-0.5 \, \tau_6'(1/\mu_o+1/\mu], \tag{16}$$

where t_{M1N} is the transmissivity of the atmosphere below the cloud (layers $M+1$ through N). The diffuse reflectance from the surface back through the cloud is parameterized to include three reflections between the cloud base and the surface. It is approximated as

$$\rho_{dir} = [1-A_{cd6} - \alpha_{cd6}] \, \kappa_{dif} \, [1+ \kappa_{dif} \, \alpha_{cd6} \, (1 + \alpha_{cd6} \, \kappa_{dif})], \tag{17}$$

where

$$\kappa_{dif} = t_{M1Nd} \, \alpha_{sd6} \, [1-A_{c6}(\mu_o)-\alpha_{c6}(\mu_o)], \tag{18}$$

A_{c6} is the cloud absorptance, α_{sd6} is the diffuse surface albedo, A_{cd6} is the diffuse cloud absorptance, α_{cd6} is the diffuse cloud albedo, and t_{BNd} is the two-way diffuse transmittance of atmospheric layer below the cloud. The atmospheric layer gaseous optical depths used to compute the transmissivities above and below the cloud layer are computed using the correlated k-distribution method for the appropriate spectral interval.

These forward calculations are used to estimate the clear-sky reflectances used in the scene classification procedure and the TOA BTs and reflectances in cloudy conditions to match with the observed values as discussed below.

3.4   Theoretical Description

The approach taken by SatCORPS-A is similar to that used for the CERES CCPRS. All processing is performed on 8x12 pixel tiles for which the average expected clear-sky radiances and the layer attenuation parameters have been computed. Within the tile each pixel is classified as clear or cloudy by determining if one or more of the channel radiances differs substantially from the expected clear-sky values or channel BT difference values meet certain thresholds. If a pixel is identified as clear, then its radiances can be used to update the clear radiances for the tile and possibly to update the expected clear-sky albedo value for the observed region. The surface skin temperatures of the clear pixels in each tile are also estimated if certain criteria are met. If the pixel is cloudy, then three spectral radiances are compared to corresponding radiances computed using the forward models for specified cloud properties. By iteration, the optimal match between the observed and modeled radiances is obtained simultaneously yielding COD, CER, and CET. From these parameters, additional quantities, including CEH, CTH, CBH, etc., are estimated using empirical parameterizations. The shortwave (SW) and longwave (LW) outgoing fluxes are estimated from the radiance data using empirical formulas relating broadband and narrowband fluxes.

3.4.1   Physical and Mathematical Description

Many of the fundamentals and mathematical descriptions of the SatCORPS-A cloud mask and retrieval modules are detailed in Minnis et al. (2008), Trepte et al. (2002), Minnis et al. (2011), and references therein. The following discussion will provide an overview of the SatCORPS-A and only the mathematical or schematic description deemed necessary for understanding the overview is included. Any differences in algorithms between the SatCORPS-A and those described in the references or new advancements since the papers' publication are explained in detail.

The detection and retrieval of clouds and their properties are based on the assumption that the combination of the different channel radiances emanating from a particular scene depends on the spectral properties of the scene components and that each component has a unique set of spectral signatures. Thus, by examining the spectral radiances, it is possible to identify the components comprising the scene (clear, cloudy, etc.). The observed radiance at a particular wavelength depends, to varying degrees, on the temperature, concentration, habit, phase, and size of the cloud particles as well as the thickness of the cloud. Specifically, for the algorithms described here, the IRW (10.8 μm) BT, T_4, primarily depends on effective cloud temperature (CET) T_{eff}, while the VIS channel reflectance ρ_1 is mainly determined by the cloud optical depth (COD) τ, which is the convolution over the thickness of the cloud of the hydrometeor concentration or number density N, the extinction coefficient Q_e, and the effective cross-sectional area of the particle. The last variable is defined as the cross-sectional area of a droplet having the effective radius CER,

$$r_e = \frac{\int_{r_1}^{r_2} r \pi r^2 n(r) dr}{\int_{r_1}^{r_2} \pi r^2 n(r) dr}, \tag{19}$$

where the integration is over a size distribution having the number density of particles $n(r)$ of radius r between r_1 and r_2. Thus,

$$\tau_\lambda = \pi Q_e \int_{z_1}^{z_2} N r_e^2 dr. \tag{20}$$

Similarly, the ice crystal effective radius for ice clouds is defined in the same manner except that the ice crystals within a given size distribution are first converted to equivalent spheres before solving Eq (19). The cloud liquid or ice water path, or cloud water path can be computed as

$$CWP = 4 \rho \tau r_e / 3 Q_e, \tag{21a}$$

where the water density, which is 1.0 and 0.9 g cm^{-3} for liquid and solid water, respectively. In this formulation, it is assumed that r_e is constant throughout the depth of the cloud. Since the value of r_e retrieved using the SIR channel corresponds to an optical depth of $\sim$3 or less at the top of the cloud, it is not necessarily representative of the entire cloud. The adiabatic approximation

$$LWP = 10 \tau r_e / 9 Q_e. \tag{21a}$$

has been found to provide more accurate results if r_e is retrieved using the MODIS 2.1-μm channel (Seethal and Horvath, 2010). It is not necessarily more accurate when using the SIR retrieval of r_e, although it appears to be more accurate for marine stratus clouds (e.g., Painemal et al. 2012). CWP can be computed from r_e and τ values retrieved by the SatCORPS-A using any desired formula. The SatCORPS-A uses Eq (21a) for all CWP computations.

CET is the effective radiating temperature of the cloud and typically is located at distance from cloud top corresponding to a COD value of $\sim$ 1.1. It varies with VZA. CEH is determined from CET and the cloud top and base heights, CTH and CBH, are derived from empirical methods based on CET, phase, and COD. The surface skin temperature T_{skin} is estimated for clear pixels when certain conditions are met. Longwave (LW) flux and shortwave (SW) albedo are estimated from the narrowband AVHRR channels using empirical relationships.

3.4.1.1 AVHRR Scene Classification

The AVHRR scene classification is one of the two main parts of the SatCORPS-A, which is shown schematically in Figure 3. Specifically, this section describes the algorithms that constitute process (K) in Figure 3.

To define a pixel as cloudy or clear (cloud mask), the system ingests the radiance and ancillary data described earlier on a pixel tile basis. Each tile consists of an array of pixels defined by 12 scan lines and 8 elements, corresponding at nadir to 36 km x 32 km which

approximates the 32 km^2 tile size used by the CCPRS. Although each pixel is analyzed individually, all pixels within a given tile use the same predicted clear radiances and atmospheric corrections in the retrieval.

After ingesting the input data, the expected clear-sky radiances and clear-cloudy thresholds for the tile are computed for each channel, and the observed radiances are compared to the thresholds to determine if each pixel within the tile is clear or cloudy. If cloudy, the pixel is passed to the cloud property retrieval component where cloud properties are determined. If no valid results can be obtained, the pixel is given a no-retrieval classification and tested within that system to determine if it warrants a clear classification. If categorized as clear in the original mask, the pixels may be used to update the clear radiance map for a given 10' region and then are passed into the cloud property retrieval subsystem along with any cloudy pixels from the same tile. The predicted clear-sky radiances for the tile are also passed into the retrieval subsystem.
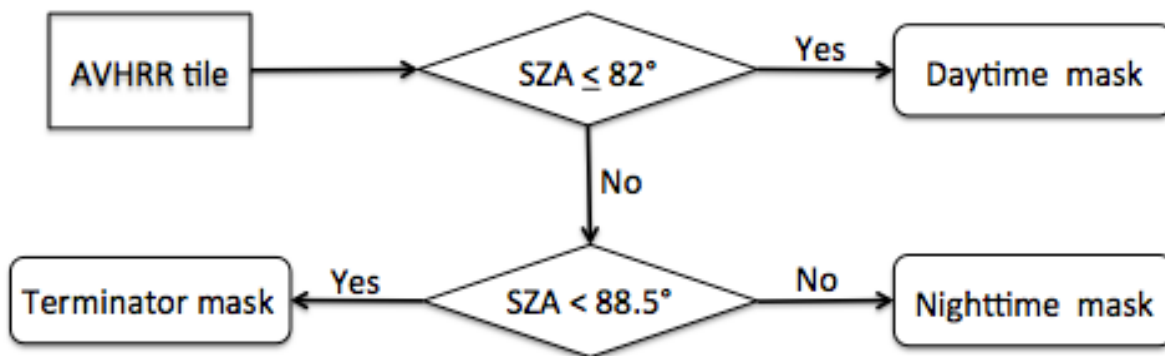
Figure 5: Cloud mask selection process.

Pixel classification uses a selected set of threshold tests and logic that depend on the SZA at the center of the tile, as illustrated in Figure 5. For SZA < 82°, the daytime set of tests is used (Figure 6). Otherwise, the nighttime or terminator mask is applied. The mask uses up to three sets of sequential tests, designated A, B, and C for daytime and A, D, and E for terminator or night. These are described in the remainder of this section. The actual formulations will vary depending on the available complement. All of the tests described here are for SatCORPS-A1. Any tests requiring the SWC will be altered for SatCORPS-A3, while those using SIR data during the day will be altered for SatCORPS-A2.

The first step (A test) in all cases is to check T_4 to determine if it is colder than a preset temperature limit, T_{lim}. The value of T_{lim} is equal to the temperature at 500 hPa over land or to 260K over water. It is not used if $T_s < 270$ K or if $Z_s > 4$ km. If the A test is positive, the pixel is classified as a good cloud. Otherwise, the B and D tests are applied during daytime and nighttime, respectively. These tests determine if T_4, ρ_1, and BTD$_{34}$ differ from each of their expected clear-sky counterparts by the thresholds σ_{cs4}, σ_{cs1}, and σ_{cs34}, respectively, which are estimates of the combined spatial and temporal standard deviation of the expected clear-sky value for the particular tile. BTD$_{34}$ is the difference
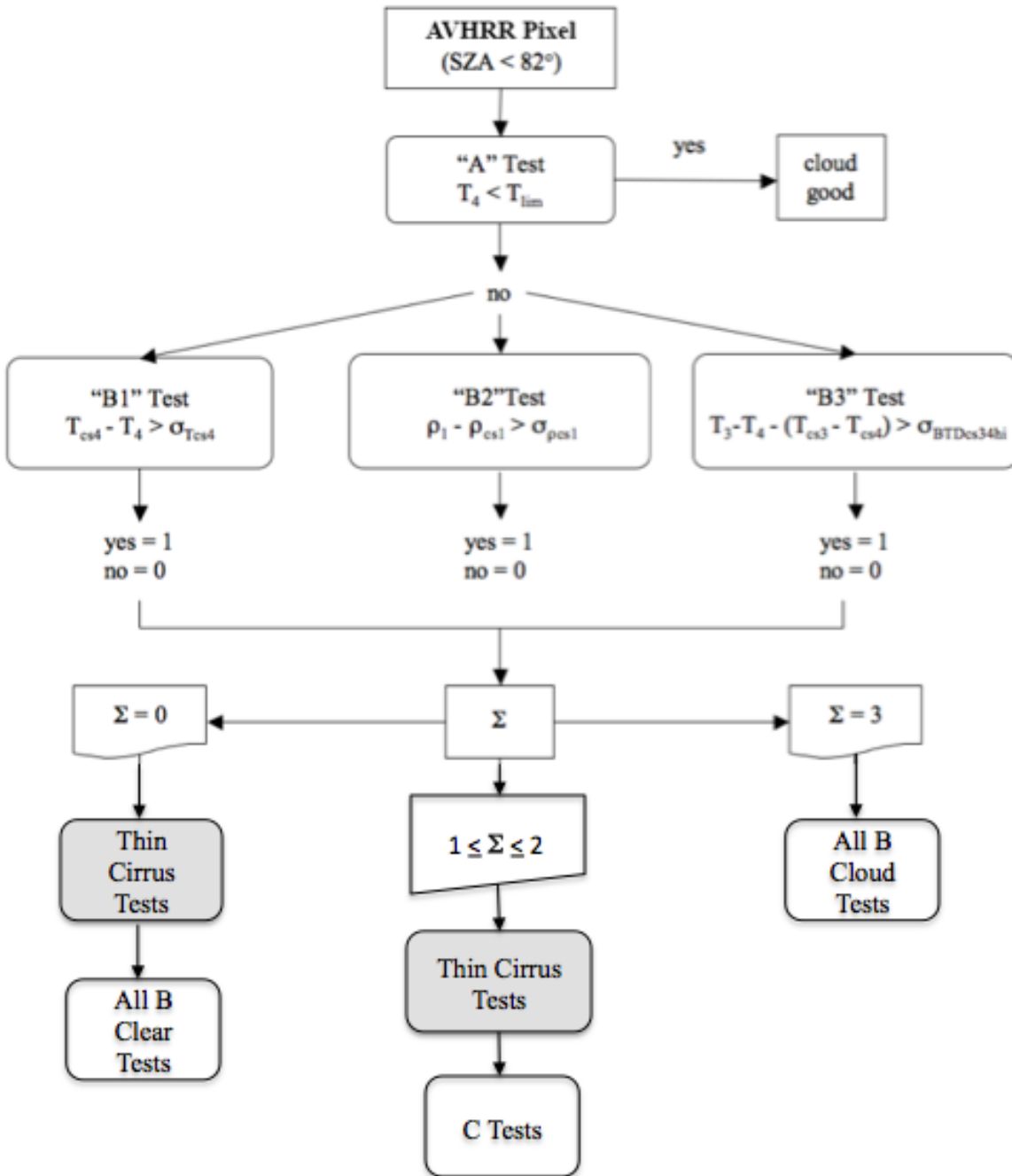
Figure 6: Schematic overview of daytime scene identification algorithm.

between the T_3 and T_4. Tests B1 and D1 rely on the fact that clouds typically radiate at temperatures that are less than those at the surface, unless they occur where significant surface radiative cooling occurs. Also, accurately predicting the surface radiating temperature is often difficult over land. Test B2 is based on the assumption that a cloud will generally cause an increase in ρ_1 relative to the background. Exceptions to this

land

open ocean

$$T_{cs4} - T_4 > 2 \ \& \ T_3 - T_4 > T_{cs3} - T_{cs4} + 1$$
$$\& \ (T_4 - T_5 > T_{PW45} \text{ or } T_4 - T_5 > \sigma_{ci})$$

yes   no

thin Ci clouds

$$T_{cs4} - T_4 > 2.5K \ \&$$
$$T_4 - T_5 > \sigma_{ci} \ \& \ T_4 - T_5 > T_{cs4} - T_{cs5} \ \&$$
$$\rho_1 - \rho_{cs1} > \sigma_{cs1} \ \& \ \rho_1/\rho_3 > 1.4$$

$$T_4 - T_5 > \sigma_{ci} \ \& \ \rho_2/\rho_1 < 1.1 \ \&$$
$$T_3 - T_4 > T_{cs3} - T_{cs4} \ \& \ T_3 - T_4 > 7$$

yes   no

thin Ci clouds

thin Ci clouds   clear good

land: $T_{45PW} = T_{cs4} \ T_{cs5} - 0.5K.$
desert.: $T_{45PW} = -0.845 + 1.3918*PW - 0.128*PW^2.$
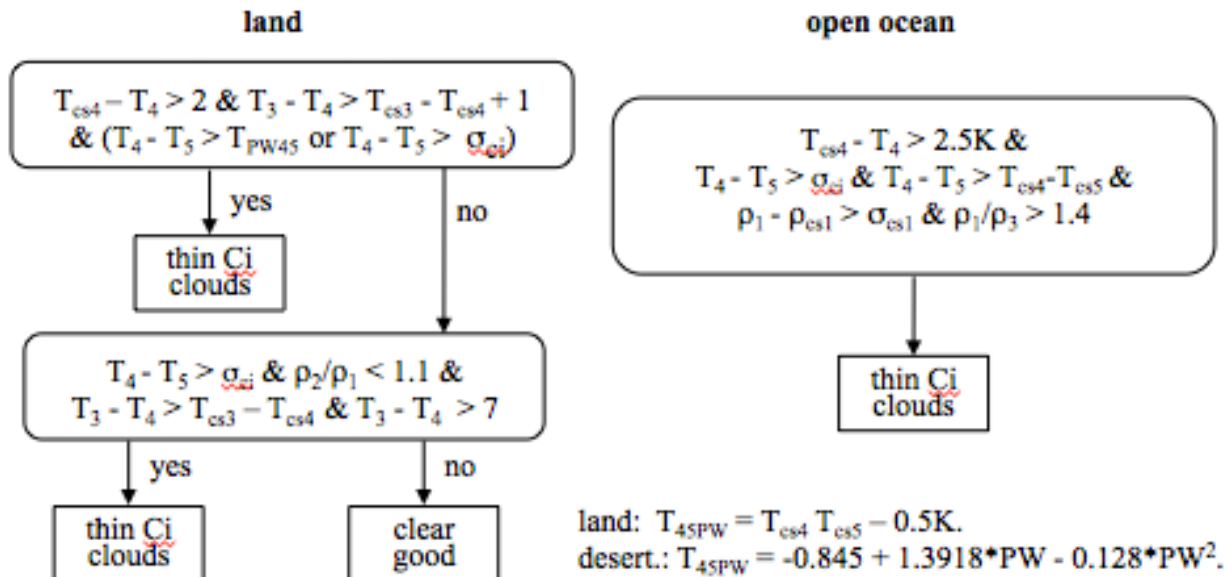
Figure 7: Daytime thin cirrus tests for SatCORPS-A1.

expectation include thin clouds at certain angles (e.g., Minnis et al. 1991), low clouds in the shadows of higher clouds, the presence of heavy dust, or moderately thin clouds over bright surfaces. Test B3 is based on the fact that in the SIR wavelength range, clouds increase the reflectance of the solar radiation in the band relative to that from the surface and hence raise T_3. Thus, during the daytime, T_3 for a cloudy pixel should be greater than that for a clear pixel. BTD$_{34}$ is used instead of T_{cs3} because the predicted difference is not particularly sensitive to typical errors in the modeled surface temperature. Thus, the test compares the predicted clear-sky and observed BTD$_{34}$. High clouds shadowing low clouds tend to eliminate the reflected component, so that B3 is not always reliable during the daytime. For SATCORPS-A2, the B3 test is replaced by ($\rho_6 - \rho_{cs6} > \sigma_{\rho cs6}$).

If all three B tests fail, the pixel is tentatively considered to be a strong (good) clear pixel. The pixel is further examined first with thin cirrus checks and, if still clear, up to three additional tests (All B Clear Tests): high clouds shadowing low clouds, small 'tradewind cumulus' test over ocean, and a snow test over high latitude land. The thin cirrus tests (Figure 7) utilize various thresholds including the cirrus threshold σ_{ci}, which is taken from Gustafson et al. (1994). If all three B tests are positive, then the pixel is tentatively classified as a strong cloud and subject to as many as two additional tests (All B Cloud Tests): strong sunglint test and a desert test. For polar regions, other tests may be applied as discussed below. For pixels that pass only 1 or 2 B tests, the radiances are examined further. They are checked to see if thin cirrus clouds are in the scene. The BTD$_{45}$ (i.e., $T_4 - T_5$) is compared to two different clear-sky estimates of the difference: values of σ_{ci} and empirical values over land based on the total column precipitable water (PW) as indicated in Figure 7. The comparison determines if the pixel contains a thin cirrus cloud. Differences in the absorptive properties of ice at the IRW and SWI wavelengths cause BTD$_{45}$ to increase

above its background radiance for thin cirrus clouds. If the thin cirrus test is positive, the pixel is classified as a cloud. Otherwise, it is classified using one of six C test sets (Table 4) that is selected based on the particular combination of B tests that passed or failed. The thin cirrus test and other tests using BTD_{45} were altered to use various combinations of BTD_{34}, VIS, and IRW values for SatCORPS-A3, since T_5 is unavailable.

The C tests are discussed by Minnis et al. (2008a) for the CERES Edition 2 MODIS mask algorithms. Some of those tests have been slightly altered for CERES Edition 4. Except for the updated C test sets that utilize thermal channels unavailable on the AVHRR (e.g., 6.7 µm), they are the same for SatCORPS-A unless otherwise noted. Other CERES CCPRS tests utilize the 1.6 or 2.13-µm reflectances from MODIS. If additional information is contained in the VEG channel, then ρ_2 replaces those MODIS reflectances in the relevant tests. Otherwise, those specific tests are not used in the SatCORPS-A. The C tests tighten or loosen the σ values and utilize additional radiances from available channels (ρ_2 and T_5). Since T_3 is unavailable for SatCORPS-A2, parallel sets of All-B and C tests were developed using ρ_6, ρ_{cs6} and $\sigma_{\rho cs6}$ in place of tests involving channel 3. In some cases, the tests are quite different.

For example, Figure 8 shows the AVHRR version of the C1 test over land for SatCORPS-A1/3. A different version is used for SatCORPS-A2. It is much simpler than that used for the MODIS retrievals (Figure 9 in Minnis et al., 2008a) because several sets of tests were eliminated because some MODIS tests use NIR channels unavailable on AVHRR. In addition to identifying a cloud or clear pixel as weak or strong (good), the C tests can also classify a clear pixel as having a surface that is covered by snow, obscured by smoke, aerosols, fire, or in sunglint conditions. They can also indicate whether the cloud is shadowed or viewed in sunglint.

During the night (Figure 9), when there is no T_3 solar component, the BTD_{34} tests rely on differences between the cloud optical properties at SIR and IRW wavelengths. Scattering of SIR radiation by water droplets tends to reduce emission and as the cloud thickens, T_3 drops below T_4. Thus, for thicker low clouds, BTD_{34} tends to be negative at night. This basis for test D3 is less reliable for thin low clouds. For thin ice clouds, BTD_{34} increases to a maximum at $\tau \sim 4$ and then decreases with increasing COD (e.g., Figure 21 of Minnis et al. 1998). This increase in BTD_{34} for high clouds is the basis for the D2 test. For thicker ice clouds, BTD_{34} would be become negative and more reliance on D1 is required. Similarly, for optically thin clouds or those with very large particles, BTD_{34} and tests D2 and D3 become less reliable. Tests D2 and D3 are mutually exclusive, so only one of them can be satisfied for a given pixel.

Table 4. Selection of C and E tests based on B/D test results.

Daytime B Test Set Results	Daytime C Test Set Selection	Nighttime D Test Set Results	Nighttime E Test Set Selection
B1 = 0, B2 = 1, B3 = 1	C1	D1 = 1, D2 = 1, D3 = 0	E1
B1 = 0, B2 = 0, B3 = 1	C2	D1 = 0, D2 = 0, D3 = 1	E2

B1 = 0, B2 = 1, B3 = 0	C3	D1 = 0, D2 = 1, D3 = 0	E3
B1 = 1, B2 = 0, B3 = 1	C4	D1 = 1, D2 = 0, D3 = 1	E4
B1 = 1, B2 = 0, B3 = 0	C5	D1 = 1, D2 = 0, D3 = 0	E5
B1 = 1, B2 = 1, B3 = 0	C6		

B tests pattern: (a) IR = 0, (b) VIS = 1, (c) 3-4 = 1

snow tests
$T_{skin} < 277K$ or Snow Map = 1 or Ice Map > 0
and $T_4 < 277$ and $\rho_1 - \rho_{cs1} > 2\sigma_{cs1}$ and
(solzen < 70 and $T_3 - T_4 < 6$) or
(solzen >= 70 and $T_3 - T_4 < 4$ and $T_{cs4} - T_4 < 0.5*\sigma_{cs4}$)

clear snow

no

b: $\rho_1 - \rho_{cs1} > 1.5\sigma_{cs1}$
c: $T_3 - T_4 - (T_{cs3} - T_{cs4}) > *rlx\_fctr*\sigma_{cs34}$
yes = 1   no = 0

b=1 c=1   b=1 c=0   b=0 c=1   b=0 c=0

smoke tests over forest
$T_{cs4} - T_4 > 0.5*\sigma_{Tcs4}$

yes   no

clear smoke   clear weak

$T_{cs4} - T_4 > 2.5$ or $\rho_1 - \rho_{cs1} > 3\sigma_{cs1}$

yes   no

cloud good   clear weak

smoke tests over forest
$\rho_1 - \rho_{cs1} < 3\sigma_{cs1}$

yes   no

clear smoke

$T_{cs4} - T_4 > 2.5$ or $\rho_1 - \rho_{cs1} > 3\sigma_{cs1}$

yes   no

cloud good   clear weak

$T_{cs4} - T_4 > 2.5$

yes   no

cloud good   clear weak

*rlx_fctr = 2.0 for desert
= 1.5 for land

fire tests over forest
$T_3 > 314$ K & $T_3 - T_4 > 10K$
$\rho_1 - \rho_{cs1} < 2\sigma_{pcs1}$

clear fire

Figure 8: C1 test over land for SatCORPS-A1/3.

AVHRR Pixel
(SZA > 82°)

"A" Test
$T_4 < T_{lim}$

yes → cloud good

no

"D1" Test
$T_{cs4} - T_4 > \sigma_{Tcs4}$

"D2" Test
$T_3 - T_4 - (T_{cs3} - T_{cs4}) > \sigma_{nBTDcs34hi}$

"D3" Test
$T_3 - T_4 - (T_{cs3} - T_{cs4}) < -\sigma_{nBTDcs34lo}$ *

yes = 1
no = 0

yes = 1
no = 0

yes = 1
no = 0

$\Sigma = 0$

Σ

can not = 3 •

All D Clear tests

$1 <= \Sigma <= 2$

• Because D2 and D3 can not equal to 1 at the same time.

"E" Tests

* $\sigma_{nBTDcs34lo} = \sigma_{nBTDcs34hi} - 0.5K$

Figure 9: Same as Figure 6, except for night.

a: $T_{4cs} - T_4 > 0.5\sigma_4$
b: $T_3 - T_4 > T_{3cs} - T_{4cs} + 1.5\sigma_{cs34}$

Figure 10: Schematic of nighttime E3 test for SatCORPS-A1/2.

If all D tests fail, then the scene is conditionally clear. Otherwise, one of the five E tests is performed (Table 4). Like the C tests during the day, in the E tests, the values of σ are loosened or tightened and additional checks are performed. Figure 10 shows the diagram of test E3, which is the SatCORPS-A1/2 version of the test shown in Figure 16 of Minnis et al. (2008a) that was mislabeled as E1.

Additional tests are performed for pixels in polar regions in general or for specific areas within the polar regions. These areas are defined by flags that are set equal to 1, if they meet the criteria in Table 5. These special tests are used because the signal-to-noise ratio increases for T_3 as the temperature decreases and other tests are not as effective in those areas. They were developed empirically through visual examination of multispectral imagery and testing against Cloud-Aerosol Lidar and Infrared Pathfinder Satellite Observation (CALIPSO; Winker et al., 2007) lidar cloud detections. These tests are listed below where the symbol "&" refers to "and".

Table 5. Criteria for setting special regional flags.

Flag	Criteria
Polar, POL	$\lvert LAT \rvert > 55°$ and $\{(T_s < 275$ K and Snow $= 1)$ or (Ice % $> 0)\}$
Antarctica, ANT	LAT $< -60°$ and $Z_s > 2.5$ km and SCP $= 1$
Super Cold Plateau, SCP	$(T_s < 230$ K and $T_4 < 230$ K and $Z_s > 1.0$ km and Ice % $= 100)$ or (IGBP $= 15$ and $Z_s > 2.5$ km)
Open Water Flag, OWF	WP $= 100$ and Ice % $= 0$ and IGBP $= 17$ and $T_s > 270$

For daytime,

1. *If All B cloudy, reclassify as clear snow if* POL $= 1$ &
$[T_4 - T_{cs4} > 2\sigma_4$ & $\rho_1/\rho_3 > 35$ & $(BTD_{34} < 8$ or $\rho_3 < 0.025)]$ or $(\rho_1/\rho_3 > 35$ & $\rho_1 > 0.5)$

2. *If classified as clear at end of tests, reclassify as cloudy if* POL $= 1$, $\rho_3 > 0.02$, &
$\{[ANT = 1$ & $BTD_{34} > 8$ & $BTD_{34} > (BTD_{cs34} + \sigma_{34})]$ or

$[ANT = 0$ & $(T_4 - T_{cs4}) > 5$ or $(BTD_{34} - BTD_{cs34}) > 7]\}$.

During night,

1. *If All D test $\Sigma = 0$ & Thin Cirrus test is positive, then classify as clear snow if*
   POL $= 1$ & $BTD_{34} < 2$ & $[(BTD_{34} < 2$ & $BTD_{34} - BTD_{cs34})$ or $< 0.5\sigma_{cs4}$ & $BTD_{45} < 0.9$.

2. *If All D test $\Sigma = 0$ & Thin Cirrus test is positive, then classify as strong clear if*
   $[50 < LAT \leq 70$ or $(LAT > 60$ & OWF $= 1)]$ & $BTD_{45} < 2.0$ &
   $[(BTD_{34} < 2$ & $BTD_{34} - BTD_{cs34} < 0.5\sigma_{cs4})$ or $T_4 - T_{cs4} < 1]$.

3. *Classify as weak cloud if* POL $= 1$ & ANT $= 0$ & T4 > 220 &
   $\{(BTD_{35} < -0.75$ or $(BTD_{35} < -0.5$ & $BTD_{45} < 0.5)$ or $[(T_4 - T_{cs4}) < -4$ & $BTD_{45} < 0.5]\}$.

4. *If classified as clear at end of tests and POL $= 1$, reclassify as cloudy if*
   $T_4 > 225$ & $[(BTD_{35} < -0.5$ & $BTD_{45} < 0.5)$ or $(T_4 - T_{cs4} < -2)$ or $(BTD_{34} > BTD_{cs34}$
   & $BTD_{45} > 0.5)]$.

5. *If classified as cloudy at end of tests and POL $= 1$, reclassify as clear if*
   ANT $= 0$ & $T_4 - T_{cs4} < 12.5$ & $BTD_{45} < 0.8$ & $[BTD_{34} < 1.5$ or
   $(BTD_{34} - BTD_{cs34} < 0.5\sigma_{cs4}$ & $BTD_{34} > -1.0)]$.

6. *If classified as cloudy at end of tests and ANT $= 1$, reclassify as clear if*
   $T_4 < 218$ & $BTD_{45} < 0.5$ & $T_{cs4} < 228$ or $T_4 - T_{cs4} < 5$ & $-0.3 < BTD_{45} < 0.3$.
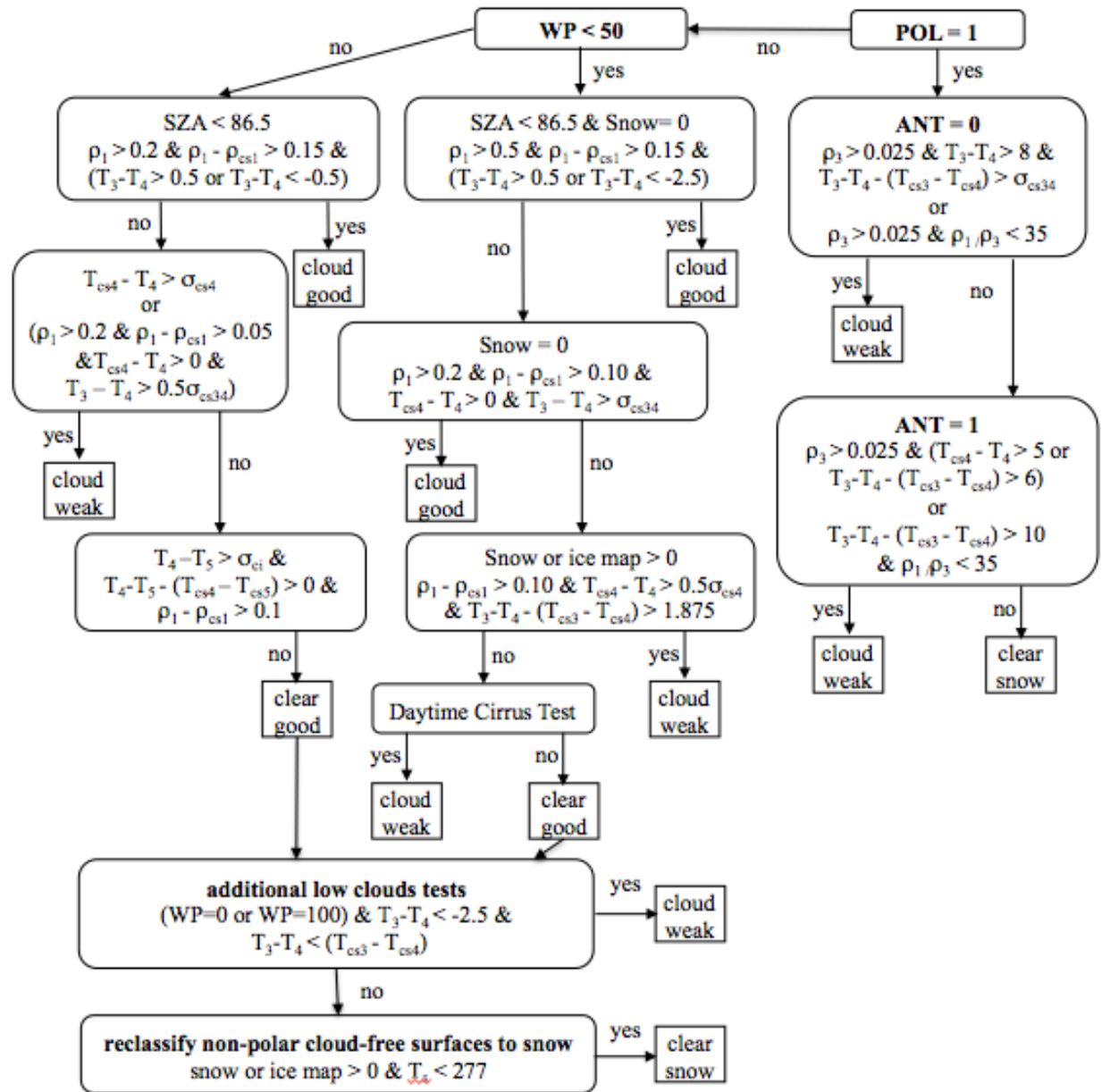
Figure 11. Same as Figure 9, except for terminator conditions, 82° < SZA $\leq$ 88.5°, SatCORPS-A1 only.

A separate set of tests is used for pixels in the terminator zone, which is defined as areas having 82° < SZA < 88.5°. This set is similar to the nighttime set but some VIS data are used to supplement the available information. This is necessary because under low sun conditions, the reflected component tends to offset the decreased cloud emission making it difficult to discern cloudy pixels from BTD_{cs34}. This is especially true for low clouds. For the terminator cases, $\sigma_{cs34} = 5.228*(\mu_o - 1.0) + 6.0$. For SATCORPS-A2, the tests involving ρ_6 are employed unless there is a valid T_3 value. If neither a valid T_3 nor ρ_6 value is present, then a

bad data flag is returned. The twilight tests were adjusted for SATCORPS-A3 to account for the absence of T_5.

Figure 11 shows a schematic of the terminator tests starting in the upper right corner. Only two tests are applied for polar regions, one for the Antarctic Plateau and the other for all other regions. Only weak clouds or clear snow result from these tests. For non-polar regions, the mask is split into two parts, land or ocean. If the result is clear, then up to 2 additional tests are performed, one to detect low clouds and the other to classify the clear scene as snow-covered.

The final result of this cascade of tests is the classification of each pixel as strong clear or cloudy or as weak clear or cloudy. Weak cloudy or clear pixels are those that are less certain because the classification is somewhat ambiguous. Roughly 83% of the daytime pixels are classified using the A and B tests. The remaining pixels are classified using the C tests. At night, the A and D tests account for ~78% of the classifications, while the E tests resolve the other 22% of the pixels. Additional details regarding the formulation of the masks can be found in Minnis et al. (2008a) and in flowcharts of the C and E tests in Appendix C.

Figures 12 and 13 show a daytime case from the N18 AVHRR over Alaska and environs. The pseudo-RGB image (Figure 12a) reveals some clear land over western Canada and central Alaska. Some of the mountainous areas in southern and northern Alaska are covered by snow (magenta color). Clear ocean areas are mainly deep blue, while ice-covered parts of the Arctic Ocean north of Alaska are covered by ice (magenta). High ice clouds overlay northern Alaska and the adjacent ocean and the waters west of the Canadian coast. Low and midlevel clouds prevail over much of the image. The observed VIS reflectance (Figure 12b) is generally greater than 0.5 for most of the cloudy and snow-covered areas, while it is mostly less than 0.2 over clear snow-free areas except near the edges of the image. The predicted values of clear-sky reflectance (Figure 12d) are very similar to the clear regions except in some of the northern Alaska snowy regions. Unless the region is classified as permanent snow, the initial value ρ_{cs1} will be estimated using the assumption that the surface is snow-free. The threshold reflectance values (Figure 12c) are mostly less than 0.03, except over the permanent snow regions.

The IRW and SIR observed, predicted clear-sky, and threshold temperatures for this case are mapped in Figure 13. The values of T_4 (Figure 13a) in most of the clear areas are similar to the predicted values in Figure 13b. The larger IRW thresholds over land (Figure 13c) reflect the greater uncertainty in the modeled values and the variability within a given 0.5° region. Most of the cloudy pixel BTD_{34} values exceed 4 K (Figure 13d). Over clear areas, BTD_{34} varies from 1K over some water areas up to 5 or 6 K over the prairies of southwestern Alberta, Canada in the lower right part of the image. The predicted clear-sky values (Figure (13e) are generally in line with observed values in the clearer portions of the image. A minimum threshold value of 2.5 K is used over water, snow, ice, tundra, and some forest areas (Figure 13f). The threshold can be as large as 6 K over some land areas.

A controlled copy of this document is maintained in the CDR Program Library.

Approved for public release. Distribution is unlimited.

42

Using those clear-sky values and thresholds yield the cloud mask shown in Figure 14b. Visually, the clear and cloudy areas correspond well with the apparent clear regions in Figure 14a. Three different clear categories were identified in this image as seen in Figure 14c. Most of the pixels are classified as good clear, while some of those near clouds are
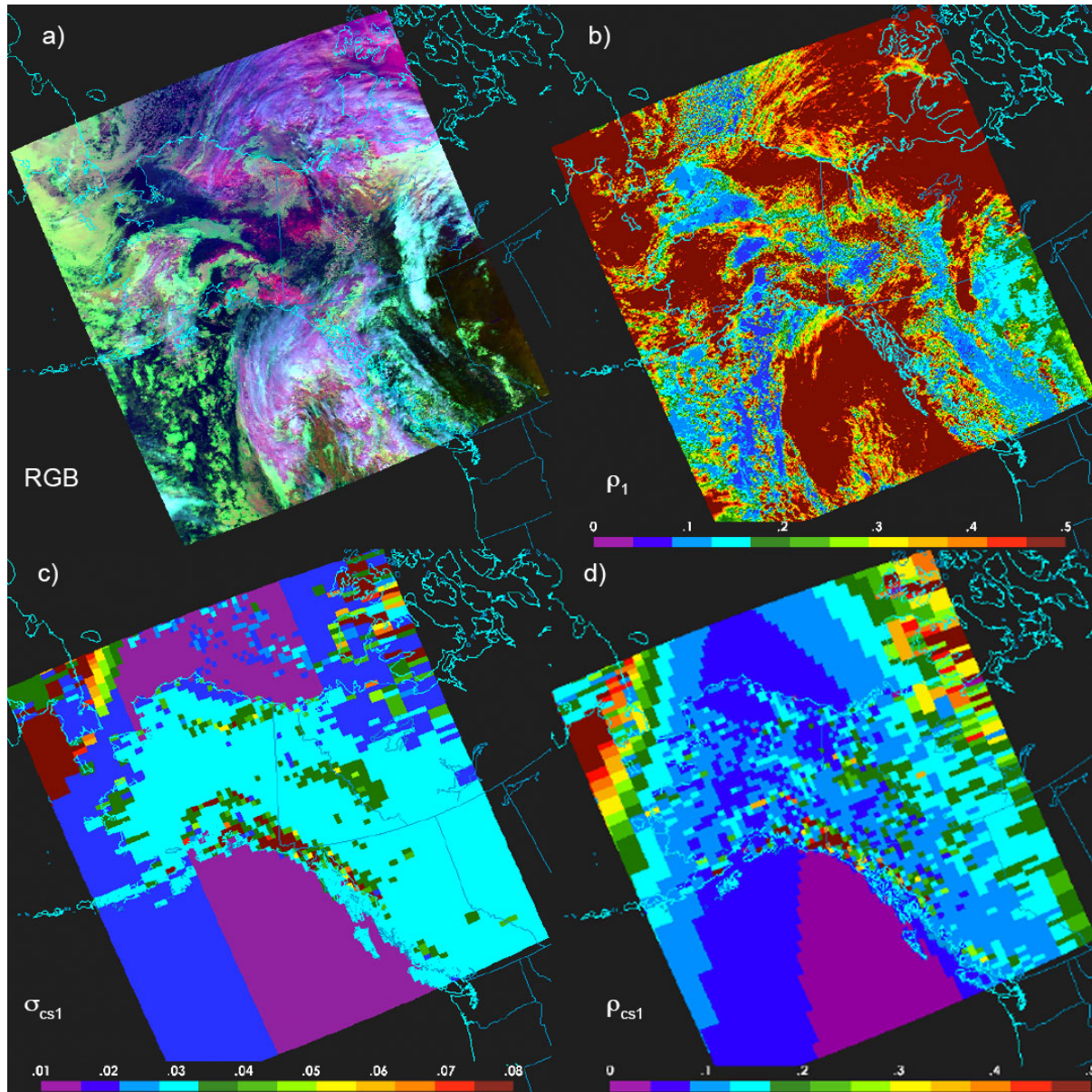
Figure 12: VIS reflectance parameters for (a) NOAA-18 AVHRR image, 2331 UTC, 1 October 2012. (b) observed reflectance, (c) standard deviation of clear-sky reflectance, and (d) predicted clear-sky reflectance.

denoted as weak clear. Areas of clear sky with snow or ice on the ground are identified over Alaska and in the upper right corner of the image. The snow classification is not meant to be exhaustive. Some pixels are not tested for snow cover. The branch used to select clear or

cloudy is indicated in Figure 14d. It is immediately apparent that the A (white), clear B (green), and cloudy B (gray) account for the bulk of the pixel classifications. Over land, the thin cirrus tests (pink) detect many clouds that were missed in many of the other tests. The C1 test (cyan) is next most prominent test followed by the C3 test (blue). The C4 (purple) tests were mainly invoked over some mountains, near coastlines, and near the terminator
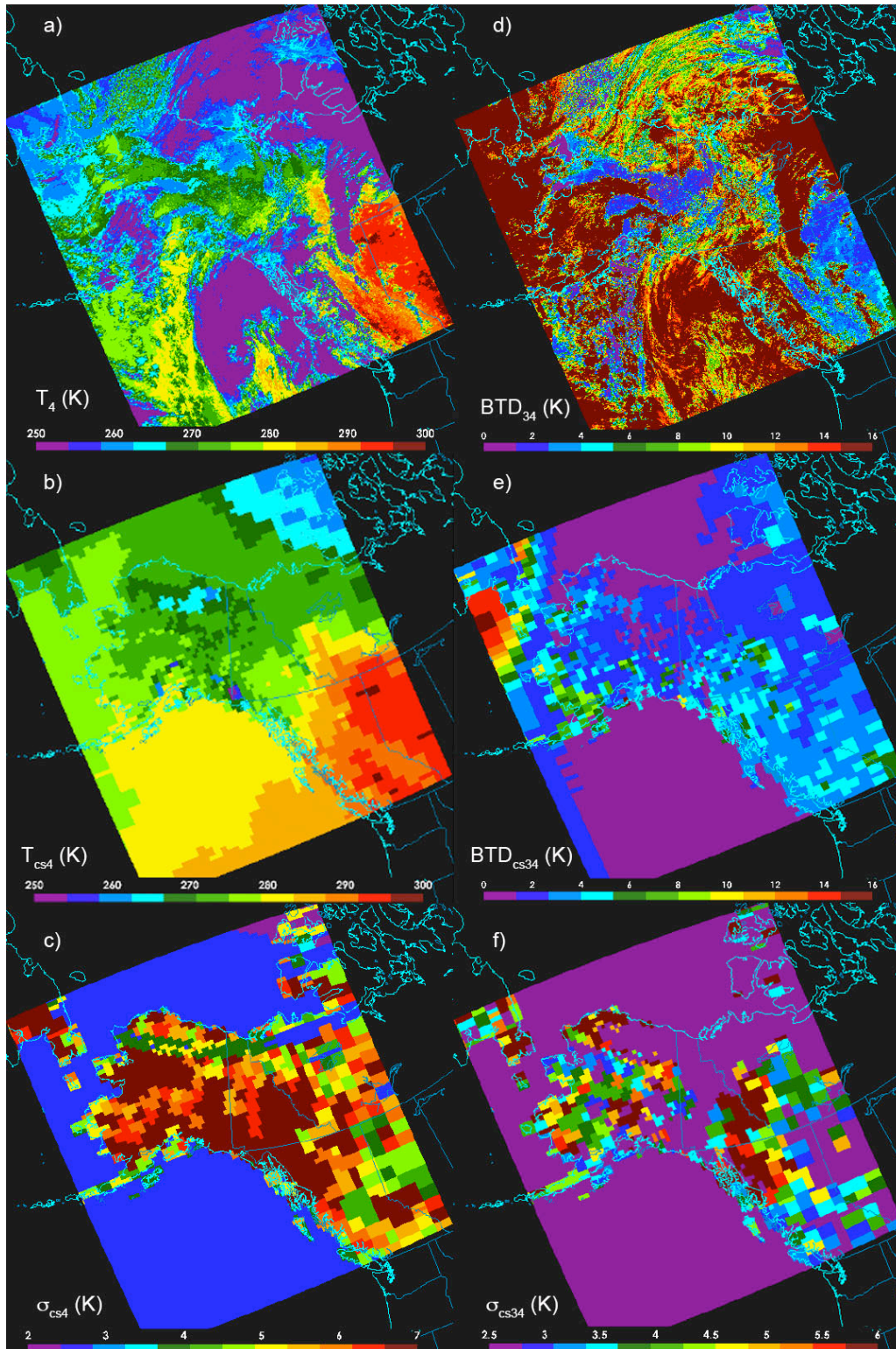
Figure 13. Same as Figure 12, except for IRW and SIR channels.(a) observed T_4, (b) Predicted T_{cs4}, (c) standard deviation of predicted T_{cs4}, (d) observed BTD_{34}, (e) predicted clear-sky BTD_{34}, (f) standard deviation of predicted BTD_{cs34}.
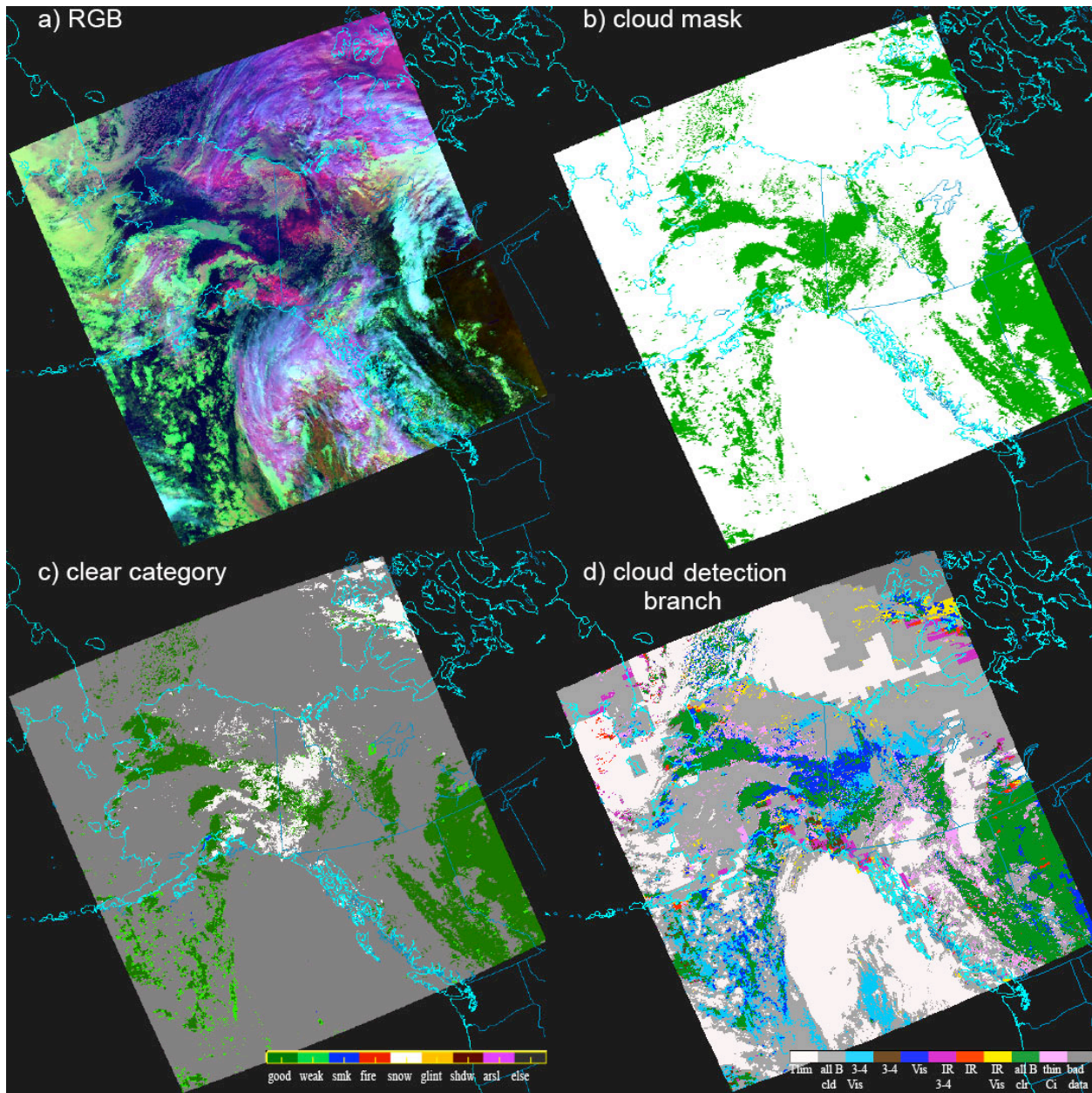
Figure 14. Cloud mask for NOAA-18 AVHRR image, 2331 UTC, 1 October 2008.

(SZA = 82°) line. Very few C2 (brown) or and C5 (orange) tests were performed, while the few C6 (yellow) tests were mostly positive, i.e., cloudy.

3.4.1.2   AVHRR Cloud Property Retrieval

Retrieval of the cloud properties depends on the available channels and SZA. The most reliable in terms of the range of retrievable properties and history is the VISST, which utilizes AVHRR channels 1, 3B, 4, and 5 and is used when SZA ≤ 82°. For SatCORPS-A2, the VINT is used when SZA ≤ 82°, but uses channel 6 (3A). For all other conditions when SZA >

82°, the SIST is employed if channels 3B, 4, and 5 are available. For some satellites, channel 5 was not operating. Thus, for SatCORPS-A3, the 2-channel Shortwave-infrared Infrared-window Technique (SIRT) is employed with channels 3B and 4 at night and the VISST reduces to the Visible Infrared Shortwave-infrared Technique (VIST), which is identical to the VISST except that all tests using the SWI channel are eliminated. It is expected that the VISST, VINT, and SIST produce the most reliable results because more spectral data are used in those algorithms. The diminished information used in the other techniques increases the uncertainties in the results (see sections 6.2.4 and 6.2.5). The algorithms described here constitute the procedures that are executed within process P in Figure 3.

3.4.1.2.1 Daytime retrievals

The VISST iterative approach to the daytime retrievals seeks the values of cloud phase, T_c, τ, and r_e that produce the TOA BTs and reflectances that best match their observed counterparts. The VISST iterative procedure (Figure 15) estimates T_c, τ, and r_e for either one or two phases as a result of matching the VIS, SIR, and IRW observations to their model-computed TOA counterparts. Nominally, for a given pixel, the iterative process is performed for each phase, beginning with an initial guess of r_e = 8 μm and $T_c = T(Z = 3$ km) for liquid clouds and r_e = 25 μm and $T_c = T(Z = 9$ km). However, if $T_4 < 233$ K, it is assumed that the pixel contains an ice cloud and only the ice loop (A) is executed.

Values of ρ_{TOA1} are computed for each case using Eq (12) and interpolated to match the observed VIS reflectance to yield τ and ε_4, which is then used to recompute T_c with Eq (1). These parameters are then used to compute T_3' using Eq (6) for each particle size model, yielding minimum and maximum values, T_{3min}', and T_{3max}', respectively. If it is the first iteration and $T_3 < T_{3min}'$ or $T_3 > T_{3max}'$, the assumed particle size is reset to the maximum or minimum particle size, respectively, and τ and T_c are recomputed and the process is repeated in the second iteration. If T_3 is beyond either model extreme after the first iteration, then it is assumed that no retrieval is possible with that set of models. If T_3 is within the extreme model values during any iteration, then r_e is estimated by interpolating between the values of T_3' to match T_3. For water clouds, if $|r_e - r_e'| < 0.5$ μm, the iteration stops, otherwise a new value of r_e' is computed as the average of r_e and the original r_e', and the process is repeated. A no-retrieval value results if convergence does not occur after 20 iterations. The same procedure is used for the ice clouds, except that the ice crystal models (see section 3.3.5.1 for description of the cloud reflectance models) replace their water droplet counterparts and the iteration stops when $|r_e - r_e'| < 1.2$ μm. The VINT follows the same procedure, except that the model calculations for the SIR BTs are replaced by $\rho_6' = f(r_e, \tau, T_c)$ as in Eq (14).

Over snow surfaces, the CCPRS uses the 1.24-μm channel instead of the VIS channel to retrieve COD with the Shortwave-infrared Infrared Near-infrared Technique (SINT; Minnis et al. 2011a). Generally, the 1.24-μm reflectance from a cloud-free snow scene is less than for a cloud-covered scene, making it possible to obtain a solution. This is not the case for cloudy scene VIS reflectances, which often prohibit completing a retrieval. SatCORPS-A relies on the VIS channel for COD retrieval during the daytime over all surface types. Modeling of the clear snow scene reflectance field is notoriously difficult because slight

textural changes in the snowpack or snow grain size induce significant changes in the bidirectional reflectances. To minimize the no-retrievals and provide better estimates of COD when the
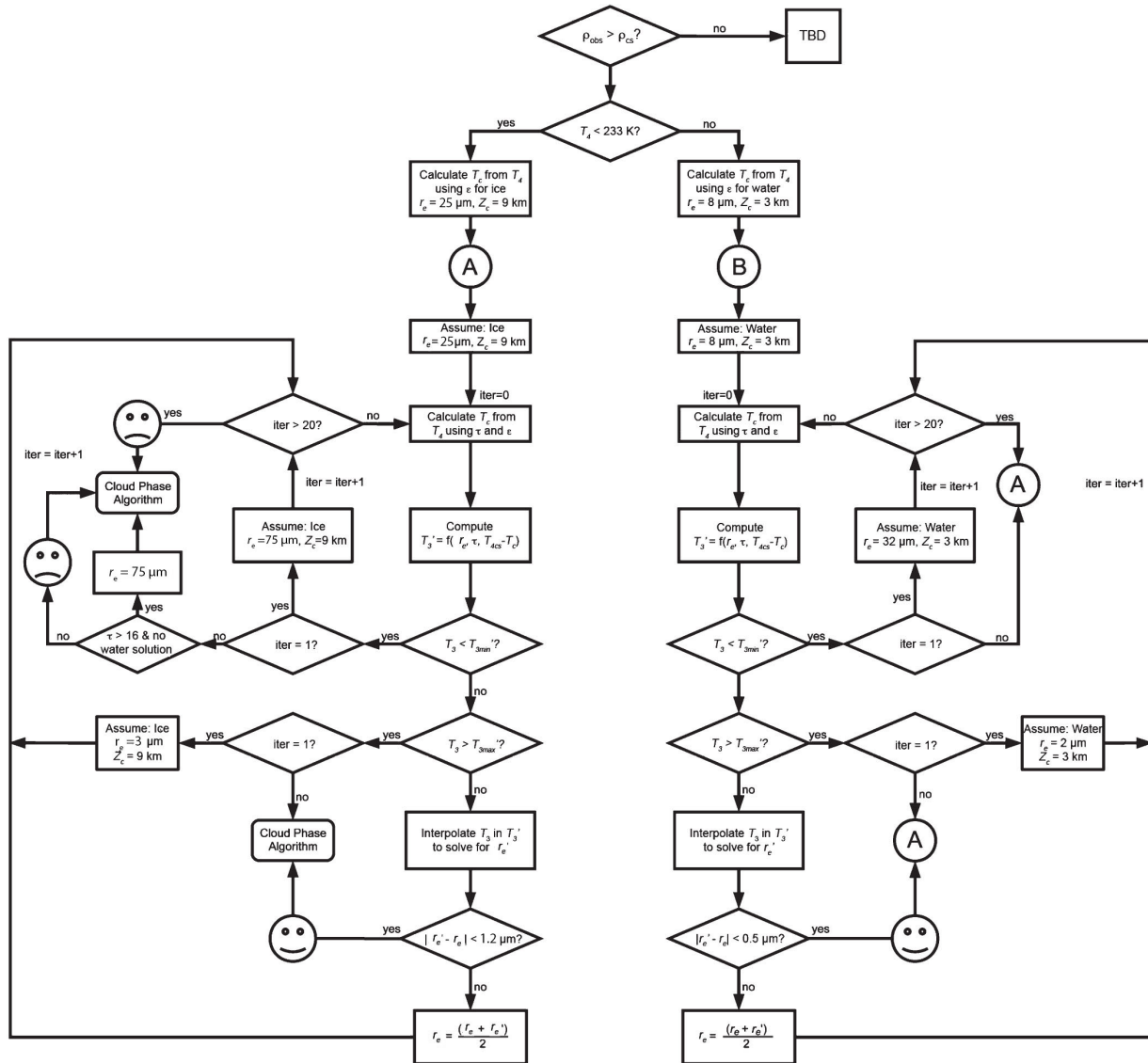
Figure 15: Schematic of VISST/VINT iterative processing. Smiling and frowning faces denote favorable and unfavorable termination of iteration, respectively.

clouds are optically thin, the value of ρ_{cs1} may be changed and results from the SIST may be used instead of the corresponding VISST or VINT values. For a tile that is indicated as being snow or ice covered and if $\rho_{cs1} < \rho_1$, then ρ_{cs1} is set equal to the average of the five lowest reflectances observed in the tile minus 0.015. Although the accuracy of this method has not been evaluated yet, it greatly reduces an otherwise very large number of no-retrieval pixels

and yields values comparable to other retrieval methods over snow. The SIST is also applied to the pixels for all snow and ice covered tiles. The T_c, τ, and r_e results from the VISST are replaced with the SIST results, if

$$\tau(SIST) > 0 \text{ and } T_4 < T_{cs4} \text{ and } \{\tau(SIST) < 6 \text{ or } [\tau(VISST) = 0.05 \text{ or } \tau(VISST) \geq 150]\}. \quad (22)$$

This approach also has not been validated extensively, but visually appears to yield more realistic values than the VISST. It should be noted for the reader that, to date, validation of COD and CER derived over snow-covered surfaces for any passive cloud retrieval method is piecemeal and rare.
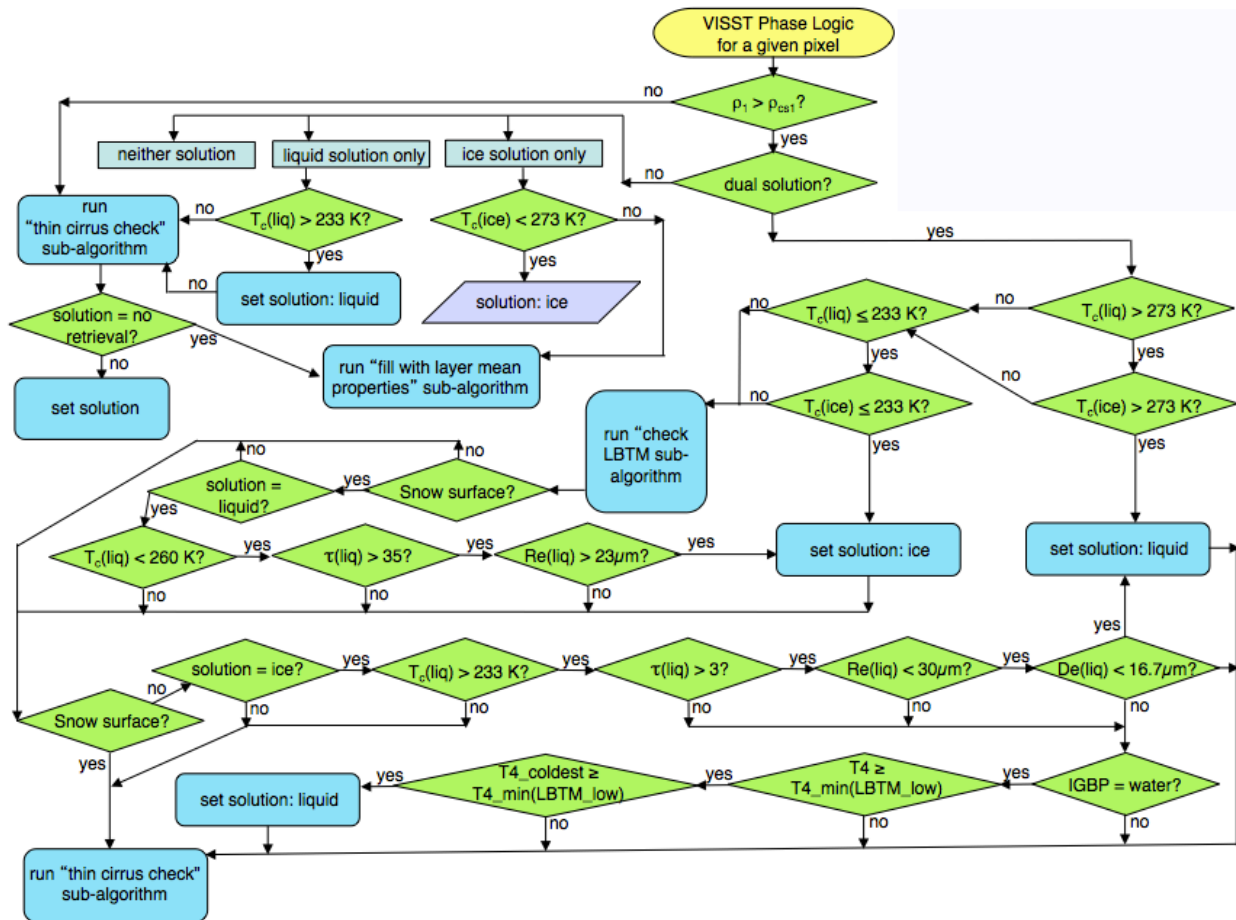
Figure 16: Flow diagram of phase determination process for VISST and VINT.

For SatCORPS-A2, the estimation of τ over snow/ice using a modified SINT takes primacy. In this version of the SINT, values of CER are assumed to be 10.0 and 33.1 µm for liquid and ice clouds, respectively, and τ and T_c are estimated using only the 1.6 and 11 µm channels. The assumed value of ice CER corresponds to the boreal summertime average over the Arctic, while the liquid value is slightly smaller than the CERES mean in order to maximize the range of possible liquid τ retrievals and still remain realistic. The TOA 1.6-µm reflectances and 11-µm brightness temperatures are computed for all model τ values for

the assumed liquid CER using low and high cloud temperatures, T_L = 235 and T_H = T_4 + 6 K and for the assumed ice CER using T_H = T_4 + 6 K and T_L =T_p. These values define curves of TOA BT and reflectance pairs for a given τ at T_L and T_H. To estimate $\tau(T_4,\rho_6)$, the observed value of T_4 is first matched with $\tau[\text{BT}(T_L),\rho_{6L}]$ and $\tau[\text{BT}(T_H),\rho_{6H}]$ from the curves. Bilinear interpolation is then performed in optical depth to estimate $\tau(T_4,\rho_6)$ and T_c. The maximum optical depth that is possible to retrieve with this approach is designated as τ_{max} and has values of ~32 and ~16 for liquid and ice, respectively, depending on the viewing and illumination angles. If ρ_6 exceeds $\rho_6(\tau_{max})$, then the optical depth is set equal to τ_{max}. The liquid or ice solution is selected based on several different conditions that vary the ice-liquid threshold temperature between 236 and 255 K, depending on the availability of valid solutions. Invalid solutions are overwritten with the 2-channel SIST described above.

Phase is then chosen using several tests. If the $T_4 \leq 236.0$ and an ice solution exists, then it is assumed that it is too cold to be water, and the ice phase and solution are used. Similarly, if $T_c \leq 242.0$ for the water solution, it is assumed to be too cold to be water, so the ice cloud phase and solution are used. If the ice cloud optical depth solution is less than or equal to 3.0 and T_c < 255.0, the pixel is assumed to be a thin cirrus cloud. If T_c < 250.0 for water, yet the ice solution corresponds to the maximum 1.6 reflectance bin, the ice solution is chosen because the ice solution is strongly indicated and the water solution is judged to unreliable. If no solution has yet to be found, then the original VINT solution is examined. If the VINT solution is water and ρ_6 > $\rho_6(\tau_{max})$ for both T_L and T_H, then the modified SIST water solution is used. As a final attempt to determine phase, the original VINT phase is used and the newly calculated phase-appropriate solutions are used for τ, T_c and emittance.

The VISST cloud thermodynamic phase is selected using a set of sequential tests. These are illustrated in Figure 16. If the ρ_1 < ρ_{cs1}, it is likely a no-retrieval pixel and is assigned the mean layer results (depending on T_4), if it is not reclassified as clear. This assignment is given on the assumption that it is a cloud beneath the shadow of a taller cloud nearby. If there is only one phase solution and T_c is physically reasonable, the phase is accepted for that solution. If T_c is unreasonable, then it follows the same path as the no solution case. If there are dual phase solutions, a simple temperature check is applied: if T_c > 273 K ($\leq$ 233 K) for both results, the liquid (ice) solution is used, unless the ice cloud is over snow.
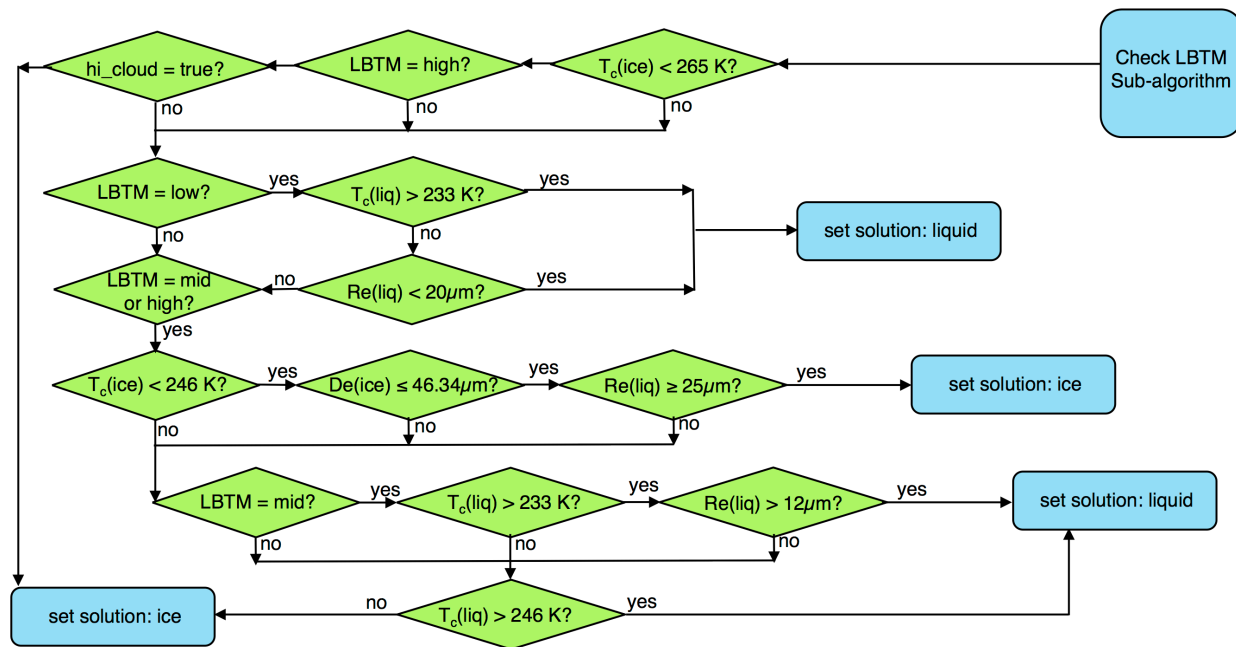
Figure 17: LBTM sub-algorithm flowchart for phase determination.

Otherwise, a more complicated series of tests are applied. These additional tests incorporate results from two other separate algorithms, the Layer Bispectral Threshold Method (LBTM; see Minnis et al. 1993) and the thin cirrus test.

The LBTM sub-algorithm phase logic, applied in less than 5% of the cases, is diagrammed in figure 17. The LBTM uses a two-dimensional VIS-IR histogram to provide an estimate of the cloud layer that includes the pixel. It also determines a parameter, designated "hi_cold", that indicates whether or not there is at least one pixel in the high layer having T_4 less than the coldest pixel in the low cloud layer. This parameter is used to reclassify thin cirrus pixels that would otherwise be called liquid cloud pixels. This approach is used because edge and other thin or partially filled pixels associated with low clouds can be misinterpreted as thin cirrus clouds because they are relatively dark and yield no water cloud solution, but produce an ice solution. To apply this test, it is assumed that if low clouds ($T_c > T_{low}$) are present and no pixels classified as ice have a value of $T_4 < T_{Lmin}$, then no ice clouds are present. The low cloud temperature limit is T_{low}, which corresponds to an altitude of 3 km in the tropics that gradually drops to 2 km at 60° latitude as a function of cos(LAT). The value of T_{Lmin} is lowest value of T_c in LBTM low-cloud category.

Figure 18 shows the logic used for the thin cirrus (Figure 18a) and marine stratocumulus edge (Figure 18b) tests that provide independent assessments of the cloud phase. The thin cirrus test is invoked by the main phase selection process for certain conditions as seen in Figure 16. The marine stratocumulus edge test is used to overwrite ice phase solutions for certain dual solution results. It generally applies to clouds classified as low optical depth ice clouds. The thin and partly cloudy edges of low stratus clouds often have signatures similar to thin cirrus clouds and are therefore occasionally misidentified as thin cirrus clouds. This test reclassifies some but not all of those misidentifications.

a)

```
                                                                    thin cirrus check
                                                                    sub-algorithm
                                                                          |
                                                                          v
yes   τ(liq) < 0.75?   no   sunglint?   yes   solution = liq?   yes   ABtest =      no   Snow surface?
                                                                      thin cirrus
                       no              yes               no                     no                yes
                        |               |                 |                      |                 |
                        v               v                 |                      |                 v
                   solution: liquid                       |                      |            set solution
                                                          |                      |
                                                          v                      |
   set solution:   no   T(RHmax) < 242?   yes   BTD34 >                          |
   no retrieval                                 BTD34(Cs) + 2?                   |
                        |                          |                             |
                       yes                         no                            |
                        v                          v                             |
              run "set ice solution with max   set solution:
              RH level" sub-algorithm          no retrieval

         BTD34 >          yes   T(RHmax) < 242?   no   solution: liquid
         BTD34(Cs) + 2?
              |                      |
             no                     yes
              v                      v
       solution: liquid    run "set ice solution with max
                           RH level" sub-algorithm
```

b)

```
                                                    stratocumulus edge
                                                    pixel test
                                                          |
                                       no                 v
                      <----------------------  solution = ice?
                      |                                   |
                      |                                  yes
                      |                                   v
   set solution: liquid   yes   T4_coldest ≥   yes   T4 ≥            yes   τ(liq) < 2 or ice   yes   IGBP = water?
                                T4_min(LBTM_low)      T4_min(LBTM_low)      solution only
                                     |                   |                      |                    |
                                    no                  no                     no                   no
                                     |                   |                      |                    |
                                     v                   v                      v                    v
   set solution: ice  <-------------------------------------------------------------------------------
```
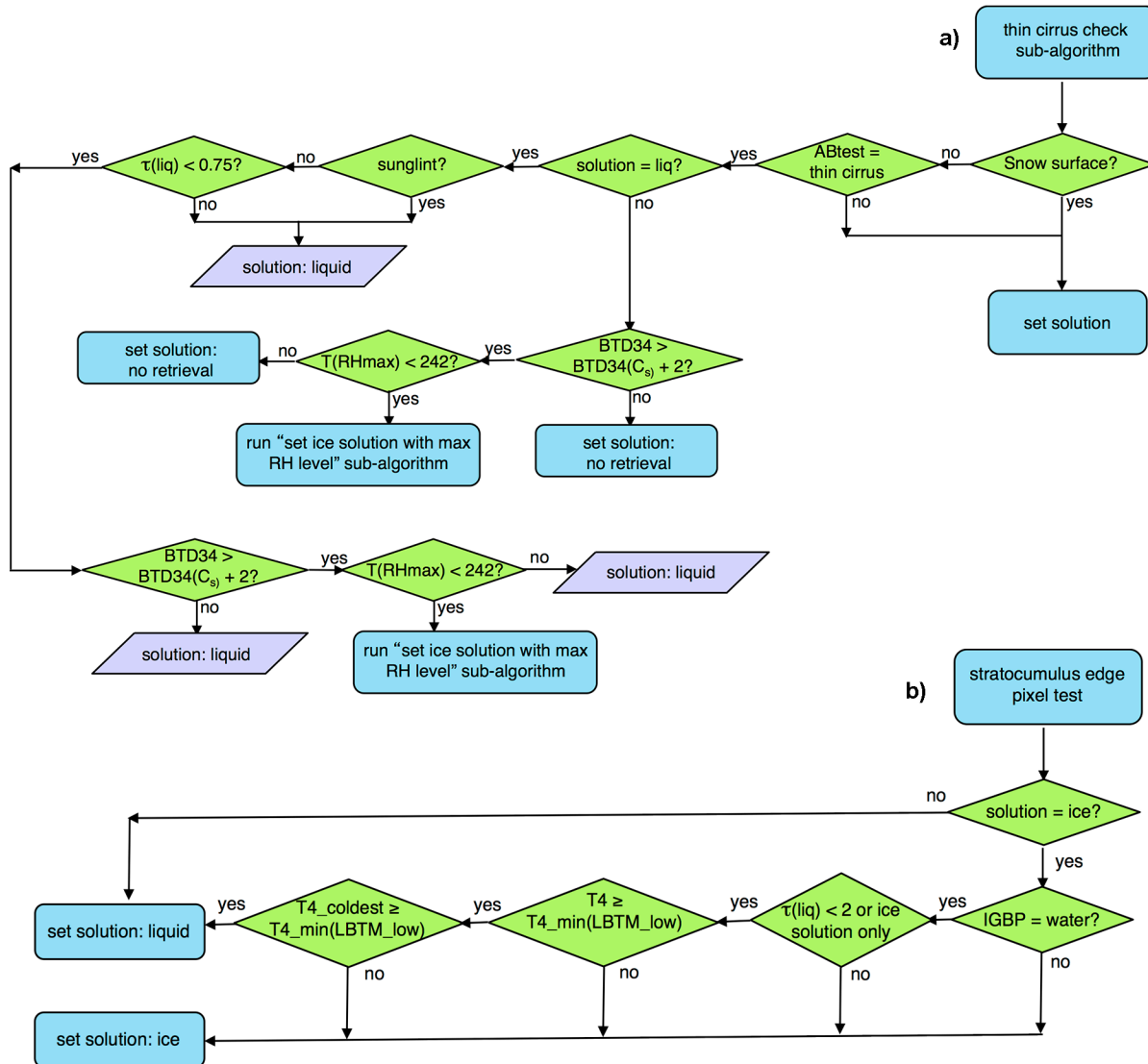
Figure 18: Flowcharts for phase determination. (a) Thin cirrus test sub-algorithm, (b) marine stratocumulus edge pixel test applied to ice cloud pixels.
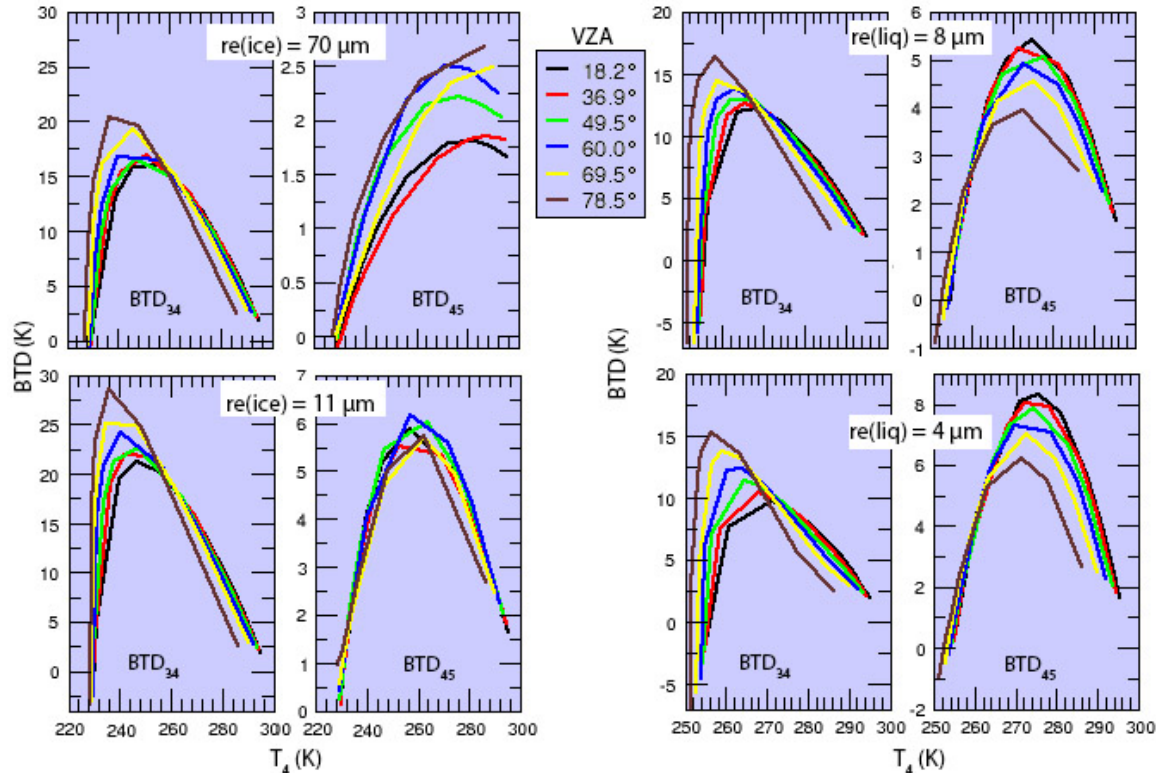
Figure 19: Theoretical variation of BTD_{34} and BTD_{45} with T_4 for ice (left) and liquid water (right) clouds in a tropical atmosphere. T_c = 230 K and 255 K for the ice and water clouds, respectively.

3.4.1.2.2   Nighttime and terminator retrievals

The primary goal of the nighttime retrievals is to adjust cloud temperature and, hence, the height for semi-transparent clouds to provide some consistency between day and night. Although the SIST derives CER and COD for clouds it identifies as optically thin, COD is more reliable and is used to adjust the height. The theoretical basis and heritage of the SIST, as well as relevant references, are provided by Minnis et al. (1995). The SIST relies on T_4, BTD_{34}, and BTD_{45} to solve for T_c, τ, and r_e. Figure 19 shows theoretical plots of BTD_{34} and BTD_{45} as functions of T_4 for two ice cloud models (left) and two water droplet models (right). The upper panels are for larger values of r_e than the lower panels. The COD increases with decreasing values of T_4. The value of BTD_{34} reaches a peak where COD is ~ 2 then decreases rapidly, while the peak value of BTD_{45} corresponds to $\tau \le 1$. The differences depend on the VZA and atmospheric absorption. In general, larger values of CER yield smaller values of both BTD_{34} and BTD_{45}. However, for liquid water clouds, the value of BTD_{34} decreases more with decreasing VZA for r_e = 4 μm than for r_e = 8 μm. It is clear that, in most instances, little unique information is available for values of $\tau > 5$ or so, as all of the curves converge. Thus, a retrieval is only attempted for optically thin clouds.

Given an optically thin cloud ($\tau < 6$), μ, and the background (theoretically, it can be either clear or cloudy below) temperatures for channels 3, 4, and 5, it is assumed that a given pair of BTD_{34} and BTD_{45} at a particular value of T_4 uniquely defines a cloud characterized by T_c,

r_e, and τ for a given phase. These parameters are determined by matching the three measured quantities as closely as possible to the same parameters calculated using Eq (1) and, in the case of near terminator conditions, Eq (6). Each observed quantity should fall between the corresponding pair of discrete theoretical calculations for a given phase. The distance in BTD from the model values to the observed values for both BTD_{34} and BTD_{45} are used to interpolate between each model and parameter to assign a value of T_c, r_e and τ to the pixel. In the absence of temperature constraints ($T_c > 273$ K or $T_c < 233$ K), the phase is selected based on how closely the channel 3 and 5 parameters agree with each other.

SIST attempts to determine τ, T_C, and particle size through an iterative process that minimizes the differences between model-derived and observed values of BTD_{34} and BTD_{45} for the observed T_4. This procedure is described in detail by Minnis et al. (2011a). The iteration continues until the increment is less than 0.1 K or up to 15 times. In the latter case, the results from the penultimate iteration are accepted. If the resultant optical depth exceeds 16, then τ is reset to 16. The assignment of these default values is strictly arbitrary and is used to indicate that the cloud is optically thick. No skill is expected from the assignment of the COD value.

The iteration procedures comprise only one part of the complete SIST, which is illustrated schematically in Figure 20. Given the input parameters, it is first determined if the cloud is colder than its background. If $T_4 > T_b$, a set of default values are applied. Otherwise, the input parameters are checked to see of the cloud is likely to be optically thick based on

Figure 20: Schematic diagram of SIST procedure.

BTD_{34} and, if so, a phase is selected based on the temperature. The background temperature is simply the equivalent brightness temperature of the upwelling radiance of layer (*j-1*) in Eq (1). The threshold for determining whether it is optically thin or thick

$$\Delta T_{34} = 0.095 \, (T_4 - T_b) - 4.175. \tag{23}$$

This formula was derived from a set of radiative transfer computations using a wide range of particle sizes and a range of optical depths up to 16. A relatively conservative threshold, it does not eliminate all clouds having $\tau > 16$ and is imposed mainly to facilitate processing. Because extremely cold, optically thick clouds near the tropopause often fail this test, clouds were also deemed to be thick if they exhibited a large BTD_{34} (>20K) and the observed brightness temperature was much colder (> 70K) than the tile skin temperature and relatively close (within 10K) to the tropopause temperature. The clouds determined to be thick at this point are given a default value of $\tau = 32$. If $BTD_{34} \geq \Delta T_{34}$, then the iterative procedures are applied either using one phase or both. If solutions for both phases are determined, then the final model selection depends on the errors e_{35} as discussed by Minnis et al. (2011a). The performance of the SIST relative to that of the VISST is discussed by Minnis et al. (2011b).

For SatCORPS-A3, which uses AVHRR data with no channel 5 radiances, the SIST approach is run in a 2-channel mode where the value of r_e is assumed and the retrieval reduces to 2 parameters, COD and CET, found with two observations, BTD_{34} and T_4. The monthly mean regional values of r_e from the daytime NOAA-18 analyses are used to specify CER for the SIRT retrievals. For the SIRT, only COD and T_c are valid retrievals

3.4.1.2.3 Cloud altitude parameters

Several different cloud heights and pressures are derived to estimate the vertical extent of the detected clouds. These parameters are cloud effective height and pressure, cloud-top height, temperature, and pressure, cloud thickness, and cloud base height, temperature, and pressure.

Cloud effective height and pressure: The cloud effective height Z_c and pressure p_c are defined as the lowest altitude and corresponding pressure, respectively, where T_c is found in the profile. Vertical profiles of temperature and pressure measured by radiosondes and output from numerical weather analyses often fail to properly account for the magnitude and location of the temperature inversion near the top of the boundary-layer (e.g., Sun-Mack et al. 2014 and references therein). The results typically overestimate cloud-top height for low clouds because the cloud-top temperature observed by the satellite is often found higher in the temperature profile than at the actual location of the boundary-layer inversion. To overcome this sounding bias when relating cloud temperature to altitude, the lower portion of the temperature profile in SatCORPS-A is first adjusted based on the surface temperature and a fixed lapse rate.

The temperature profile is adjusted using the technique and database of Sun-Mack et al. (2014) between the surface and pressures, *P1* and *P2*, which are functions of three surface types and three latitude zones. They have constant values for the tropics (-30° < LAT < 30°) and polar regions (LAT > 60° or LAT < -60°). For mid-latitudes (30° ≤ LAT ≤ 60° or -60° ≤ LAT ≤ -30°), *P1* and *P2* vary according to the formulae below.

$$f = (0.866 - cos(LAT))/0.366 \qquad (24)$$

$$P2 = (1 + f \times 0.103) \times B2 \qquad (25)$$

$$P1 = (1 + f \times 0.06) \times B1, \qquad (26)$$

where LAT is given in degrees, B2 = 650, 665, and 680 hPa and B1 = 750, 765, and 780 hPa over land, coast and water, respectively. Table 6 lists pressure levels, *P1* and *P2*, for each of the three latitude zones (tropics, mid-latitudes and polar region) over three different snow-free surfaces (land, coast and water)

The apparent boundary layer lapse rate Γ_a is used to build a new temperature profile for pressures $p > P1$ by first computing the temperatures at a given altitude, which is converted to pressure. Thus,

$$T(z + z_s) = T_s + \Gamma_a(z - z_s), \qquad (27)$$

where z_s is the surface elevation above mean sea level. Over ocean and land surfaces, the value of T_s is, respectively, the sea surface temperature and the running 24-h mean surface air temperature from MERRA.

Table 6. Transition pressure levels P1 and P2 for each of the three latitude zones (tropics, midlatitudes, and polar regions) over three different snow-free surfaces (land, coast, and water). The lapse rates are used to rebuild temperature profiles at altitudes below the height of pressure P1. Between P1 and P2, the temperature profile is a blend of the lapse rate and model values. For lower pressures, only the model values are used.

	Pressure (hPa) Land	Pressure (hPa) Coast	Pressure (hPa) water
Tropics (-30° < LAT < 30°)			
P2	650	665	680
P1	750	765	780
Midlatitudes (-60° < LAT < -30° and 30° < LAT < 60°)			
P1 and P2	Vary as a function of LAT, see Eqs (24) – (26)		
Polar Regions (LAT < -60° or LAT > 60°)			
P2	717	733	750
P1	795	811	827

For pressure levels between *P1* and *P2*, the MERRA temperature is unchanged if it is less than the temperature at the adjacent lower level. Otherwise, a new temperature is calculated based on linear interpolation between the MERRA temperatures at *P1* and *P2*. If the newly calculated temperature is still greater than that for the level below, then the lapse rate is used to compute the temperature at the inversion level. Thus, for *p < P1*, the modified sounding cannot be any warmer than the original sounding. For *p < P2*, the original MERRA temperature profile is retained. This procedure is used because the exact location of the inversion, if it exists, is unknown, the cloud droplets may be colder than the air temperature, and it is desirable to use a realistic sounding for as much of the atmospheric column as possible. The value of Z_c is set equal to the lowest height in the modified profile where the temperature $T = T_c$. If T_c is warmer than the greatest temperature in the profile, then Z_c is set equal to the surface elevation plus 0.1 km. The pressure corresponding to Z_c is assigned to p_c.

Cloud-top height, temperature, and pressure: Because the value of T_c corresponds more closely to the center of the cloud in optically thin cases (e.g., Minnis et al. 1990a) and to some depth below the cloud top for optically thick clouds, e.g. Dong et al. (2008), it differs from the actual physical top of the cloud. For cirrus clouds, a strong correlation was found between emissivity defined relative to the physical cloud-top temperature T_t and the cloud effective temperature Minnis et al. (1990a). Here, that type of relationship is used to estimate T_t and, thereby, the physical cloud-top height Z_t and pressure p_t from the

temperature profile. In many cases, the value of T_t is found for channel 4 by substituting the cloud-top emissivity ε_t for ε_4, T_t for T_c, and T_4 for T_i in Eq (1), then solving for T_t.

For ice clouds having $T_c < 245$ K and $\tau \leq 2$, the regression fit from Minnis et al. (1990b) is used to find ε_t:

$$\varepsilon_t = \varepsilon_4 \ (2.966 - 0.009141 \ T_c). \tag{28}$$

If $\varepsilon_t > \varepsilon_4$, ε_t is set equal to ε_4. If $2 < \tau \leq 6$, ε_t is found by linearly interpolating in τ between the result of Eq (28) and ε_4 using τ values of 2 and 6 as the respective independent variables. For all clouds having $\tau > 6$, $\varepsilon_t = \varepsilon_4$. Similarly, for ice clouds having $T_c > 245$ K and $\tau \leq 2$,

$$\varepsilon_t = \varepsilon_4 \ (0.00753 \ T_c - 1.12). \tag{29}$$

This equation is based on linear interpolation between the results of Eq (28) and the water cloud values at 280 K. For other clouds having $T_c > 245$ K and $\tau > 2$, ε_t is found in the same manner as for clouds having $T_c \leq 245$ K, except Eq (29) is used in place of Eq (28) for the interpolations.

For liquid water clouds having $\tau > 6$, $\varepsilon_t = \varepsilon_4$. If $\tau < 2$, $\varepsilon_t = 0.99 \ \varepsilon_4$. For clouds having $2 < \tau \leq 6$, ε_t is found by linearly interpolating in τ between the result of Eq (28) and ε_4 using τ values of 2 and 6 as the respective independent variables. This difference between ε_t and ε_4 is very small for water clouds because the differences between the cloud top and effective heights for water clouds are usually less than 0.2 km, which is less than the accuracy of the height determination.

After the initial value of T_t is computed for clouds having $T_c < 265$ K, additional adjustments are made if $2 < \tau \leq 6$. A new value of T_t is found by linearly interpolating in τ between the original value of T_t and T_t' using τ values of 2 and 6 as the respective independent variables, where

$$T_t' = 0.622 \ T_c + 77.7 \ K, \tag{30a}$$

for $T_c < 242$ K and

$$T_t' = 1.011 \ T_c - 14.4 \ K, \tag{30b}$$

for 265 K $< T_c \leq 242$ K. If $T_t' > T_c - 2$ for $T_c < 242$ K, T_t' is reset to $T_c - 2$. The adjustments represented by Eq (30) and the interpolations were developed from additional unpublished comparisons of surface radar and satellite-based cloud top temperatures. And finally, T_t is constrained to be less than or equal to the tropopause temperature T_p. For ice clouds having $\tau > 8$ and $Z_c > 4.2$ km, the cloud-top height is estimated in km using the empirical relationship,

$$Z_t = 1.7905 + 1.01378 \ Z_c, \tag{30c}$$

that was determined by Minnis et al. (2008).

For thick ice clouds identified as overshooting tops, both Z_c and Z_t are redefined in the following manner. First, it is assumed there is no attenuation of the channel 4 radiance above the cloud, so $T_c = T_4$. If $T_4 < T_p$, then

$$Z_c = Z_p - (T_c - T_p) / 8, \qquad (31a)$$

where Z_p is the tropopause height. This approach assumes an 8 K km^{-1} lapse rate above the tropopause. This lapse rate is based upon analysis of MODIS and CloudSat observations of overshooting cloud tops (OT) where the OT-surrounding anvil BT difference was divided by the height difference between the OT and anvil for 111 CloudSat OT overpasses described by Bedka et al (2012), resulting in an 8 K km^{-1} mean lapse rate. Otherwise,

$$Z_c = Z_p + 0.75. \qquad (31b)$$

The cloud top height and temperature are

$$Z_t = Z_c + 0.5 \qquad (32)$$

and

$$T_t = T_c - 4, \qquad (33)$$

respectively, where the 4 K corresponds to 0.5 km above the effective height.

One final adjustment is made after Z_t is determined from T_t to ensure that there is a reasonable depth to the layer above Z_c in high clouds. If $Z_t > 6$ km and $Z_t - Z_c < 0.333$ km, 0.5 K is subtracted from T_t and Z_t is recomputed, T_t remains greater than the tropopause temperature.

Cloud thickness; cloud-base height, temperature, and pressure: Cloud base height is estimated as $Z_b = Z_t - \Delta Z$. The cloud base pressure p_b is determined from Z_b and the MERRA vertical pressure profile. The cloud thickness ΔZ is computed in km using empirical formulae. For all liquid water clouds,

$$\Delta Z = 0.39 \ln \tau - 0.01, \qquad (31)$$

if $\tau > 1$. Otherwise,

$$\Delta Z = 0.085 \tau^{1/2}. \qquad (32)$$

The minimum allowable ΔZ is 0.02 km. Equation (31) was derived from the results of Chakrapani et al. (2002), while Eq (32) is based on the results of Minnis et al. (1992). For ice clouds, an empirically derived parameterization, described in Section 3.3.6.1 is used to estimate cloud thickness.

3.4.1.3   AVHRR Clear-Sky Surface Skin Temperature Retrieval

The method for calculating a surface skin temperature from T_4 is an updated version of that described by Scarino *et al.* (2013). For each 8 × 12-pixel tile, a value of T_s is determined from the clear pixel radiances if at least 20% of the pixels are classified as

clear. The 20% criterion is used to minimize the influence of cloudy pixels on the final temperature value while maximizing the number of samples. If fewer than 20% of the pixels are clear, then no skin temperature is calculated.

The value of T_{stile} is determined by adjusting the initial MERRA T_s based on the difference between the mean observed IRW clear-sky TOA BT T_{clr4} and the modeled T_{cs4} for each tile. A correction is applied to the MERRA T_s and temperature and specific humidity profiles such that, when the corrected values are used in Eq (1), the resulting value of T_{cs4} agrees with T_{clr4}. At this point, observed T_{clr4} represents the mean for a tile, whereas the modeled T_{cs4} represents the tile value interpolated from point values from the MERRA grid. Thus T_s is, to some extent, limited by the resolution of the MERRA region used in processing.

Solving Eq (1) for the tile skin temperature in clear skies for channel 4 yields:

$$T_{stile} = B_4^{-1}([\{[B_4(T_{cs4}) - L_{U4J1}] / t_{U4J1}\} - L_{D41J} (1 - \varepsilon_{s4})]/ \varepsilon_{s4}) \qquad (34)$$

Described above is the nominal process for deriving T_{stile} at the same spatial resolution as the tile. A value of T_s could be retrieved for each pixel using Eq (34), but it is more economical to simply estimate it as

$$T_s = B_4^{-1}[B_4(T_4) B(T_{stile})/B(T_{clr4})], \qquad (35)$$

where T_4 is the observed value for a given clear pixel within the tile. This approach relies on the assumption that the attenuation of the surface-emitted radiance is the same for each pixel in the tile.

The accuracy of T_s is sensitive to a number of factors, most notably misclassified scene types, residual cloud contamination, and the spatial variations of the actual atmosphere and surface emissivity. To address these issues and other minor inherent measurement/model uncertainties, several quality control filters are implemented. First, any pixel having $T_s < T_4$ is not assigned a value of T_s because it is expected that the atmosphere will reduce the temperature between the surface and the TOA. Second, for each pixel classified as clear, if the 10' CERES-based water percentage and ice percentage maps indicate greater than 90% water fraction and less than 50% ice fraction, then a pixel is not assigned a value of T_s if $T_s < 271.25$ K, the freezing temperature of sea water. Third, a somewhat complicated set of tests is employed to reduce T_s correction uncertainties owing to mixed surface types in coastal regions. The tests, however, do attempt to preserve T_s retrievals over lakes and rivers that are wide enough to be uncontaminated by nearby land pixels. Finally, if the 10' water fraction is 100% and the MERRA-based ocean fraction is 100%, then clear pixels are discarded if $T_s > 315.0$ K, thereby reducing the occurrence of unrealistically high T_s values over ocean. An example of a gridded monthly-averaged global skin temperature retrieval map is shown in Figure 21 for October 2008. The daytime (Figure 21a) land temperatures are dramatically greater than their nocturnal (Figure 21b) counterparts. Over water there is minimal diurnal change in T_s.
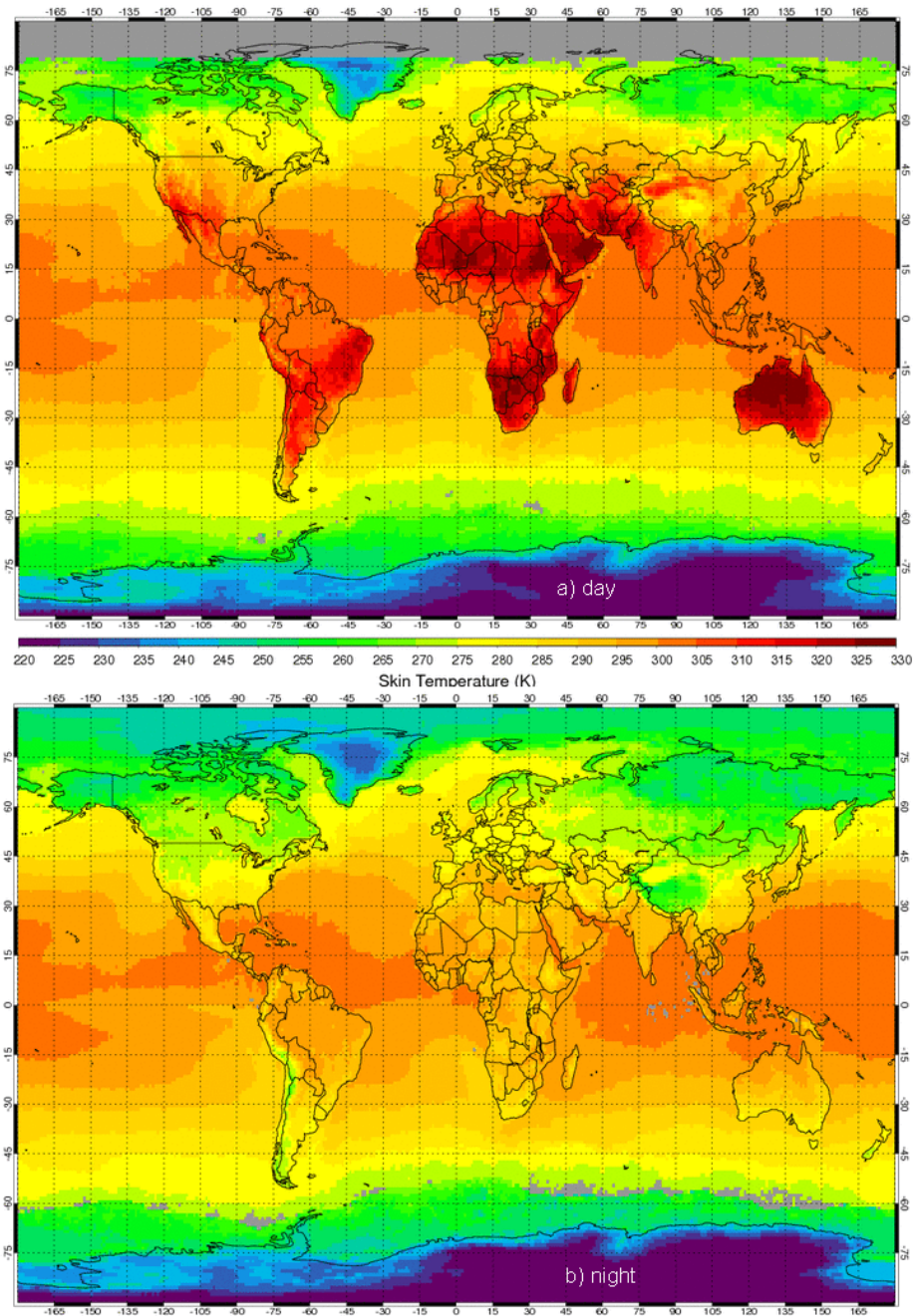
Figure 21: NOAA-18 1° gridded monthly-averaged clear-sky skin temperature retrieval for October 2008 fromSatCORPS-A1.

3.4.1.4   AVHRR Overshooting Convective Cloud Top Detection

Numerous studies have demonstrated that convective storms with overshooting convective cloud top (OT) signatures in weather satellite imagery often produce hazardous weather at the earth's surface, such as heavy rainfall (Negri and Adler 1981), damaging winds (Heymsfield et al. 1991), large hail (Reynolds 1980), and tornadoes (Heymsfield and

Blackmer 1988; Fujita 1989; Kellenbenz et al. 2007). Due to the hazardous nature of storms with OTs, objective OT and enhanced-V signature detection was a product requirement for the future GOES-R Advanced Baseline Imager (ABI) program (Schmit et al. 2005; see also: http://www.goes-r.gov/products/option2.html). Bedka et al. (2010; 2011) describe the GOES-R OT detection algorithm in full detail, but a short summary is provided here for context. The algorithm is formulated around the premise that OTs appear as small clusters of pixels (diameter ≤ 15 km) that are significantly colder than the surrounding anvil cloud. OTs continue to cool at a rate of 7–9 K km^{-1} as they ascend into the lower stratosphere, producing a significant BT contrast between the OT region and the surrounding anvil cloud. Relative T_4 minima that are ≤ 217.5 K are first identified by the algorithm. These pixels are then compared to the MERRA Tp temperature to ensure that they correspond to cloud tops "overshooting" through the tropopause region. Checks are then performed to ensure that
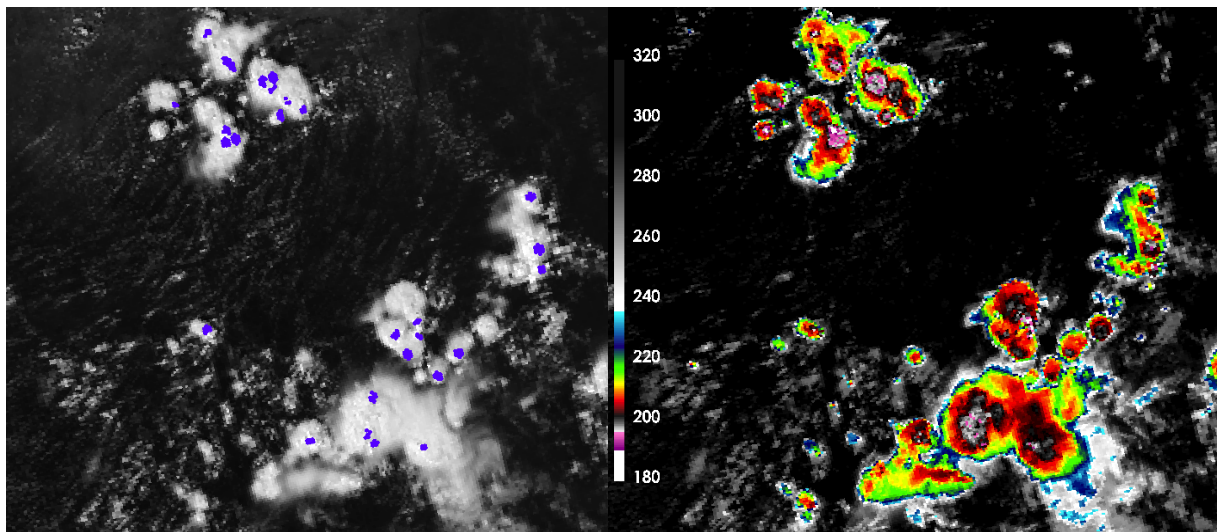

Figure 22: (left) NOAA-9 visible reflectance imagery over the Congo overlaid with the overshooting convective cloud top pixel detection mask (blue). (right) NOAA-9 color-enhanced IRW BT imagery for the same scene.

no minima are located within 15 km of each other so that portions of the same OT are not classified as two independent tops. The IRW BT of the anvil cloud surrounding the potential OT is then sampled at a radius of ~8-km in 16 directions. The surrounding anvil pixels must have T_4 ≤ 227.5 K to be included in the mean computation. At least five valid anvil pixels must be present. The 5-of-16-pixel criterion is imposed to ensure that the anvil is of relatively large horizontal extent but allows an anvil to occupy as small as a 90° quadrant, which might be the case when strong upper-tropospheric winds are present. A pixel is classified as an overshooting top if it is ≥ 6.0 K less than the mean T_4 of the surrounding anvil cloud. An example of the AVHRR OT pixel detection mask included in the TCDR is shown in Figure 22.

The 217.5-K OT BT, 227.5-K anvil cloud T_4, and 6.0-K thresholds for detecting OTs described above were selected based on detailed analysis of 450 warm season OT events in 1-km MODIS and AVHRR HRPT imagery. Testing was done with alternative thresholds

including a 220 K OT BT, 230 K anvil cloud BT, and 4.5 K OT magnitude during the GOES-R ABI AWG development process and it was determined that these thresholds provided detection accuracy that would not meet the 25% maximum FAR criterion mandated by the AWG program. Reducing the required OT BT threshold could improve detection of weak OT signals, but at the expense of producing a significant number of false detections.

This OT detection method has been demonstrated using GEO data over the continental U.S. (Figure 23a) and Europe (Figure 23c), global AVHRR GAC data (Fig. 23d), and MODIS data for individual UTLS-penetrating events directly observed by CloudSat (Bedka et al. 2010; Bedka 2011; Bedka et al. 2012). To provide the diurnal context for the AVHRR data, an 18-year Eastern U.S. OT database was generated using half-hourly GOES observations (Figure 23d), which have a spatial resolution comparable to that of the AVHRR GAC dataset. This database shows the distribution of intense deep convective updrafts over land and ocean
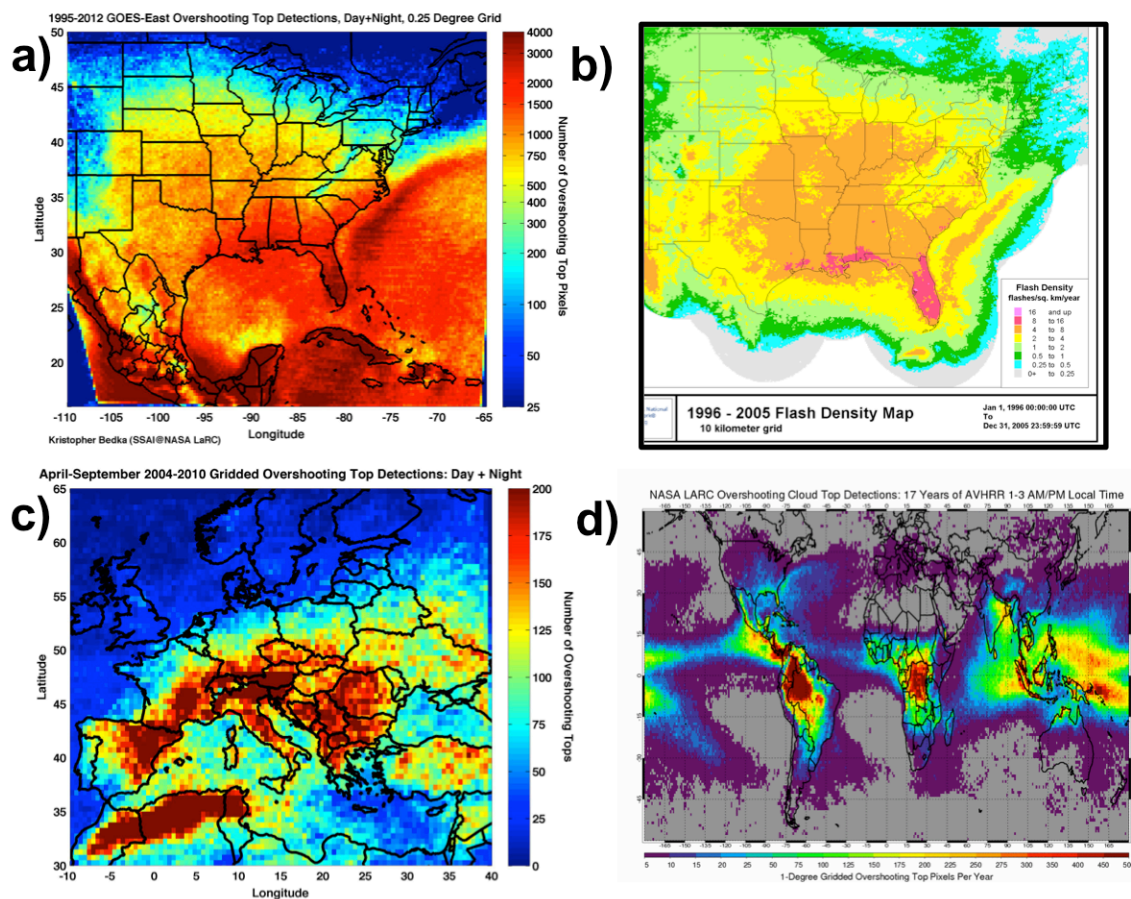

Figure 23: (a) Number of OT pixel detections per 0.25° grid box using 18 years of half-hourly GOES data. (b) 10-year Vaisala cloud-to-ground lightning flash density database over eastern U.S. Image, cropped to approximate domain in(a). (c) Number of OT detections per 0.5°region using 7 years of 15-min MSG SEVIRI data. Note that only the coldest pixel in an OT is counted here versus the GOES analysis in (a) where all pixels in an OT are counted. (d) Number of OT pixels per year per 1° grid box using 17 years of AVHRR GAC data with observations between 0100 and 0300 AM/PM LT.

with a level of detail beyond any existing long-term dataset. When animated, diurnal variability in convective storm activity is clearly evident across the continental U.S., the Gulf Stream ocean current, and the Gulf of Mexico. (See the following animation: http://cloudsgate2.larc.nasa.gov/site/people/data/kbedka//OTclimatology_1995-2012_30minscans_solartime.gif). A 10-year cloud-top-ground lightning database from the Vaisala National Lightning Detection Network (Figure 23b) shows similar patterns to the GOES OT database over land and near-shore regions. Having OT retrievals from satellites offers the opportunity to study the frequency and distribution of deep convective updrafts over open water and regions where other observations of convective storms are unavailable. The current 18-year global AVHRR OT database highlights distinct maxima over the Amazon rainforest, the Congo, and the Tropical Western Pacific, regions typically associated with the most frequent deep convection in the world (Figure 28d). This database only highlights OT activity in the 1-3 AM/PM timeframe because AVHRR observed these two 2-hour periods more than any other during its history (Figure 1). The Bedka et al. (2010) OT detection method is a state-of-the-art algorithm that detects OTs as well as or better than other existing methods (Bedka et al. 2010, 2012). Statistical comparisons of the results indicate strong relationships with lightning, heavy rainfall, and severe weather (Dworak et al. 2012; Punge et al. 2014).

OT detections are also being used to improve cloud-top height retrieval within the SatCORPS-A. As in CCPRS Edition 4, the difference between T_4 and T_p is computed and the pixel cloud height is elevated above the tropopause height using a lapse rate of 8 K km^{-1}. This lapse rate was derived from a combined MODIS and CloudSat analysis of the 111 OT events observed by the NASA A-Train described by Bedka et al. (2012). For example, if $T_4 - T_p$ = 12 K for a given pixel at a tropopause height of 15 km, then the pixel would be assigned a height of 16.5 km. This procedure makes deep convective cloud heights in OT regions much more realistic than limiting cloud height to the tropopause which was done in the CCPRS Edition 2 algorithm.

3.4.1.5   Broadband Shortwave and Longwave Fluxes

Instruments specifically designed to measure LW (5 - 100 μm) and SW (0.2 – 5 μm) radiation are best suited for providing CDR quality estimates of Earth's radiation budget. Hence, programs such as Earth Radiation Budget Experiment (ERBE) and CERES have produced the most accurate measurements to date, but their records are not complete. ERBE only measured the entire Earth from 1985 through 1989, while CERES has been observing the earth system since 2000. Filling the gaps in this record is important for studying climate trends. The narrow spectral bands used for satellite imagers have long been used to estimate the LW and SW fluxes exiting the Earth-atmosphere system via narrowband (NB) to broadband (BB) conversion functions (e.g., Gruber and Winston, 1978; Minnis and Harrison, 1984; Minnis et al. 1991). The quality of such estimates depends on many factors including the specific narrowband channels that are used, their calibrations, and the quality of the corrections for anisotropy and water vapor among other variables. The SW fluxes exiting at the TOA and the TOA LW fluxes or outgoing LW radiation (OLR) are estimated using an update of the methodology of Minnis and Smith (1998) with the anticipation for enhancements in the future.

For this version, the CERES unfiltered BB TOA SW albedo, α_{SWE}, and OLR, M_{LWE}, comprise the reference values and are taken from the CERES Aqua Edition 3A Surface Fluxes and Clouds (SFC) product (Wielicki et al. 1999; CERES, 2014a). The SFC product represents a nested 1° gridded average of α_{SWE} and M_{LWE} from CERES footprints (20 km at nadir for Aqua) within the Single Scanner Footprint, TOA and Surface Flux, Clouds product (SSF; Minnis et al. 2011a; CERES, 2014b). The NOAA-18 AVHRR data from a preliminary dataset (with a VIS calibration slightly lower by 0.005%) was gridded to match the CERES SFC 1° latitude x 1° longitude resolution between 45°S and 45°N. The SFC resolution then changes to 1° latitude x 2° longitude between 45° and 70°; 1° x 4° between 70° and 80°; and 1°x 8° between 80° and 89°. Filters were applied to both AVHRR and CERES data to ensure the box averages include sufficient sampling from all VZAs and latitudes within each box. In order to be considered a match, the averaged AVHRR and CERES grid box latitudes and averaged longitudes for 45°S-45°N were required to be within 0.1° of each other and the averaged longitudes poleward of 45°S and 45°N had to be within 0.25°.

To estimate the SW albedos, the AVHRR VIS channel reflectance is first converted to VIS albedo, α_1. The anisotropy of the VIS reflectances is removed in computing α_1 by dividing the reflectance by the appropriate TRMM CERES Angular Distribution Models (ADMs), which depend on cloud and surface type (Loeb et al, 2003). The ADMs are available for 6 general land scene types account for several variables including cloud fraction, phase, and optical depth.

The AVHRR SW BB albedo, α_{SWA}, is then estimated as

$$\alpha_{SWA} = a_0 + a_1\,\alpha_1 + a_2\,\alpha_1{}^2 + a_3\,ln(1/\,\mu_o), \qquad\qquad (36)$$

where the coefficients, a_i, are determined using a multiple regression fit using matched gridded NOAA-18 AVHRR α_1, and corresponding CERES Aqua α_{SWE} (Minnis and Smith, 1998). The values of α_1 selected for inclusion in the regression are also required to be within 15 minutes of the CERES observations and to be < 1.0 once normalized to the corresponding CERES-defined μ_o , which must be greater than 0.17365 (corresponds to SZA = 80°). Both CERES and AVHRR gridded values must have VZA < 65°. The resulting global matched data were fitted to Eq (36) for each month in 2008 over three scene types: land, ocean, and snow. Each selected AVHRR grid box must include at least 85% of one of those scene types. The derived monthly, scene-specific coefficients are then used to convert NB VIS albedos to BB SW albedos for the corresponding months and scene types in 2008 and other years. BB SW fluxes are computed as the product of the BB SW solar constant (1365.1 Wm^{-2}), α_{SWA}, μ_o, and the Earth-Sun distance correction factor.

Figure 24 shows an example of NOAA-18 AVHRR α_1 regressed with *Aqua* CERES α_{SWE} using data over ocean during January 2008. For a given value of α_1, α_{SWE} increases with increases SZA as indicated by the transition from light blue to red points. The last term of Eq (36) accounts for this dependency. For the 163,300 matches, the average ocean α_{SWE} and α_1 are
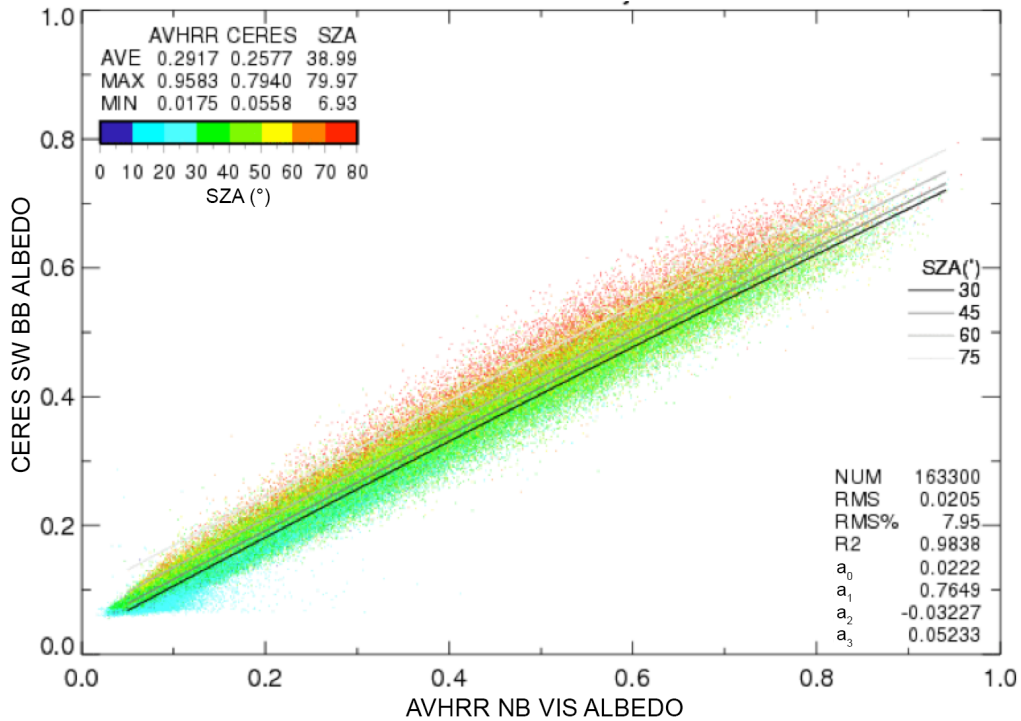
Fig. 24: Regression of global SW AVHRR α_{SWA} versus Aqua CERES α_{SWE}, for the ocean scene type during January 2008. The NB-BB conversion coefficients, a_i, are listed at lower right.

Table 7. Albedo RMS errors (unitless, and also expressed as percent) for 2008 monthly SW NOAA-18 AVHRR vs CERES *Aqua* NB-BB fits by scene type.

	SW Albedo Fit RMS Errors, 2008		
Month	**Land**	**Ocean**	**Snow**
January	0.0227 (8.0%)	0.0205 (8.0%)	0.0375 (6.8%)
February	0.0223 (8.0%)	0.0234 (8.9%)	0.0389 (7.1%)
March	0.0205 (7.5%)	0.0241 (9.1%)	0.0409 (7.6%)
April	0.0212 (7.8%)	0.0264 (10.1%)	0.0370 (6.7%)
May	0.0226 (8.3%)	0.0274 (10.8%)	0.0387 (7.1%)
June	0.0249 (8.9%)	0.0263 (10.5%)	0.0379 (7.6%)
July	0.0239 (8.5%)	0.0258 (10.1%)	0.0416 (9.5%)
August	0.0222 (8.1%)	0.0255 (9.9%)	0.0407 (8.7%)
September	0.0232 (8.2%)	0.0265 (10.1%)	0.0430 (7.8%)
October	0.0261 (9.2%)	0.0235 (9.3%)	0.0413 (7.3%)
November	0.0273 (9.7%)	0.0237 (9.2%)	0.0385 (6.6%)
December	0.0267 (9.3%)	0.0232 (9.0%)	0.0394 (7.0%)

0.2577 and 0.2917, respectively. The regression RMS error is 0.0205 (7.95%). The resulting coefficients for Eq (36) are listed in the lower right of the figure. The RMS errors for the fits representing the each scene type and all months of 2008 are summarized in Table 7. Over land, the albedo RMS varies from 7.5% to less than 10%, while over ocean, the RMS error is between 8 and 11%. In relative terms, the error is smallest, 6.8-9.5%, over snow scenes, even though the absolute RMS error is largest nearly double the values over land and ocean. The mean albedo is considerably greater over snow-covered scenes than elsewhere.

Similarly, the initial AVHRR LW flux is obtained from the matched data as

$$M'_{LWA} = b_0 + b_1 M_4 + b_2 M_4{}^2 + b_3 \ln(CRH), \qquad (37)$$

where M_4 is the IRW channel irradiance, CRH is the column averaged relative humidity above the radiating surface estimated from MERRA, and the coefficients, b_i, are obtained through multiple regression using the matched averaged NOAA-18 AVHRR M_4 and CERES Aqua irradiances M_{LWE}. The IRW radiance is multiplied by the appropriate CERES LW ADM (Loeb et al. 2003) to compute the irradiance. As with the SW approach, 2008 monthly global fits were derived over the three scene types separatley for daytime ($\mu_o < 90°$) and nighttime. Values of M_4 used for the fits were required to be < 80 Wm^{-2}.

As an example, Figure 25 shows NB-BB LW fits for January 2008 over ocean. For the 163,360 matches, the average daytime (Figure 25a) CERES M_{LWE} is 244.5 Wm^{-2}, corresponding to the CERES M_4 mean of 42.2 Wm^{-2}. The RMS error is 3.04%. At night (Figure 25b), the M_{LWE} and M_4 averages are 242.2 and 41.4 Wm^{-2}, respectively, for 172,574 samples. The fit yields an RMS error of 3.11%. The regression coefficients, b_i, for Eq (37) are listed in the lower right portion of the plots. LW regressions were performed for all scene types for the remaining months of 2008. The resulting monthly RMS errors listed in Table 8 range from 2.3 – 3.7%.

For a given value of M_4, M_{LWE} tends to increase with decreasing humidity above the radiating surface. This is evident in the vertical change in CRH indicated by the lower green points and higher blue points. The last term of Eq (37) accounts for most of this behavior, as seen in the lines fitted to the data for several constant CRH values. The form of Eq (37), however, fails to capture the relationship at the low end of the range, resulting in an overestimate for very cold scenes. In some instances, there can also be a bias at the higher end for daytime snow and land. These biases are the reason for M'_{LWA} being defined as an initial estimate. An adjustment is computed using a 3rd order polynomial to minimize the bias. The final estimate of AVHRR LW irradiance is

$$M_{LWA} = c_0 + c_1 M'_{LWA} + c_2 M'_{LWA}{}^2 + c_3 M'_{LWA}{}^3, \qquad (38)$$

where the coefficients c_i are determined through the least-squares method using average values of M'_{LWA} and M_{LWE} for every 10 Wm^{-2} interval that contains at least 20 matches. An adjustment is applied at both the upper and lower ends of the range for the snow and land daytime fits, but all other fits target a low-end correction only. Thus, for snow and land
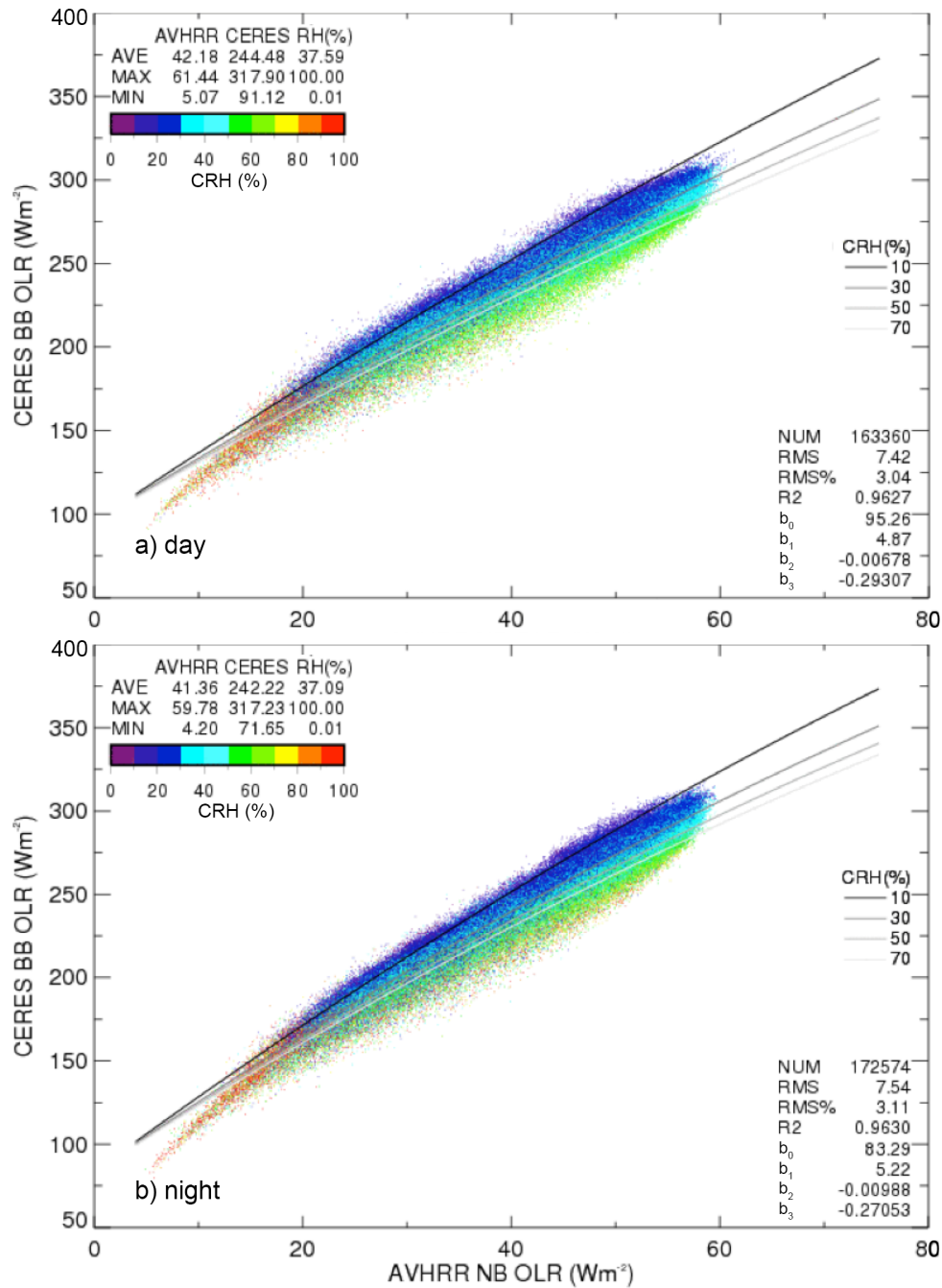
Fig. 25: As in Figure 24, but for LW AVHRR M_4 and Aqua CERES M_{LWE} during (a) daytime and (b) nighttime. The NB-BB conversion coefficients, b_i, are listed in lower right corner.

during daytime, equal values of M'_{LWA} and M_{LWE} were assumed between 50 Wm^{-2} above the minimum bin value, to 50 Wm^{-2} below the maximum bin value. For the other scene conditions, equal values of M'_{LWA} and M_{LWE} were assumed from 50 Wm^{-2} above the minimum bin, throughout the rest of the upper range.

**Table 8. RMS errors in Wm^{-2} (%) for 2008 monthly NOAA-18 AVHRR vs CERES
Aqua NB IRW-BB LW fits for three scene types.**

|	LW Flux Fit RMS Error Wm^{-2}, 2008					
	Land		**Ocean**		**Snow**	
Month	**DAY**	**NIGHT**	**DAY**	**NIGHT**	**DAY**	**NIGHT**
January	8.60 (3.2%)	7.11 (3.0%)	7.42 (3.0%)	7.54 (3.1%)	7.32 (3.7%)	6.44 (3.7%)
February	9.49 (3.5%)	7.73 (3.2%)	7.32 (3.0%)	7.22 (3.0%)	6.32 (3.4%)	6.20 (3.4%)
March	8.95 (3.3%)	7.82 (3.2%)	6.63 (2.7%)	6.76 (2.8%)	5.14 (2.7%)	5.37 (3.0%)
April	8.95 (3.3%)	7.32 (3.0%)	6.46 (2.7%)	6.65 (2.8%)	5.19 (2.7%)	5.41 (3.0%)
May	9.14 (3.4%)	7.47 (3.1%)	6.75 (2.8%)	6.81 (2.8%)	5.20 (2.5%)	5.79 (3.4%)
June	8.85 (3.3%)	8.73 (3.4%)	7.40 (3.0%)	7.34 (3.0%)	5.10 (2.3%)	5.78 (3.6%)
July	8.35 (3.1%)	7.94 (3.1%)	7.53 (3.1%)	7.55 (3.1%)	5.92 (2.6%)	5.74 (3.6%)
August	8.20 (3.0%)	7.48 (3.0%)	7.20 (2.9%)	7.27 (3.0%)	6.06 (3.0%)	5.61 (3.5%)
September	8.26 (3.0%)	7.08 (2.8%)	7.28 (3.0%)	7.24 (3.0%)	5.10 (2.7%)	5.65 (3.3%)
October	8.31 (3.1%)	6.86 (2.8%)	6.89 (2.8%)	7.09 (2.9%)	5.47 (2.9%)	5.31 (2.9%)
November	9.00 (3.3%)	7.14 (3.0%)	7.27 (3.0%)	7.09 (2.9%)	6.15 (3.2%)	5.35 (2.9%)
December	8.62 (3.3%)	7.72 (3.2%)	7.26 (3.0%)	7.30 (3.0%)	7.01 (3.6%)	5.89 (3.3%)
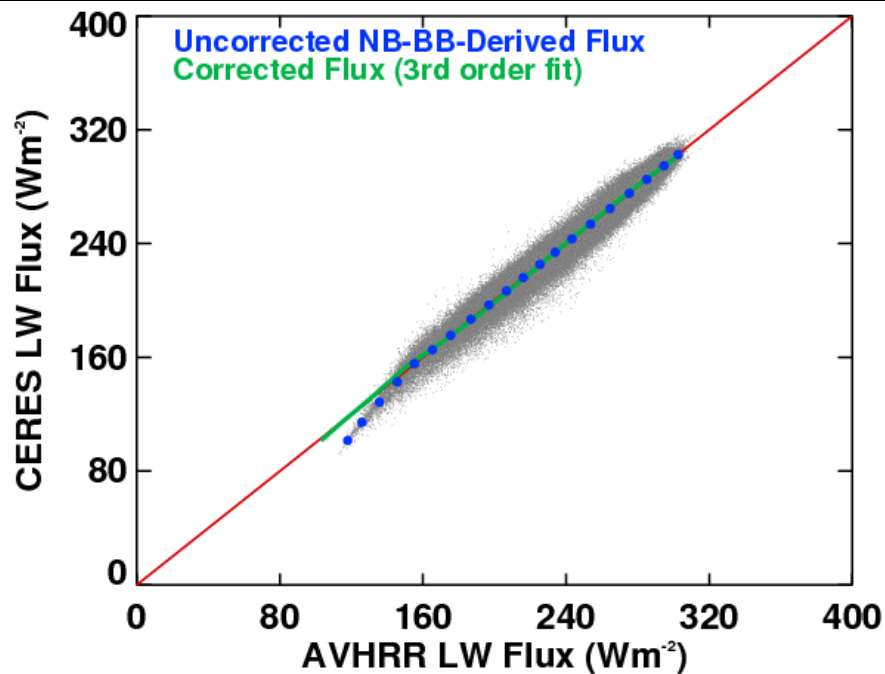
**Fig. 26: Demonstration of third order adjustment applied to daytime January
2008 AVHRR-derived M'_{LWA} plotted against CERES *Aqua* M_{LWE} for ocean scenes.
Unadjusted data (gray points) in the biased range are averaged into 10 Wm^{-2}**

bins (blue dots). Final mean values, M_{LWA}, after adjustment are in green.

Figure 26 provides an illustration of this adjustment for daytime January 2008 data over ocean. The gray points represent the results of applying Eq (37) to the AVHRR NB fluxes, while the blue points indicate the interval means. The fit to Eq (38) was developed from those points and used to compute M_{LWA}. The green line, showing the bin averages computed from the resulting values of M_{LWA}, demonstrates that the low-end bias is eliminated. Sets of c_i coefficients were computed for each scene type and month of 2008. They are used to adjust the fluxes computed using Eq (37) for other years.

3.4.2   Data Merging Strategy

While this document only describes the production of pixel data parameters from the AVHRR instrument, the creation of average product time series will ultimately be needed to study trends in the retrieved cloud parameters. Such trends will require the merging of data from various satellites to obtain multi-decade records. It is recommended that the merging of data from different satellites be performed using data from those satellites having nearly the same ECT. Thus, using Figure 1, three different trend lines of the parameters could be developed by merging data from satellites with nominal ECTs of 0730, 0930, and 1430 LT. Thus, for an 0730-LT trend, AVHRR data from N10, N12, and N15 can be merged to obtain a record of ~13 y beginning in 1987, while N17, M1, and M2 could be used to develop a trend line from 2003 to the present at ~0930 LT. The longest record that can be obtained would need to merge results from TIROS-N, N7, N9, N11, N14, N16, N18, and N19 for data taken at ~1430 ECT beginning in late 1978.

The process of merging the data will have to consider the drift in the satellite orbit (Figure 1), which will produce artificial trends in the data because of regular changes in cloudiness over the diurnal cycle. Also, a minimum number of samples will need to be required for a given time unit (e.g., day, month, or year) to establish reliable representation for each data point. While not always possible, data from periods of overlap should be used to ensure consistency across platforms, if feasible.

3.4.3   Numerical Strategy

The numerical strategies used in each component of the cloud detection and cloud property retrieval process have been laid out elsewhere in this document.

3.4.4   Calculations

The calculation steps have been laid out elsewhere in this document.

3.4.5   Look-Up Table Description

3.4.5.1   Cloud Reflectance LUTs

All reflectance LUTs were computed using the discrete ordinates method of Stamnes et al. (1988) using the optical properties described below. The output for each channel, particle size and optical depth consists of reflectances filling an array defined by 21 VZA, 21

SZA, and 24 RAAs, where the backscattering direction is RAA =180°. The VZA and SZA nodes are given in values of μ and μ_o, respectively. These angular nodes are listed in Table 9.

The VIS cloud reflectance LUTs were developed for seven water droplet distributions having effective variances of 0.1 and for nine roughened hexagonal ice crystal column models. The hexagonal ice column distributions described by Minnis et al. (1998) were used, but their optical properties were determined using crystals having a normalized surface roughness of 1.0, as defined by Yang et al. (2008b). Altogether there are 16 particle size models. The LUTs are provided at discrete values of COD between 0.25 and 256 with a maximum retrieved value of τ = 150. The model values of CER and COD used to create the LUTs are also listed in Table 9.

Table 9. Angular nodes, optical depths and particle sizes used for cloud reflectance LUTs.

μ or μ_o		RAA (°)		COD	Liquid r_e (μm)	Ice r_e (μm)
1.00	0.45	0	95	0.25	2	2.82
0.95	0.40	2.5	105	0.50	4	8.35
0.90	0.35	5	115	1.0	6	10.9
0.85	0.30	10	125	2	8	14.2
0.80	0.25	15	135	3	12	23.2
0.75	0.20	25	145	4	16	32.7
0.70	0.15	35	155	8	32	57.7
0.65	0.10	45	165	16		70.1
0.60	0.05	55	170	32		78.0
0.55	0.01	65	175	64		
0.50		75	177.5	96		
		85	180	128		
				256		

The cloud BRDF arrays $\rho_{c1}(R, \tau; \mu_o, \mu, \phi)$ were integrated to produce the cloud albedo $\alpha_{c1}(R, \tau; \mu_o)$ at each SZA for each phase, CER, and COD. Those albedos were convolved over the range of SZAs to yield the spherical or diffuse albedos $\alpha_{cd1}(R, \tau)$.

Similar reflectance and albedo LUTs were developed for the SIR and NIR channels, except that the maximum COD value is 64 because the albedos reach their maximum asymptotic values at or below that COD at those wavelengths. The optical depths used in those calculations are adjusted such that

$$\tau_i = \tau_1 \, Q_{ei}(R) \, / \, Q_{e1}, \qquad (39)$$

where i corresponds to a channel or subinterval of a channel. The values of Q_e vary with channel, phase, and particle size. Thus, the NIR or SIR LUT reflectances/albedos correspond to their VIS LUT counterparts at the same VIS COD. In addition to the reflectance LUTs, cloud absorption $A_{cd6}(R, \tau; \mu_o)$ and diffuse absorption $A_{cd6}(R, \tau)$ LUTs were computed for the NIR channels. Values of Q_e, single-scatter albedo, and asymmetry factors are also available for use in the programs.

The SIR reflectance LUTs were computed for the same five sub-intervals used for the atmospheric absorption computations (Sec. 3.2.4.1). The reflectances in the sub-intervals were convolved with the SRF and sub-interval solar constant to obtain the weighted mean reflectances for each AVHRR response function. Those values are used in the LUTs.

Finding a reflectance for a given value of τ and r_e at a specified set of viewing and illumination angles is obtained by tri-linear interpolation first between the angular nodes for the two nearest r_e and τ nodes, then further interpolation in r_e and τ space.

3.4.5.2   Surface and clear-sky reflectance models

The clear-sky and surface reflectances are determined in a variety of ways depending on the channel and surface type. As noted in Section 3.2.4.2, for water surfaces (K = 16), the respective VIS, NIR, and SIR surface bidirectional reflectances , ρ_{s1}, ρ_{s6}, and ρ_{s3}, and diffuse albedos, α_{sd1}, α_{sd6}, and α_{sd3}, are computed as a function of wind speed using the model of Jin et al. (2006) with a sea-salt aerosol having an optical depth of 0.1. The LUTs correspond to three wind speeds, 3, 6, and 12 m s^{-1}. The reflectance tables were computed for 11 SZA angles corresponding to μo = 1.0, 0.95, 0.85, …, 0.05; 10 VZAs at 0, 10, 20, …, 80, and 88°; 13 RAAs: 0, 15, 30, …, 165, and 180°. Quadrilinear interpolation is used to compute the values for a specific set of angles and wind speed.

For permanent snow surfaces (K=17), a theoretical model of snow reflectance was developed using a mixture of ice crystal habits, columns, column aggregates, plates, and bullet rosettes, of various sizes to achieve a value of r_e = 100 μm. The optical properties of these particles were computed using a surface roughness of 0.1 as defined by Yang et al. (2008b). Reflectances were computed for channels 1, 3, and 6 at 18 values of SZA and VZA between 0 and 90° and at 19 values of RAA between 0 and 180° using an optical depth of 1000. Diffuse albedos α_{sd} were also computed for each channel. Tri-linear interpolation in angular space is used to obtain the snow reflectance at a particular set of angles.

For other surface types, a combination of normalized directional albedo models $\delta_i(K; \mu_o)$ and normalized BRDFs $\chi_i(K; \theta_o, \theta, \phi)$ are employed to compute $\alpha_i(K, LAT, LON; \theta_o=0°)$ from the overhead albedo $\alpha_i(K, LAT, LON; \theta_o=0°)$ of the 10' region corresponding to the center of the tile for the given date.

The clear-sky reflectance for a given location (LAT, LON) and set of viewing and illumination conditions is

$$\rho_{cs1}(LAT, LON; \theta_o, \theta, \phi) = \delta_1(K; \mu_o)\ \alpha_1(K, LAT, LON; \theta_o=0°)\chi_1(K; \theta_o, \theta, \phi). \qquad (40)$$

The normalized land SW BRDF values from Suttles et al. (1988) are used for $\chi_1(K; \theta_o, \theta, \phi)$ for vegetated land and coast (K = 1-14, 18, 19) and the desert model of Suttles et al. (1988) for K = 16.

The NIR surface reflectances ρ_{s6} are determined in the same manner as the VIS clear-sky reflectances in Eq (40), except that the four 1.6-μm normalized BRDFs from Kriebel (1978) are used to provide values of χ for the NIR channel over most land surfaces. The coniferous forest model is used for all forests (K = 1-5); the bog model is used for K= 11, 18, and 19; savannah data are used for K = 6, 7, 8, 9, and 13; and pasture results are used for K = 10, 12, 14. The models from Kriebel provide values at ten 10° SZA and VZA nodes from 0 – 90°, and seven 30° RAA nodes from 0 – 180°. The broadband desert model of Suttles et al. (1988) was used for the NIR and SIR for deserts. It uses 10 SZA bins corresponding to μ_o = 0.95, 0.85, 0.75, …, 0.15, and 0.05; 7 VZA bins bounded by 0, 15, 27, 39, 51, 63, 75, and 90°; and 8 RAA bins bounded by 0, 9, 30, 60, 90, 120, 150, 171, and 180°.

Having only sparse information about SIR BRDFs for land surfaces, the four 2.13-μm normalized BRDFs from Kriebel (1978) are employed for the SIR channel in the same manner as the 1.6-μm models were used for the NIR channel. No directional model of SIR albedo is currently available, therefore, it is assumed that albedo is constant with μ_o and it is simply one minus the surface emissivity. Thus, the SIR surface reflectance is estimated as

$$\rho_{s3} = (1 - \varepsilon_{s3}) \; \chi_3(K; \theta_o, \theta, \phi). \tag{41}$$

where χ_3 corresponds to the 2.13-μm normalized BRDFs.

The clear-sky and surface albedo data are compiled for each month of the year for each 10' of LAT and LON. Two sets each, snow-free and snow-covered, are provided for
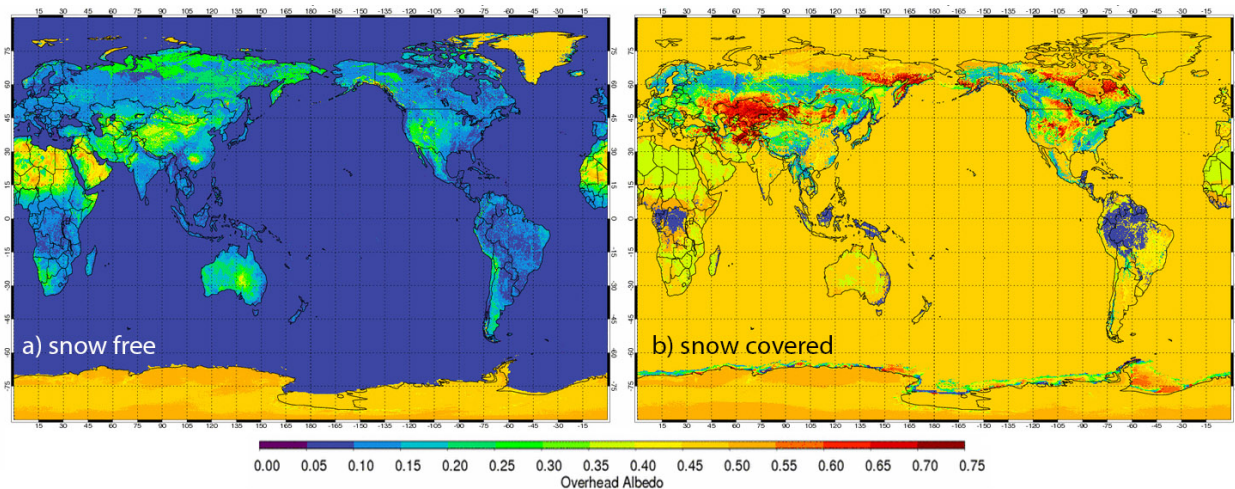

Figure 27: Clear-sky VIS overhead-sun albedos for January over a) snow free and b) snow covered surfaces.

the VIS and NIR channels. Figure 27 provides examples of $\alpha_1(K, LAT, LON; \theta_o=0°)$ for January 2008 for both snow-free and snow-covered conditions. It is clear that many areas

(e.g., Amazon Basin) never experience snow cover despite being assigned a value for an overhead-sun snow albedo. These values are simply provided as placeholders to fill out the arrays. They are taken from global mean values for each IGBP type.

The corresponding average un-normalized VIS clear-sky directional albedo models for permanent snow/ice, ocean, desert, and the four Kriebel categories are shown in Figure 28. The curves are based on polynomial fits to observations. The values of $\delta_1(K; \mu_o)$ used by the SatCORPS-A were obtained by dividing the value of $\alpha_1(K; \mu_o)$ by $\alpha_1(K; \mu_o=0°)$. Both
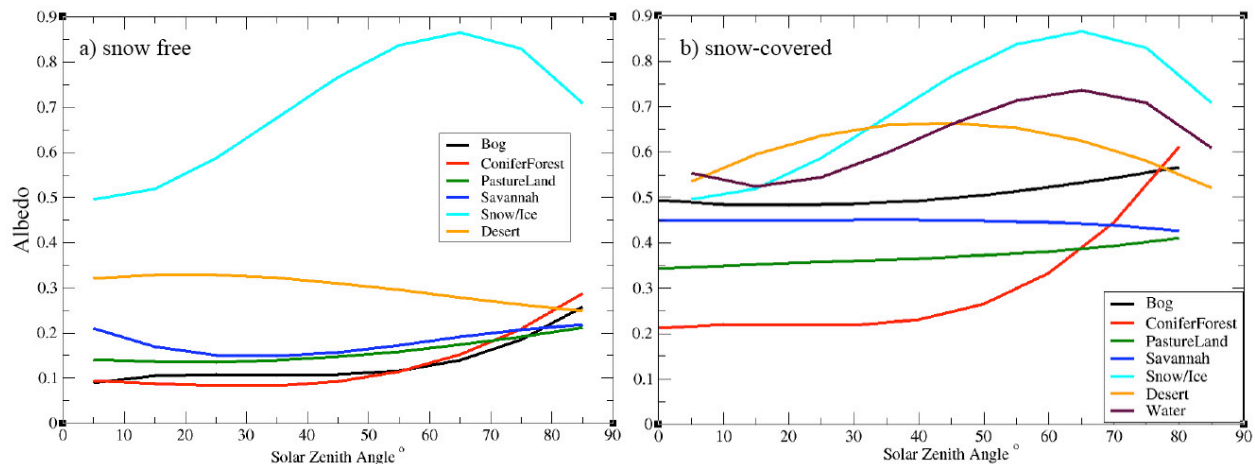

Figure 28: Mean clear-sky VIS albedo variation with SZA for major surface-type categories.

permanent and variable ice-covered water surfaces as well as permanent snow regions use the permanent snow BRDF model, but adjust it according to the average value of α_1(K, LAT, LON; $\theta_o=0°$). The snow-covered BRDFs used for other surfaces that have seasonal snow cover are hybrids BRDFs constructed from the permanent snow and snow-free BRDFs for the particular surface type as in Chen et al. (2010). The average albedos for snow-covered surfaces at smaller SZAs are typically based on only a few data points and then are probably in areas without extensive snow cover that is often partially melted. Thus, the lower values of $\alpha_1(K; \mu_o=0°)$ are not likely to be for the same snow cover conditions at larger SZA values. Nevertheless, the curves typically increase with increasing SZA so that $\alpha_1(K; \mu_o)$ can be quite large for the SZAs that correspond to the actual observations. For example, $\alpha_1(\mu_o=0°)$ over Greenland is only ~0.50. However, Greenland is only illuminated at SZAs typically exceeding 50°, so that the clear-sky albedo would be between 0.7 and 0.9.

3.4.5.3   Rayleigh scattering model

The Rayleigh scattering reflectance, albedo, and diffuse albedo LUTs used here were reported by Minnis et al. (1993). LUTS of reflectance $\rho_R(\tau_R; \mu_o, \mu, \phi)$, albedo ($\alpha_R(\tau_R; \mu_o)$, and $\alpha_{Rd}(\tau_R)$ were computed at optical depths corresponding to p = 250, 500, 750, and 1000 hPa. At 1000 hPa is τ_R~0.0471 and is linear in pressure. The LUT reflectances are listed for 10 SZAs corresponding to μ_o = 0.05, 0.15, …, 0.95; 10 VZAs corresponding to μ = 0.1, 0.2, …, 1.0; and 17 RAAs, ϕ = 0, 5, 15, 30, …, 150, 165, 175, 180°. The Rayleigh scattering depends on

A controlled copy of this document is maintained in the CDR Program Library.

Approved for public release. Distribution is unlimited.

74

the SRF of each sensor. Therefore, the Rayleigh optical depth at 1000 hPa, τ_R(SRF), is computed for each sensor's VIS channel. Because the reflectances and albedos are linear in τ_R, the Rayleigh albedo and reflectance values for a given sensor are simply the LUT values multiplied by the ratio τ_R(SRF)/0.0471.

3.4.6   Parameterization

Some of the parameterizations used in the SatCORPS-A have already been described. This section reviews those parameterizations that have not yet been characterized in this document.

3.4.6.1   Optically thick ice cloud thickness parameterization

For ice clouds having $\tau > 8$ and $T_c < 245$ K, ice cloud thickness is estimated using the retrieved variables in a parameterization that was developed from matched CERES Aqua MODIS Ed2 cloud parameters and CloudSat and CALIPSO cloud top and base measurements. The cloud top heights were provided by the CALIPSO lidar measurements and the base heights were from the lowest CloudSat return having no precipitation flag. The thickness ΔZ_{CC} is simply the difference between the top and base heights. Only single-layer contiguous clouds were used in the development of the parameterization. It was found that the independent variables showing the greatest correlations with ice cloud thickness are T_c, $\ln(\tau)$, and $\ln(IWP)$. The initial estimate is computed as

$$\Delta Z' = a_0 + a_1 T_c + a_2 \ln(\tau) + a_3 \ln(IWP). \tag{42}$$

This formula does not fully capture the variation in ΔZ, so a second correction ΔZC is applied depending on the value of $\Delta Z'$ between Z_x and Z_y, where

$$If\ \Delta Z' > Z_y, \qquad then\ \Delta ZC = 0. \tag{43a}$$

$$If\ Z_x < \Delta Z' \leq Z_y,\ then\ \Delta ZC = b_0 + b_1 \Delta Z' + b_2\ \Delta Z'^2 + b_3\ l\Delta Z'^3. \tag{43b}$$

$$If\ Z_w < \Delta Z' \leq Z_x,\ then\ \Delta ZC = 0. \tag{43c}$$

$$If\ \Delta Z' \leq Z_w, \qquad then\ \Delta ZC = C. \tag{43d}$$

The value of cloud thickness is then estimated as

$$\Delta Z = \Delta Z' + \Delta ZC. \tag{44}$$

The coefficients and parameters for Eqs (42) and (43) are listed in Table 10. In practice, the L1 coefficients are used for tropical areas between 20°N and 20°S, while the L2 parameters are used for all areas poleward of 50° latitude. In the midlatitudes (20°N – 50°N, 20°S –

Table 10: Coefficients and constants used for thick ice cloud thickness estimates.

Geotype	a_0	a_1	a_2	a_3	Z_w	Z_x
Land L1	8.904	-0.031	1.145	0.516	1.0	2.5
Land L2	3.036	-0.009	0.299	0.751	0.0	0.0
Ocean L1	10.859	-0.040	1.085	0.571	1.0	2.4
Ocean L2	7.454	-0.027	0.633	0.721	0.0	0.0
	b_0	b_1	b_2	b_3	Z_y	C
Land L1	2.634	-1.3405	0.1748	-0.00636	13.0	0.5
Land L2	0.0	0.0	0.0	0.0	0.0	0.0
Ocean L1	2.153	-1.5548	0.2595	-0.1120	19.0	0.5
Ocean L2	0.0	0.0	0.0	0.0	0.0	0.0

50°S), the initial thicknesses, $\Delta Z'$(L1) and $\Delta Z'$(L2), are computed first and then $\Delta Z'$ is computed by linear interpolating between 20° and 50° use |LAT| for the pixel. Over midlatitude ocean, ΔZ is computed as $\Delta Z'$+ 0.5 km or $\Delta Z'$ - 0.5 km, if $\Delta Z' >$ 1.6 km or if $\Delta Z' <$ 0.5 km, respectively. In all other midlatitude cases, $\Delta Z = \Delta Z'$.

3.4.6.2   Cloud emissivity parameterization

Cloud emissivity is estimated using the following parameterization, which is tabulated for 9 discrete values of τ between 0.25 and 32 for each of the three thermal channels, 3, 4, and 5.

$$\varepsilon(\zeta, \mu, \xi) = \sum_{i=0}^{2} \sum_{j=0}^{4} \sum_{k=0}^{1} d_{ijk} \zeta^i \mu^j \xi^k, \qquad (45)$$

where $\zeta = (1/\Delta T_{sc})$, $\xi = 1/\ln(T_{bk})$, and the coefficents d_{ijk} are unique for each value of τ, phase, and r_e. The value of T_{bk} is $B_4^{-1}(L_{U4Jj-1})$, j-1 indicates the layer below the cloud, and $\Delta T_{sc} = T_s - T_{bk}$. The variables, i, j, and k, here are coefficient indices.

For $0.25 < \tau < 16$, four-point Lagrangian interpolation is used to find ε for a given value of τ off the node points. Linear interpolation is used for $\tau < 0.25$ and $16 < \tau < 32$, while for $\tau > 32$, $\varepsilon = \varepsilon(\tau=32)$. The values of the coefficients were computed as in Minnis et al. (1998) using the water droplet and smooth ice crystal optical properties described therein. Because ice crystal surface roughness has a negligible impact on the emission and absorption of the crystals at thermal wavelengths and the ice crystal size distributions used for the rough crystal calculations are essentially the same as those of Minnis et al. (1998), the SIR coefficients developed by Minnis et al. (1998) for MODIS are used here, while the GOES IRW and SWI channel coefficients are used for channels 4 and 5, respectively, in the SatCORPS-A. Details of the parameterization development can be found in Minnis et al. (1998).

3.4.7   Algorithm Output

The SatCORPS-A processes an AVHRR GAC orbit file in 1000 scan line segments. The last scan segment of the orbit often lacks 1000 scan lines as it is very rare that an orbit would have a number of scan lines evenly divisible by 1000. Internally-compressed NetCDF-4

format files with the 33 parameters listed in Table 11 are written for each of the orbit segments. This set of files is then processed by a Fortran program that 1) computes the beginning and ending scan time and maximum latitude and longitude for all the files from a given orbit, 2) merges all the segments into a single internally-compressed NetCDF-4 format file matching the array dimensions of the original GAC Level 1B orbit file, and 3) adds the metadata from step 1 in addition to other metadata required by the NOAA CDR program.

The output filenames have the following structure: NSS.GHRR.N?.DYYDDD.SHHMM.EHHMM_NASA_LaRC_cloud_properties.nc. The first 6 segments of the filename (separated by periods) match the filename from the AVHRR GAC Level 1B orbit file described in Section 2.2. The remainder of the filename identifies the source of the data (NASA LaRC) and the type of data stored in the file (cloud properties).

Table 11: Parameters provided in the AVHRR Cloud TCDR NetCDF-4 output files. A brief description of each parameter and its unit, the data type of the parameter in the NetCDF file, the valid data range, and the dimensions of each array are provided. The variable *nlines* corresponds to the number of scan lines in an AVHRR GAC orbit. The number of pixels is always 409 for GAC files. CDR-quality parameters are indicated in bold.

NetCDF Parameter Name	Parameter Description (Units)	Data Type	Valid Data Range	Dimensions
TCDR Parameters				
reflectance_063micron	Calibrated reflectance for AVHRR 0.63 μm Channel 1 (unitless)	Integer	0-12.5	*nlines* x 409 pixels
reflectance_086micron	Calibrated reflectance for AVHRR 0.86 μm Channel 2 (unitless)	Integer	0-12.5	*nlines* x 409 pixels
reflectance_1.61micron	Calibrated reflectance for AVHRR 1.61 μm Channel 3a (unitless)	Integer	0-12.5	*nlines* x 409 pixels
cloud_mask	Cloud mask (count)	Byte	0-3	*nlines* x 409 pixels
cloud_phase*	Cloud microphysical phase (count)	Byte	0-7	*nlines* x 409 pixels
optical_depth**	Cloud optical depth (unitless)	Unsigned Short	0-150	*nlines* x 409 pixels
effective_radius**	Water droplet or ice crystal effective radius (μm)	Unsigned Short	0-150 μm	*nlines* x 409 pixels
cloud_top_pressure	Pressure at cloud top (hPa)	Unsigned Short	0-1100 hPa	*nlines* x 409 pixels
cloud_effective_pressure	Pressure at radiative center of cloud (hPa)	Unsigned Short	0-1100 hPa	*nlines* x 409 pixels
cloud_base_pressure	Pressure at cloud base (hPa)	Unsigned Short	0-1100 hPa	*nlines* x 409 pixels

A controlled copy of this document is maintained in the CDR Program Library.

Approved for public release. Distribution is unlimited.

77

cloud_top_height	Height at cloud top (km)	Unsigned Short	0-25 km	*nlines* x 409 pixels
cloud_effective_height	Height at radiative center of cloud (km)	Unsigned Short	0-25 km	*nlines* x 409 pixels
cloud_base_height	Height at cloud base (km)	Unsigned Short	0-25 km	*nlines* x 409 pixels
cloud_top_temperature	Ambient temperature at cloud top (K)	Unsigned Short	160-340 K	*nlines* x 409 pixels
cloud_effective_temperature	Ambient temperature at radiative center of cloud (K)	Unsigned Short	160-340 K	*nlines* x 409 pixels
overshooting_mask	Overshooting convective cloud top pixel detection (count)	Byte	0-1	*nlines* x 409 pixels
pixel_skin_temperature	Land or water surface skin temperature (K)	Unsigned Short	180-340 K	*nlines* x 409 pixels
shortwave_broadband_albedo	Top of Atmosphere Shortwave Broadband Albedo (unitless)	Unsigned Short	0-12.5	*nlines* x 409 pixels
longwave_broadband_flux	Top of Atmosphere Longwave Broadband Flux (Wm^{-2})	Unsigned Short	0-500 Wm^{-2}	*nlines* x 409 pixels
Ancillary Parameters				
Latitude	Pixel latitude (degrees)	Float	-90° - 90°	*nlines* x 409 pixels
Longitude	Pixel longitude (degrees, negative for Western Hemisphere)	Float	-180° - 180°	*nlines* x 409 pixels
year_and_dayofyear	Year and day of year of scan line, YYYYDDD format	Integer	1979001-2019365	*nlines*
time	Time of scan line (seconds)	Integer	0-172799	*nlines*
brightness_temperature_374micron	AVHRR observed 3.74 µm brightness temperature (K)	Unsigned Short	160-340 K	*nlines* x 409 pixels
brightness_temperature_108micron	AVHRR observed 10.8 µm brightness temperature (K)	Unsigned Short	160-340 K	*nlines* x 409 pixels
brightness_temperature_120micron	AVHRR observed 12.0 µm brightness temperature (K)	Unsigned Short	160-340 K	*nlines* x 409 pixels
relative_azimuth	Relative azimuth angle (degrees)	Unsigned Short	0°-180°	*nlines* x 409 pixels
viewing_zenith	Viewing zenith angle (degrees)	Unsigned Short	0°-90°	*nlines* x 409 pixels
solar_zenith	Solar zenith angle (degrees)	Unsigned Short	0°-180°	*nlines* x 409 pixels

snowice_flag	Snow or sea ice flag from MERRA, AVHRR, and IGBP maps (count)	Byte	0-1	*nlines* x 409 pixels
pixel_skin_temperature_quality_flag	Quality flag for pixel skin temperature retrieval (unitless)	Byte	0-2	*nlines* x 409 pixels
clear_sky_category	Clear sky pixel classification	Byte	0-8	*nlines* x 409 pixels
cloud_category	Cloudy pixel classification	Byte	0-4	*nlines* x 409 pixels

* CDR quality daytime only

** CDR quality daytime over non-snow areas only

4. Test Datasets and Outputs

4.1 Test Input Datasets

The reproducibility of SatCORPS-A output is investigated through the processing of one AVHRR GAC file from October 2008: NSS.GHRR.NN.D08275.S0828.E1010.B1734445.GC.

The reproducibility analysis is described in Section 4.2.

4.2 Test Output Analysis

4.2.1 Reproducibility

The reproducibility of the results was examined by comparing retrieval output from two SatCORPS-A runs using the same GAC input file. As described in detail in Section 5.6, the SatCORPS-A processes a scan-line orbit file, typically having ~13,000 scans, by separating the data into segments of 1000 scan lines (except the final segment which will have variable size). The scan segments are fed to different processors within the NASA LaRC large-scale computing architecture. The final Cloud TCDR output file for an orbit is assembled by merging scan segment output into a file with the dimensions of the original GAC file.

This computing architecture comprises several hundred processors with multiple users constantly submitting jobs to the processing queue. Thus it is unlikely that the same set of processors were used to process both SatCORPS-A runs. Therefore, comparison of output from the two runs provides an estimate of the SatCORPS-A reproducibility. No cloud mask pixels changed from run to run. Only 5 out of 4,992,663 (.0001%) pixels had retrieval values that changed. This result is similar to findings from previous studies using MODIS data within the CCPRS. The changes in the 5 pixels are likely caused by subtle differences in the computer operating system across the cores used to process the two runs.

4.2.2 Precision and Accuracy

The precision and accuracy expectations can be estimated using both theoretical and empirical methods. Theoretical methods can serve as a basis for evaluating the precision and accuracy for the cloud parameters, but they rely on a variety of assumptions that may occur infrequently in nature, i.e., that clouds are plane parallel, have particular vertical distributions of r_e and LWC or IWC, and are single-layered (see discussion in Han et al. 1994). A host of theoretical sensitivity studies could be conducted in an attempt to account for the infinite variety of cloud vertical and horizontal structures encountered in a global cloud retrieval system, but they still cannot reproduce the actual conditions encountered because they remain gross simplifications of the actual clouds. Thus, they cannot be considered as true estimates of accuracy and precision.

Precision and accuracy can also be determined empirically by comparisons with reference data, that is, measurements considered to be more reliable than the passive visible and infrared satellite retrieval. It is important to understand, however, that those reference measurements are also subject to their own uncertainties. For scene classification, cloud phase and height, and thin cloud optical depth, lidar or radar data are preferred because they, especially the former, detect the hydrometeors actively, objectively and confidently in most cases. Examples of these comparisons are given in Section 5.5.2 and the results are summarized in Section 4.2.3. The precision and accuracy of the cloud particle effective radius and optical depth retrievals and subsequent column ice or liquid water path can be estimated using theoretical calculations and by comparison with other measurements such as microwave radiometer retrievals of LWP, surface-based radiometer retrievals of COD (e.g., Min et al. 2005) and CER and the resulting CWP (e.g., Dong et al. 2002, 2008), lidar or radar retrievals of COD, IWP, LWP, and CER (e.g., Mace et al 1998, 2005), and comparisons with in situ data (e.g., Young et al. 1998, Painemal et al. 2012). A combination of the theoretical and empirical methods is most suitable for understanding the overall uncertainties in the retrievals.

Using exact adding-doubling radiative transfer model calculations of the reflectance fields with specified values of CER, the retrieved values of CER have a precision of ~12%, respectively, of their specified input counterparts and an accuracy of ~-0.2 µm (e.g., Han et al. 1994). The visible reflectance parameterization used in the VISST is an approximation of detailed adding-doubling model and predicts reflectances with accuracies of -0.01 to 0.03% for clouds over surfaces having albedos between 6, 30, and 70%, respectively. The corresponding precision values are 0.53, and 1.04% (Minnis et al. 2011a). A 2% difference between the modeled and observed reflectance results in a precision of ~10% (e.g., Dong et al. 2008). Considering the retrieval technique and its approximations, the LWP accuracy is roughly -2% with a precision of ~16%. All retrievals assume that the each cloud pixel is entirely filled by a cloud and the particle size is uniform throughout the cloud, but that is not always the case. Droplet size typically increases with height within a liquid cloud and ice crystal size generally decreases with height in an ice cloud. A pixel will often be partially filled with clouds in cumulus and broken cloud fields. When a given pixel is partially cloud filled, COD will be underestimated and CER overestimated for the cloudy portion of the pixel. It is expected that the dependence of the errors on pixel fractional cloud coverage will be much like that reported by Han et al. (1994). Comparisons with CALIPSO (Sec. 5.5.2) suggest that ~10% of the pixels in nonpolar regions are partially filled with clouds; fewer partly cloudy pixels occur in polar regions.

The pixel classification and retrievals depend on the quality of the predicted clear-sky values for each channel. A comparison of the predicted and observed clear-sky VIS reflectances was performed for the October 2008 results and it was found that for a given snow-free surface type, the average bias in clear-sky reflectance is between +10% with typical RMS values between 20 and 30% for most surfaces. Much larger errors occur for snow or ice covered surfaces because the BRDF for snow and ice-covered surfaces is extremely variable and poorly characterized. Altering the clear-sky values by the mean bias for each surface type had essentially no impact on the mean global retrieved cloud

A controlled copy of this document is maintained in the CDR Program Library.

Approved for public release. Distribution is unlimited.

81

properties. For overcast scenes, the predicted TOA IRW and SIR radiances depend on the input surface temperatures, atmospheric profiles, and surface emissivities. The uncertainties resulting from those inputs are discussed by Minnis et al. (2011a) for the nighttime retrievals.

The following section along with Sections 5.5 and 6.0 provide more details of the accuracy and precision of the products and how they may be improved.

Table 12. Error budget for SatCORPS-A1 global cloud fraction and phase based on differences between N18 and CALIPSO data, January, April, July, and October 2008. SF – snow/ice free, SI – Snow or ice covered surfaces.

Product	Constraint	Fraction Correct	Fraction Bias*	Number of Pixels x 10^3
Cloud fraction All pixels	SF Night	0.888	-0.021	1,292
	SF Day	0.873	-0.011	1,231
	SI Night	0.715	-0.065	727
	SI Day	0.825	-0.093	404
Cloud fraction Overcast only	SF Night	0.917	-0.028	1,165
	SF Day	0.903	-0.027	1,102
	SI Night	0.717	-0.067	721
	SI Day	0.827	-0.094	400
Cloud Phase	SF Night	0.916	0.024	416
	SF Day	0.918	0.072	406
	SI Night	0.882	-0.078	149
	SI Day	0.782	-0.099	73
Cloud Phase for CALIPSO mixed phase pixels	**Constraint**	**Fraction Water**	**Fraction Ice**	**Number of pixels x 10^{-3}**
	Night	0.578	0.422	164
	Day	0.729	0.271	119

*For cloud phase, positive indicates too much liquid water

4.2.3   Error Budget

The best error estimates for this dataset are based on the validation efforts conducted through comparisons with reference data sources (Sections 5.5.1 – 5.5.2). The values for assessing the errors include instantaneous comparisons and monthly averages. Future studies will provide more comprehensive comparisons of instantaneous matched retrievals. The error budgets are summarized here. Additional details describing the comparisons and their results, as well as discussion of the reference uncertainties are given in Sections 5.5.1-5.5.2.

For cloud fraction, phase, cloud-top height, and non-opaque cloud COD and water path, the errors are based on matched N18-CALIPSO data for January, April, July, and October 2008. Together, the fraction correct and the fractional bias provide a measure of instantaneous errors expected for identification of a given pixel as clear or cloudy. If the fractional bias is negative, the AVHRR underestimates the cloud cover by the given amount, on average. Conversely, a positive value denotes a cloud overestimate. Typically, 15 333-m CALIPSO profiles fit within an AVHRR footprint, so that the CALIPSO cloud fraction could be clear (no clouds), partly cloudy (PC, between 1 and 14 cloudy shots), or overcast (OC, no clear). Two approaches are taken for assessing cloud fraction. One uses all pixels with CALIPSO PC pixels being classified as either clear if fewer than 8 shots are cloudy. Otherwise, the pixel is cloudy. In order to minimize noise, the second approach does not use any PC pixels. The results from both methods are summarized in Table 12. For the method using all pixels, the scene classification is correct 87-89% of the time for scenes without snow and ice and cloud fraction is underestimated by -0.016, on average. The results are worse at night over snow- and ice-covered surfaces because of the reduced contrast between clouds and snow in both the IRW and VIS channels. The second approach raises the fraction of pixels correctly identified to between 90 and 92%, but the underestimate increases up to 0.028 for snow-free scenes and to 0.067 for snow-covered surfaces. This clearly shows that the fraction correct is impacted by the noise of the PC scene selection, but all pixels must be included to fully assess the bias.

The phase comparison, also summarized in Table 12, is based on only those AVHRR pixels that are matched with single-phase, OC CALIPSO data. No ice-over-water multilayer clouds or a mix of ice and water shots are included in the matchup. When the CALIPSO phase is constant within a given GAC pixel, the SatCORPS-A1 correctly identifies the phase ~92% of the time over non-polar snow-free surfaces, but only 78-88% of the time over snow-covered scenes. Over snow, the SatCORPS-A1 tends to overestimate ice cloud amount (negative fraction bias), while it tends to overestimate water clouds over snow-free scenes (positive fraction bias). Listed at the bottom of Table 12 are the phase selections by SatCORPS-A1 for OC multi-phase CALIPSO pixels that were not included in the direct phase comparison. More of those pixels were classified as liquid during the day than at night. The reasons for these differences in phase selection are discussed in Section 5.5.2.3.

Cloud-top heights are compared only for single-phase, OC CALIPSO pixels. The mean height is computed using the top of highest cloud in the column for these cases. Table 13 summarizes the comparisons for liquid and ice clouds. For liquid clouds over snow-free areas, SatCORPS-A1 overestimates the CTH by 0.35 km at night and underestimates it by 0.26 km during the day. The precision is ~0.80, on average. Over snow-covered scenes, mainly in polar regions, CTH is overestimated by 0.58 ± 1.26 km. Ice-cloud top heights over snow-free scenes are underestimated by 1.41 and 1.65 km during night and day, respectively, with respective precisions of 1.89 and 1.75 km. Over snow, the mean underestimate is -2.03 ± 2.90 km.

Cloud base height is validated using the 5-km CloudSat Radar-Lidar Geometrical Profile (RL-GeoProf) product, which combines CALIPSO and CloudSat data (Mace and Zhang 2014). For that comparison, each RL-GeoProf pixel is matched with the nearest AVHRR

pixel. Again, only single-phase OC pixels are used. At night over snow-free surfaces, the liquid CBH height is overestimated by 0.91 ± 0.88 km, but during the day is nearly

Table 13. Error budget for single-layer liquid cloud-top height from N18-CALIPSO differences from January, April, July, and October 2008. SF – snow/ice free, SI – Snow or ice covered surfaces.

Product	Constraint	Reference	Accuracy (km)	Precision (km)	Number of Pixels x 10^3
Liquid cloud top height	SF Night		0.35	0.84	222.9
	SF Day	CALIPSO	-0.26	0.78	236.2
	SI Total		0.58	1.26	51.8
Ice cloud top height	SF Night		-1.41	1.89	158.0
	SF Day	CALIPSO	-1.65	1.75	135.7
	SI Total		-2.03	2.90	136.7
Liquid cloud base height	SF Night		0.91	0.88	183.4
	SF Day	RL-GeoProf	-0.01	0.81	178.3
	SI Total		1.05	1.41	45.1
Ice cloud base height	SF Night		1.27	2.31	99.5
	SF Day	RL-GeoProf	-0.18	2.23	87.9
	SI Total		0.39	2.63	99.5

unbiased with a precision of 0.81 km. Liquid CBH over snow-covered areas is overestimated by 1.05 ± 1.41 km, on average. Ice CBH is 1.27 ± 2.31 km too high at night over snow-free scenes, but too low, in the mean, by 0.18 ± 2.23 km during the day. Over snow and ice surface, ice CBH is too high by 0.39 ± 2.63 km. Further discussion of the top and height errors is provided in Section 5.5.2.3.1.

Defining errors for the cloud optical parameters, COD and CER, is more difficult because of fewer reference source materials. Since these data are defined relative to CERES, the CERES-MODIS retrievals comprise one reference source. While future direct comparisons of instantaneous matched CERES-MODIS and AVHRR data will provide estimates of relative accuracy and precision, for this version, the accuracy is assessed using mean values and the precision is estimated from Table II of Minnis et al. (2011b). The results are given briefly in Table 14. For all nonpolar liquid water clouds, the mean SatCORPS-A1 COD is 12% less than that from CERES with an estimated precision of 35%, while mean ice COD is 11% greater on average than the CERES-MODIS value with an estimated precision of 50%. For CER, the accuracy is ~1 and 5 µm for liquid and ice clouds, respectively. The corresponding precision values are estimated as 2.3 and 6.5 µm. Because all pixels were used in this assessment of the accuracy, the biases probably reflect the effects of the phase differences noted above. Ice clouds interpreted as water clouds will yield larger values of CER and if optically thin ice clouds are the type most misclassified, the average ice COD will increase

and the liquid COD will decrease. These results are subject to change as additional validation studies are performed.

Table 14. Error budget for COD, LWP, and IWP for single-phase clouds from differences between N18 and reference datasets. SF – snow/ice free, SI – Snow or ice covered surfaces. NP – non-polar, P – polar.

Product	Constraint	Reference	Accuracy	Precision	Number of Samples x 10^{-3}
COD, liquid	NP Day	CERES MODIS	-1.2 (-12%)	35%	*
COD, ice	NP Day	CERES MODIS	1.5 (11%)	50%	*
COD, Ice, non-opaque	SF Day	CALIPSO	1.27	2.45	22.3
	SF Night		0.33	1.17	45.6
CER, liquid	NP Day	CERES-MODIS	-0.9 μm (7%)	2.3 μm	*
CER, ice	NP Day	CERES-MODIS	5.1 μm (19%)	6.5 μm	*
LWP	NP Day	CERES-MODIS	-7 gm^{-2} (8%)	5 gm^{-2}	*
	P Day		-14 gm^{-2} (7%)	5 gm^{-2}	*
LWP	SF Ocean Day	AMSR-E	2.5 gm^{-2}	49.5 gm^{-2}	110
IWP	NP Day	CERES-MODIS	77 gm^{-2}	100 gm^{-2}	*
IWP, non-opaque, Day	SF Ocean	CALIPSO	15.5 gm^{-2}	52.6 gm^{-2}	17.8
	SF Land		21.3 gm^{-2}	53.4 gm^{-2}	4.5
IWP, non-opaque night	SF Ocean	CALIPSO	0.9 gm^{-2}	21.7 gm^{-2}	28.5
	SF Land		0.6 gm^{-2}	17.6 gm^{-2}	17.2

* Based on zonal averages from January, April, July and October 2008.

Another means for assessing ice COD, at least for optically thin ice clouds, is to compare with CALIPSO data. Table 14 shows that for non-opaque ice clouds (those clouds that permit a surface reflection to be measured by CALIPSO), the COD is severely overestimated during the day but only slightly overestimated at night. This result is similar to other comparisons using CERES-MODIS and CALIPSO data (Minnis et al. 2014) and the MODIS Atmosphere Science Team (MAST) Collection 5 results and CALIPSO (Holz et al. 2015). The nocturnal retrievals are based on infrared channels, which are minimally sensitive to the scattering phase function. Conversely, the VIS-based retrieval is highly dependent on the ice crystal optical properties, which can yield a wide range of retrieved optical depths for a

Table 15. Error budget for radiation parameters.

Product	Constraint	Reference	Accuracy	Precision†	Number of Samples
Liquid Cloud Effective Temperature	NP Day	CERES-MODIS	1.9 K	1.3 K	*
	NP Night		-3.1 K	0.9 K	*
Ice Cloud Effective Temperature	NP Day	CERES-MODIS	5.6 K	4.0 K	*
	NP Night		8.9 K	5.3 K	*
Clear-sky surface skin temperature	Ocean	OISST	-0.07 K	0.66 K	$3{,}007 \times 10^3$
	Land	SURFRAD	0.48 K	2.29 K	1,152
	Land	ARM SGP	-1.23 K	2.19 K	264
TOA SW flux	Global	CERES	-0.5 Wm^{-2}	19.2 Wm^{-2}	$1{,}238 \times 10^3$
			-0.22%	7.92%	
TOA LW flux	Global	CERES	-1.9 Wm^{-2}	6.6 Wm^{-2}	$2{,}525 \times 10^3$
			0.81%	2.86%	

*Based on zonal averages from January, April, July and October 2008.

†Standard deviation of zonal differences for effective temperature.

given observed reflectance. The model ice crystal properties yield a nearly factor of two overestimate. This issue will be addressed in the next version of the SatCORPS-A TCDR.

The N18 LWP data were compared with 2008 CERES-MODIS zonal means for all nonpolar liquid clouds and with Aqua AMSR-E data for all overcast, ice-free ocean AMSR-E pixels. On average, as seen In Table 14, the AVHRR LWP computed with the homogeneous assumption is 2.5 gm^{-2} greater than its microwave counterpart with a standard deviation of 49 gm^{-2}. Use of the adiabatic assumption would yield a mean difference of -7 gm^{-2}. Compared to CERES, the mean AVHRR LWPs are 8% and 7% lower in nonpolar areas and polar areas, respectively. For nonpolar areas, the AVHRR IWP is 77 gm^{-2} greater than its CERES counterpart. These biases in LWP and IWP are likely the result of the phase selection differences mentioned above. For optically thin cirrus, the IWP is significantly overestimated during the day and in very good agreement at night. Again, the differences follow from the scattering phase function issues discussed previously.

The radiation parameter error budgets are summarized in Table 15. Because the cloud effective temperature is by definition the brightness temperature that satisfies the model calculations, it will be affected by the atmospheric corrections, IRW channel calibration, VZA, and, for optically thin clouds, the phase selected and the optical properties of the model clouds. Thus, it will, on average, vary with algorithm and, to some extent, with satellite. If all phase selections and pixel resolutions were the same for the CCPRS and SatCORPS-A retrievals, a close match of T_c would be expected for the datasets resulting

from analysis of the same time periods. In Table 15, some notable differences are evident. The mean value of T_c for AVHRR liquid clouds is ~2 K greater during the day and ~3 K less at night than its CERES counterparts. For T_c at night, the AVHRR means are 5.6 and 9 K greater than the CERES averages. These differences result from, at least, two factors. The lower resolution of the AVHRR data yields higher effective pressures (greater T_c) for both ice and water clouds. Additionally, the phase selection differences will cause significant differences between the CERES and AVHRR datasets. In other words, the averages come from two different populations. Thus, it is important in the future to assess the CERES-MODIS and SatCORPS-A consistency by performing direct comparisons of pixel-level retrievals.

Estimation of the clear-sky surface skin temperature errors (Table 15) is more straightforward and can be objectively assessed using surface observations and other validated measurement methods. The sea surface temperatures (SST) were compared to the NOAA "Optimum Interpolation" SST (OISST) Version-2 dataset (Reynolds et al. 2007) and the land surface temperatures (LST) were compared to surface based radiometer measurements at high-quality sites in the United States: the Atmospheric Radiation Measurement (ARM) Southern Great Plains (SGP) Climate Research Facility and seven NOAA ESRL Surface Radiation (SURFRAD) sites. The mean SatCORPS-A1 SSTs have an accuracy of -0.07 ± 0.66 K compared to OISST. Compared to all surface sites, the AVHRR LSTs are, on average, too large by ~0.3 K with a precision of ~2.3 K.

To estimate the SW and LW flux errors, the N18 AVHRR-based fluxes were compared with matched CERES Aqua scanner fluxes from JAJO 2007 and are listed in Table 15. The fluxes are very close, on average, with a SW bias of -0.2% and a precision of 8%. The OLR is underestimated by 0.8% with a precision of 2.9%. Additional comparisons with results from other NOAA satellites will help solidify these initial error estimates.

The error budget for overshooting top detection is based on comparisons with surface radar and CloudSat radar data. According to those comparisons, the false-alarm detection rate is between 6 and 17%, while the probability of detection is 55%. These error estimates and those for the other parameters are discussed in detail in Section 5.5.

5. Practical Considerations

5.1 Numerical Computation Considerations

Endian
The SatCORPS-A requires an IEEE little-endian environment.

Precision
The codes have only been tested in 64-bit mode.

Parallelization
While the SatCORPS-A could benefit from parallelization, no such capability is currently enabled.

Numerical Computation Considerations
There are no situations where a numerical computation can lead to inaccurate results, exceptions, or infinite loops.

5.2 Programming and Procedural Considerations

None

5.3 Quality Assessment and Diagnostics

The quality of output products can be assessed through algorithm validation. The validation plan and current validation results are discussed in Section 5.5.

One can diagnose anomalies by computing globally averaged values of retrieved parameters for each day of AVHRR data. Daily global mean retrievals should be relatively stable from day to day. Any sharp departure of a daily mean from the recent trend would indicate an anomaly that requires further investigation. Comparisons of time series with independent datasets such as those from the ISCCP and CERES can also reveal relative anomalies that require further investigation. Additionally, maps of monthly mean values and plots of zonal averages can also be used to assess the quality of the output at a larger time scale. These maps can be compared to running means for the particular month to determine if there are any significant departures.

5.4 Exception Handling

Several exceptions may occur in the processing stream. Those exceptions that are not discussed in other sections are listed below along with the procedures used to handle them.

- If a pixel or line is flagged as bad within the NOAA CLASS QC flags, the pixel values are set to missing and no mask or retrieval is performed.

- If a pixel or line is flagged as bad by the processing data filtering algorithms (see Section 3.2.3), no mask or retrieval is performed.

- If the MERRA profile has fewer than 5 valid levels, the predicted clear-sky temperatures for channels 3, 4, and 5 are set equal to zero, and no mask or retrieval is performed.

- If $T_3 < 150$ K or $T_3 > 360$ K, no mask or retrieval is performed.

- If fewer than 25% of the pixels in given daytime tile have valid VIS and IRW radiances or in a given nighttime tile have valid IRW radiances, no retrievals are performed for the tile.

- If the retrieved value of T_c or Z_c is less than or greater than, respectively, the values for the uppermost level in the temperature profile, the pixel is designated as a no retrieval.

- If the radiance for any channel is equal to or less than zero and it should have a positive value (e.g., VIS channel during daytime), the data are reclassified as bad data and no retrieval is performed.

5.5   Algorithm Validation

Quality assurance for AVHRR Cloud TCDR products is conducted through: 1) comparison of gridded monthly- and zonally-averaged TCDR products with existing and publically available global cloud property climatologies from the CERES Edition 4 (Ed 4) Clouds Subsystem, the NASA MODIS Atmosphere Science Team (MAST), the International Satellite Cloud Climatology Project (ISCCP, see Rossow and Schiffer 1999), the CM-SAF cLoud, Albedo and Radiation (CLARA-A1, see Karlsson et al. 2013) AVHRR, Pathfinder Atmospheres-Extended (PATMOS-X, see Heidinger et al., 2014), and CALIPSO and 2) comparison of pixel-level product output with cloud properties from space-based instrumentation such as the NASA A-Train and other ground-based sensors/datasets. N18 AVHRR data taken during 2008 will be the focus of the quality assurance since this satellite has an equatorial overpass time that is closest to that of the NASA A-Train, allowing for reasonably accurate temporal and spatial matching of pixel-level products with A-Train observations.

5.5.1   Comparisons With Other Global Cloud Property Climatologies

SatCORPS-A1 cloud products were compared with existing and publically available monthly mean global cloud properties for JAJO 2008 with an emphasis on October 2008. The CERES Ed 4 monthly-averaged data were acquired directly from the CERES Data Management Team. The MAST Collection 6 (Baum et al. 2012; Frey et al. 2008, 2012), hereafter MAST C6, monthly-averaged data were ordered from the GSFC Level 1 and Atmosphere Archive and Distribution System (http://ladsweb.nascom.nasa.gov). The specific MAST products used in the comparisons have the filename prefix MYD08_M3 for Aqua MODIS. The ISCCP D2 monthly-averaged data were ordered from the NASA LaRC Atmospheric Sciences Data Center (http://eosweb.larc.nasa.gov). CALIPSO monthly-averaged cloud fraction datasets were produced at NASA LaRC. CALIPSO cloud fraction is derived at a 5° spatial resolution and ISCCP products are interpolated to a 2.5° spatial resolution grid. The other datasets use a 1° grid. Zonal means are weighted by the cloud fraction in each grid box so regions with greater cloud cover have a greater impact on the zonal average.

Cloud fraction is the only product available as a monthly average from all of the above datasets. CALIPSO data are considered "truth" due to the highly detailed vertical and 0.33-km spatial sampling from its lidar that can resolve the gamut of clouds including those that are very optically thin. The passive sensor data typically have trouble detecting clouds with COD < 0.3 or so. Since CALIPSO only samples along a single 2-D 0.33 km FOV time/height profile and CALIPSO COD retrievals are limited to $\tau < 3$, only CALIPSO CF and CTH are compared with SatCORPS-A1 monthly means. Other parameters are compared at the pixel level.

Several other products are available from the non-CALIPSO datasets, including day+night CF, CTP, CTT, and water path, and daytime cloud optical depth. This section focuses on CF, CTP, and COD in addition to CER and other cloud phase-based comparisons only available for the SatCORPS-A1, CERES MODIS, CLARA-A1, and the MAST.

Regional and zonal mean total (i.e., both day and night) cloud fractions from SatCORPS-A1, CERES Ed 4, MAST, ISSCP, and CALIPSO from October 2008 are shown in Figure 29. Qualitative examination of the maps indicates a general agreement of the cloud amount distributions among the datasets in non-polar regions (60°S - 60°N). The results over polar regions differ substantially among the different products with the CERES and MAST being the closest to CALIPSO. MODIS has several spectral channels, such as the 6.7, 7.3, and 13.3 µm channels, that allow for improved cloud discrimination over nocturnal sea ice and snow covered scenes relative to the SatCORPS-A1 TCDR and 2-channel ISCCP. In non-polar regions, the climatologies differ most in the tropics where small cumulus and very optically thin cirrus are better detected by the MODIS-based products due to higher resolution pixels and the use of the 1.38-µm channel for thin cirrus detection during the day.

Total cloud fraction was weighted by cos(LAT) to account for zonal differences in grid-box areal coverage to derive a single number for global cloud coverage for each climatology for the seasonal months of 2008. Table 16 shows that the SatCORPS-A1 cloud fraction is 2.3-3.4% greater than the CERES Edition 4 averages. The SatCORPS-A1 cloud amounts are 0.6-2.3% lower than the CALIPSO means, primarily due to missed clouds over the northern polar region, the tropics, and deserts during certain months. In general, all averages from the passive sensors should be lower than CALIPSO because passive instruments with 1-5 km spatial resolution cannot observe all the cloud features that are resolved by an active lidar instrument. The SatCORPS-A1 results have the greatest cloud amounts, except for those from CALIPSO.
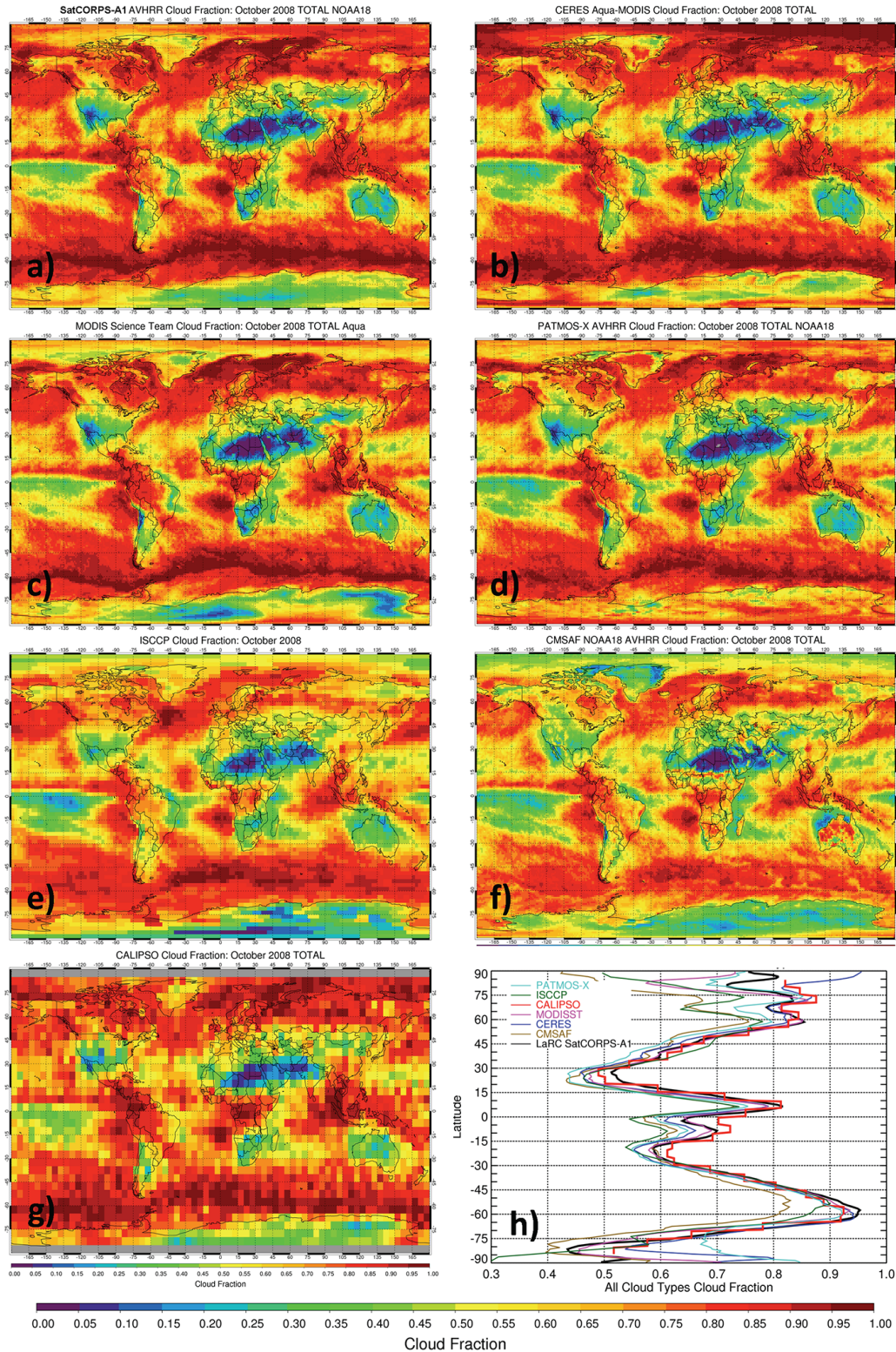
Figure 29: October 2008 day + night cloud fraction. Regional means from (a) N18 SatCORPS-A1, (b) CERES Aqua Ed 4, (c) Aqua MAST C6, (d) PATMOS-X N18, (e) ISSCP D2, (f) CLARA-A1 N18, and (g) CALIPSO. (h) Zonal means. Resolution is 1°, except for ISCCP (2.5°) and CALIPSO (5°).

Table 16. Monthly mean total cloud fraction from six climatologies.

Month 2008	SatCORPS-A1	CERES Edition 4	CALIPSO	MAST Aqua Collection 6	ISCCP-D	CLARA-A1
January	0.694	0.667	0.717	0.687	0.672	0.624
April	0.688	0.656	0.705	0.655	0.655	0.603
July	0.680	0.657	0.692	0.662	0.633	0.601
October	0.697	0.673	0.703	0.679	0.649	0.623

Table 17. Monthly mean daytime and nighttime global cloud fraction from CALIPSO and SatCORPS-A1.

Month 2008	Day		Night	
	SatCORPS-A1	CALIPSO	SatCORPS-A1	CALIPSO
January	0.677	0.692	0.714	0.748
April	0.668	0.683	0.665	0.674
July	0.665	0.674	0.689	0.707
October	0.671	0.679	0.721	0.729

Table 17 highlights the seasonal SatCORPS-A1 and CALIPSO CF averages for day and night. During both day and night, the SatCORPS cloud coverage is slightly less than CALIPSO's. Both show an increase from day to night.

October 2008 global maps and zonal averages of total CTP are shown in Figure 29. The results from the SatCORPS-A1 TCDR and CERES Edition 4 agree well, but there are distinct differences from the MAST pressures. In general, the SatCORPS-A1, CERES, PATMOS-X, ISCCP, CLARA-A1, and MAST zonal means show the same patterns, but the mean MAST CTP is up to 150 hPa greater than all other retrievals over some latitude bands. ISCCP yields the lowest mean pressures over the midlatitudes, while PATMOS-X yields the lowest pressures over both the polar regions. The SatCORPS-A1 N18 JAJO 2008 cloud effective temperature averages, which correspond to the effective cloud pressures, were also compared to those from CERES and are summarized in Table 15 and discussed in Section 4.2.3.

Water cloud fraction maps and zonal averages for water and ice cloud fractions are shown in Figure 30 for SatCORPS-A1 N18, CERES Aqua Ed4, MAST Aqua C6, and PATMOS-X N18. The MAST and PATMOS-X water cloud fractions are the lowest among the products. PATMOS-X provides 4 categories within their cloud mask: cloudy, probably cloudy, probably clear, and clear. Only the cloudy and probably cloudy pixels were used in the creation of Figure 30. The PATMOS-X water (ice) fraction is also less (greater) than that from SatCORPS-A1 and CERES Ed4, particularly in mid-latitudes. The SatCORPS-A1 and MAST ice fractions are similar equatorward of 45° latitude. Overall, SatCORPS-A1 has the smallest average ice cloud fraction. The reasons for the differences compared to CERES and other products are discussed in the next section.
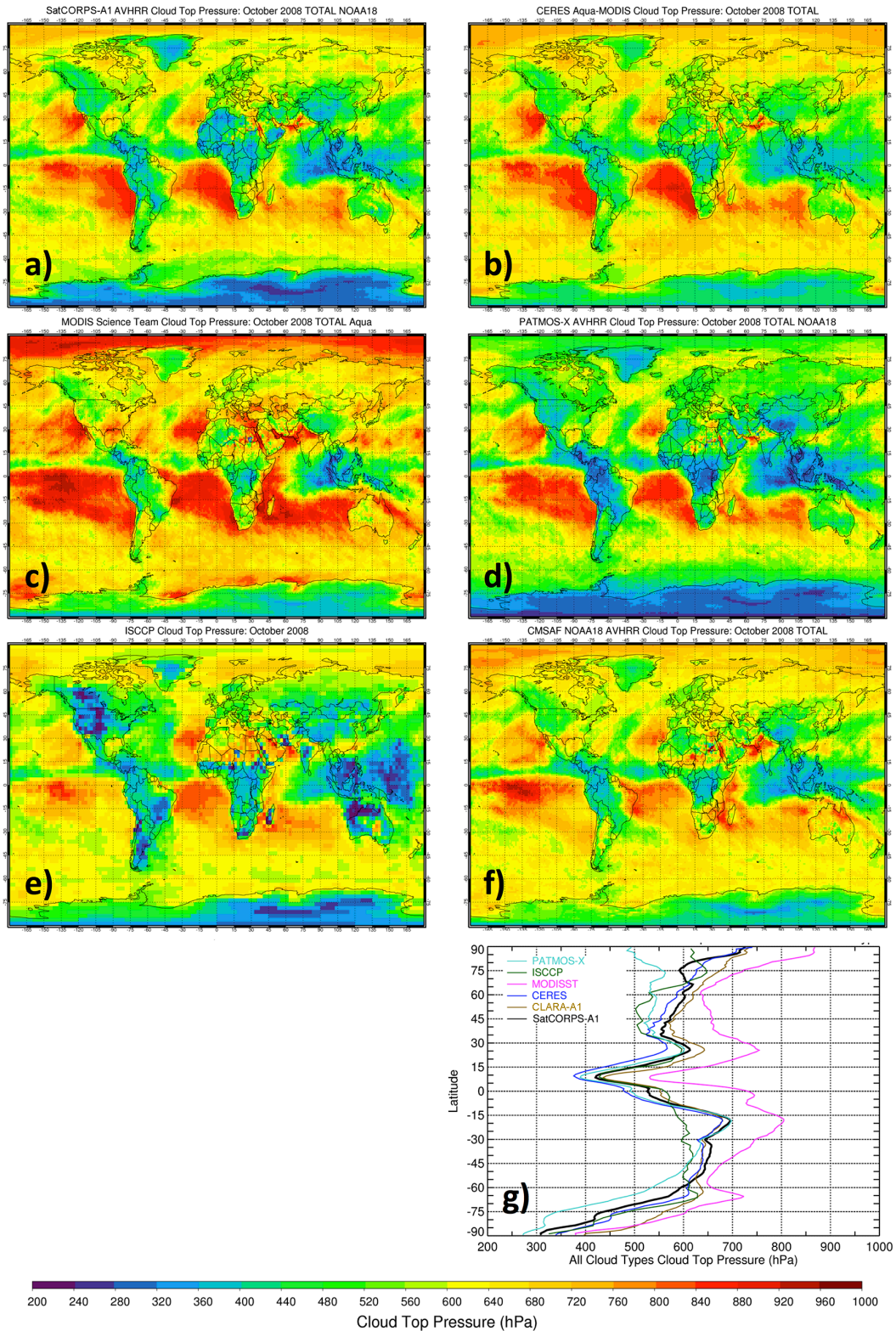
Figure 30: Same as Figure 29, except for mean cloud top pressure. (a) N18 SatCORPS-A1, (b) CERES Aqua Ed 4, (c) MAST Aqua C6, (d) PATMOS-X N18, (e)
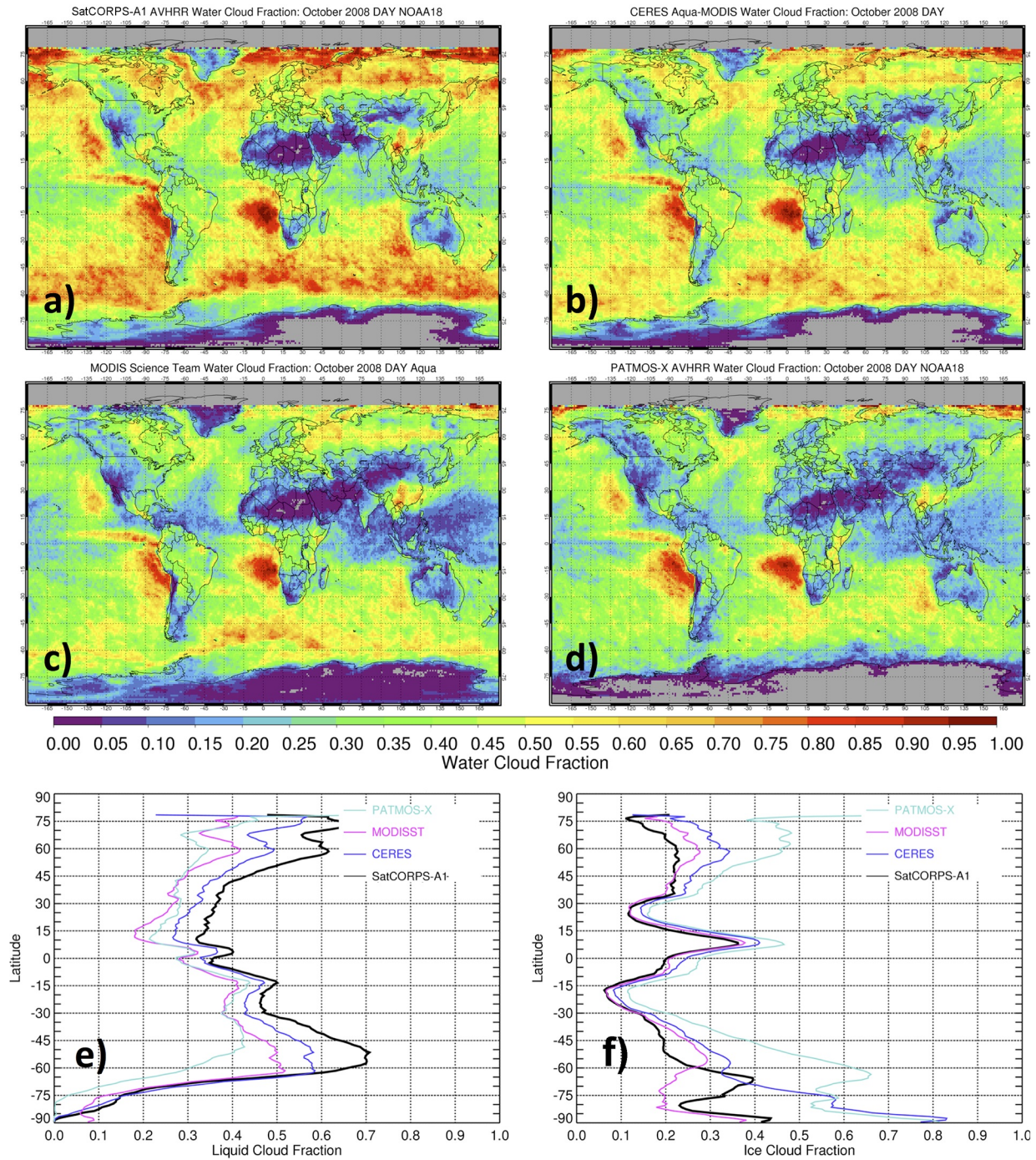
ISSCP D, (f) CLARA-A1 N18. (g) Zonal means.

Figure 31: Same as Figure 29, except daytime, 1° regional mean liquid (a-c) and ice (d-f) cloud fractions from (a) SatCORPS-A1 N18, (b) CERES Aqua MODIS Ed4, (c) MAST Collection 5, and (d) PATMOS-X N18. Zonal averages for (e) liquid and (f) ice cloud fraction.

Figure 32: October 2008 daytime zonal mean cloud optical depths from SatCORPS-A1 N18, CERES Aqua MODIS Ed 4, MAST C6, and PATMOS-X N18. (a) liquid and (b) ice clouds.

The zonal mean SatCORPS-A1 and CERES Ed 4 CODs (Figure 32) also agree well. On average for JAJO 2008, the CERES and SatCORPS water and ice COD means agree to within ± 8% over non-polar regions (Table 14), but the SatCORPS water (Figure 32a) and ice (Figure 32b) CODs are systematically smaller and larger than their CERES counterparts, respectively. The SatCORPS mean liquid CODs are very close to those of PATMOS-X for nonpolar areas and close to the CLARA-A1 values in the tropics. They are considerably smaller than the MAST values. Although the MAST Collection 6 averages include retrievals from their partly cloudy and undetermined (classified as liquid) categories, there likely remain a significant number of optically thin cloudy pixels that did not meet the retrieval criteria (Platnick et al. 2015). Thus, many small optical depth clouds are not included in the MAST averages resulting in a larger mean COD than other retrieval algorithms (Stubenrauch et al. 2013). The SatCORPS-A1 and CERES CODs differ over polar regions due to CERES's and MAST's use of the MODIS 1.24-µm for COD over ice and snow-covered surfaces, while SatCORPS-A1 uses the VIS channel and SIST. While the use of the VIS channel over ice and snow generally leads to overestimates of COD (PATMOS-X and CLARA-A1), the SIST algorithm, as described in Section 3.3.1.2.1, is applied in certain situations over polar regions. The SIST is designed for retrievals of optically thin clouds, particularly for ice clouds. If the SIST is used inappropriately for optically thick clouds or for thin ice over thick water clouds, it will severely underestimate COD. This can explain why the SatCORPS-A1 ice COD is considerably less than the other values over Antarctica. The MAST ice COD means are lower than others probably due to their use of a new ice crystal reflectance model that yields significantly smaller CODs (Platnick et al. 2015).

October 2008 cloud effective radius zonal means are compared in Figure 33 for 4 of the methods. For tropical areas, all methods produce nearly identical water CER results (Figure 33a), while in the southern midlatitudes, SatCORPS and PATMOS-X water CER means are close, while the CERES and MAST are lower. The MAST means shown here are from their 3.7-µm retrievals, which are typically 2-3 µm less than the MAST reference values of CER

that are based on the 2.13-μm channel (e.g., Minnis et al. 2011). The SatCORPS-A1 zonal ice CER means mimic the CERES averages (Figure 33b), but are larger by ~5 μm. The PATMOS-X, CERES, and MAST averages are comparable in the tropics, but diverge poleward of 30° latitude. The larger AVHRR values may be due to the misclassification of thin cirrus clouds discussed in Section 5.5.2.2. Additional study is needed to fully explain the bias.
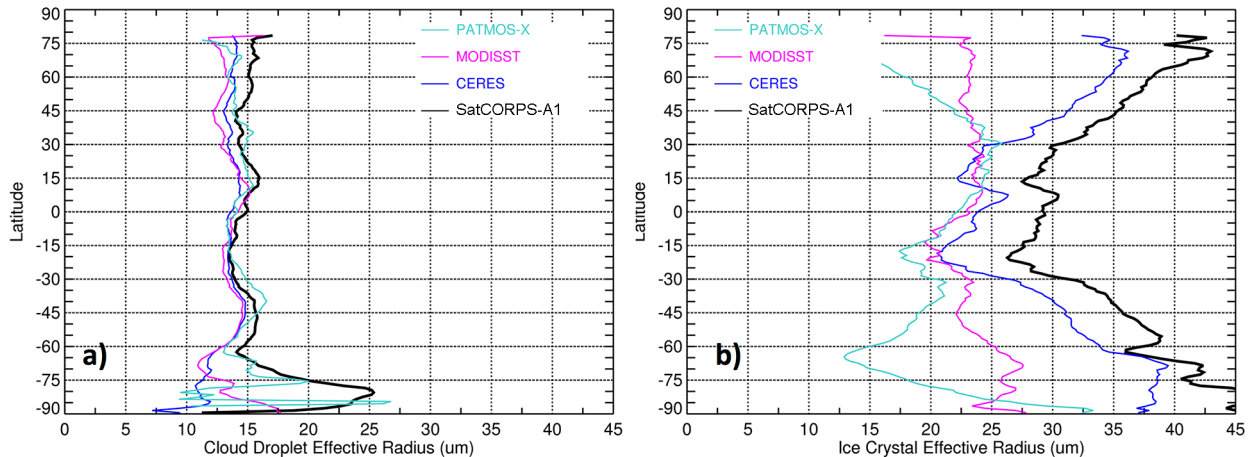

Figure 33: October 2008 zonal mean cloud particle effective radius from SatCORPS-A1 N18, CERES Aqua MODIS Ed 4, PATMOS-X N18, and MAST C6 3.7-μm retrieval. (a) water droplets and (b) ice crystals.

Despite the fact that SatCORPS-A1 is based on the CERES Edition 4 CCPRS algorithms, some biases in the AVHRR TCDR results are evident. One reason for the discrepancy is the difference in pixel spatial resolution. The GAC averaging smoothes out high-resolution (1 km) gradients and variability that might be present in the imagery, thereby adversely impacting cloud detection and retrievals. The CCPRS subsets every other MODIS scan line and every fourth pixel, so the FOV size for each pixel is still effectively 1 km and no smoothing occurs.

To investigate this effect, the impact of spatial resolution variations on retrieved cloud properties was analyzed over the Central U.S. for October 2008. MODIS data were processed at 1, 2, and 4-km spatial resolutions using algorithms that nearly match those used by CERES. Resolution degradation to 2 km was achieved by averaging the radiances from 4 pixels and to 4 km by averaging radiances for 16 pixels. A domain-averaged value was derived from the retrieved properties for each resolution.

The results of this analysis are shown in Table 18. Regardless of cloud phase, negligible change occurs in average cloud fraction with decreasing spatial resolution. However, CTP increases by 8-14 hPa when the data are degraded to 4 km. COD decreases by 11% for water clouds, but is virtually unaffected for ice clouds. Small cumulus clouds typically exhibit a relatively high COD for only a few pixels. If averaged with nearby clear pixels, the resulting VIS reflectances will yield reduced CODs. Ice clouds on the other hand are generally more spatially uniform than cumulus, so smoothing will have less effect on the optical depth retrieval (Wielicki and Parker 1988). This effect is partially evident in the

zonal averages shown in Figure 32, where the SatCORPS-A1 water COD is less than its CERES counterpart. The ice CODs, however, are somewhat larger than CERES.

Another effect that would result in AVHRR having a greater ice COD average and a smaller mean liquid COD compared to CERES would be that of phase selection. A greater proportion of the SatCORPS clouds are classified as liquid relative to CERES (Figure 31), so that some ice clouds are interpreted as liquid clouds. If the misclassifications are preponderantly optically thin ice clouds, then they would tend to reduce the mean liquid COD and their absence would raise the mean ice COD relative to CERES. Both the resolution and phase selection effects likely contribute to the differences between SatCORPS-A1 and CERES-MODIS.

In summary, the results shown here indicate that the SatCORPS-A1 AVHRR TCDR is well within the bounds of other available global cloud property climatologies in non-polar regions, save for the water cloud fraction. The TCDR results agree well with CERES Edition 4 for most of the parameters shown here. Thus it is concluded that the SatCORPS-A1 TCDR will be mostly consistent with the CERES cloud data, effectively extending the CERES cloud record back to 1979. Future versions will likely resolve some of the phase selection differences.

Table 18. Analysis of imager spatial resolution impact on domain-averaged cloud fraction, cloud top pressure, and optical depth using 30 days of MODIS data over the central U.S.A. during April 2008.

Phase	WATER			ICE		
Resolution	1 km	2 km	4 km	1 km	2 km	4 km
CLOUD FRACTION						
Day	0.29	0.30	0.30	0.17	0.17	0.18
Night	0.17	0.17	0.17	0.32	0.32	0.32
Total	0.23	0.24	0.24	0.24	0.24	0.25
CLOUD TOP PRESSURE (hPa)						
Day	693.2	699.4	707.2	400.4	404.4	410.4
Night	763.3	763.7	765.3	317.7	319.2	322.5
Total	720.4	723.8	729.0	345.9	348.8	353.8
OPTICAL DEPTH						
Day	20.2	18.9	17.6	23.8	23.5	23.5
Night	11.6	11.3	10.8	5.8	5.7	5.6
Total	17.1	16.2	15.3	12.1	12.1	12.1

5.5.2   Pixel-Level TCDR Validation

Quantitative comparisons of pixel-level AVHRR TCDR products with space- and selected ground-based datasets are currently based on NOAA-18 data during JAJO 2007 and 2008.

Cloud detection and property retrieval validation includes data from 2008, whereas land and sea surface skin temperature validation includes all of 2008. Some specific quality assurance datasets that have been or may be used in the future for quantitative pixel-level validation are listed below. Microwave radiometers (MWR) on various satellites have been used for estimating LWP and ocean temperature and can serve as independent validation sources. Retrieval products are available from the Defense Meteorological Satellite Program (DMSP; Wentz 1997), Aqua Advanced Microwave Sounding Radiometer-EOS AMSR-E (Wentz and Meissner 2000), the Thermal Microwave Imager (TMI, Kummerow et al. 1998), and some surface sites. Here, the Aqua AMSR-E data from JAJO 2008 are used to assess the results. Additionally, combined CloudSat and CALIPSO data in the form of the RL-GeoProf product are used to evaluate cloud-base height.

5.5.2.1   Pixel-Level Validation Procedures

For AVHRR-CALIPSO comparisons, the spatial and temporal matching process for AVHRR begins with examination of the temporal bounds of a SatCORPS-A1 Cloud TCDR NetCDF output file (described in Section 3.3.7). Once the bounds are determined, the segment of the CALIPSO track corresponding to the same time span is identified. Given the 4-km GAC pixel resolution, spatial matching of AVHRR pixels with CALIPSO footprints is done at the 5-km resolution of the CALIPSO Cloud Layers Product that is used to validate several of the AVHRR products. The 5-km resolution CALIPSO product is actually derived using data from the nominal 0.33-km CALIPSO data, and this higher resolution is incorporated in the AVHRR cloud mask, phase, and top height validation as described below. Any AVHRR pixels located within a 2.5-km radius from the center of the 5-km CALIPSO footprint are considered matches with CALIPSO, which typically yields one to two AVHRR pixels. When multiple matching AVHRR pixels are found, the mean of each AVHRR cloud property is computed giving equal weight to each pixel. The maximum time difference between the AVHRR scan line and the CALIPSO footprint timestamps is 15 min in these comparisons.

The spatial matching logic for AVHRR, AMSR-E, and CloudSat is slightly different than CALIPSO matching due to differences in spatial resolution. Any AVHRR pixels within a 6-km radius of the AMSR-E footprint are considered matches with AMSR-E, which has a resolution of ~25 km. The mean AVHRR LWP is computed if multiple cloudy AVHRR pixels are found. AMSR-E and CALIPSO data are matched by associating each 5-km segment of CALIPSO data with the nearest AMSR-E footprint. The process is similar for matching GeoProf cloud base height retrievals except a distance threshold of 2.5 km is used since the CloudSat footprint is smaller than AMSR-E.

The SatCORPS-A1 cloud mask is verified using the CALIPSO vertical feature mask (VFM), which has horizontal resolution ranging from 0.33-km to 80 km, which is aggregated to a 5-km pixel to determine a clear or cloudy outcome at the AVHRR resolution. For AVHRR, a cloudy outcome is determined if CF ≥ 0.50. In practice, CF is often equal to 0.0 or 1.0 because often only one AVHRR pixel is matched to a given CALIPSO 5-km segment. For CALIPSO, a cloudy outcome is determined if the 5-km product reports one or more cloud layers or if the CF computed from the 0.33-km product exceeds 0.50 within the 5-km segment of the flight track matched to the AVHRR pixel. CALIPSO and AVHRR data that

match to within ±15 minutes are used. CALIPSO views the Earth at a VZA of 3°, while the matched AVHRR data have a VZA between 0 and 40° for the 15-min matching constraint. The AVHRR data are parallax corrected to the nadir view. In addition, all CALIPSO cloud detections must be assigned a Quality Assurance (QA) Flag value of 3, indicating the highest confidence that the signal comes from a cloud and not clear air, aerosols, the surface, etc. All scenes containing any amount of cloud detected by CALIPSO at the 80-km scale are excluded from the analysis even if the QA Flag is set to 3. It is assumed that AVHRR is unable to detect these very weakly scattering/absorbing clouds.

AVHRR cloud thermodynamic phase is also validated using the CALIPSO VFM product. The validation is carried out only for single-phase cloud scenes as determined by the 0.33-km CALIPSO observation. Furthermore, the scene must be overcast (i.e., CF = 1.0). The overcast and single-phase conditions must be true for AVHRR if two matching pixels are found. All other AVHRR-CALIPSO cloud macro and micro-physical property validations, cloud altitude, COD, LWP, and IWP, are carried out for overcast, single-phase scenes in order to minimize differences due to inhomogeneous FOVs and different spatial sampling.

The CALIPSO 0.33 and 5-km Cloud Layers products are used to validate AVHRR CTH retrievals and the CloudSat 2B-GEOPROF-LIDAR (RL-GeoProf) product was used to validate CBH retrievals. Any scenes in which the CloudSat data indicated the presence of multi-layer clouds were excluded from the CBH validation. No CloudSat data are used to validate CTH.

COD is validated using the column optical depths reported in the CALIPSO 5-km Cloud Layers product only. COD values are not reported in the 0.33-km product. Due to attenuation of the lidar beam in the presence of thick, strongly scattering clouds, COD can only be validated for optically thin clouds using CALIPSO. Other approaches can be used for optically thick clouds, but are not yet available for this dataset. These include comparisons with surface observations at ARM sites (e.g., Min et al. 2004) or with CloudSat retrievals (e.g., Smith 2014). Here it is assumed that comparisons with LWP or IWP for thick clouds are a proxy validation of COD since the water path is based on the product of COD and CER. The distinction between optically thin and thick clouds is determined by two criteria. The CALIPSO beam attenuation flag is checked to see if the lidar beam was completely attenuated by the cloud features in the atmospheric column. If the flag indicates that all cloud layers were transparent, then the corresponding column COD is used for validation. The CALIPSO 5-km Cloud Layers product is used for IWP validation and is also limited to optically thin ice clouds.

The AMSR-E LWP retrievals (Wentz and Meissner, 2000) are used to validate LWP from coincident AVHRR data. Because the AMSR-E retrievals utilize measurements in the microwave spectrum to retrieve LWP, the validation includes both optically thin and thick liquid water clouds only over ocean surfaces. Rainfall can contaminate the microwave retrievals, so FOVs in which the AMSR-E quality assurance data indicate rainfall of any intensity are excluded from the LWP validation.

Table 19 lists the various potential validation datasets and their limitations. They are listed according to the retrieved parameter.

Table 19. AVHRR cloud and clear sky parameters available within the SatCORPS Cloud TCDR that can be validated using datasets listed in the center column. Caveats and limitations are also provided.

Cloud Property Climate Data Record Parameter	Quality Assurance Dataset	Caveats and Dataset Limitations
Global Space-Based Quality Assurance Datasets		
Cloud Detection	CALIPSO Vertical Feature Mask Product	Available only after June 2006
Cloud Top Height/Pressure	CALIPSO Cloud Layers Product, CloudSat GEOPROF-LIDAR Product	Only for single layer cloud scenes determined by CALIPSO/CloudSat[1]
Cloud Base Height/Pressure	CloudSat GEOPROF-LIDAR Product	Only for single layer cloud scenes[1]
Cloud Phase	CALIPSO Vertical Feature Mask Product	Only for single cloud layer and single phase scenes[1]
Cloud Optical Depth	CALIPSO Cloud Layers Product	Only for single layer cloud scenes and optically thin clouds with CALIPSO-derived optical depth less than 3[1]
Liquid Water Path	AMSR-E Level 2 Ocean Product DMSP LWP Product TMI LWP Product	Only for single layer cloud scenes. retrievals available only over water bodies and for non-precipitating clouds[2]
Ice Water Path	CALIPSO Cloud Layers Product CloudSat IWC/IWP Product	Only for single layer cloud scenes and for optically thin clouds with CALIPSO-derived optical depth less than 3[1]; CloudSat IWP best for thick clouds
Ground-Based Quality Assurance Datasets		
Cloud Detection and Height/Base	DOE ARM Program Active Remotely-Sensed Clouds Locations (ARSCL) Product Suite	Only available at a few locations from November 1996-March 2011
Liquid Water Path	DOE ARM Program Microwave Radiometer	Only available at a few locations from 1995-Present
Sea Surface Temperature	NOAA OISST Product AMSR-E, DMSP SST Product	Only for AVHRR clear sky scenes. [3]
Land Surface Temperature	DOE ARM Program IR Thermometer SURFRAD PIR	Only for AVHRR clear sky scenes[4]

[1] Available from June 2006-Present

[2] Available from July 1987-Present

[3] Available from January 1981-Present

[4] Only available at a few locations from 1995-Present

Table 20. Comparison of SatCORPS-A1 NOAA-18 cloud mask using the CALIPSO Vertical Feature Mask Product, January, April, July, and October 2008. Numbers in parentheses are 100% clear or cloudy aggregate CALIPSO pixes. SF – snow/ice free, SI – snow/ice covered.

Surface Type, Region, Time of Day	Fraction Correct		Bias (AVHRR-CERES)		Number of Matches x 10⁻³	
DAYTIME (0° ≤ SZA < 82°)						
Land, 60 S – 60 N, SF	0.848	(0.865)	-0.076	(-0.082)	286	(265)
Land, Polar, SF	0.878	(0.897)	-0.039	(-0.042)	31	(29)
Ocean, 60 S – 60 N, SF	0.875	(0.913)	0.009	(-0.011)	844	(740)
Ocean, Polar, SF	0.943	(0.953)	0.021	(0.017)	70	(67)
Land & Ocean, Global, SF	0.873	(0.903)	-0.011	(-0.027)	1230	(1102)
Land & Ocean, Global, SI	0.825	(0.827)	-0.093	(-0.094)	404	(400)
NIGHT (SZA ≥ 82°)						
Land, 60 S – 60 N, SF	0.870	(0.876)	-0.086	(-0.082)	288	(280)
Land, Polar, SF	0.875	(0.880)	-0.045	(-0.042)	24	(23)
Ocean, 60 S – 60 N, SF	0.888	(0.927)	-0.004	(-0.013)	880	(763)
Ocean, Polar, SF	0.951	(0.961)	0.015	(0.005)	101	(98)
Land & Ocean, Global, SF	0.888	(0.917)	-0.021	(-0.028)	1292	(1165)
Land & Ocean, Global, SI	0.715	(0.717)	-0.059	(-0.057)	728	(721)

5.5.2.2   Cloud Detection and Phase

Table 20 lists the fraction of JAJO 2008 SatCORPS-A1 N18 AVHRR pixels that were correctly identified as clear or cloudy according to CALIPSO 5-km vertical feature mask along with the bias and number of samples. The values in parentheses are the results using only 100% clear or cloudy CALIPSO composite pixels. Using all pixels, overcast, clear, and partly cloudy yields agreement during daytime ranging from ~0.83 over snow-covered scenes up to 0.95 over ice-free polar ocean areas. Cloud amount is underestimated 0.08 to 0.09 over snow-free land and snow/ice covered areas and differs by only a small amount over ice-free ocean areas during the day. Similar agreement is seen at night, except that the agreement drops to ~0.72 over snow-covered areas, where, despite the lower agreement, the bias is smaller than that during the day. If only clear and overcast CALIPSO pixels are used, the level of fraction correct increases by 0.03 over snow/ice free areas, but only by a small amount over cryospheric surfaces. Little difference is seen in the biases, however. Thus, the smaller fraction correct based on all pixels is likely due to matching uncertainties and the noise in calling a partly cloudy pixel cloudy or clear. Thus, the overcast- and clear- only analysis probably yields a more accurate assessment of the fraction correct. The fractions correct from the snow-free 100% clear/cloudy pixels are much the same as that found by the MAST team for nonpolar regions (Ackerman et al. 2014) and for CERES Ed4 snow/ice free regions (Minnis et al. 2015).

Table 21: Monthly mean fraction of SatCORPS-A1 correct clear or cloudy pixel matches relative to the CALIPSO Cloud Layers Product, 2008. Values in parentheses estimated for snow/ice-free areas using only 100% clear or cloudy pixels.

Month	DAYTIME (0° ≤ SZA < 82°)		NIGHT (SZA ≥ 82°)	
	Fraction Correct	**Number of Matches X 10^{-3}**	**Fraction Correct**	**Number of Matches X 10^{-3}**
January 2008	0.864 (0.907)	396	0.820 (0.911)	485
April 2008	0.847 (0.889)	404	0.807 (0.897)	500
July 2008	0.860 (0.903)	412	0.834 (0.927)	504
October 2008	0.872 (0.915)	423	0.841 (0.935)	531

 The global averages based on all pixels for each month are listed in Table 21 for day and night separately. The agreement is best during October and worst during April. The overall means appear smaller than expected from Table 20. The global average is heavily influenced by the measurements over the poles where the number of samples (Table 20) greatly outweighs the ~13% contribution of the poles to the global average cloud cover. Adjusting the values based on all samples by the ratio of the snow-free global JAJO mean in Table 20 to the column average in Table 21 provides a better estimate of fraction correct for snow-free areas. Adjusting further by multiplying the ratio of the 100% clear and cloudy fraction correct to the all-pixel average in Table 20 yields the best estimate for fraction correct over the seasonal cycle. The results of those adjustments, shown in parentheses in Table 21, provide a best estimate of the seasonal in fraction correct for snow-free areas.

Cloud phase validation is summarized in Table 22, which lists the fraction correct according to CALIPSO, the false alarm rates for water and ice cloud selection, and the number of samples. For AVHRR cloudy pixels classified as overcast and single phase by CALIPSO, the SatCORPS-A1 selects the correct phase ~92% and 78% of the time over snow-free and snow/ice-covered surfaces, respectively, during the day. Similar results are found at night, except that the fraction correct increases to 88% over snow/ice surfaces. Phase selection appears to be more robust over water than over land, particularly during the day. The false alarm rates for ice clouds are relatively low, while the false water cloud rates are high, between 10 and 25% during the day and 4 and 26% at night. These false alarm rates translate to the biases in phase selections reported in Table 12 and help explain why the water cloud selection by SatCORPS-A1 is higher than the other climatologies (Figure 31). A similar analysis of the CERES Ed4 results found that the CERES water cloud bias is less than 0.02 compared to the 0.07 bias in Table 12. The reasons for this difference are under investigation. Future versions will minimize the bias.

The SatCORPS-A classifies a given pixel as being liquid or ice water only. However, about half of the cloudy pixels are identified by CALIPSO as being a mixed-phase cloud or multilayered cloud system having ice and water clouds at different levels. To be classified as the latter, the higher clouds of the system must have τ < 2 for the lidar to detect the lower cloud. Thus, if the upper-level cloud were thicker than that limit, the cloud would

Table 22: Comparison of TCDR NOAA-18 pixel cloud phase using the CALIPSO Vertical Feature Mask, October 2008. SF – snow/ice free, SI – snow/ice covered.

Month and Time of Comparison	Fraction Correct	False Alarm Rate AVHRR Ice Phase	False Alarm Rate AVHRR Water Phase	Number of Matches x 10^{-3}
DAYTIME (0° ≤ SZA < 82°)				
Land, 60 S – 60 N, SF	0.893	0.012	0.221	56
Land, Polar, SF	0.874	0.027	0.179	6
Ocean, 60 S – 60 N, SF	0.923	0.016	0.105	321
Ocean, Polar, SF	0.907	0.050	0.101	28
Land & Ocean, Global, SF	0.918	0.016	0.117	406
Land & Ocean, Global, SI	0.782	0.170	0.251	73
NIGHT (SZA ≥ 82°)				
Land, 60 S – 60 N, SF	0.904	0.024	0.258	64
Land, Polar, SF	0.861	0.091	0.212	5
Ocean, 60 S – 60 N, SF	0.925	0.070	0.079	319
Ocean, Polar, SF	0.860	0.250	0.036	28
Land & Ocean, Global, SF	0.916	0.072	0.091	416
Land & Ocean, Global, SI	0.882	0.124	0.130	150
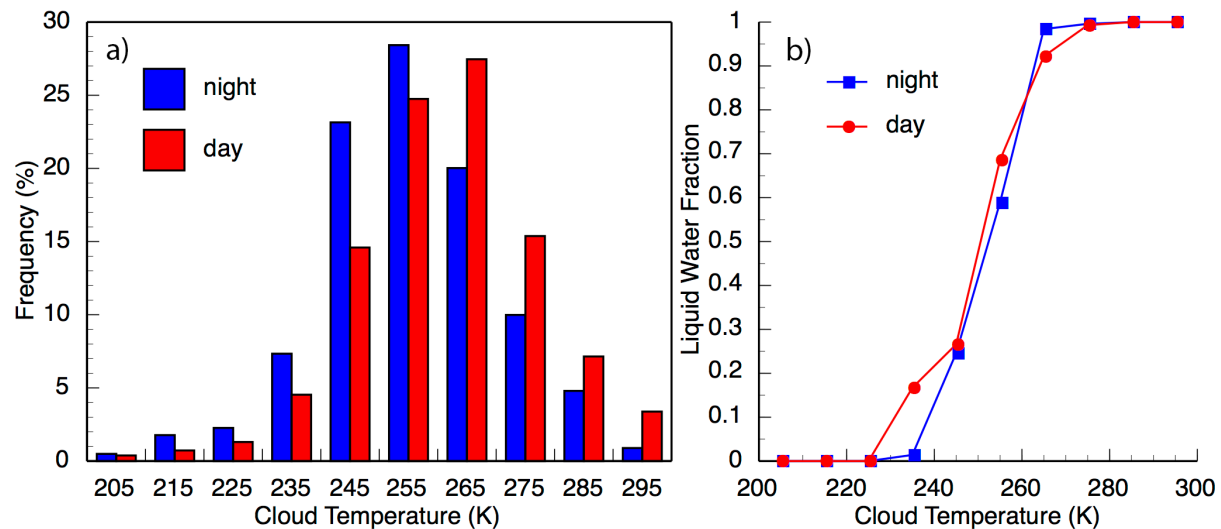
Figure 34. Classification of CALIPSO-determined mixed-phase cloudy pixels by SatCORPS-A1 during October 2008 using N18 data. (a) frequency of mixed-phase pixels as a function of T_c from SatCORPS-A1. (b) Percentage of mixed-phase pixels classified as liquid water by SatCORPS-A1 as a function T_c.

appear to be a single-layer single-phase cloud. So, the analysis in Table 21 is valid only for the single-phase aggregate CALIPSO pixels. To determine how the SatCORPS-A1 phase selection handles mixed phase cases, the phase distributions of the matched pixels for those cases are plotted in Figure 34 as a function of T_c. It is clear from Figure 34a that most of the mixed phase clouds yield cloud effective temperatures within the supercooled temperature range, 233 – 273 K. The mixed-phase clouds tend to be slightly warmer during the day than at night. The fraction of mixed-phase clouds classified as liquid water (Figure 34b) is greater at the low end of the temperature range during daytime than at night. This results in more mixed-phase clouds being classified as water during the daytime, as seen at the bottom of Table 12. Until a reliable method for classifying a pixel as being mixed-phase or multi-layered, all such pixels are treated as either ice or water only.
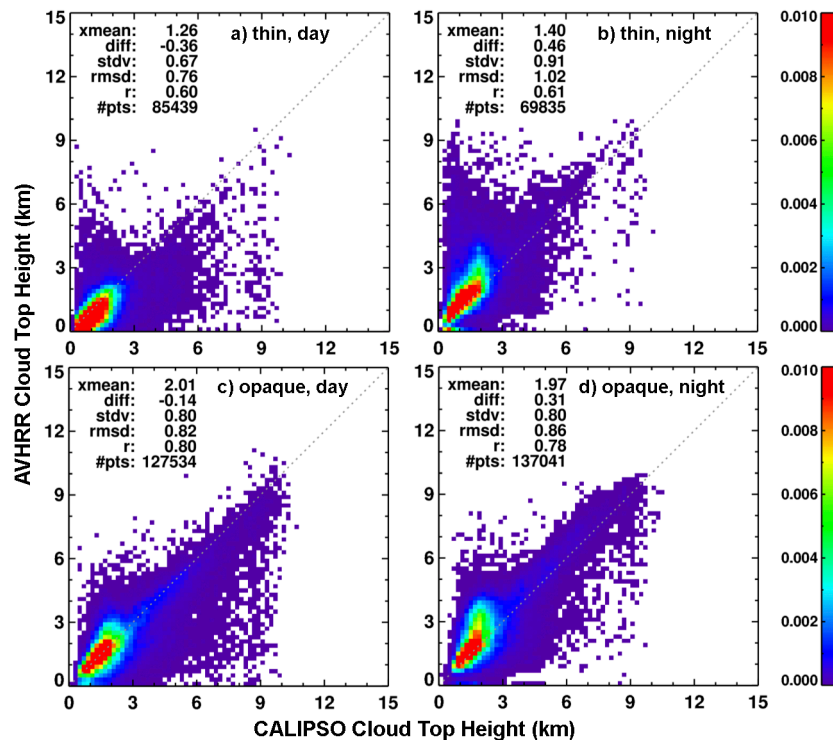
Figure 35: JAJO 2008 matched SatCORPS-A1 N18 and CALIPSO single-phase liquid water cloud top heights.

5.5.2.3   Cloud Properties

Cloud top and base heights and thin cloud optical depth and IWP are evaluated using CALIPSO data, while marine LWP is examined using AMSR-E data. The results are summarized in Tables 13 and 14.

5.5.2.3.1   Cloud Top Height

Figure 35 presents scatterplots and statistics of matched JAJO 2008 single-phase CALIPSO and N18 AVHRR liquid water CTHs for global ice-free water surfaces. The main body of
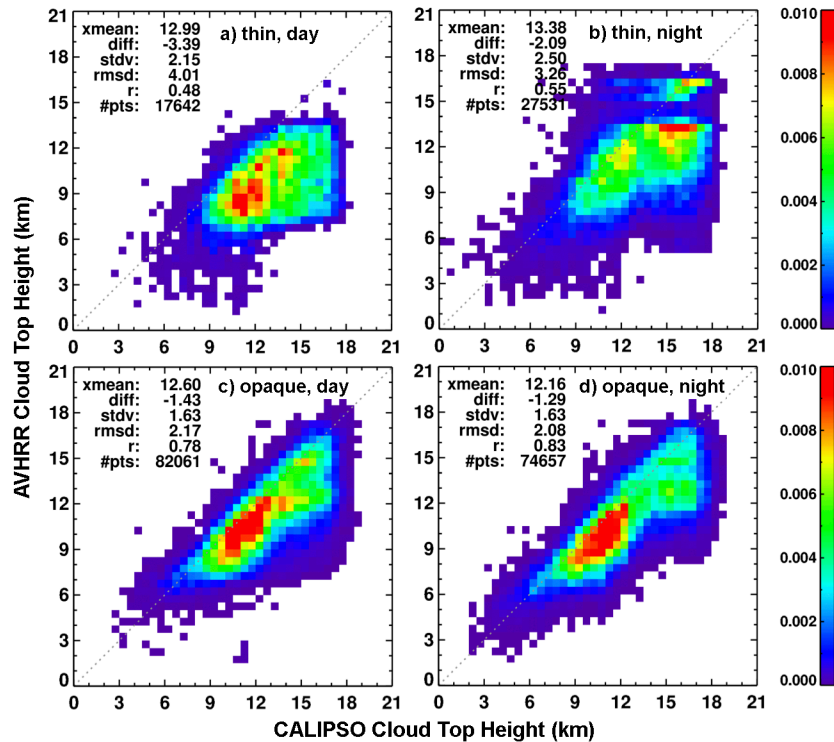
Figure 36. Same as Figure 35, except for ice clouds over nonpolar water surfaces.

points is scattered about the 1:1 line, but some tendency of SatCORPS-A1 to overestimate CTH at an altitude around 2 km is evident in three of the plots. This altitude is close to the pressure cutoff (Table 6) for application of the boundary layer lapse rates used to determine cloud CTH, suggesting that the cutoff is too high for many low clouds. At night, the heights tend to be overestimated (Figures 35b, d), while during the day, they are underestimated, in the mean, by 0.36 and 0.14 km for thin (Figure 35a) and opaque (Figure 35c) liquid clouds. The SDDs range from 0.7 to 0.9 km.

The ice CTH values from JAJO 2008 single-phase CALIPSO and N18 AVHRR for nonpolar ice-free water surfaces are plotted in Figure 36. In all cases, the CTHs are underestimated with largest bias for thin cirrus during the daytime (Figure 36a) and the best for opaque clouds at night (Figure 36d). The SDDs are largest for thin cirrus at night (Figure 36b) and least for the opaque clouds during the day (Figure 36c) and night. The agreement found here is not as good as that found for matched CERES Ed4 Aqua and CALIPSO data (Minnis et al. 2014), which produced much smaller biases.

All results for snow-free and snow-covered surfaces are summarized in Table 23, which reveals that the findings in Figures 35 and 36 are fairly typical for snow-free surfaces. During the day, the biases and SDDs for liquid clouds are larger than those for snow-free conditions, but are smaller for ice clouds. At night, the biases for water clouds drop, while those for ice cloud increase. This is not surprising given the somewhat isothermal

atmosphere during polar night. The results for all cases are further summarized further in Table 13.

Table 23: Comparison of TCDR NOAA-18 pixel cloud top height (km) using the CALIPSO Cloud Layers Product, October 2008. SF – snow/ice free, SI – snow/ice covered.

| Month and Time of Comparison	Optically Thick Cloud Bias	Optically Thick Cloud SSD	Number of Optically Thick Cloud Matches	Optically Thin Cloud Bias	Optically Thin Cloud SSD	Number of Optically Thin Cloud Matches
DAYTIME (0° ≤ SZA < 82°)			X 10^{-2}			X 10^{-2}
Water Cloud, SF	-0.16	0.82	1404	-0.41	0.72	958
Water Cloud, SI	0.82	1.49	224	0.48	1.28	81
Ice Cloud, SF	-1.35	1.64	1132	-3.15	2.15	225
Ice Cloud, SI	-0.67	1.27	168	-1.87	2.26	98
NIGHT (SZA ≥ 82°)						
Water Cloud, SF	0.31	0.80	1480	0.44	0.92	749
Water Cloud, SI	0.42	1.02	160	0.18	0.75	53
Ice Cloud, SF	-1.34	1.64	1119	-1.92	2.41	461
Ice Cloud, SI	-1.87	2.27	503	-2.58	3.99	597
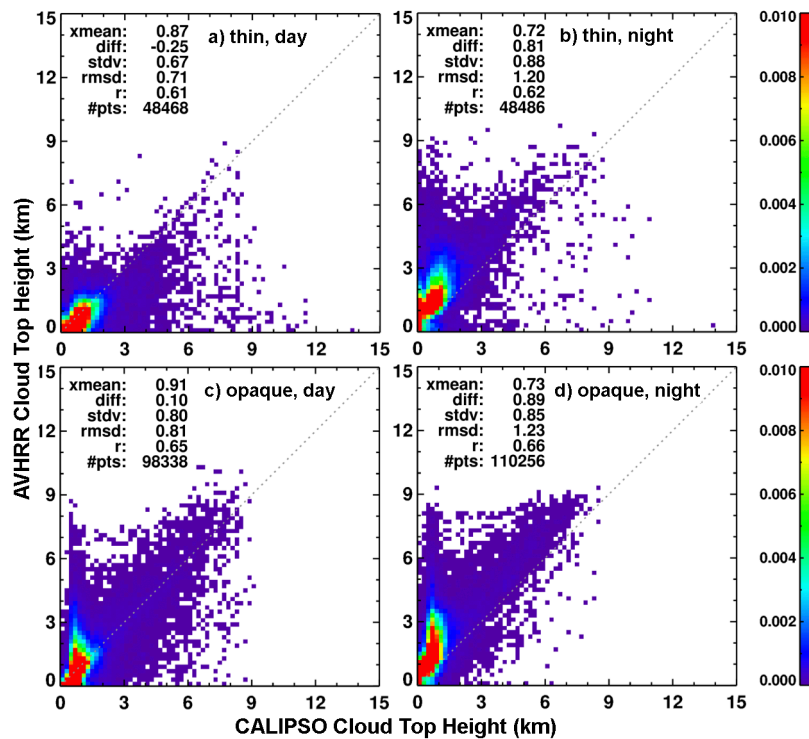
Figure 37. JAJO 2008 matched SatCORPS-A1 N18 and CALIPSO single-phase liquid water cloud base heights over nonpolar water surfaces.

A controlled copy of this document is maintained in the CDR Program Library.
Approved for public release. Distribution is unlimited.

5.5.2.3.2   Cloud Base Height

Similar comparisons were performed for the matched GEOPROF and N18 pixels to assess CBH. Figure 37 shows the comparison of liquid water CBH over all ice-free
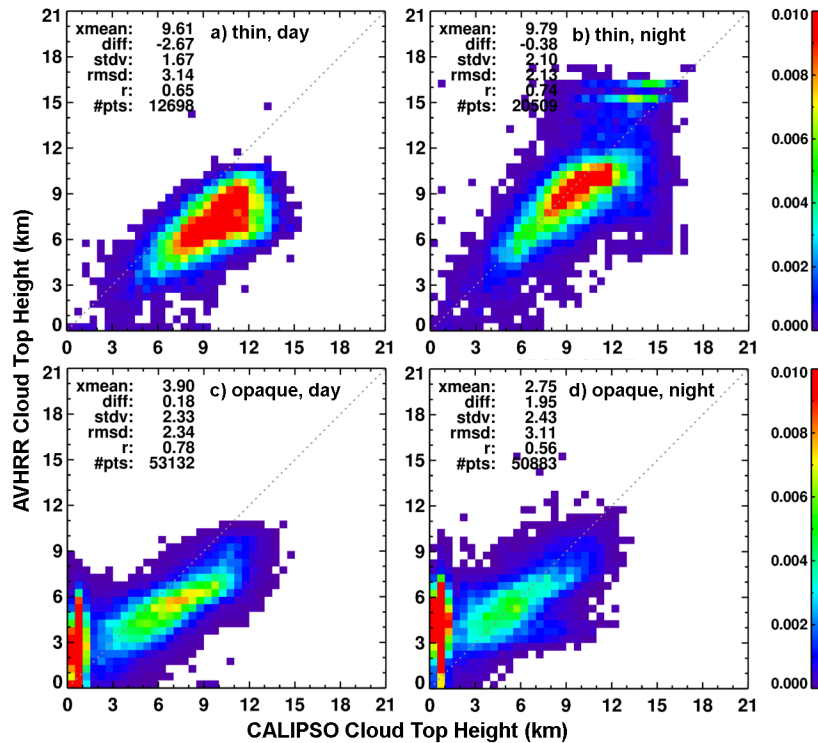

Figure 38. Same as Figure 37, except for ice cloud base heights.

water surfaces During daytime, CBH is underestimated by 0.25km, on average, for thin water clouds (Figure 37a) and overestimated by 0.10 km for opaque water clouds (Figure 37c). At night, the overestimation is close to 0.85 km for both thin and thick clouds (Figure 37b,d). The poorer agreement at night is due to the lack of COD information, which is required for estimating cloud thickness.

Comparisons for ice CBH for nonpolar ice-free water scenes are plotted in Figure 38. Like the CTH, the thin cirrus CBH is underestimated by 2.67 ± 1.67 km during the day (Figure 38a), while opaque ice CBH, in the mean, is overestimated by 0.18 ± 2.33 km (Figure 38c). At night, the thin cirrus CBH (Figure 38b) is too low by only 0.38 ± 2.10 km because the COD is reasonably accurate. However, the thick ice cloud CBH is overestimated by 1.95 ± 2.43 km due to limited COD estimates.

These results are fairly representative of all snow/ice-free scenes as seen in Table 24, which summarizes the results for all ice/snow-free and -covered matched GEOPROF pixels. The magnitudes of the bias are relatively small for opaque ice and water clouds and for thin water clouds over snow-free areas during the day and for thin cirrus at night. In some cases, the statistics are even better than those for CTH. For other cloud types, the biases are substantial because of the infrared opacity of the clouds at COD of ~4 or so.

Table 24: Differences between TCDR NOAA-18 and RL-GEOPROF single-phase cloud base heights (km), JAJO 2008. SF – snow/ice free, SI – snow/ice covered.

Month and Time of Comparison	Optically Thick Cloud Bias	Optically Thick Cloud SSD	Number of Optically Thick Cloud Matches	Optically Thin Cloud Bias	Optically Thin Cloud SSD	Number of Optically Thin Cloud Matches
DAYTIME (0° ≤ SZA < 82°)			X 10^{-2}			X 10^{-2}
Water Cloud, SF	0.12	0.83	1208	-0.28	0.72	575
Water Cloud, SI	1.41	1.74	195	0.68	1.33	66
Ice Cloud, SF	0.26	2.32	747	-2.49	1.72	161
Ice Cloud, SI	0.58	1.96	133	-1.30	2.85	71
NIGHT (SZA ≥ 82°)						
Water Cloud, SF	0.95	0.88	1298	0.78	0.88	537
Water Cloud, SI	0.98	1.06	144	-0.52	-0.70	417
Ice Cloud, SF	1.90	2.38	660	0.04	2.11	336
Ice Cloud, SI	1.66	1.81	374	-0.52	3.51	417

5.5.2.3.3   Cloud Optical Depth

Non-opaque ice CODs from JAJO 2008 SatCORPS-A1 N18 and CALIPSO are compared in Figure 39 for cirrus over ice-free water surfaces. During daytime (Figure 39a), the AVHRR COD is twice the CALIPSO mean. At night, the bias is diminished by 2/3 (Figure 39b), when, for COD < 0.5, the agreement is good, but SatCORPS-A1 tends to overestimate at higher values. For all snow/ice-free surfaces, the mean daytime and nighttime overestimates are 1.27 ± 2.3 and 0.33 ± 1.17, respectively. The bias during the day is due to the reflectance model discussed earlier. The errors over snow are much larger.
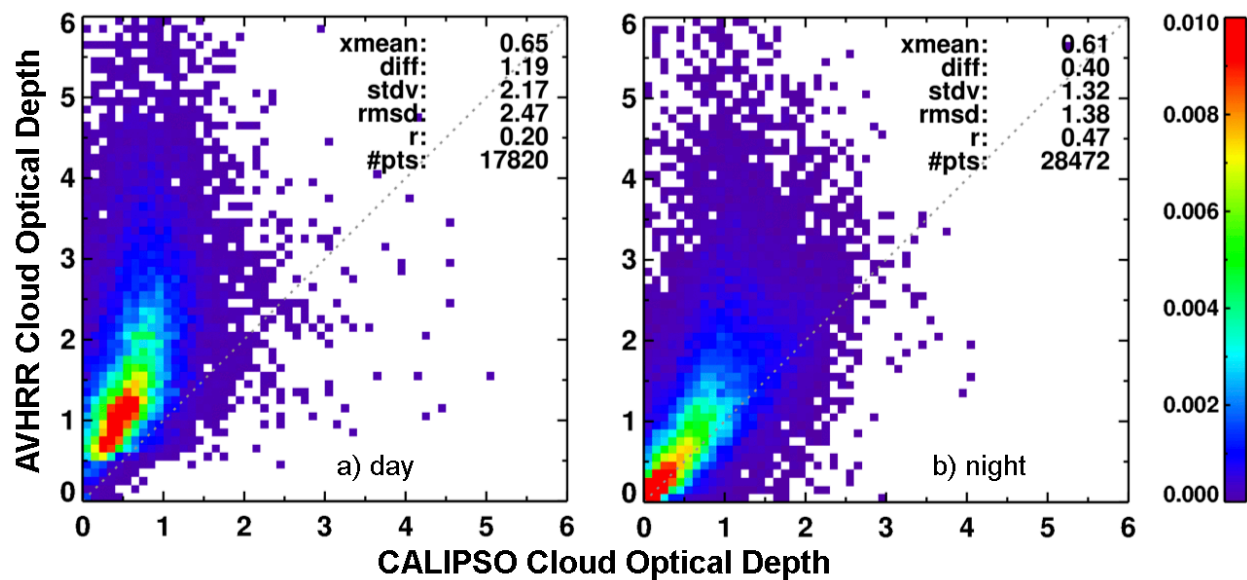

Figure 39: JAJO 2008 matched SatCORPS-A1 N18 and CALIPSO ice COD for CALIPSO non-opaque clouds over ice-free water surfaces. (day), (b) night.
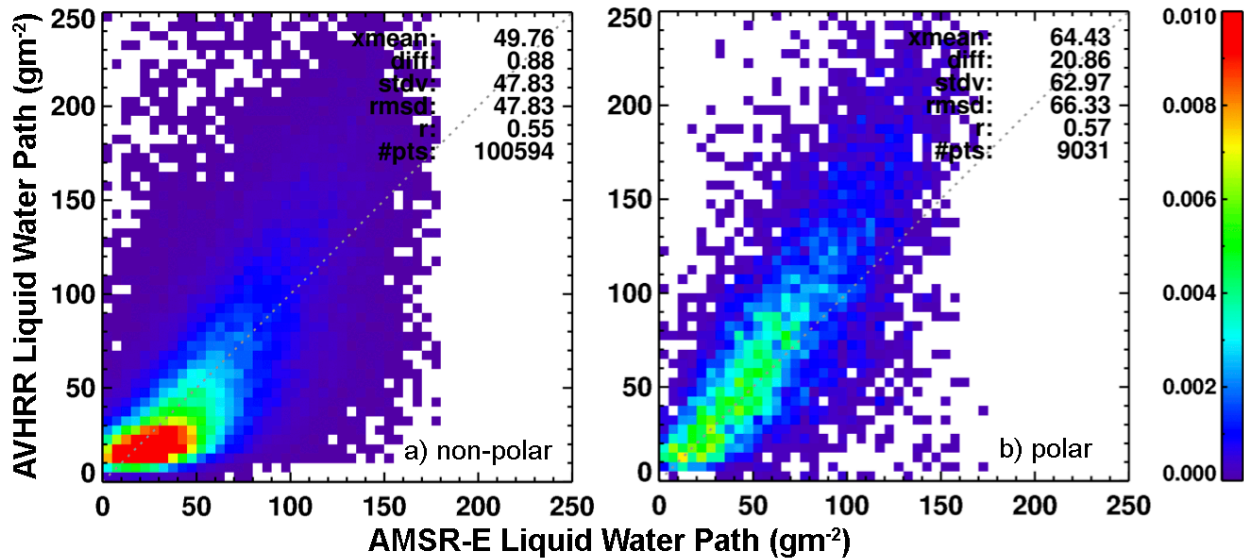
Figure 40: JAJO 2008 matched SatCORPS-A1 N18 AVHRR and Aqua AMSR-E LWP over ice-free water surfaces during daytime. (a) nonpolar, (b) polar waters.

5.5.2.3.4   Cloud Water Path

The LWP from AVHRR and AMSR-E are compared in Figure 40 for JAJO 2008 over ice-free water during the day. Over nonpolar areas (Figure 40a), the AVHRR retrieval appears to too low for small LWPs and too large for AMSR-E LWP > 80 gm^{-2}. On average, the difference is ∼ 1 ± 48 gm^{-2}. Over polar waters (Figure 40b), the agreement is quite good for AMSR-E LWP < 70 gm^{-2}, but AVHRR LWP is greater than AMSR-E for larger values. On average, for all ice-free waters, the difference is 2.5 ± 49.2 gm^{-2}.
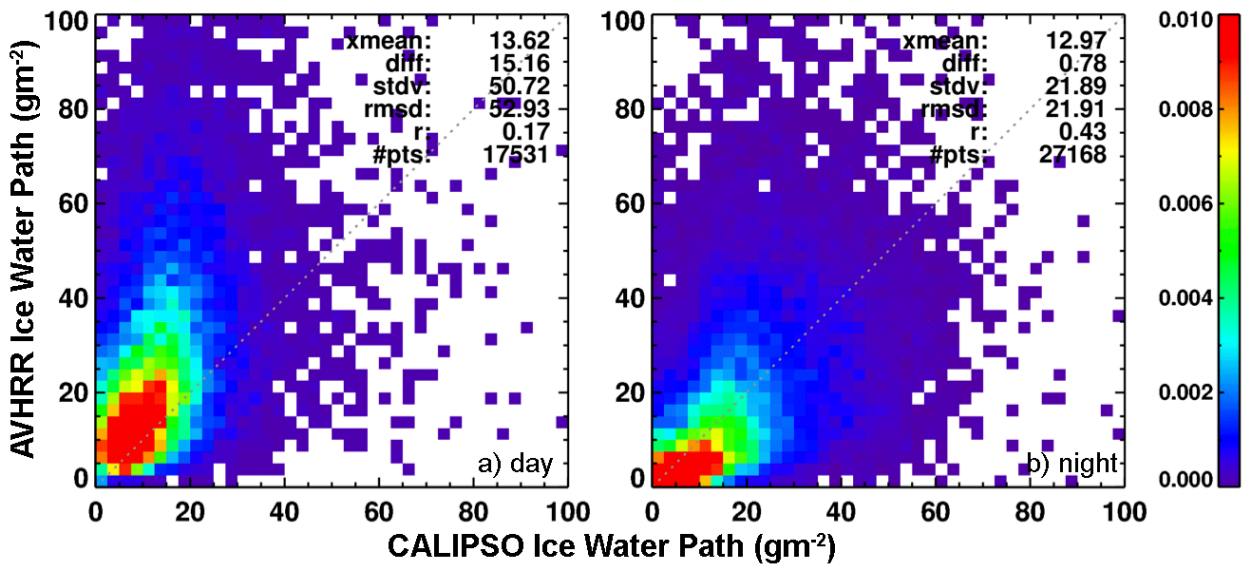

Figure 41: Same as Figure 39, except for IWP. (day), (b) night.

The SatCORPS-A1 IWP was compared with CALIPSO for CALIPSO non-opaque ice cloud retrievals. Figure 41 shows the comparisons for cirrus over ice/snow-free surfaces during JAJO 2008. During the day, some of the AVHRR COD overestimate is countered by the CER retrievals that produce an IWP bias that is comparable to the mean CALIPSO-retrieval (Figure 41a). At night, the mean IWP bias is < 1 ± 22 gm^{-2} (Figure 41b). The mean biases for all snow/ice free surfaces are listed in Table 14.
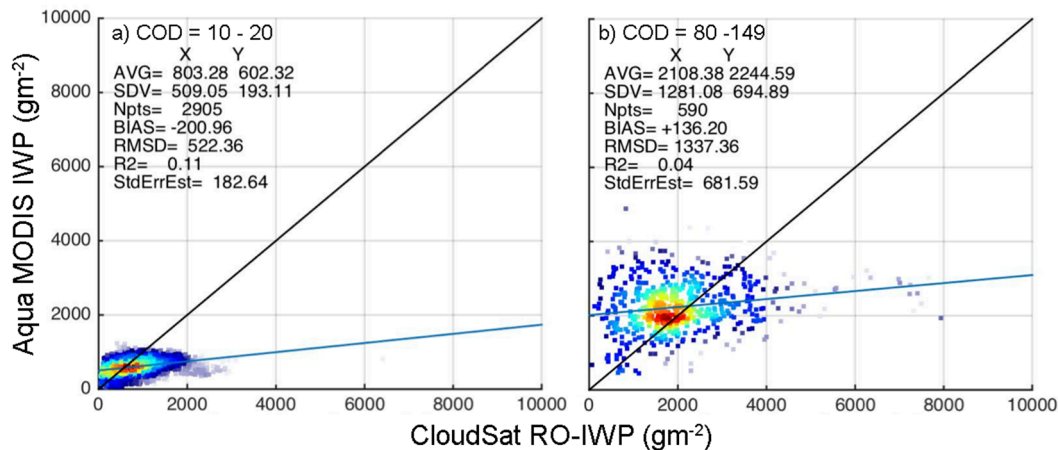

Figure 42: Comparison of April 2010 CloudSat Radar only and CERES Ed4 Aqua IWP over CONUS for CERES COD between (a) 10 and 20, and (b) 80 and 149.
Courtesy of William R. Smith, Jr., NASA.

To date, no comparisons of AVHRR IWP and the CloudSat radar-only (IWP-RO) product (Austin et al. 2009) have been performed. However, IWP retrievals from CERES Ed4 Aqua MODIS taken over the CONUS during April 2010 have been compared with matched IWP-RO values for ice clouds having COD > 10. IWP-RO was computed as the integral of ice water content over all layers above the level corresponding to a temperature of 253 K. Comparison of the IWP integral with that for total water path (integral over all levels including liquid layers) revealed little difference between the two quantities suggesting that no retrievals were performed for temperatures above 253 K. Figure 42 shows the results for COD between 10 and 20 (Figure 42a) and between 80 and 149 gm^{-2} (Figure 42b). The correlation is very small and the differences are -201 and 136, respectively, with corresponding SDDs of 482 and 1330 gm^{-2}. For all ice clouds having COD > 10, the bias is -155 ± 760 gm^{-2}. This translates to a bias of -15% ± 72%. Given that the mean IWP difference between SatCORPS-A1 N18 and CERES Ed4 is 77 gm^{-2}, it is likely that the bias relative to IWP-RO will be smaller for the N18 results. It should be noted, however, that the TWP for those clouds is significantly larger, so that the SatCORPS-A estimate of IWP, by itself, will be less than the TWP. Correction with a parameterization such as that developed by Smith (2014) would allow a more accurate estimate of TWP. Analyses similar to the CERES-CloudSat comparison will be performed to validate the N18 results.

5.5.2.4   Overshooting Convective Cloud Top Detection

The OT detection mask has been validated using NOAA National Weather Service Radar-88 Doppler (WSR-88D) composite reflectivity and precipitation echo top heights and CloudSat OT observations. These validations have been described in detail by Dworak et al. (2012), Bedka et al. (2011), and Bedka et al. (2012), respectively. The results from these studies are summarized in Table 25 below. Since AVHRR GAC data have a spatial resolution approximately equal to current geostationary (GEO) imager data, only the validation results for GOES or other GEO imagers are shown in Table 25.

Table 25: A summary of current geostationary imager overshooting convective cloud top detection validation results from Dworak et al. (2012), Bedka et al. (2011), and Bedka et al. (2012).

Validation Data Source	OT Detection False Alarm Rate	OT Probability of Detection	Number of Pixels
CloudSat-Observed OT Events	17.2%	55.2%	265
OT Detections With WSR-88D Composite Reflectivity > 30 dBZ	17.1%	N/A	27775
OT Detections With WSR-88D Precipitation Echo Top Above The Tropopause	5.9%	N/A	18203

5.5.2.5   Clear-Sky Skin Temperature

Validation of the SatCORPS-A1 surface temperature product is performed separately for land and ocean (including large lake) pixels. The SatCORPS-A1 SST values are compared to climatologies established by NOAA ESRL using their daily high-resolution blended analysis SSTs (Reynolds et al. 2007). The NOAA "Optimum Interpolation" SST (OISST) Version-2 high-resolution dataset consists of a global 0.25°x0.25° grid of blended satellite and in situ measurements of daily SST, starting from January 1981 to the present date. Daily validations of SatCORPS-A1 SST and NOAA OISST are performed for different NOAA satellites to ensure temporal stability and consistency. The AVHRR SST pixel data are first gridded to match the NOAA OISST 0.25° resolution. Only pixels that are classified as clear with 100% water fraction and are not present in a sun-glint region, are used in the daily grid averages. Furthermore, each grid box must contain an average from a minimum of 10 pixels, thereby preventing an inordinately small sample of measurements from representing an entire 0.25°x0.25° region.

The demonstration dataset uses NOAA-18 SSTs from 1 January 2008 through 31 December 2008. Figure 43 plots the July 2008 mean SST values from AVHRR (Figure 43a), NOAA OISST (Figure 43b), and their differences (Figure 43c), revealing the good regional agreement of the two products. The scatterplot of the daily matched 0.25° regional means (Figure 43d) shows a very small average bias (-0.06K) and a standard deviation of the differences (SDD) of 0.62 K. This result is typical as the monthly biases for 2008 range from

A controlled copy of this document is maintained in the CDR Program Library.
Approved for public release. Distribution is unlimited.
111

-0.04 K to -0.11 K, while corresponding SDDs vary between 0.58 and 0.66 K (Scarino et al. 2015).
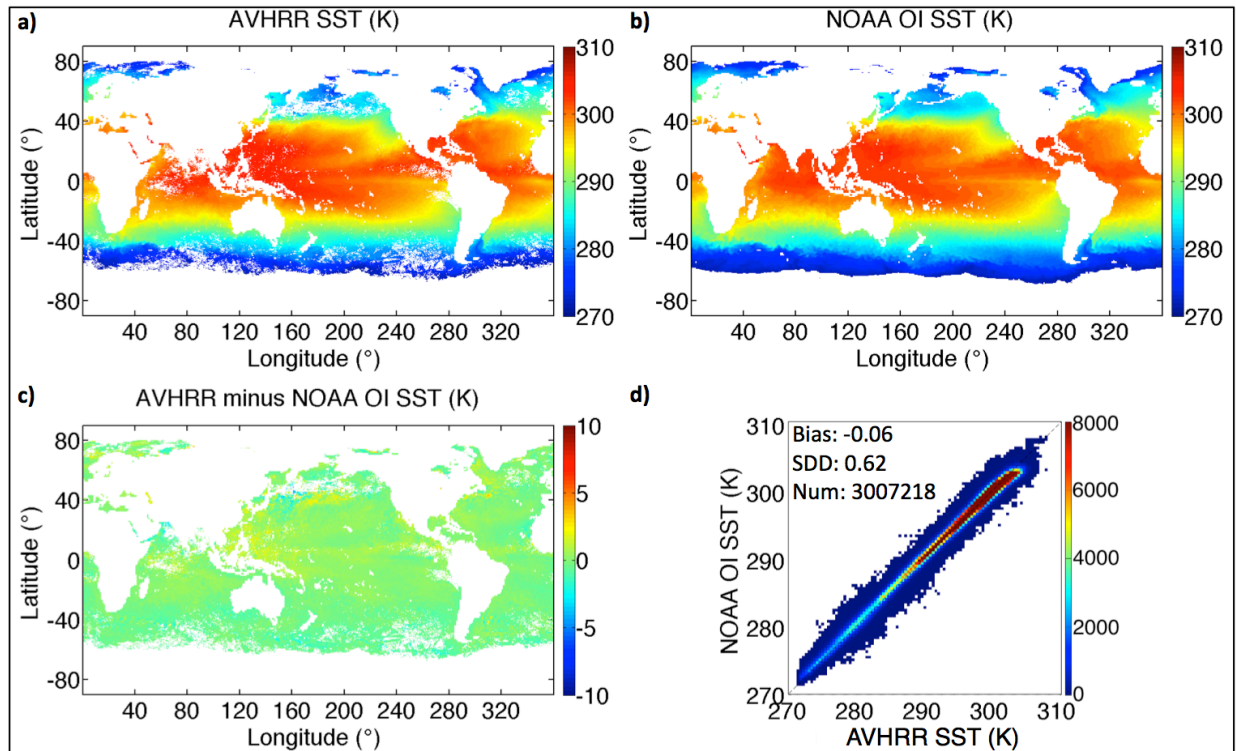

Figure 43: Mean July 2008 (a) AVHRR SST, (b) NOAA ESRL Optimum Interpolation SST, and (c) their differences with 1° land mask applied. (d) The scatterplot of instantaneous 0.25° regional values, where the color scale indicates the number of points.

Land surface temperature (LST; including snow) is validated against the Atmospheric Radiation Measurement (ARM) Climate Research Facility 11-µm upwelling infrared thermometer (IRT) and the NOAA ESRL Surface Radiation (SURFRAD) network precision broadband infrared radiometers (PIR) located at seven sites around the CONUS. The ARM 10-meter-height IRT measures the IR radiant energy from the ground every 60 seconds, which is used to compute the surface temperature using the same surface emissivities used for the AVHRR analysis. The SURFRAD network consists of eight stations scattered across the continental U.S. (only seven stations available for validation at the time of this write-up), where the PIRs measured the upwelling thermal infrared irradiance (L_{Ru}) every 180 seconds. Surface temperature (T_{sR}) is determined from L_{Ru} by

$$T_{sR} = \{[L_{Ru} - (1 - e_s)\, L_{Rd}]\, /\, \sigma\, \varepsilon_s\}^{0.25}, \qquad (46)$$

where ε_s is the broadband emissivity (Wilber et al. 1999), σ is the Stefan-Boltzmann constant, and L_{Rd} is the downwelling thermal infrared irradiance.
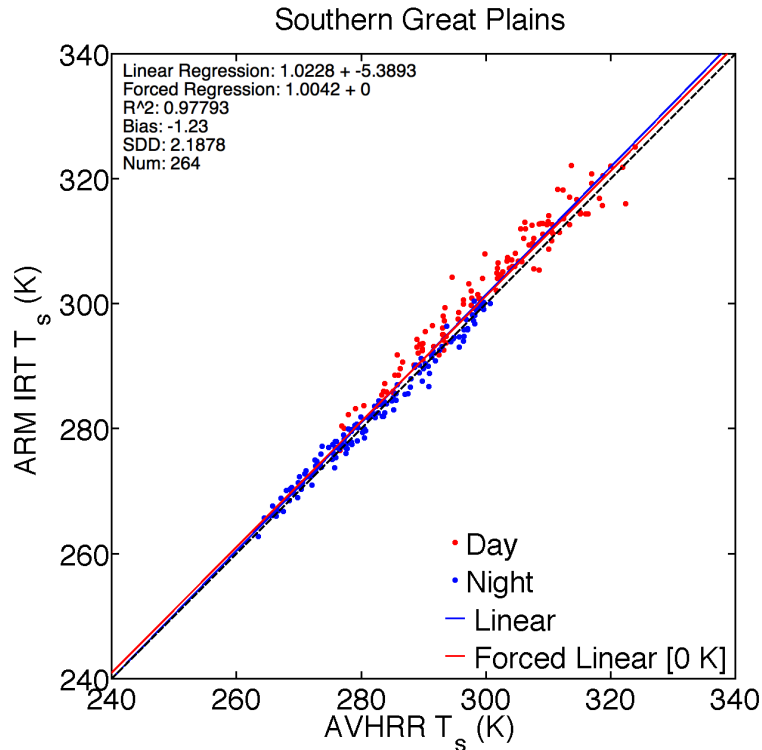
**Figure 44: AVHRR Land Surface Temperature compared to matched ARM SGP
IRT temperatures, January-December 2008.**

Figure 44 is a comparison of AVHRR LST to the ARM IRT measurements for 2008. Figure 45
shows a similar analysis using two SURFRAD sites – Desert Rock, NV and Sioux Falls, SD,
which are color-coded by day and night, respectively. These show 3x3 AVHRR clear pixel
mean LST compared with ARM (SURFRAD) values averaged using 5 (3) consecutive
measurements, centered within 2 (4) minutes of the satellite overpass time. The biases are
larger over land compared to ocean, but are nevertheless reasonable, ranging from -1.23 K
over the ARM site to 0.1 K over Sioux Falls with uncertainties (SDD) varying from 1.5 K to
2.2 K. Greater variations are evident in the daytime and summer comparisons (red dots).
For all 7 SURFRAD stations, the bias and SSD are 0.49 K and 2.29 K, respectively.

The higher uncertainties over land are due to several factors:

a. The difficulty in comparing large-area satellite retrievals with the point-like
    measurements from the IR thermometers. Land-use across even one AVHRR pixel
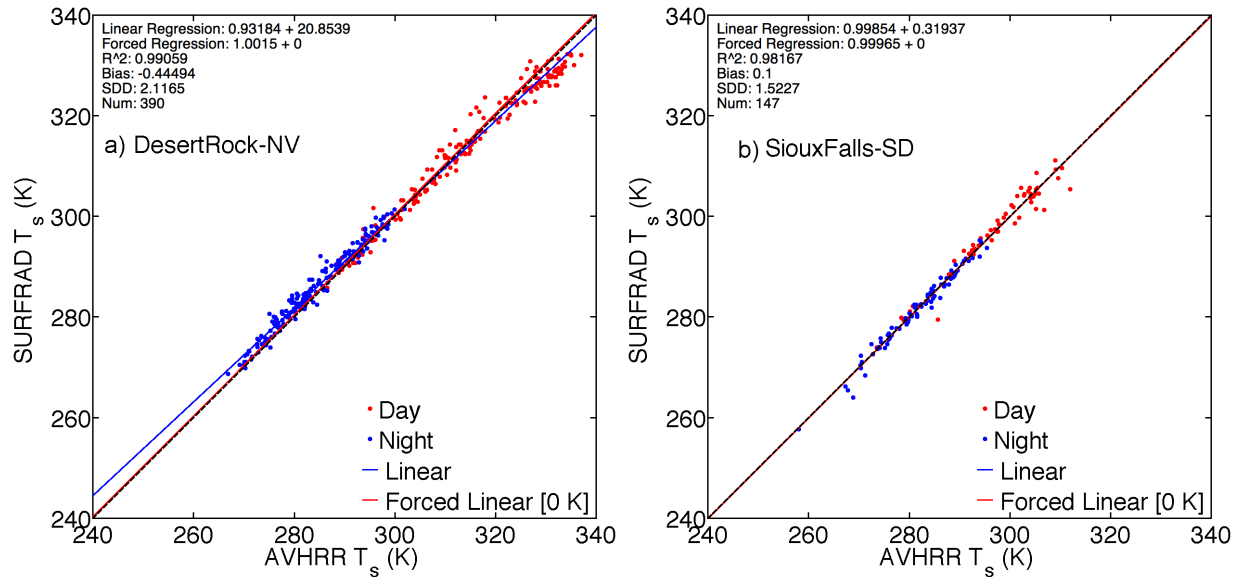   can vary significantly.

A controlled copy of this document is maintained in the CDR Program Library.
Approved for public release. Distribution is unlimited.
113

Figure 45: AVHRR Land Surface Temperature compared to SURFRAD (a) Desert Rock, NV and (b) Sioux Falls, SD PIR measurements, January-December 2008.

b. The angular dependence of the observed surface radiance. Due to shadowing and surface emissivity variations with VZA, the radiance exiting the surface can vary substantially as a function of viewing and illumination conditions, vegetation type, and terrain (e.g., Minnis and Khaiyer 2000; Minnis et al. 2004).

c. Differences between the model and actual profiles of temperature and humidity.

Despite these drawbacks, however, the biases and uncertainties indicate good agreement of the AVHRR LST product relative to ground-based instruments and are within the 2.5 K accuracy requirements for GOES-R (Yu et al. 2012).

5.5.2.6 TOA Broadband Fluxes

The broadband SW and LW fluxes can be validated for certain periods using broadband radiation measurements from the ERBE scanners (1985-1989) and the CERES scanners (2000 – present). Wherever the ERBE or CERES data overlap simultaneously with the AVHRR footprints, the AVHRR data will be matched with the corresponding ERBE or CERES fields of view in the same manner used for deriving the narrowband-to-broadband conversion coefficients (Section 3.3.1.5). The mean and standard deviations of the differences are used to assess the errors in the fluxes.

Figure 46 shows plots comparing the N18 AVHRR and CERES Aqua fluxes for October 2007 using coefficients derived from 2008 data. For both the OLR (Figure 46a) and SW flux (Figure 46b), the bulk of the points are located along the line of agreement. The OLR bias is -1.7 Wm^{-2} (-0.72%) with SDD = 6.4 Wm^{-2} (2.8%). The SW flux bias and SDD are -0.4 Wm^{-2} (-0.18%) and 17.8 Wm^{-2} (7.4%), respectively. Results for April 2007 are very similar. Thus,

the initial validation indicates that off-year flux estimates are within the uncertainties of the original fits.
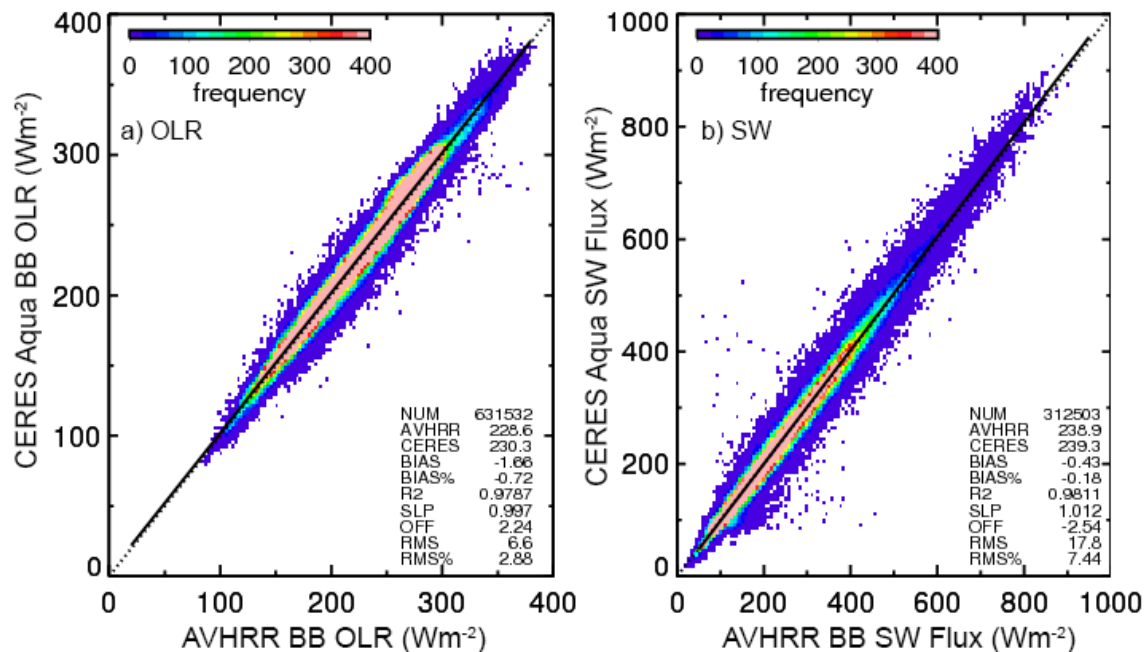

Figure 46: Scatterplots of CERES Aqua and NOAA-18 AVHRR measurements of (a) OLR and (b) reflected SW flux for all scenes and times of day during October 2007.

5.5.2.7   Qualitative Algorithm Validation

An online cloud detection and property retrieval visualization tool has also been developed for AVHRR TCDR team members at NASA LaRC to closely inspect results and identify areas needing improvement. The tool allows a user to select one or more cloud product graphics, toggle/fade between images, and zoom on features of interest, capabilities that are very helpful for assessing product quality. See an example of this tool for a NOAA-18 scene over the Northwest Pacific Ocean at http://go.usa.gov/cjYzz. In addition to this online tool, SatCORPS-A output has been analyzed extensively using the McIDAS-X and McIDAS-V software packages. These software tools allow TCDR algorithm developers to interactively probe values for individual pixels, helping the assessment of product quality and identifying problematic data in SatCORPS-A NetCDF output files.

Simulated clear-sky reflectances and BTs are examined qualitatively through the creation of red, green, blue (RGB) composite imagery. As emphasized in Section 3, accurate clear-sky reflectances and BTs are essential for reliable cloud detection and retrievals. It can be challenging and time-consuming to validate each of the channels of simulated clear sky data. An RGB composite can be created from the clear sky data and compared with an RGB created from the observed data, allowing one to qualitatively assess the accuracy of multiple channels of simulated data in one image. Figure 47 shows the predicted clear-sky versus observed RGBs for two NOAA-18 scenes. The RGB images in these scenes were

A controlled copy of this document is maintained in the CDR Program Library.
Approved for public release. Distribution is unlimited.
115

created by assigning the VIS reflectance to the red channel, BTD_{34} to the green channel, and the reversed T_4 to the blue channel. Water clouds typically appear as white or peach and ice clouds appear in shades of magenta and gray. Snow cover and sea ice appear as bright magenta. Clear-sky water surfaces appear as blue. The simulated clear-sky RGB composites in Figures 47b,d match the clear portions of the observed (Figures 47a,c) RGBs quite well considering the complex land surface and snow cover present in these scenes and the low resolution of the simulated data, providing confidence that the clear-sky data passed into the cloud detection and retrieval modules are of high quality. Such images and other simulated images are used for qualitatively verifying the SatCORPS-A input and output.
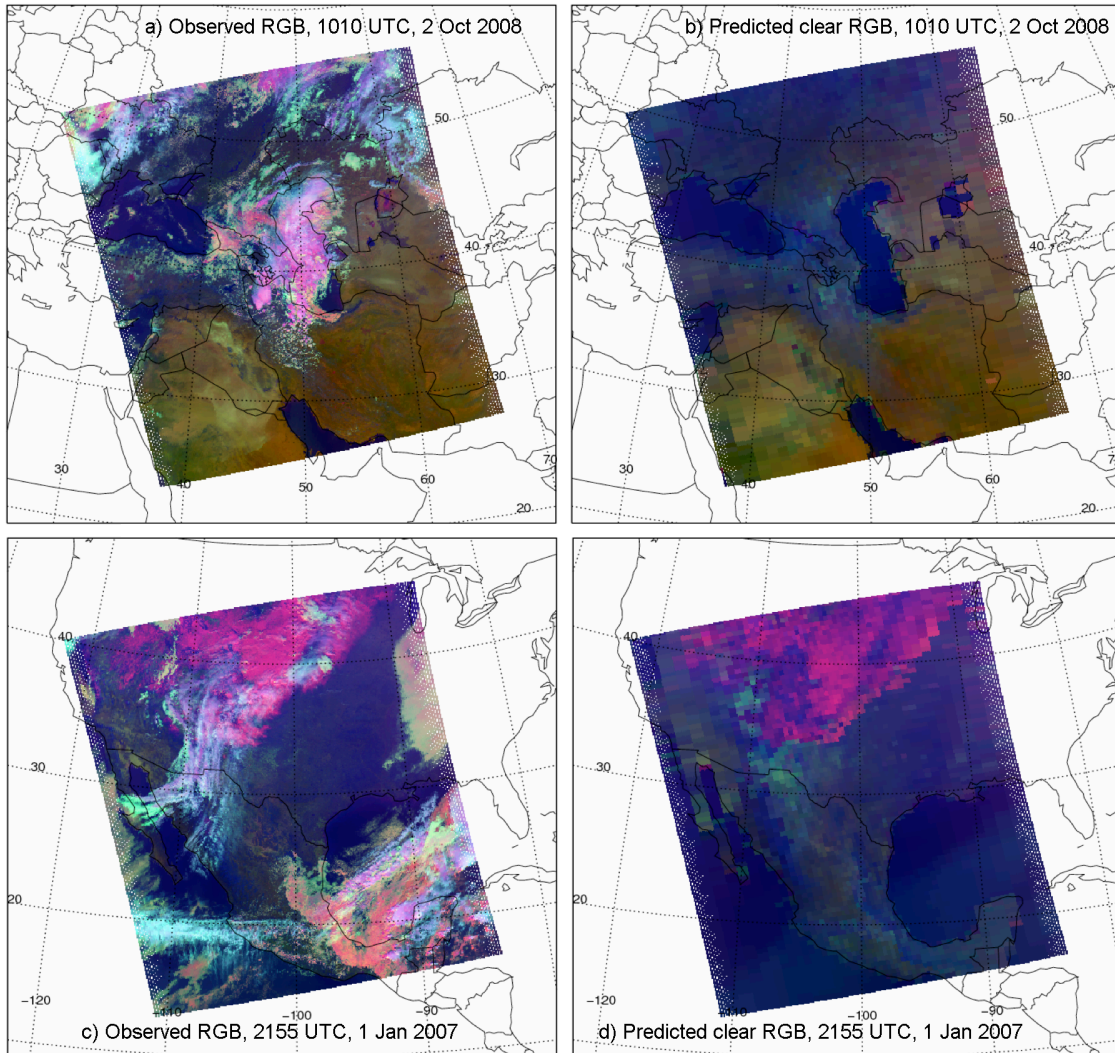

Figure 47: Example of RGB composites for two NOAA-18 AVHRR scenes using VIS reflectance for the red channel, BTD_{34} for the green channel, and T_4 for the blue channel. AVHRR observed RGBs and predicted clear-sky RGB images over the (a, b) Middle East and (c,d) southern North America and simulated clear-sky RGB right panels use simulated clear-sky reflectance and BTs.

## 5.6	Processing Environment and Resources

The NASA Atmospheric Sciences Data Center (ASDC) Modernization through Integration (AMI) system is a large-scale processing and storage environment based on IBM HPC technologies for supporting science data product generation and climate data analysis and research. AMI is used to produce the AVHRR Cloud TCDR. The system provides highly reliable computing and storage resources to over 500 scientists and engineers supporting the Science Directorate at NASA Langley Research Center in Hampton, Virginia. It contains a mixture of IBM Power6 and Power7+ and various Intel x86 processors totaling approximately 900 CPU cores. A two petabyte online data storage requirement is met utilizing IBM GPFS storage systems. The SatCORPS-A utilizes a maximum of 125 CPU cores for TCDR processing.

The SatCORPS-A is a combination of C and Fortran code. It is linked to a library from the McIDAS-X software package that contains a routine allowing one to easily pass command line arguments to the SatCORPS-A. The SatCORPS-A is linked to NetCDF-4 and HDF-5 libraries to allow reading of pre-processed AVHRR GAC input data (see Section 3.3.3) and creation of TCDR NetCDF output files. The AVHRR GAC pre-processing software, SAPS, requires the assembly language library used in reading the AVHRR GAC Level 1B files. The SatCORPS-A is also linked to HDF-4 libraries to allow reading of MERRA data. The SatCORPS-A is compiled with gfortran and requires Intel x86 processors with a Linux operating system.

The SatCORPS-A is driven by a set of bash shell scripts that pre-process the AVHRR GAC input data (see Section 3.3.3), separate a typical 13000 scanline AVHRR orbit into 1000 scanline (maximum) chunks, and then distribute each of these chunks to separate processors within the NASA LaRC AMI computer system. The NetCDF output file for each of the 1000 scanline chunks occupies ~10-13 MB of storage. When the processing for the entire orbit is complete, a Fortran program merges the segments into a single NetCDF file containing each segment within the entire AVHRR GAC orbit and adds all NetCDF metadata required by the NOAA CDR program. The NetCDF data for the scanline chunks are removed by the bash script after the Fortran merging software is complete. A typical TCDR NetCDF output file occupies ~130-150 MB of disk space. A month of SatCORPS-A NetCDF output occupies ~60 GB for a single NOAA satellite.

With the computing setup described above, the processing for an entire GAC orbit file takes approximately 5-6.5 min of wall clock time depending on the amount of cloud cover in the orbit. A year of processing takes ~2.5 days of wall clock time to complete for a single NOAA satellite. The exact amount of CPU time needed for processing has not yet been determined.

6. Assumptions and Limitations

6.1 Algorithm Performance

6.1.1 MERRA Time Series Stability

Three "streams" of MERRA data are available through the 35-year AVHRR time series (Schubert et al.: http://gmao.gsfc.nasa.gov/pubs/docs/Schubert352.pdf). The MERRA100 stream used for the period from 1979-1988, the MERRA200 stream is used for 1989 through 1997, and the MERRA300 stream is used from 1998 to the present. Schubert et al. indicate that considerable effort was devoted to minimizing artificial trends induced by MERRA stream changes. It is almost a certainty that the quality of MERRA analyses has improved over time from 1979 to the present as a greater volume of increasingly high quality remotely sensed and other observational data are assimilated into the MERRA analysis. We rely exclusively on MERRA for surface observations and vertical profiles of temperature, moisture, ozone, and snow cover given that 1) MERRA offers superior temporal, horizontal, and vertical resolution over other available analyses that cover the AVHRR data record, and 2) the full MERRA data record is online at NASA LaRC. Also, recent MERRA analyses are relatively consistent with the GEOS-5 analyses used for the CCPRS. It is assumed that time trends in MERRA fields are minimal. But if significant trends or anomalies were to be discovered in MERRA fields, this could induce trends in AVHRR cloud property retrievals, the magnitude of which are unknown at this time. To explore the sensitivity of cloud retrievals to numerical model analyses, the LaRC SatCORPS-A could be run using data from another long-term dataset such as the NCEP/NCAR reanalysis.

6.1.2 Spatial Consistency of MERRA Analyses

It is assumed that MERRA data are of comparable accuracy across the globe throughout the MERRA time series. Retrieval quality depends on the accuracy of the 2-D surface analysis and 3-D profiles. For example, an errant surface temperature analysis can produce errors in cloud detection and height assignment. For an overcast tile, a misclassification of the region as snow free would greatly impact the retrieval of COD if the surface were snow-covered. It is expected that errors in parameters such as snow/ice cover and surface temperature are not regionally dependent. The regional consistency assumption, however, may not be valid for regions with very few in-situ observations (i.e. polar regions) near the beginning of the AVHRR data record when few high quality satellite observations were available.

6.1.3 Solar Channel Calibration Stability

It is assumed that the solar channel calibration gains provided by the companion AVHRR calibration FCDR (Doelling et al., 2015) will produce a stable time series of 0.63, 0.86, and 1.61-µm reflectances. Given the high quality and extensive validation of the FCDR, this is not anticipated to be an issue, but subtle trends in reflectance would introduce trends in

A controlled copy of this document is maintained in the CDR Program Library.
Approved for public release. Distribution is unlimited.
118

cloud property retrievals that could interfere with trends induced by global climate signals present in our datasets.

6.2   Sensor Performance

6.2.1   Assumed Stability of AVHRR Thermal Channel Calibrations

Given that the AVHRR sensor has on-board calibration of the thermal infrared channels, it is assumed that the signal provided by these channels is stable throughout the course of the instrument lifetime. It is clear, however, that some temporal variations occur for, at least, some of the sensors (e.g., Mittaz and Harris, 2011). Any trends in the IRW channel calibration will introduce artificial trends in various parameters including surface temperature as well as cloud top and effective temperature, height, and pressure, and possibly cloud fraction. Initial analyses indicate some significant biases in the SIR channel of NOAA-7 for the period between October 1982 and 1983. These biased values result in increased cloud fraction for the period and affect other retrievals as well.

A variety of factors affect the IR channel response and hence the accuracy of the thermal channel brightness temperatures. Periodically, solar contamination affects the temperatures by heating the onboard blackbody reference.

6.2.2   Performance Degradation Induced By SIR Channel Noise

Though extensive effort has gone toward minimizing the impact of noise in the SIR data in the AVHRR pre-processing phase, the example shown in Figure 8 indicates that a "perfect" noise-filtered dataset is not possible when the original data are of such poor quality. It has been noted that sensor noise is most pronounced for BT < 255 K and, given that there are only 1 (TIROS-N, NOAA-6, -8, and -10) to 2 (remainder of NOAA and IJPS satellites) other IR channels available at night, it is expected that the cloud mask and retrieval quality will suffer over cold polar land or sea ice surfaces. This is especially true for SATCORPS-A3, which lacks the SWI channel.

6.2.3   Performance Degradation Induced By Changes in SIR Channel

Spectral Response Function and Calibration

The AVHRR SIR calibration changed with the AVHRR/3 series, beginning with NOAA-15. Figure 48 shows a comparison of BTD34 as a function of IRW BT for NOAA-9 and NOAA-18 over the same region of Africa and same month of year. The maximum IRW BT appears to be limited to 328 K for NOAA-9 but can approach 340 K for NOAA-18. The maximum SIR BT is limited to 320 K for NOAA-9 but exceeds 340 K for NOAA-18. Within the cloud mask component of the SatCORPS-A, there are thresholds based on parameters such as the observed BTD34 and the observed minus simulated clear sky BTD34 that are used to discriminate clear vs. cloudy pixels. Efforts have been directed to compensate for these instrument calibration changes by adjusting the thresholds, but there may be some

A controlled copy of this document is maintained in the CDR Program Library.

Approved for public release. Distribution is unlimited.

119

degradation in cloud mask performance. We do not anticipate any impact on the cloud retrievals because clouds typically do not have IR BTs greater than 320 K.
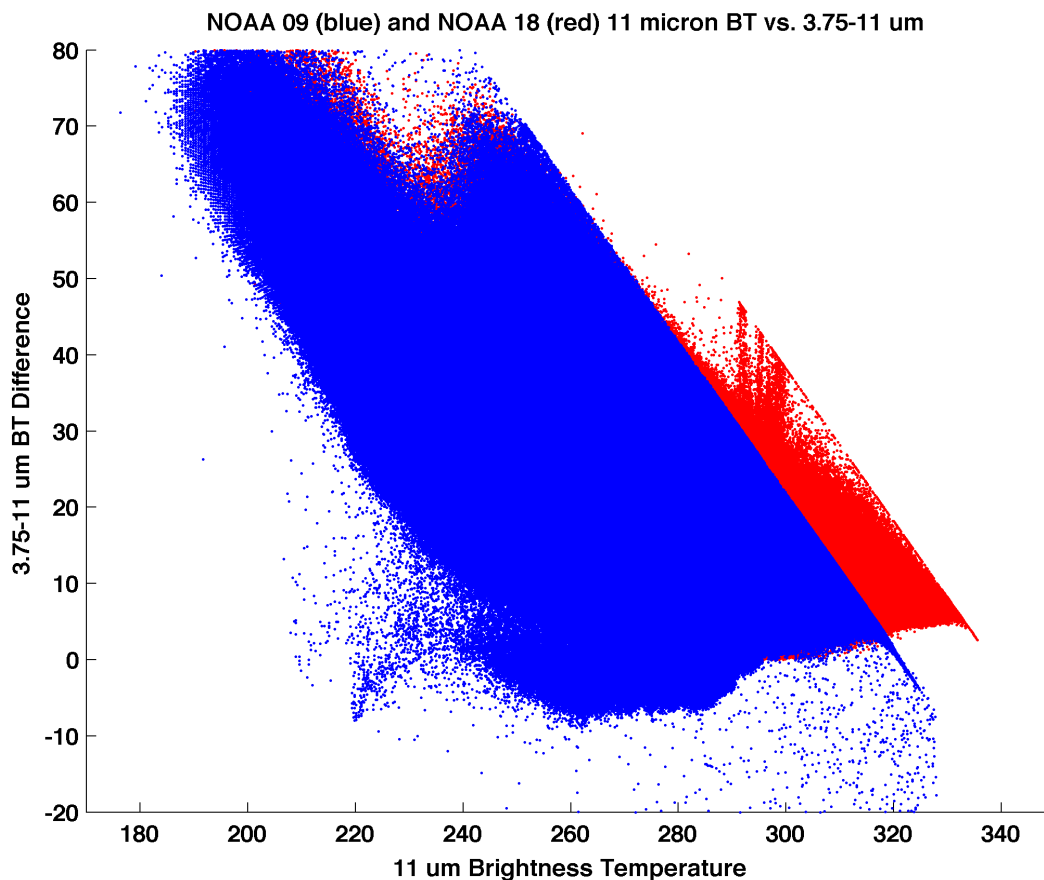

Figure 48: AVHRR BTD$_{34}$ (y-axis) as a function of T_4 for October 1986 NOAA-9 (blue) and October 2008 NOAA-18 (red) data over southern Africa.

6.2.4   Performance Degradation Induced by the Absence of SWC Channel on TIROS-N, NOAA-6, -8, and -10: SatCORPS-A3

In the 3-channel nighttime retrieval algorithm, SIST, the 12-µm channel provides independent information about CER and COD. For instruments missing the SWC channel, the nighttime cloud properties are retrieved by minimizing the differences between the observed and calculated BTs for 11 and 3.7 µm only. The greatest impact of eliminating the SWC channel is seen in the particle size retrieval since it is not possible to solve for 3 parameters with only 2 channels. Thus, a climatological value is substituted into the output files for TIROS-N, NOAA-6 -8, and -10. To assess the impact of the missing SWC channel on other retrieved properties, 6 nighttime scenes from NOAA-9 were analyzed using both the 2-channel SIRT and the 3-channel SIST retrieval algorithm. The scenes selected covered a variety of surface types and latitude ranges, and contained nearly 1.7 million cloudy pixels.

Using the SIRT led to a 12% reduction in the number of water clouds, a 1.3% decrease in mean cloud temperature, and a 1% increase in mean cloud optical depth. The most significant differences in CET and COD were for pixels with differing phase. Figure 49 shows the retrieved values of T_c (Figure 49b) and COD (Figure 49a), respectively, for all of the scenes. The CET values are highly correlated, although for warmer clouds ($T_c >$ ~250K), the 2-channel retrieval tends to yield slightly lower cloud temperatures than the SIST. Most of the COD retrievals are highly correlated, although some differences occur, particularly for low optical depth clouds. Based on this sensitivity study, large differences are not expected in the mean COD or CET values retrieved for TIROS-N, NOAA-6 -8, or -10 relative to those from other AVHRRs. However, some changes in cloud phase are likely.
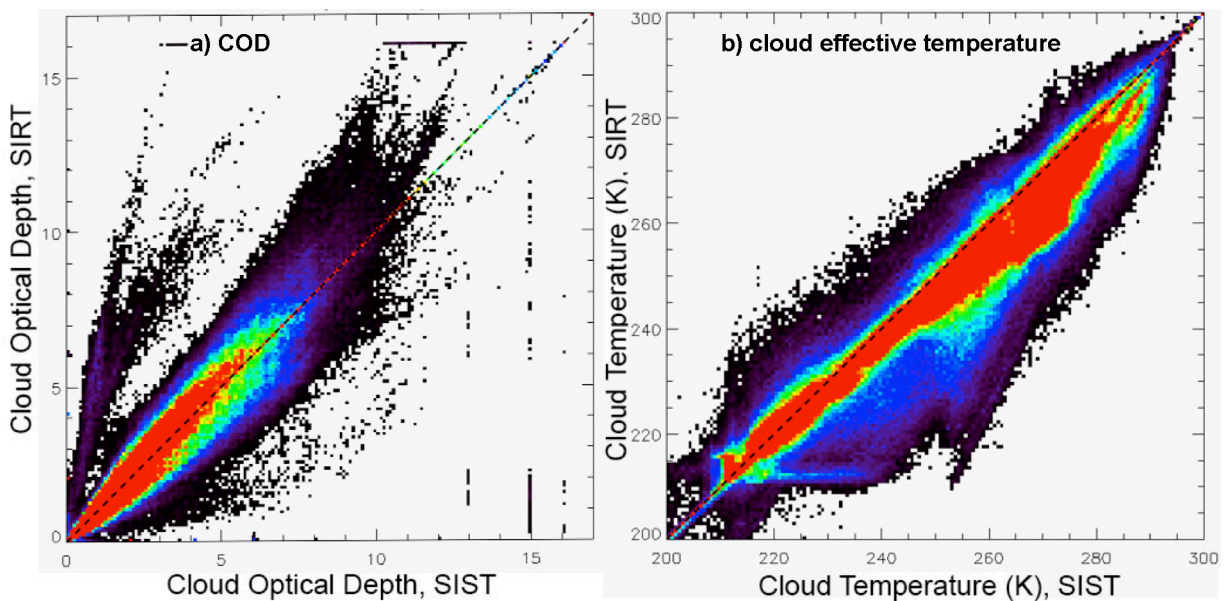

Figure 49: Comparison of nighttime retrievals using 3-channel SIST and 2-channel SIRT (no SWC channel) of a) COD and b) CET for 6 scenes from NOAA-9 (~1.7 million pixels).

6.2.5   Performance Degradation Induced By Absence of Daytime SIR Channel Data on NOAA-15, NOAA-17, MetOp-A, and MetOp-B: SatCORPS-A2

The daytime cloud detection and retrieval are highly dependent on the SIR channel. It is expected that there will be some degradation in cloud detectability using the NIR channel over land because the 1.6-μm surface reflectance is often greater than 0.30 there, and, over deserts, the average overhead-sun albedo exceeds 0.50 (Chen et al. 2006). The albedos at 3.8 μm over land are generally less than 0.10 and over deserts are, on average, ~0.20 (Chen et al. 2004). With reduced contrast, it is difficult to detect thin clouds over those surfaces using the NIR channel. This degradation will be evaluated using data from another satellite, Terra MODIS or NPP VIIRS, having both channels.

While CER and phase can be retrieved using the NIR channel, there will likely be some biases between the values of CER derived using the SIR and NIR channels due to differing sensitivities to the depth of the cloud, in addition to greater uncertainties in the values for
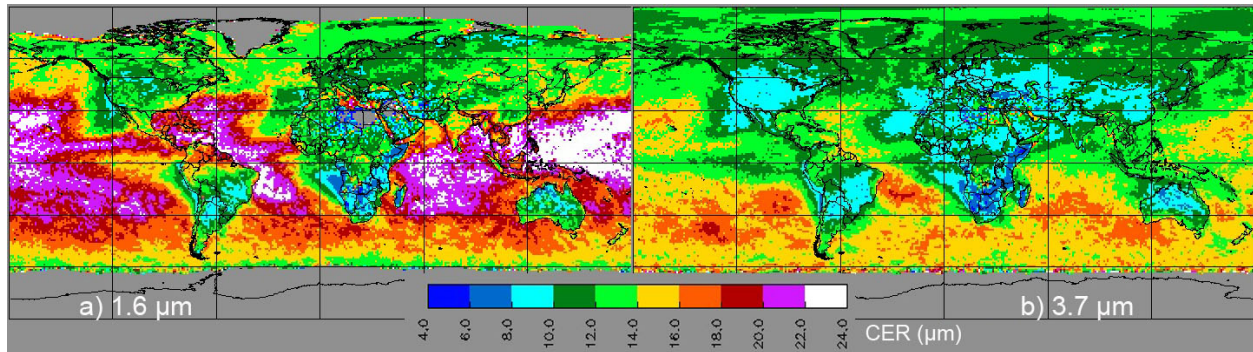

Figure 50: Mean water droplet effective radius from NPP VIIRS data (July 2013) using (a) 1.6 μm and (b) 3.7 μm.

detected thin clouds. The differences between water CER retrieved from MODIS by the MAST using the 1.6-μm channel and that using the 3.7-μm channel are typically between 2 and 7 μm (Zhang and Platnick 2011). The CCPRS applied to VIIRS data yields similar results. Figure 50 shows the average values of CER for water droplets from 1.6 μm (Figure 50a) and from 3.7 μm (50b). Over ocean the 1.6-μm values significantly exceed their 3.7-μm counterparts in most ocean locations by 2 - 9 μm. Smaller differences are seen over marine stratocumulus areas. The 1.6-μm CER values are less than those for 3.7 μm off the west coast of south Africa. Over land, 1.6-μm CER averages are typically greater than the 3.7-μm means by 1-3 μm. On average, the biases are 5 μm over ocean and 2 μm over land. Ice crystal CER averages using 1.6 μm are ~8 and 3 μm greater than their 3.7-μm counterparts over ocean and land, respectively, for the same time period. Similar differences in CER are likely to be realized between the AVHRR sensors using 1.6-μm instead of 3.7 μm. Phase selection will need to be examined using Terra MODIS or VIIRS data.

7.   Future Enhancements

Cloud retrieval techniques and calibrations are being continuously improved as more validation information becomes available and new analysis methods are developed. Such improvements will be valuable for future enhancements. Some of them are described below.

7.1   Improved ice crystal reflectance models

One of the perplexing problems in the remote sensing of ice clouds is the discrepancy between the infrared and VIS cloud optical depths. Theory indicates that the VIS COD should be approximately double its IRW counterpart. The VISST uses this assumption to adjust the value of T_c and, hence Z_c, for optically thin clouds. Yet, as seen in several studies, this adjustment typically results in underestimates of Z_c, which implies that τ is too large. The source of this apparent error lay in the optical properties of the ice crystals assumed in the model computations of the reflectance LUTs. In situ measurements suggest that the asymmetry factor g of the crystals should be ~0.75, while most representations have values between 0.76 and 0.85. The lower values of g result in smaller retrieved COD values and, therefore, more accurate values of Z_c. New models having the desired and more realistic scattering properties are currently being tested and should be available soon for use in retrievals (e.g., Liu et al. 2014). It appears that the values of Z_c from VISST then should be increased for thin cirrus clouds and be more consistent with the values seen from the SIST retrievals.

7.2   Improved infrared channel calibrations

The calibrations of the AVHRR infrared channels have been the subject of considerable research during the last decade. One of the AVHRR CDR projects has been the recalibration of the AVHRR channels using the approach of Mittaz and Harris (2011). With input from that and other studies (e.g., Goldberg et al. 2011), it will be possible to have more reliable infrared calibrations, which would yield more accurate cloud properties. Reprocessing of this cloud TCDR with such improved calibrations would be an important future enhancement.

7.3   Improved phase detection

The phase detection used in the initial SatCORPS-A version overestimated the amount of liquid water clouds, classifying too many optically thin ice clouds as liquid. This had the effect of increasing the average value of CER for both liquid and ice clouds relative to CERES and decreasing the average water cloud COD and increasing the average ice cloud COD during daytime. Reprocessing with the newest phase selection method will dramatically minimize the differences with CERES.

A controlled copy of this document is maintained in the CDR Program Library.
Approved for public release. Distribution is unlimited.
123

7.4   Multilayered cloud detection and retrieval

As noted earlier, multilayered clouds can be an apparent source of error in the retrievals of COD, CEH, and other parameters, particularly when the highest cloud is optically thin and the total COD of the higher and lower clouds is relatively large. Using the BTD45 and the retrieved COD, it is possible to detect some of the multilayered systems (e.g., Heidinger and Pavolonis, 2005). Furthermore, it is possible to retrieve the upper and lower layer cloud properties if a technique similar to that developed by Chang et al. (2010) is used. Currently, this approach is being used for CERES Edition 1 for VIIRS data and one using the 13.4-μm channel on MODIS is used for the CERES Edition 4 software. Having that information allows identification of many of the pixels that are likely to have errors in CEH due to multilayered clouds and provide more useful data about those particular types of pixels.

7.5   More accurate narrow-to-broadband flux conversions

The current estimates of the SW and LW fluxes are based on three single-surface, single-channel regression formulae that employ the same angular correction models to both NB and BB radiances. Ideally, there should be separate models for the different spectra. Newer techniques under development are more accurate and can yield better estimates of broadband fluxes. They account for surface-type and seasonal dependencies, utilize two spectral channels, use radiances instead of irradiances, and apply the latest angular correction models only to the NB data after they have been converted to BB radiances. It is anticipated that such improved algorithms will become available soon for application to the AVHRR data.

7.6   Single-pixel background retrievals

Currently, the tile-based retrieval uses a single set of clear-sky radiances for cloud detection and retrievals. This approach was based on the uncertainty in the pixel location in older navigation schemes, slow computational speeds, and lack of high-resolution background maps. The results from such an approach sometimes produce false clouds near coastlines and in heterogeneous scenes such as deserts, mountains, etc. Given improved accuracy in pixel navigation, faster computational speeds, and better surface information, it will be possible to improve the resolution of the retrievals and detection, thereby reducing false or missed cloudy pixels and biases in COD due to use of a single background radiance.

7.7   Anisotropy of surface emissivity and temperature

It is currently assumed that surface emissivity is angularly insensitive, except over ocean where the VZA dependence is modeled. It is known, however, that over land, ε_s tends to decrease with increasing VZA and during the day T_s varies with solar zenith and azimuth angle because of terrain and vegetation shadowing effects (e.g., Minnis et al. 2004). The anisotropic behavior of these parameters is being studied (e.g., Scarino et al. 2015) and can be included in future enhancements to obtain more accurate surface skin temperatures over land.

7.8   Improved auxiliary input data

Improved long-term records of various input parameters such as sea ice, snow cover, temperature and humidity are being or have been generated since this project began. Generally, it is expected that these new datasets will have better resolution and long-term consistency, as well as greater accuracy than the datasets used as input for this version of the SatCORPS-A. Future versions will likely incorporate some or all of the new input datasets.

A controlled copy of this document is maintained in the CDR Program Library.
Approved for public release. Distribution is unlimited.
125

8. References

Ackerman, S. A., P. Menzel, R. Frey, K. Strabala, R. Holz, and B. Maddux (2014). MODIS Cloud Mask MOD35. C6 Atmospheres Team Webinar Series, 55 pp. http://modis-atmos.gsfc.nasa.gov/Webinar2014/MODIS_C6_MOD35_Ackerman.pdf

Austin, R. T., A. J. Heymsfield, and G. L. Stephens (2009). Retrieval of ice cloud microphysical parameters using the CloudSat millimeter-wave radar and temperature, *J. Geophys. Res.*, 114, D00A23, doi:10.1029/2008JD010049.

Baum, B. A., W. P. Menzel, R. A. Frey, D. C. Tobin, R. E. Holz, S. A. Ackerman, A. K. Heidinger, and P. Yang (2012). MODIS Cloud-top property refinements for Collection 6. *J. Appl. Meteor. Climatol.*, 51, 1145-1163.

Bedka, K. M., J. Brunner, R. Dworak, W. Feltz, J. Otkin, and T. Greenwald (2010). Objective satellite-based overshooting top detection using infrared window channel brightness temperature gradients. *J. Appl. Meteor. Climatol.*, 47, 181-202.

Bedka, K. M., J. Brunner, and W. Feltz (2011): Objective overshooting top and enhanced-V signature detection for the GOES-R Advanced Baseline Imager: Algorithm Theoretical Basis Document.

Bedka, K. M., R. Dworak, J. Brunner, and W. Feltz (2012). Validation of satellite-based objective overshooting cloud top detection methods using CloudSat Cloud Profiling Radar observations. *J. Appl. Meteor. Climatol.,* 49, 684-699.

Brest, C. L., Rossow, W. B., AND M. D. Roiter (1997), Update for radiance calibrations for ISCCP. *J. Atmos. Oceanic. Technol.*, 14, 1091-1109.

CEOS (2006). Satellite Observation of the Climate System: The Committee on Earth Observation Satellites (CEOS) Response to the Implementation Plan for the Global Observing System for Climate in Support of the UNFCCC, p. 50. [Online]. Available: http://www.ceos.org/images/PDFs/CEOSResponse_1010A.pdf

CERES (2014a). Monthly Gridded TOA/Surface Fluxes and Cloud (SFC). CERES Data Product Catalog, DPC-SFC R5V2, 20 June, 11 pp. [Online], Available: http://ceres.larc.nasa.gov/documents/DPC/DPC_current/pdfs/DPC_SFC_R5V2.pdf

CERES (2014b). Single Scanner Footprint TOA/Surface Fluxes and Cloud (SSF). CERES Data Product Catalog, DPC-SFF R5V2, 20 June, 15 pp. [Online], Available: http://ceres.larc.nasa.gov/documents/DPC/DPC_current/pdfs/DPC_SFF-Ed3_R5V2.pdf

Chakrapani, V., D. R. Doelling, A. D. Rapp, and P. Minnis (2002). Cloud thickness estimation from GOES-8 satellite data over the ARM SGP site. *Proc. 12th ARM Science Team Meeting*, April 8-12, St. Petersburg, FL, 14 pp. Available at http://www.arm.gov/publications/proceedings/conf12/extended_abs/chakrapani-v.pdf?id=34.

Chang, F.-L., P. Minnis, B. Lin, M. Khaiyer, R. Palikonda, and D. Spangenberg (2010). A modified method for inferring cloud top height using GOES-12 imager 10.7- and 13.3-μm data. *J. Geophys. Res.*, 115, D06208, doi:10.1029/2009JD012304.

Chen, Y., P. Minnis, S. Sun-Mack, R. F. Arduini, and Q. Z. Trepte (2010). Clear-sky and surface narrowband albedo datasets derived from MODIS data. *Proc. AMS 13th Conf. Atmos. Rad. and Cloud Phys.*, Portland, OR, June 27 – July 2, JP1.2.

Chen, Y., S. Sun-Mack, P. Minnis, D. F. Young, and W. L. Smith, Jr. (2004). Seasonal surface spectral emissivity derived from Terra MODIS data. *Proc. 13th AMS Conf. Satellite Oceanogr. and Meteorol.*, Norfolk, VA, Sept. 20-24, CD-ROM, P2.4.

Chen, Y., S. Sun-Mack, P. Minnis, and R. F. Arduini (2006). Clear-sky narrowband albedo variations derived from VIRS and MODIS data. *Proc. AMS 12th Conf. Atmos. Radiation*, Madison, WI, July 10-14, CD-ROM, 5.6.

Doelling, D. R. and co-authors (2015). Calibration of historical and future AVHRR and GOES visible and near-infrared sensors Climate Algorithm Theoretical Basis Document (C-ATBD). *NOAA C-ATBD DSR-XXX*, available at NCDC.

Dong, X., P. Minnis, G. G. Mace, W. L. Smith, Jr., M. Poellot, R. T. Marchand, and A. D. Rapp (2002). Comparison of stratus cloud properties deduced from surface, GOES, and aircraft data during the March 2000 ARM Cloud IOP. *J. Atmos. Sci.*, 59, 3256-3284.

Dong, X., P. Minnis, B. Xi, S. Sun-Mack, and Y. Chen (2008). Comparison of CERES-MODIS stratus cloud properties with ground-based measurements at the DOE ARM Southern Great Plains site. *J. Geophys. Res.*, 113, D03204, doi:10.1029/2007JD008438.

Dworak, R., K. M. Bedka, J. Brunner, and W. Feltz (2012). Comparison between GOES-12 overshooting top detections, WSR-88D radar reflectivity, and severe storm reports. *Wea. Forecasting*. **10**, 1811-1822.

Esquerdo, J. C. D. M., J. F. G. Antunes, D. G. Baldwin, W. J. Emery, and J. Zullo, Jr. (2006). An automatic system for AVHRR land surface product generation. *Int. J. Remote Sens.*, 27, 3925–3942.

Foster, M. and A. K. Heidinger (2012). PATMOS-X: Results from diurnally-corrected thirty-year satellite cloud climatology. *J. Climate*, 26, 414-425, doi:10.1175/JCLI-D-11-00666.1.

Frey, R. A., S. A. Ackerman, Y. Liu, K. I. Strabala, H. Zhang, J. Key, and X. Wang (2008). Cloud detection with MODIS. Part I: Recent improvements in the MODIS cloud mask. *J. Atmos. Oceanic Technol.*, 25, 1057-1072.

Frey, R., P. Menzel, and S. Ackerman (2012). Collection 6 algorithm updates, MODIS cloud mask (MOD35) and cloud top pressure (MOD06CT). *MODIS Sci. Team Mtg.*, 8 May. Available at http://modis-atmos.gsfc.nasa.gov/_docs/MODIS_Aqua_C6_Cloud_Mask_Updates.pdf.

Fujita, T. T. (1989). The Teton-Yellowstone Tornado of 21 July 1987. *Monthly Weather Review*, **117**, 1913-1940.

Goldberg, M., G. Ohring, J. Butler, C. Cao, R. Datla, D. Doelling, V. Gärtner, T. Hewison, B. Iacovazzi, D. Kim, T. Kurino, J. Lafeuille, P. Minnis, D. Renaut, J. Schmetz, D. Tobin, L. Wang, F. Weng, X. Wu, F. Yu, P. Zhang, and T. Zhu (2011). The Global Space-based Inter-Calibration System (GSICS). *Bull. Am. Meteorol. Soc.*, 92, 467-475.

Goody, R., R. West, L. Chen, and D. Crisp (1989). The correlated-k method for radiation calculations in nonhomogeneous atmospheres. *J. Quant. Spectrosc. Radiat. Transfer*, 42, 539–550.

Gruber, A. and J. S. Winston (1978). Earth-atmosphere radiative heating based on NOAA scanning radiometer measurements. *Bull. Amer. Meteorol. Soc.*, 59, 1570-1573.

Gustafson, G. B., R. G. Isaacs, R. P. d'Entremont, C. F. Ivaldi, J. Doherty, and C. C. Scott (1994). Support of Environmental Requirements for Cloud Analysis and Archive (SERCAA): Algorithm Descriptions. *AF Phillips Laboratory Technical Report Number PL-TR-94-2114*, Hanscom AFB, MA.

Han, Q., W. B. Rossow, and A. A. Lacis (1994). Near-global survey of effective droplet radii in liquid water clouds using ISCCP data. *J. Climate*, 7, 465-496.

Heidinger, A. K., A. T. Evan, M. J. Foster, and A. Walther (2012). A naïve Bayesian cloud-detection scheme derived from CALIPSO and applied within PATMOS-x. *J. Appl. Meteor. Climatol.*, 51, 1129-1144. Doi:10.1175/JAMC-D-11-02.1.

Heidinger, A. K., M. J. Foster, A. Walther, and X. Zhao (2012), The Pathfinder Atmospheres-Extended dataset. *Bull. Amer. Meteorol. Soc.*, 93,909-922.

Heidinger, A. K. and M. J. Pavolonis (2005). Global daytime distribution of overlapping cirrus cloud from NOAA's Advanced Very High Resolution Radiometer. *J. Climate*, 18, 4772-4784.

Heymsfield, G. M., and R. H., Blackmer (1988). Satellite-observed characteristics of Midwest severe thunderstorm anvils. *Monthly Weather Review*, **116**, 2200-2224.

Heymsfield, G.M., R. Fulton, and J.D. Spinhirne (1991). Aircraft overflight measurements of Midwest severe storms: Implications and geosynchronous satellite interpretations. *Mon. Wea. Rev.*, **119**, 436–456.

Holz, R., S. Platnick, K. Meyer, M. Vaughan, A. Heidinger, P. Yang, G. Wind, S. Dutcher, S. Ackerman, N. Amarasinghe, F. Nagle, and C. Wang (2015). Resolving ice cloud optical thickness biases between CALIOP and MODIS using infrared retrievals. *Atmos. Chem. Phys. Discuss.*, 15, 29455-29495, doi:10.5194/acpd-15-29455-2015.

Jin, Z., T. P. Charlock, K. Rutledge, K. Stamnes, and Y. Wang (2006). Analytical solution of radiative transfer in the coupled atmosphere-ocean system with a rough surface. *Appl. Opt.*, 45, 7443-7455.

Karlsson, K.-G., A. Rühelä, R. Müller, J. F. Meirink, J. Sedlar, M. Stengel, M. Lockhoff, J. Trentman, F. Kaspar, R. Hollmann, and E. Wolters, (2013). CALARA-A1: a cloud, albedo, and radiation dataset from 28 yr of global AVHRR data. *Atmos. Chem. Phys.*, 13, 5351-5367, doi:10.5195/acp-13-5351-2013.

Kellenbenz, D. J., T. J. Grafenauer, and J. M. Davies (2007). The North Dakota Tornadic Supercells of 18 July 2004: Issues Concerning High LCL Heights and Evapotranspiration. *Weather and Forecasting*, **22**, 1200-1213.

Kratz, D. P. (1995). The correlated k-distribution technique as applied to the AVHRR channels. *J. Quant. Spectrosc. Radiat. Transfer*, 53, 501–507.

Kriebel, K. T. (1978). Measured spectral bidirectional reflection properties of four vegetated surfaces. *Appl. Opt.*, 17, 253–259.

Kummerrow, C., W. Barnes, T. Kozu, J. Shuie, and J. Simpson (1998). The Tropical Rainfall Measuring Mission (TRMM) sensor package. *J. Atmos. Tech.*, 15, 808-816.

Loeb, N. G., N. Manalo-Smith, S. Kato, W. F. Miller, S. Gupta, P. Minnis, and B. A. Wielicki, 2003: Angular distribution models for top-of-atmosphere radiative flux estimation from the Clouds and the Earth's Radiant Energy System instrument on the Tropical Rainfall Measuring Mission satellite. Part I: Methodology. *J. Appl. Meteorol.*, 42, 240-265.

Liu, C., P. Yang, P. Minnis, N. Loeb, A. Heymsfield, and C. Schmitt (2014). A two-habit model for the microphysical and optical properties of ice clouds. *Atmos. Chem. Phys.*, 14, 13719-13737, doi: 10.5194/acp-14-13719-2014.

Luo, Y., A. P. Trishchenko, and K. V. Khlopenkov (2008). Developing clear-sky, cloud and cloud shadow mask for producing clear-sky composites at 250-meter spatial resolution for the seven MODIS land bands over Canada and North America. *Remote Sens. Environ.*, 112, 4167–4185.

Mace, G. G., T. P. Ackerman, P. Minnis, and D. F. Young (1998). Cirrus layer microphysical properties derived from surface-based millimeter radar and infrared interferometer data. *J. Geophys. Res.*, 103, 23,207-23,216.

Mace, G. G. and Q. Zhang (2014). The CloudSat radar-lidar geometrical profile product (RL-GEOPROF): Updates, improvements, and selected results. *J. Geophys. Res.*, 119, 9441-9462, doi:10.1002/2013JD021374.

Mace, G. G., Y. Zhang, S. Platnick, M. D. King, P. Minnis, and P. Yang (2005). Evaluation of cirrus cloud properties from MODIS radiances using cloud properties derived from ground-based data collected at the ARM SGP site. *J. Appl. Meteorol.*, 44, 221-240.

Min, Q, P. Minnis, and M. M. Khaiyer (2004). Comparison of cirrus optical depths from GOES-8 and surface measurements. *J. Geophys. Res.*, 109, D20119, 10.1029/2003JD004390.

Minnis, P. and E. F. Harrison (1984). Diurnal variability of regional cloud and clear-sky radiative parameters derived from GOES data, Part III: November 1978 radiative parameters. *J. Clim. Appl. Meteorol.*, **23**, 1032-1052.

Minnis, P. (1989). Viewing zenith angle dependence of cloudiness determined from coincident GOES East and GOES West data. *J. Geophys. Res.*, 94, 2303-2320.

Minnis, P., D. F. Young, K. Sassen, J. M. Alvarez, and C. J. Grund (1990a). The 27-28 October 1986 FIRE IFO Case Study: Cirrus parameter relationships derived from satellite and lidar data. *Mon. Wea. Rev.*, **118**, 2402 - 2425.

Minnis, P., P. W. Heck, and E. F. Harrison (1990b). The 27-28 October 1986 FIRE IFO Case Study: Cloud parameter fields derived from satellite data. *Mon. Wea. Rev.*, 118, 2426-2446.

Minnis, P., D. F. Young, and E. F. Harrison (1991). Examination of the relationship between infrared window radiance and the total outgoing longwave flux using satellite data. *J. Climate*, 4, 1114-1133.

Minnis, P., P. W. Heck, D. F. Young, C. W. Fairall, and J. B. Snider (1992). Stratocumulus cloud properties derived from simultaneous satellite and island-based instrumentation during FIRE. *J. Appl. Meteorol.*, 31, 317-339.

Minnis, P., Y. Takano, and K.-N. Liou (1993). Inference of cirrus cloud properties using satellite-observed visible and infrared radiances, Part I: Parameterization of radiance fields. *J. Atmos. Sci.*, 50, 1279-1304.

Minnis, P., D. P. Kratz, J. A. Coakley, Jr., M. D. King, D. Garber, P. Heck, S. Mayor, D. F. Young, and R. Arduini (1995). Cloud Optical Property Retrieval (Subsystem 4.3). Clouds and the Earth's Radiant Energy System (CERES) Algorithm Theoretical Basis Document; Cloud Analyses and Radiance Inversions (Subsystem 4). *NASA RP 1376*; CERES Science Team, Ed.; NASA: 1995; Vol. 3, pp. 135–176.

Minnis, P., D. P. Garber, D. F. Young, R. F. Arduini, and Y. Takano (1998). Parameterization of reflectance and effective emittance for satellite remote sensing of cloud properties. *J. Atmos. Sci.*, 55, 3313-3339.

Minnis, P. and W. L. Smith, Jr. (1998). Cloud and radiative fields derived from GOES-8 during SUCCESS and the ARM-UAV Spring 1996 Flight Series. *Geophys. Res. Lett.*, 25, 1113-1116.

Minnis, P., A. V. Gambheer, and D. R. Doelling (2004), Azimuthal anisotropy of longwave and infrared window radiances from CERES TRMM and Terra data. *J. Geophys. Res.*, 109, D08202, doi:10.1029/2003JD004471.

Minnis, P., Q. Z. Trepte, S. Sun-Mack, Y. Chen, D. R. Doelling, D. F. Young, D. A. Spangenberg, W. F. Miller, B. A. Wielicki, R. R. Brown, S. C. Gibson, and E. B. Geier (2008a). Cloud detection in non-polar regions for CERES using TRMM VIRS and Terra and Aqua MODIS data. *IEEE Trans. Geosci. Remote Sens.*, 46, 3857-3884.

Minnis, P., C. R. Yost, S. Sun-Mack, and Y. Chen (2008b). Estimating the physical top altitude of optically thick ice clouds from thermal infrared satellite observations using CALIPSO data. *Geophys. Res. Lett.*, **35**, L12801, doi:10.1029/2008GL033947.

Minnis, P., S. Sun-Mack, D. F. Young, P. W. Heck, D. P. Garber, Y. Chen, D. A. Spangenberg, R. F. Arduini, Q. Z. Trepte, W. L. Smith, Jr., J. K. Ayers, S. C. Gibson, W. F. Miller, V. Chakrapani, Y. Takano, K.-N. Liou, Y. Xie, and P. Yang (2011a). CERES Edition-2 cloud property retrievals using TRMM VIRS and Terra and Aqua MODIS data, Part I: Algorithms. *IEEE Trans. Geosci. Remote Sens.*, 49, 4374-4400.

Minnis, P., S. Sun-Mack, Y. Chen, M. M. Khaiyer, Y. Yi, J. K. Ayers, R. R. Brown, X. Dong, S. C. Gibson, P. W. Heck, B. Lin, M. L. Nordeen, L. Nguyen, R. Palikonda, W. L. Smith, Jr., D. A. Spangenberg, Q. Z. Trepte, and B. Xi (2011b). CERES Edition-2 cloud property retrievals using TRMM VIRS and Terra and Aqua MODIS data, Part II: Examples of average results and comparisons with other data. *IEEE Trans. Geosci. Remote Sens.*, 49, 4401-4430.

Minnis, P., et al. (2014). CERES cloud properties: MODIS, VIIRS, GEOsats. 22nd CERES-II Science Team Mtg., Toulouse, France, 7-9 October, 60 pp. Available http://ceres.larc.nasa.gov/documents/STM/2014-10/TUESDAY/CERES/Clouds.CERES.STM.10.14.pdf

A controlled copy of this document is maintained in the CDR Program Library.
Approved for public release. Distribution is unlimited.
131

Mittaz, J. and A. Harris (2011). A physical method for the calibration of the AVHRR/3 thermal IR channels. Part II: An in-orbit comparison of the AVHRR longwave thermal IR channels on board MetOp-A with IASI. *J. Atmos. Oceanic Technol.,* 28, 1072-1087.

Mittaz J., A. Harris, and J. T. Sullivan (2008). A physical method for the calibration of the AVHRR/3 thermal IR channels. Part I: The prelaunch calibration data. *J. Atmos. Oceanic Technol.,* 26, 996-1019.

Moreno, J. F, and J. Meliá (1993). A method for accurate geometric correction of NOAA AVHRR HRPT data. *IEEE Trans. Geosci. Remote Sens.*, 31, 204–226

Painemal, D., P. Minnis, J. K. Ayers, and L. O'Neill (2012). GOES-10 microphysical retrievals in marine warm clouds: Multi-instrument validation and daytime cycle over the Southeast Pacific. *J. Geophys. Res.*, 117, D06203, doi:10.1029/2012JD017822.

Platnick, S., et al. (2014). MOD06 Optical Properties Product. C6 Atmospheres Team Webinar Series, 77 pp. http://modis-atmos.gsfc.nasa.gov/Webinar2014/MODIS_Atmo_Webinar9_Platnick.pdf

Platnick, S., M. D. King, K. G. Meyer, G. Wind, N. Amarasinghe, B. Marchant, G. T. Arnold, Z. Zhang, P. A. Hubanks, B. Ridgway, and J. Riedi (2015). MODIS Cloud Optical Properties: User Guide for the Collection 6Level-2 MOD06/MYD06 Product and Associated Level-3 Datasets. Version 1, 141 pp.

Punge, H. J., A. Werner, K. M. Bedka, M. Kunz, M. Puskeiler (2014). A new physically based stochastic event catalog for hail in Europe. *Natural Hazards,* **73**, 1625-1645

Rao, C. R. N. and J. Chen (1996), Post-launch calibration of the visible and near-infrared channels of the advanced very high resolution radiometer on NOAA-14 spacecraft. *Int. J. Remote Sens.*, 17, 2743–2747.

Reynolds, D.W. (1980). Observations of damaging hailstorms from geosynchronous satellite digital data. *Mon. Wea. Rev.*, 108, 337–348.

Reynolds, R. W., T. M. Smith, C, Liu, D. B. Chelton, K. S. Casey, and M. G. Schlax (2007). Daily high-resolution-blended analyses for sea surface temperature. *J. Climate*, 20, 5473-5496.

Rienecker, M. M., M. J. Suarez, R. Gelaro, R. Todling, J. Bacmeister, E. Liu, M. G. Bosilovich, S. D. Schubert, L. Takacs, G.-K. Kim, S. Bloom, J. Chen, D. Collins, A. Conaty, and A. da Silva, et al. (2011). MERRA - NASA's Modern-Era Retrospective Analysis for Research and Applications. *J. Climate*, 24, 3624-3648, doi:10.1175/JCLI-D-11-00015.1.

Rosborough, G. W., D. G. Baldwin, and W. J. Emery (1994). Precise AVHRR image navigation. *IEEE Trans. Geosci. Remote Sens.*, 32, 644–657.

Rossow, W. B. and R. A. Schiffer (1999). Advances in understanding clouds from ISCCP. *Bull. Amer. Meteorol. Soc.*, 80, 2261-2287.

Scarino, B., P. Minnis, T. Chee, K. M. Bedka, C. R. Yost, and R. Palikonda (2015). Global clear-sky surface skin temperature from multiple satellites using a single-channel algorithm with viewing zenith angle corrections. *Atmos. Meas. Tech.*, submitted.

Scarino, B., P. Minnis, R. Palikonda, R. H. Reichle, D. Morstad, C. Yost, B. Shan, and Q. Liu (2013). Retrieving clear-sky surface skin temperature for numerical weather prediction applications from geostationary satellite data. *Remote. Sens.*, 5, 342-366.

Schmit, T. J., M. M. Gunshor, W. P. Menzel, J. J Gurka, J. Li and A. S. Bachmeier (2005). Introducing the Next-Generation Advanced Baseline Imager on GOES-R. *Bulletin of American Meteorological Society.* **86**, 1079-1096.

Simpson, J. J. and S. R. Yhann (1994). Reduction of noise in AVHRR channel 3 data with minimum distortion, *IEEE Trans. Geosci. Remote Sens.*, 32, 315-328.

Smith, W. L., Jr. (2014). 4-D cloud properties from passive satellite data and applications to resolve the flight icing threat to aircraft, *Ph.D. Dissertation*, Univ. Wisconsin-Madison, Madison, WI, 165 pp. [http://www-pm.larc.nasa.gov/icing/pub/WLS-Dissertation.pdf]

Smith, W. L., P. Minnis, H. Finney, R. Palikonda, and M. M. Khaiyer (2008). An evaluation of operational GOES-derived single-layer cloud top heights with ARSCL over the ARM Southern Great Plains site. *Geophys. Res. Lett.*, 35, L13820, doi:10.1029/2008GL034275.

Stamnes, K., S.-C. Tsay, W. Wiscombe, and K. Jayaweera (1988). Numerically stable algorithm for discrete-ordinate-method radiative transfer in multiscattering and emitting layered media. *Appl. Opt.*, 27, 2502-2509.

Stephens, G. L., D. G. Vane, S. Tanelli, E. Im, S. Durden, M. Rokey, D. Renke, P. Patrtain, G. G> Mace, R. Austin, T. L'Ecuyer, J. Haynes, M. Lebsock, K. Suzuki, D. Waliser, D. Wu, J. Kay, A. Gettelman, Z. Wang, and R. Marchand (2008). CloudSat mission: Performance and early science after first year of operation. *J. Geophys. Res.*, 113, D00A18, doi:10.1029/2008DJ009982.

Stubenrauch, C., W. B. Rossow, S. Kinne, S. Ackerman, G. Cesana, H. Chepfer, B. Getzewich, L. DiGirolamo, A. Guignard, A. Heidinger, B. Maddux, P. Menzel, P. Minnis, C. Pearl, S. Platnick, C. Poulsen, J. Riedi, S. Sun-Mack, A. Walther, D. Winker, S. Zeng, and G. Zhao (2013). Assessment of global cloud datasets from satellites: Project and database initiated by the GEWEX Radiation Panel. *Bull. Am. Meteorol. Soc.*, 94, 1031-1049, doi:10.1175/BAMS-D-12-00117.

Sun-Mack, S., P. Minnis, Y. Chen, S. Kato, Y. Yi, S. Gibson, P. W. Heck, and D. Winker, (2014). Regional apparent boundary layer lapse rates determined from CALIPSO and MODIS data for cloud height determination. *J. Appl. Meteorol. Climatol.,* 53, 990-1011, doi:10.1175/JAMC-D-13-081.1.

Suttles, J. T., R. N. Green, P. Minnis, G. L. Smith, W. F. Staylor, B. A. Wielicki, I. Walker, D. F. Young, V. R. Taylor, and L. L. Stowe (1988). Angular radiation models for Earth-atmosphere system. Vol. I - Shortwave radiation. NASA Langley Res. Center, Hampton, VA, *NASA/RP-1184*, 144 pp.

Trepte, Q., P. Minnis, and R. F. Arduini (2002). Daytime and nighttime polar cloud and snow identification using MODIS data. *Proc. SPIE 3rd Intl. Asia-Pacific Environ. Remote Sensing Symp. 2002: Remote Sens. of Atmosphere, Ocean, Environment, and Space*, Hangzhou, China, October 23-27, Vol. 4891, 449-459.

Trishchenko, A. P. (2002). Removing unwanted fluctuation in the AVHRR thermal calibration data using robust techniques. *J. Atmos. Oceanic Technol.*, 19, 1939-1954.

Trishchenko, A. P., G. Fedosejevs, L. Zhanqing, and J. Cihlar (2002). Trends and uncertainties in thermal calibration of AVHRR radiometers onboard NOAA-9 to NOAA-16. *J. Geophys. Res.*, 107, 4778, doi:10.1029/2002JD002353.

Trishchenko, A. P., and Z. Li (2001). A method for the correction of AVHRR onboard IR calibration in the event of short-term radiative contamination. *Int. J. Remote Sens.*, 22, 3619– 3624.

Walton, C. C., J. T. Sullivan, C. R. N. Rao, and M. P. Weinreb (1998). Corrections for detector nonlinearities and calibration inconsistencies of the infrared channels of the Advanced Very High Resolution Radiometer. *J. Geophys. Res.*, 103, 3323–3337.

Wentz, F. J. (1997). A well-calibrated ocean algorithm for the special sensor microwave/imager. *J. Geophys. Res.*, 102, No. C4, 8703-8718.

Wentz, F. J. and T. Meissner (2000). AMSR ocean algorithm. Algorithm Theoretical Basis Doc. 121599A-1, Remote Sensing Systems, Santa Rosa, CA, 74 pp. [Available online at http://eospso.gsfc.nasa.gov/sites/default/files/atbd/atbd-amsr-ocean.pdf.]

Wielicki, B. A., B. R. Barkstrom, B. A, Baum, T. P. Charlock, R. N. Green, D. P. Kratz, R. B. Lee, P. Minnis, G. L. Smith, D. F. Young, R. D. Cess, J. A. Coakley, D. A. H. Crommelynck, L. Donner, R. Kandel, M. D. King, A. J. Miller, V. Ramanathan, D. A. Randall, L. L. Stowe, and R. M. Welch (1998). Clouds and the Earth's Radiant Energy System (CERES): Algorithm Overview. *IEEE Trans. Geosci. Rem. Sens.*, 36, 1127-1141.

Wielicki, B. A. and L. Parker (1992). On determination of cloud cover from satellite sensors: the effect of sensor spatial resolution. *J. Geophys. Res.*, 97, 12799-12823.

Wilber, A., D. P. Kratz, and S. Gupta (1999). Surface emissivity maps for use in satellite retrievals of longwave radiation. NASA Tech. Rpt., NASA/TP-1999-209362, L-17861, NAS 1.60:209362, 32 pp.

Winker, D. M., W. H. Hunt, and M. J. McGill (2007). Initial performance assessment of CALIOP, *Geophys. Res. Lett.*, 34, L19803, doi:10.1029/2007GL030135.

WMO/TD-1338 GCOS (2006). Systematic Observation Requirements for Satellite-Based Products for Climate: Supplemental Details to the Satellite-Based Component of the "Implementation Plan for the Global Observing System for Climate in Support of the UNFCC (GCOS-92)," vol. GCOS-107, p. 103, 2006, Sep. [Online]. Available: http://www.wmo.int/pages/prog/gcos/Publications/gcos-107.pdf

Wolfe, R. E., M. Nishihama, A. J. Fleig, J. A. Kuyper, D. P. Roy, J. C. Storey, and F. S. Patt (2002). Achieving sub-pixel geolocation accuracy in support of MODIS land science. *Remote Sens. Environ.*, 83, 31–49.

Xie, Y., P. Yang, G. W. Kattawar, P. Minnis, Y. Hu, and D. Wu (2012). Determination of ice cloud models using MODIS and MISR data. *Intl. J. Remote. Sens.*, 33, 4219-4253, doi:10.1080/01431161.2011.642323.

Yang, P., G. W. Kattawar, G. Hong, P. Minnis, and Y. X. Hu (2008a). Uncertainties associated with the surface texture of ice particles in satellite-based retrieval of cirrus clouds: Part I. Single-scattering properties of ice crystals with surface roughness. *IEEE Trans. Geosci. Remote Sens.*, 46, 1940-1947, doi:10.1109/TGRS.2008.916471.

Yang, P., G. W. Kattawar, G. Hong, P. Minnis, and Y. X. Hu (2008b). Uncertainties associated with the surface texture of ice particles in satellite-based retrieval of cirrus clouds: Part II. Effect of particle surface roughness on retrieved cloud optical thickness and effective particle size. *IEEE Trans. Geosci. Remote Sens.*, 46, 1948-1957, doi:10.1109/TGRS.2008.916472.

Young, D. F., P. Minnis, D. Baumgardner, and H. Gerber (1998). Comparison of in situ and satellite-derived cloud properties during SUCCESS. *Geophys. Res. Lett.*, 25, 1125-1128.

Yu, Y., D. Tarpley, and H. Xu (2012). GOES-R Advanced Baseline Imager (ABI) Algorithm Theoretical Basis Document for Land Surface Temperature. NOAA NESDIS Star GOES-R ATBD, Version 2.5, 30 July, 93 pp. Available at [http://www.star.nesdis.noaa.gov/goesr/docs/ATBD/LST.pdf]

Zhang, Z. and S. Platnick (2011). An assessment of differences between cloud effective particle radius retrievals for marine water clouds from three MODIS spectral bands. *J. Geophys. Res.*, 116, D20215, doi:10.1029/2011JD016216.

A controlled copy of this document is maintained in the CDR Program Library.
Approved for public release. Distribution is unlimited.
135

Appendix A.   Acronyms and Abbreviations

Modify the following table to include all acronyms and abbreviations appearing in this document.

Acronym or Abbreviation	Definition
ABI	Advanced Baseline Imager
AD	Adding Doubling
ADM	Angular Distribution Model
AMSR-E	Advanced Microwave Scanning Radiometer for EOS
ARM	Atmospheric Radiation Measurement
ATBD	Algorithm Theoretical Basis Document
AVHRR	Advanced Very-High Resolution Radiometer
BB	Broadband
BRDF	Bidirectional Reflectance Distribution Function
BT	Brightness Temperature
BTD	Brightness Temperature Difference
C-ATBD	Climate Algorithm Theoretical Basis Document
CALIPSO	Cloud-Aerosol Lidar and Infrared Pathfinder Satellite Observation
CCPRS	CERES Cloud Mask and Cloud Property Retrieval System
CDR	Climate Data Record
CBH	Cloud Base Height
CEH	Cloud Effective Height
CEP	Cloud Effective Pressure
CER	Cloud Effective Radius
CERES	Clouds and the Earth's Radiant Energy System
CET	Cloud Effective Temperature
CKD	Correlated k-Distribution
CLARA-A1	CLoud, Albedo and RAdiation dataset, AVHRR Version 1
CLASS	Comprehensive Large Array-data Stewardship System
COD	Cloud Optical Depth
CRH	Column-Weighted Relative Humidity
CTH	Cloud Top Height
CTP	Cloud Top Pressure
CTT	Cloud Top Temperature
DOE	U.S. Department of Energy
DRM	Directional Reflectance Model
ECT	Equatorial Crossing Time
ERBE	Earth Radiation Budget Experiment

A controlled copy of this document is maintained in the CDR Program Library.
Approved for public release. Distribution is unlimited.
136

EUMETSAT	European Organization for the Exploitation of Meteorological Satellites
FCDR	Fundamental Climate Data Record
FFT	Fast Fourier Transform
EOS	Earth Observing System
GAC	Global Area Coverage
GEOPROF	Geometrical Profile
GEOS	GMAO Global Earth Observing System
GMAO	Global Modeling Assimilation Office
GOES	Geostationary Operational Environmental Satellite
GPFS	General Parallel File System
HDF	Hierarchical Data Format
HPC	High Performance Computing
HRPT	High Resolution Picture Transmission
IGBP	International Geosphere-Biosphere Programme
IJPS	International Joint POES System
IRW	Infrared Window (10.8 µm)
IR	Infrared
ISCCP	International Satellite Cloud Climatology Project
IWP	Ice Water Path
LAC	Local Area Coverage
LaRC	Langley Research Center
LAT	Latitude (°)
LBTM	Layer Bispectral Threshold Method
LON	Longitude (°)
LUT	Look Up Table
LW	Longwave (5 – 50 µm)
LWP	Liquid Water Path
MAST	MODIS Atmosphere Science Team
McIDAS	Man-Computer Interactive Data Access System
MERRA	Modern Era Retrospective Analysis for Research and Applications
MetOp	Meteorological Operational Polar Satellite
MODIS	Moderate Resolution Imaging Spectroradiometer
NCDC	National Climate Data Center
NASA	National Aeronautics and Space Administration
NetCDF	Network Common Data Format
NIR	Near Infrared (~1.6 µm)
NOAA	National Oceanic and Atmospheric Administration
NORAD	North American Aerospace Defense Command
NWA	Numerical Weather Analysis

PATMOS-X	Pathfinder Atmospheres Extended
POES	Polar Orbiting Environmental Satellite
OISST	Optimal Interpolation Sea Surface Temperature product
OLR	Outgoing Longwave Radiation
OT	Overshooting Convective Cloud Top
PW	Precipitable Water
RAA	Relative Azimuth Angle
RGB	Red-Green-Blue Image Composite
RL	Radar-Lidar
RMS	Root-Mean-Square
RMSD	Root-Mean-Square Difference
SAPS	SSAI AVHRR Processing System
SatCORPS-A	Satellite ClOud and Radiative Property retrieval System-AVHRR
SBAF	Spectral Band Adjustment Factor
SBBC	Solar Blackbody Contamination
SDD	Standard Deviation of Differences
SF	Snow and Ice Free
SFC	Surface Fluxes and Clouds product
SI	Snow or Ice Covered
SINT	Shortwave-infrared Infrared Near-infrared Technique
SIST	Shortwave-infrared Infrared Split-window Technique
SIR	Shortwave InfraRed (~3.75 μm)
SIRT	Shortwave-infrared Infrared-window Technique
SST	Sea Surface Temperature
SURFRAD	Surface Radiation
SW	Shortwave (0.2 – 5 μm)
SWI	Split Window Infrared (~12.0 μm)
SZA	Solar Zenith Angle
TBUS	NOAA Automatic Picture Transmission Predict Bulletins
TCDR	Thematic Climate Data Record
TLE	Two-Line Element
TOA	Top Of Atmosphere
TIROS	Television InfraRed Observation Satellite
TRMM	Tropical Rainfall Measurement Mission
UTC	Coordinated Universal Time
VIRS	Visible and Infrared Scanner
VIIRS	Visible Infrared Imager Radiometer Suite
VINST	Visible Infrared Near-infrared Split-window Technique
VINT	Visible Infrared Technique
VIS	Visible (~0.64 μm)

| VISST | Visible Infrared Shortwave-infrared Split-window Technique |
| VZA | Viewing Zenith Angle |

Appendix B.   AVHRR pre-processing software, SAPS

Within the AVHRR GAC Level 1B data acquired from CLASS, there is a set of quality indicators included for each scan line that identify potentially bad data. The following link provides a list of quality indicators for NOAA-6 through NOAA-14 AVHRR, *http://www.ncdc.noaa.gov/oa/pod-guide/ncdc/docs/podug/html/c3/sec3-1.htm - t3121-2*. The following link provides a list of these flags for NOAA-15 through MetOp-B, *http://www.ncdc.noaa.gov/oa/pod-guide/ncdc/docs/klm/html/c8/sec83143-1.htm*. If a scan line is flagged as bad, missing values are assigned to the solar channel raw counts and IR BTs and the SatCORPS-A will not process these data. Currently, SAPS does not monitor the following five flags in the NOAA-6 to -14 Level 1B data: Pseudo Noise STATUS, ASCEND/DSCEND, CHANNEL 5 Solar Blackbody Contamination (SBBC), CHANNEL 4 SBBC, and CHANNEL 3 SBBC. The following flags are not monitored for NOAA-15 through MetOp-B: bits 6-7 and 28 of the Quality Indicator Bit Field, bits 11-15 of the Calibration Problem Code; bits 6-7 of the Calibration Quality Flags for channels 3B, 4, and 5. These flags were often found where seemingly valid data were present so there was no need to exclude these data from processing.

The navigation correction component of this software is described in detail by Khlopenkov et al. (2010) but a brief summary is provided below. The major reason for AVHRR navigation error is that critical parameters for determining pixel navigation, such as the satellite state vector, sensor attitude angles, and time of image acquisition (satellite clock error), are not known with sufficient accuracy at any particular moment (Rosborough et al. 1994; Morena and Melia, 2003; Esquerdo et al. 2006). Figure B.1 shows a schematic of the three satellite attitude angles and the navigation errors that can arise if these angles are incorrectly specified. The international community has identified the requirement for geolocation accuracy for satellite climate data records (SCDRs) as 1/3 FOV (CEOS 2006; WMO 2006). AVHRR navigation errors can be quite significant, up to 200 km error or more. Accurate navigation is critical to the SatCORPS-A to ensure that input data such as clear sky
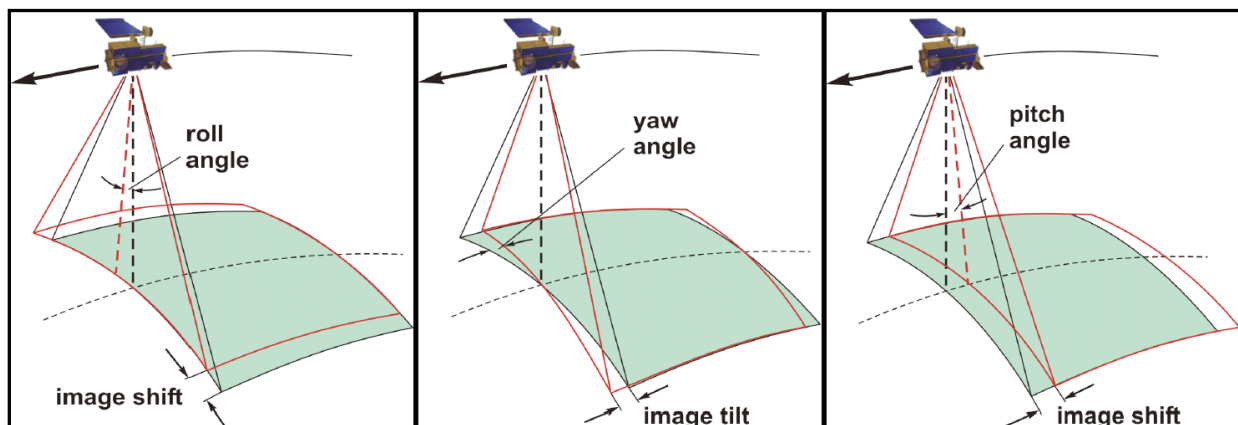

Figure B.1: Schematic demonstrating impact of errors in sensor attitude angles on satellite image navigation.

albedo and temperature, and other input data are correctly associated with a given satellite pixel. In addition, accurate navigation is critical for studying regional climate trends in that a few poorly navigated scenes can contaminate derived trends.

The navigation correction scheme was initially developed for AVHRR 1 km HRPT data but was adapted to operate on the 4-km GAC data. MODIS 250-m Level 1B granules taken during the 2005-2007 period were used to create 10-day clear-sky composite maps over a North America (see Figure B.2), Eastern Asia, Europe, and Africa based on the methodology of Luo et al. (2008). The resulting maps were combined into 12 monthly super-composite maps that are used by SAPS as reference maps for image matching and subsequent navigation correction. The navigation accuracy for the MODIS 250-m Level 1B imagery is about 50 m (Wolfe et al. 2002), which is suitable enough to achieve sub-pixel accuracy for AVHRR. Ground control points (GCP) are defined in the reference maps by an automated search for points of locally high variance of reflectance, which correspond to distinct surface features such as lakes, coastlines, and sharp land surface cover changes.

The GAC swath data are first geo-referenced using the nominal North American Aerospace Defense Command (NORAD) or NOAA Automatic Picture Transmission Predict Bulletins (TBUS) two line element (TLE) orbital parameters and assuming zero attitude angles. Then the VEG (day) or IRW (night) channel scenes are matched at the GCP locations against a corresponding reference map. A filtering algorithm sorts out well-matched GCPs, thus discarding areas of cloud contamination, to yield a set of displacement vectors required to correct the AVHRR image displacement. Each displacement vector is corrected for the local land surface elevation (so called ortho-correction or parallax correction). These vectors are then used solve the inverse problem of finding the attitude angles and correcting the satellite orbital parameters to adjust the instant satellite position. With the new satellite position and attitude angles, the geo-referencing for each AVHRR pixel is recomputed to repeat the image matching and navigation correction. The process includes several iterations until the displacement vectors reduce to sufficiently low values.

Figure B.3 shows the ground control points selected for a scene over North America. Matching the GCP composite with observations in Figure B.4 reveals that the initial error for the scene was ~3 pixels on average along the scan line (Figure B.4a). The standard deviation of the error reduces to 0.124 pixels after correcting each angle through iterative ground control point matching. The results of each step are shown in Figure B.4b-d. Testing reveals that the navigation accuracy is 0.15 to 0.20 GAC pixelS, which equates to a distance of ~500 m. Figure B.5a-b shows an extreme navigation correction for a NOAA-18 GAC image over southeastern Asia. Given the coverage of four GCP domains across the globe, it is highly unlikely that an AVHRR orbit will not pass over any of these domains. When no satisfactory GCP matches are found in an AVHRR granule (because of cloudy scenes or poor coverage of across the four GCP domains), the nominal NORAD orbital parameters are used.
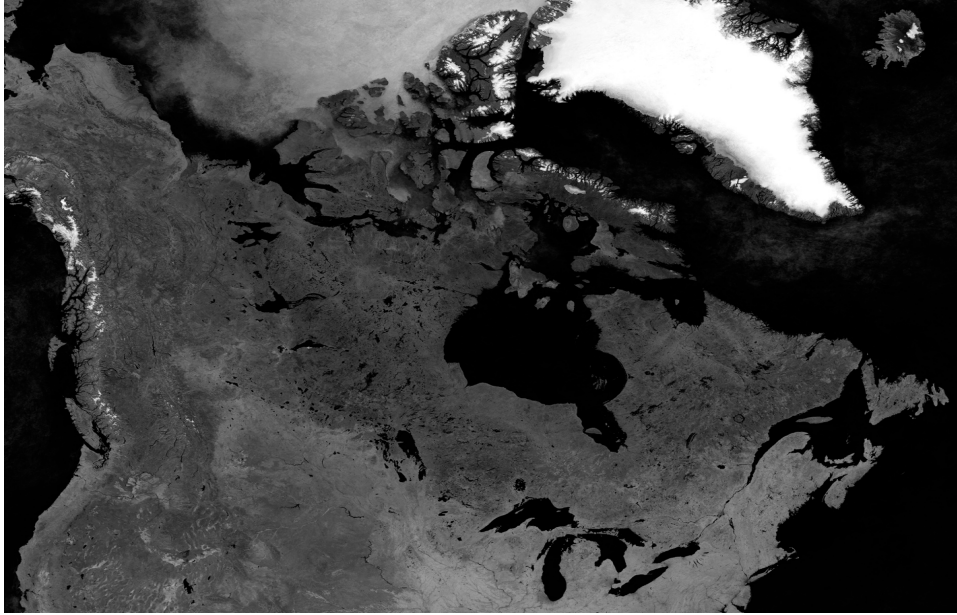
Figure B.2: Example of 0.86-µm clear-sky reference map derived from MODIS 250-m data during August 2005-2007 over the North American domain used in the SAPS navigation correction module.
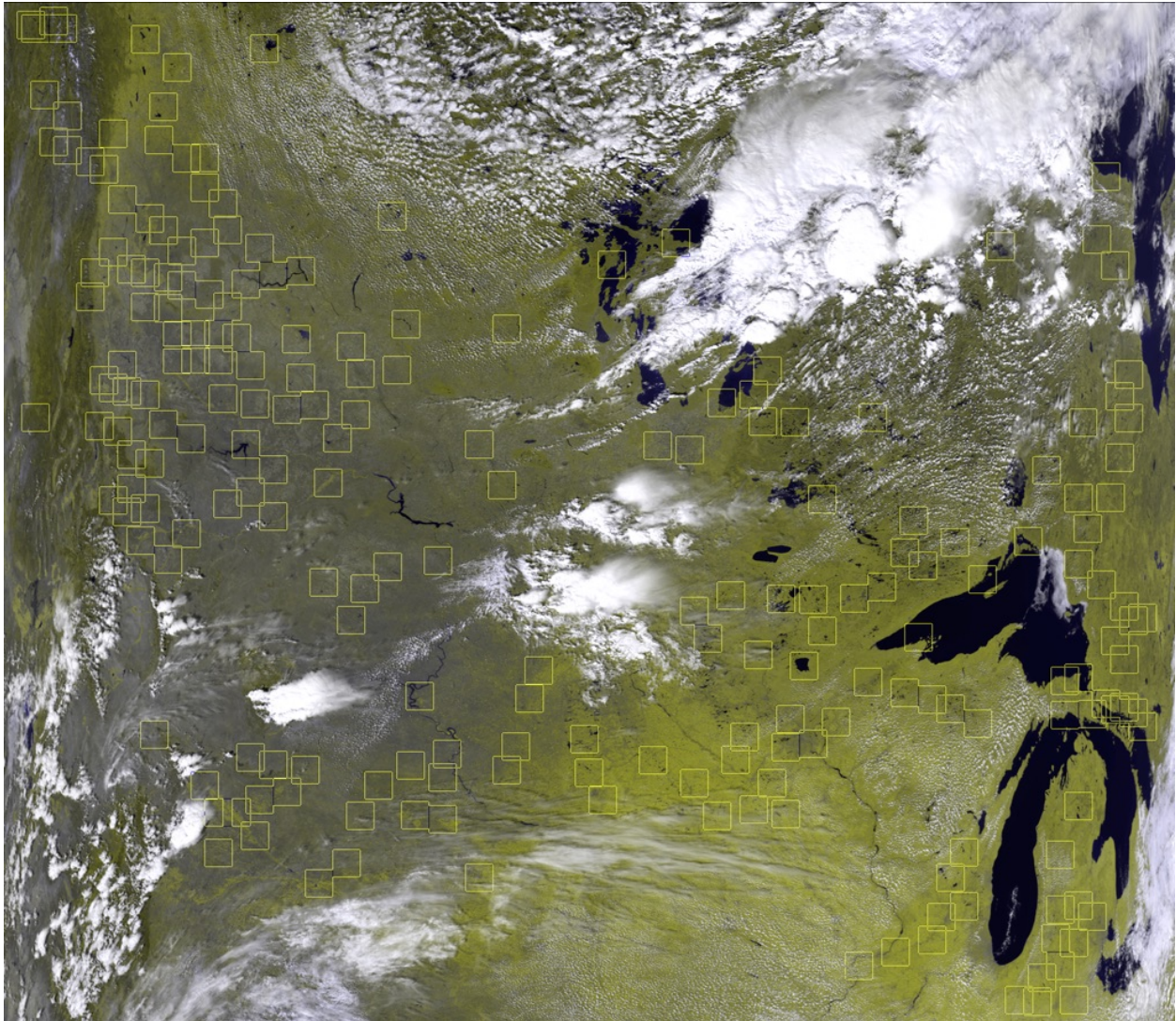
A controlled copy of this document is maintained in the CDR Program Library.
Approved for public release. Distribution is unlimited.
142

Figure B.3: Multispectral NOAA-18 AVHRR scene overlaid with the ground control points (yellow boxes) used in navigation correction.
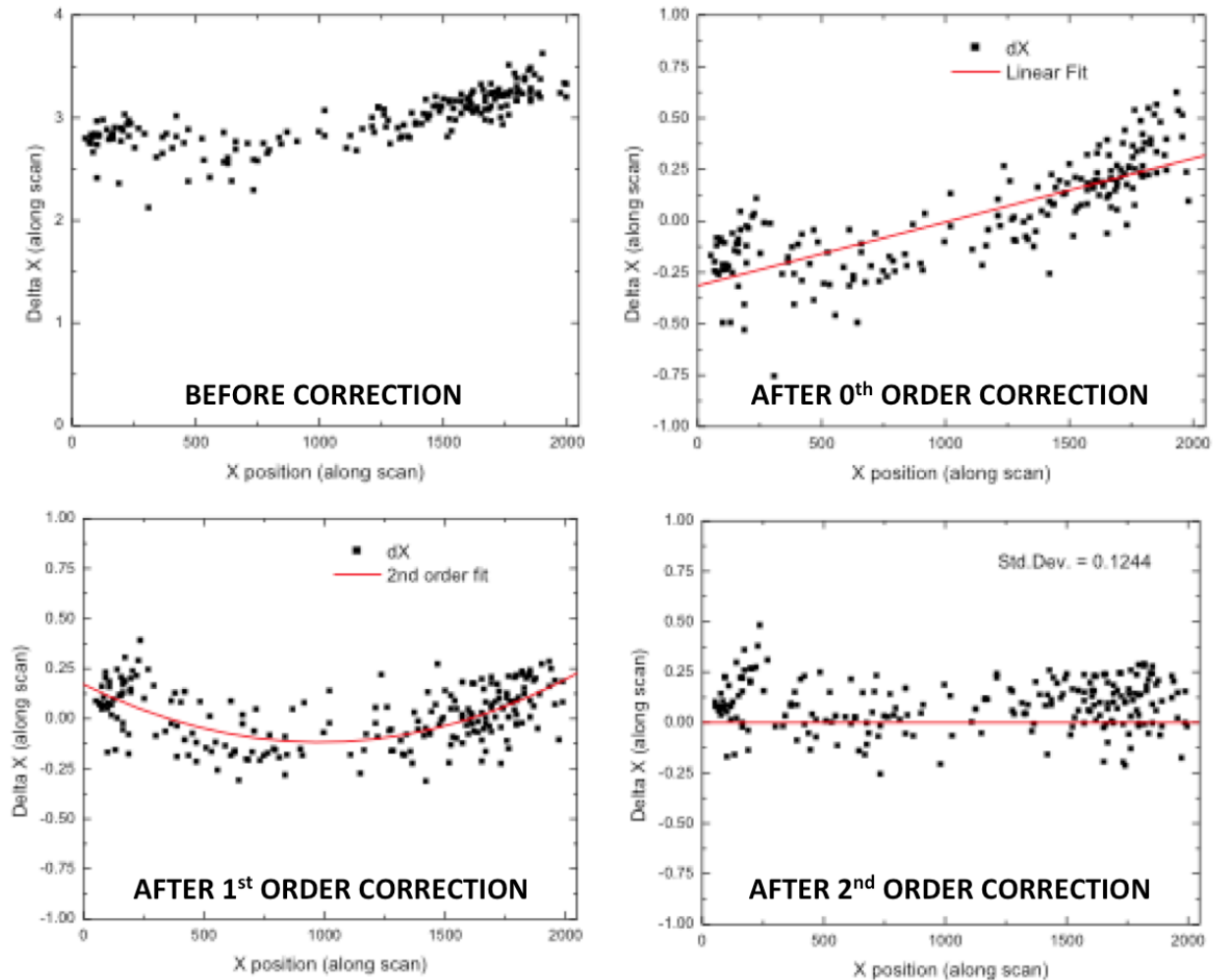
Figure B.4: Distribution of AVHRR navigation error for various ground control point matches along satellite scan direction for a selected AVHRR orbit. X-axis: AVHRR HRPT pixel position within the scan line. Y-axis: magnitude of navigation error oriented along the scan line (i.e. crossing the satellite track). Navigation error oriented along the satellite track is not shown. Improvements in navigation with each iteration of the correction routine are shown the panels. 0th-order correction: satellite roll angle adjustment. 1st-order correction: accounts for errors in satellite altitude and/or angular scan range (i.e., yaw angle). 2nd-order correction: accounts for pitch angle errors, which are equivalent to a time delay that results in a clock difference between the scan line timing & the Earth rotation. Note, change in y-axis scales from "before correction" to "after correction" panels.
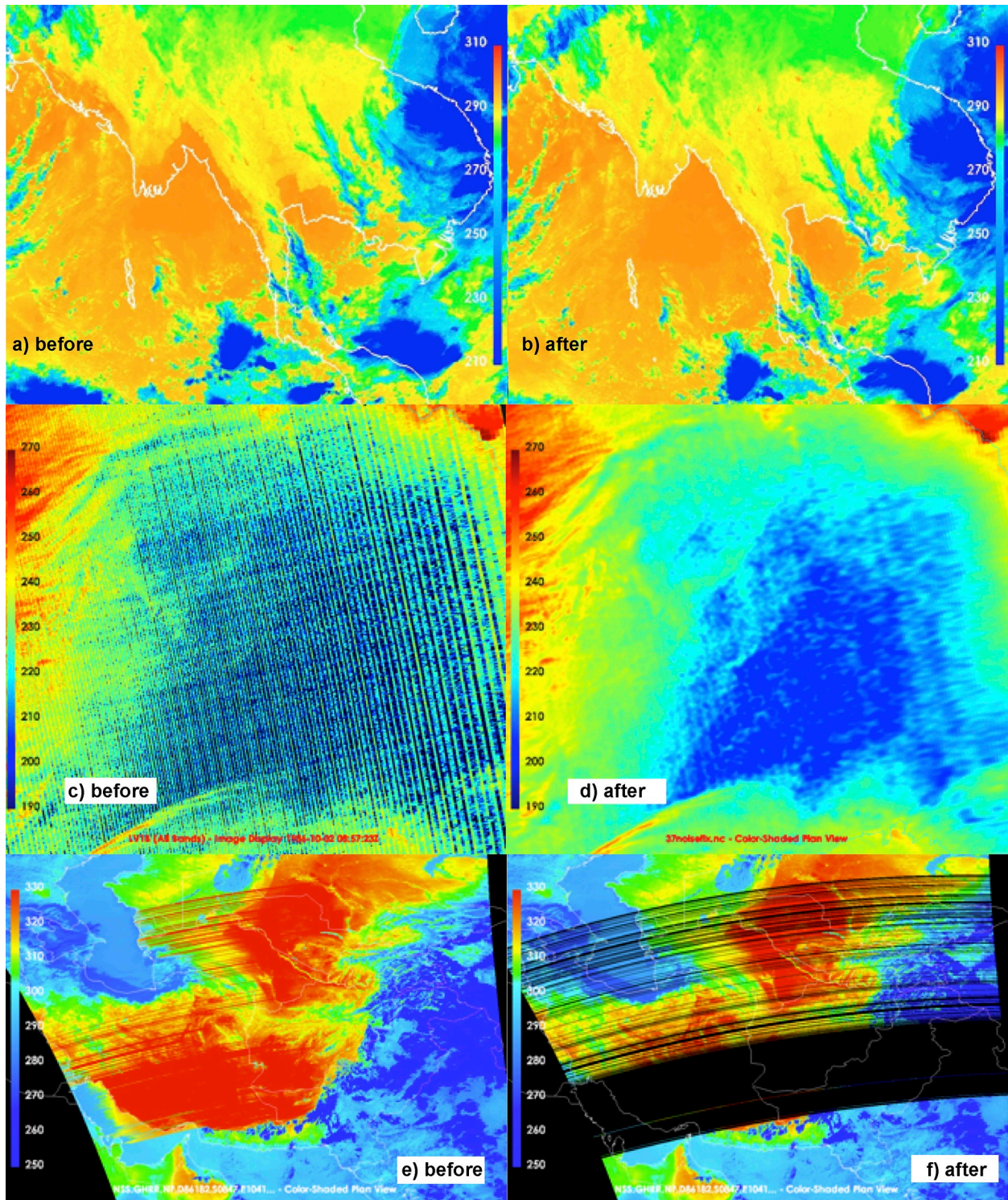
Figure B.5: Images highlighting AVHRR Level 1B data problems addressed by AVHRR pre-processing software. Color-enhanced NOAA-18 AVHRR 10.8-μm BT imagery over southeast Asia (a) before and (b) after navigation correction. The BT gradient in this scene associated with land/ocean temperature differences

should align with the coastlines (white lines). Color-enhanced NOAA-9 AVHRR 3.74-µm imagery over Antarctica (c) before and (d) after noise filtering. Color-enhanced NOAA-9 AVHRR 12.0-µm imagery over Central Asia (e) before and (f) after bad scan line detection.

NOAA-6 to -14 AVHRR SIR data exhibit two significant problems, 1) periodic noise (i.e. striping) oriented along the satellite track and 2) randomly oriented noise for BT < 255 K. A graphical example of these problems is shown in Figure B.5c-d for a scene over Antarctica. If not addressed, the degree of noise in this scene would significantly inhibit accurate cloud property retrieval.

The periodic noise is identified and suppressed by Fast Fourier Transform (FFT) analysis. An AVHRR GAC orbit is divided and processed in rectangular subsets, each having dimensions of 108 pixels and 128 lines. The number of pixels must be evenly divisible by 2 and 3 but the number of lines can only be divisible by 2 for the FFT method to operate. To accomplish this with AVHRR GAC data with 409 pixels per scan line, the subsets are selected to provide three-pixel overlap horizontally (i.e. along scan line and across satellite track) and two-line overlap in vertical direction (along satellite track). Horizontally, there are four subsets covering the following pixels:

1) Pixel range: -1…106 (with padding on the left by linear extrapolation), and   1…103 are saved to the final output;

2) Pixel range: 101…208, and 104…205 are used for output;

3) Pixel range: 203…310, and 206…307 are used for output;

4) Pixel range: 305…412 (with padding on the right by linear extrapolation), 308…409 are used for output.

The overlapping is similarly organized in the vertical direction. The last subset is padded at the bottom to make its height equal to 128. The forward 2-dimensional FFT produces a frequency matrix of complex numbers. In this matrix, only the top line is corrected, which corresponds to zero-frequency in the vertical direction. Thus, only horizontal oscillations along the scan line are affected which is the characteristic orientation of the oscillations illustrated by Figure 8 (middle left). The FFT analysis operates on the AVHRR raw counts so the maximum power of stripe-free observations should be < 1000. For noisy pixels, the power can be much higher, approaching 5000 or greater. The power in the spatial frequencies of 25, 39, and 43 is scaled down to the level of 1200, a number that has been effective for minimizing the noise while preserving good signal throughout the remainder of the rectangular subset. A frequency of N means N half-periods of oscillation per image width (that equals 108), thus the periodicity of the striping ranges from ~4-8 pixels. Once the Fourier spectrum is corrected, the inverse FFT is applied to obtain a filtered image.

At the low end of its dynamic range, the AVHRR SIR channel is plagued by increasing random noise with decreasing temperatures. Prior to filtering, a LUT is generated from the onboard thermal calibration to convert raw counts to BT. The last meaningful point in the

LUT is count 994, corresponding to BT ≈ 193 K. The following provides a sample of the SIR raw count to BT calibration table for counts 992-996:

992 count: 213.83K

993 count: 207.44K

994 count: 193.34K

995 count and further: missing value

However, the actual data may contain sometime raw counts of 995 and (rarely) 996, which end up with missing values when converted to BT. Because spatial smoothing tends to average the BT values, our algorithm linearly extrapolates the LUT by one step and assigns the extrapolated value to the raw counts, 995 and 996.

Spatial smoothing is based on a 2-dimensional cubic convolution algorithm with a Gaussian kernel. The Gaussian profile defines the weights for the neighboring pixels: the further from the current pixel, the lower the weight. Thus, the characteristic sigma of the kernel determines the strength of the smoothing. The smoothing routine works as follows:

1) Fill in all missing values with the average of the nearest neighbors.

2) Perform convolution with sigma=4 and produce an averaged image (referred to as AI4).

3) The strength of the spatial smoothing is determined by the pixel BT in AI4. If BT < 214 K, then the second convolution is applied to AI4 with sigma=4 for BT < 200 K, sigma=3 for 200 ≤ BT< 202 K, sigma=2 for 202 ≤ BT < 205 K, sigma=1.5 for 205 ≤ BT<209 K, or sigma=1 for 209 ≤ BT <214 K.

The convolution is applied to the original image with sigma=4 for 214 ≤ BT <220 K, sigma=3 for 220 ≤ BT <227 K, sigma=2 for 227 ≤ BT <235 K, sigma=1.5 for 235 ≤ BT < 243 K, or sigma=1 for 243 ≤ BT <255 K.

This approach using a variable smoothing strength provides for minimal alteration of the original data in the areas of weak noise, but a sufficient reduction of the random noise for the lower range of SIR BTs.

Areas of corrupt data across several scan lines have been observed in NOAA-9 data at the high end of the SWI BT range (e.g., Figure B.5e). Also, some isolated noise pixels not marked by the Quality Indicator flags have been noted in the 10.8 and 12.0 μm channels. To overcome this problem, a special algorithm has been developed to detect and discard corrupt scan lines and noisy pixels. The algorithm uses 3 metrics to determine if a scanline contains noise: (1) sum of square differences (SSD) between neighboring pixels within one scan line; (2) SSD of pixel pairs between neighboring lines, and (3) SSD between pixels in the same line of the IRW and SWI images. Each of these metrics is required to change gradually from line to line as it would in uncorrupted data. The algorithm determines if the 2nd derivative of each metric exceeds a certain threshold, in which case, the problematic scan line is further analyzed to detect any pixels that are too different from the average of

their neighbors. If only a few of such pixels are found, then they are replaced with the average of their neighbors. Otherwise the whole line is marked as a bad scan line and filled with missing values. Figure B.5f shows the result of this noise filtering where scan lines with bad data are filled with missing values (black).

After the data from an AVHRR GAC Level 1B file have been navigation-corrected and noise-filtered, the corrected data are written to a NetCDF-4 file which contains the 1) date and time of each scan line, 2) the 0.63, 0.86, and 1.61-µm (when available) raw counts, 3) the 3.74, 10.8 and 12.0-µm BTs, and 4) the SZA, VZA, and RAA for each pixel. This NetCDF-4 file is ingested into the SatCORPS-A in addition to the ancillary datasets required for cloud detection and cloud property retrievals.

Appendix C. Flow charts for C and E scene classification tests

      This appendix provides flow charts outlining each of the C and E tests not described in the main text. The section criteria for using one of these tests are summarized in Table X.

C.1 C Tests

      The flow chart for the C1 test is given in Figure 8. The remaining C tests are shown in Figure C.1 (C2), Figure C.2 (C3 land), Figure C.3 (C3 ocean), Figure C.4 (C4), and Figure C.5 (C5), Figure C.6 (C6 land), and Figure C.7 (C6 ocean).
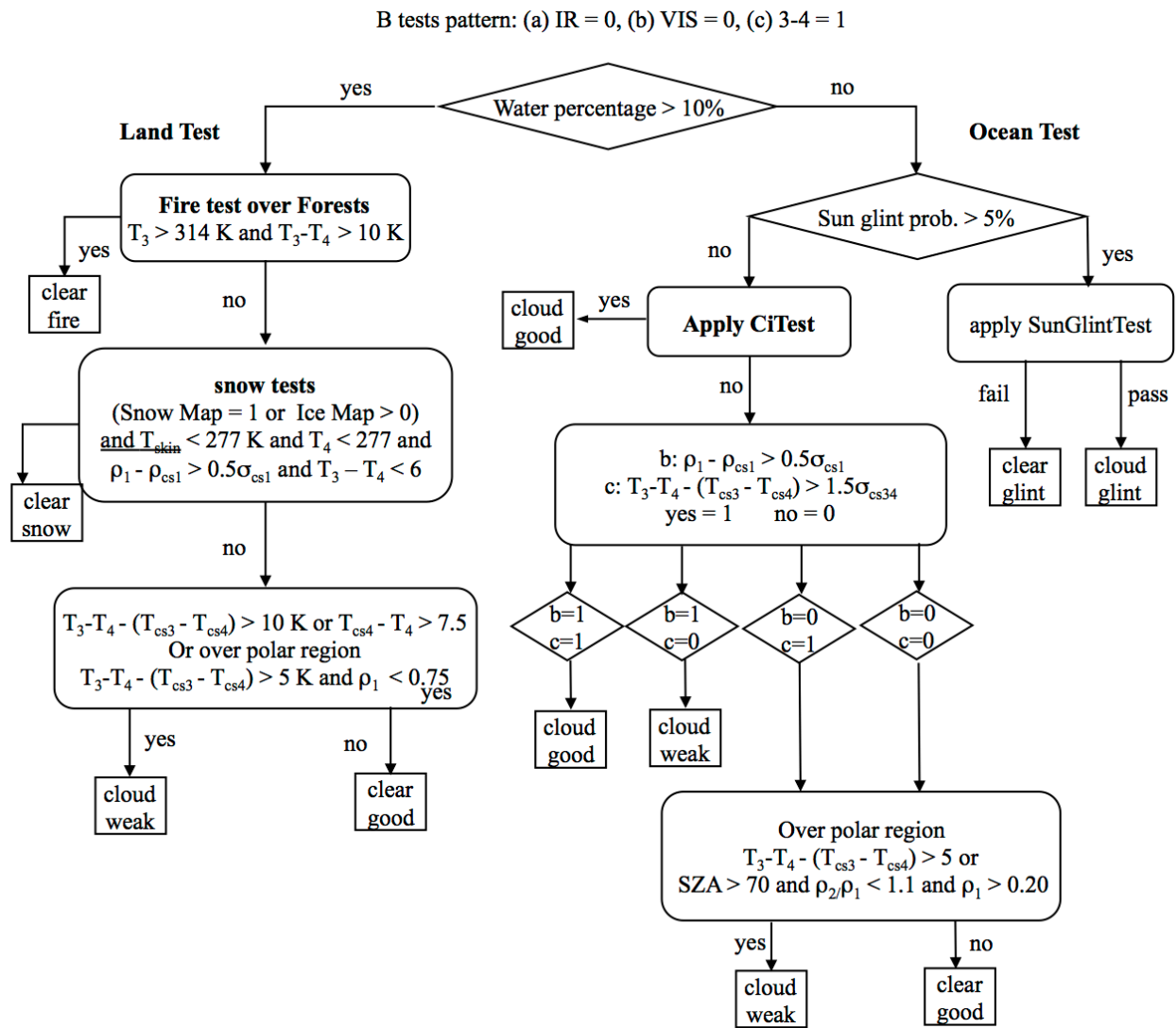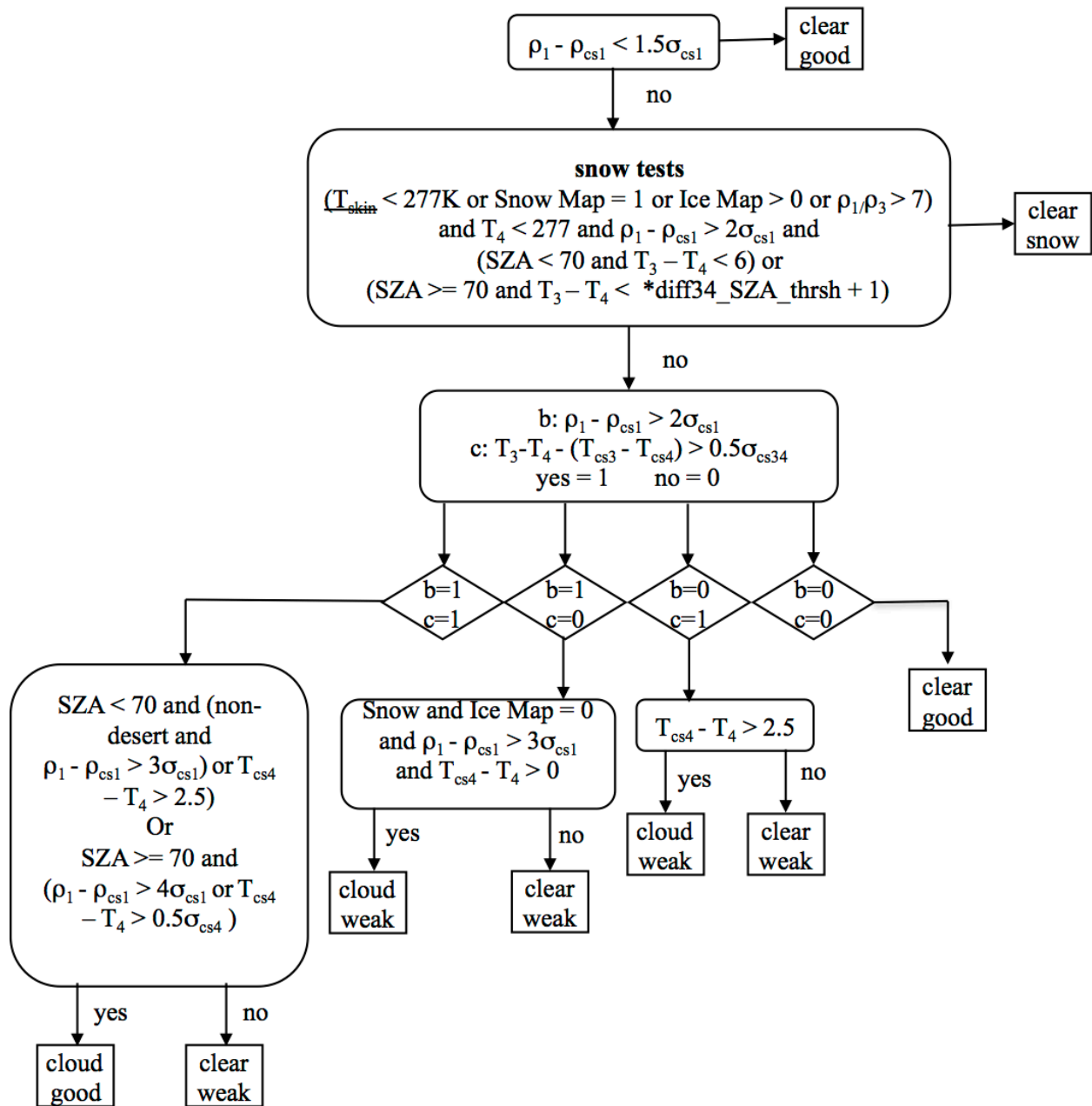
B tests pattern: (a) IR = 0, (b) VIS = 0, (c) 3-4 = 1

A controlled copy of this document is maintained in the CDR Program Library.
Approved for public release. Distribution is unlimited.
149

Figure C.1. Schematic of Sat-CORPS-A1 C2 tests.

$$*diff34\_SZA\_thrsh = 4.782*(\cos(SZA) - 1) + 6.0$$

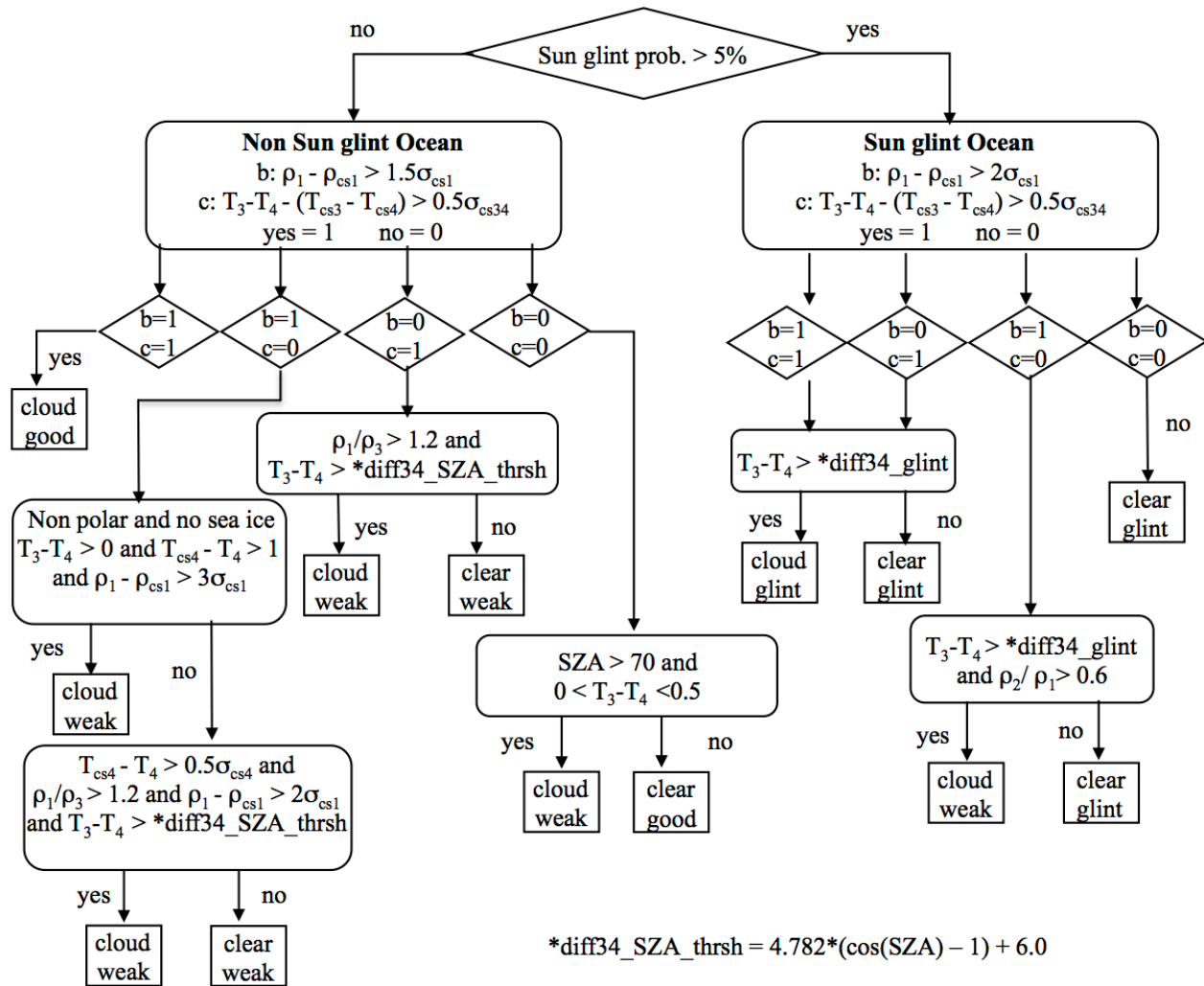**Figure C.2. Schematic of SatCORPS-A1/3 C3 tests over land.**

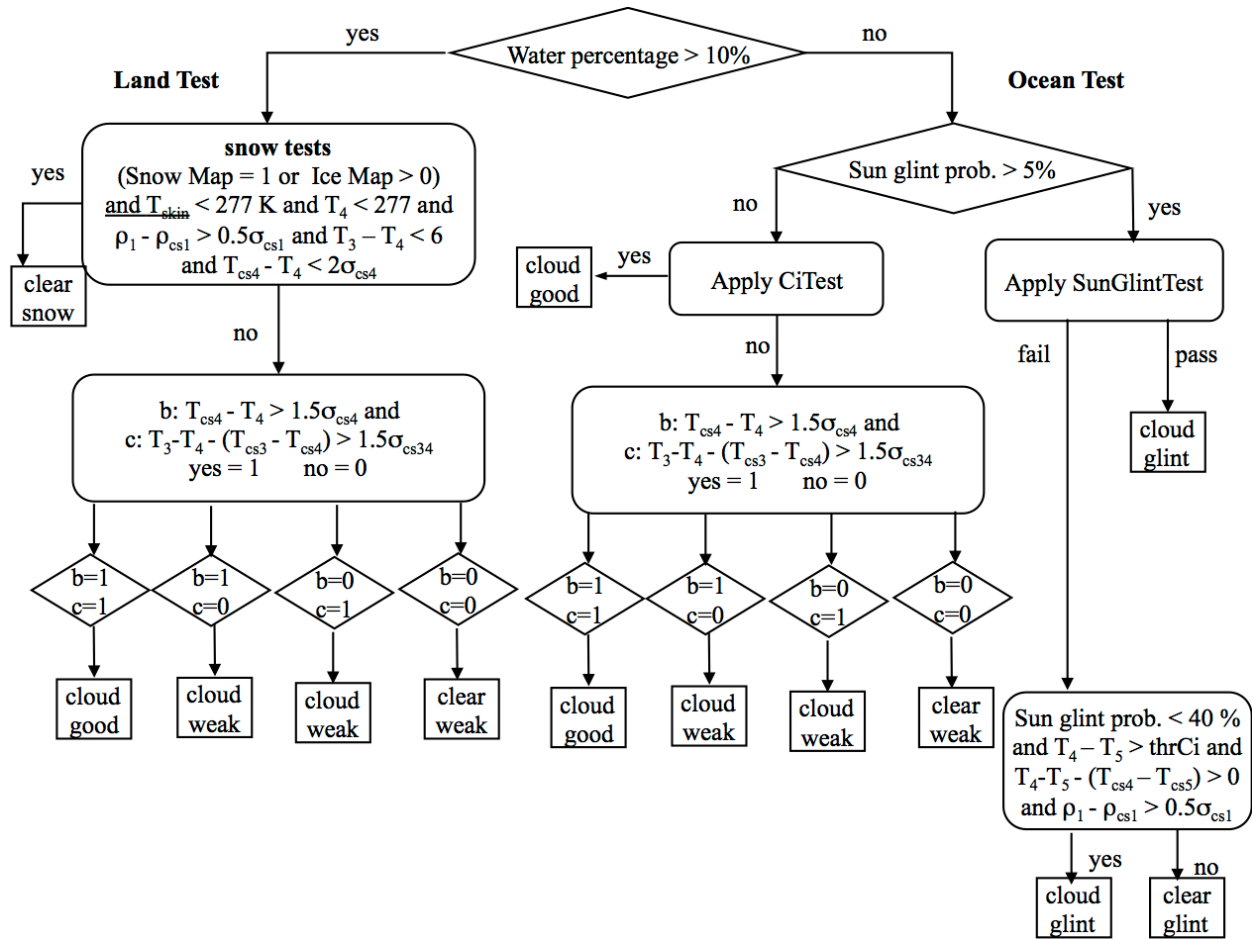**Figure C.3. Schematic of SatCORPS-A1/3 C3 tests over ocean.**

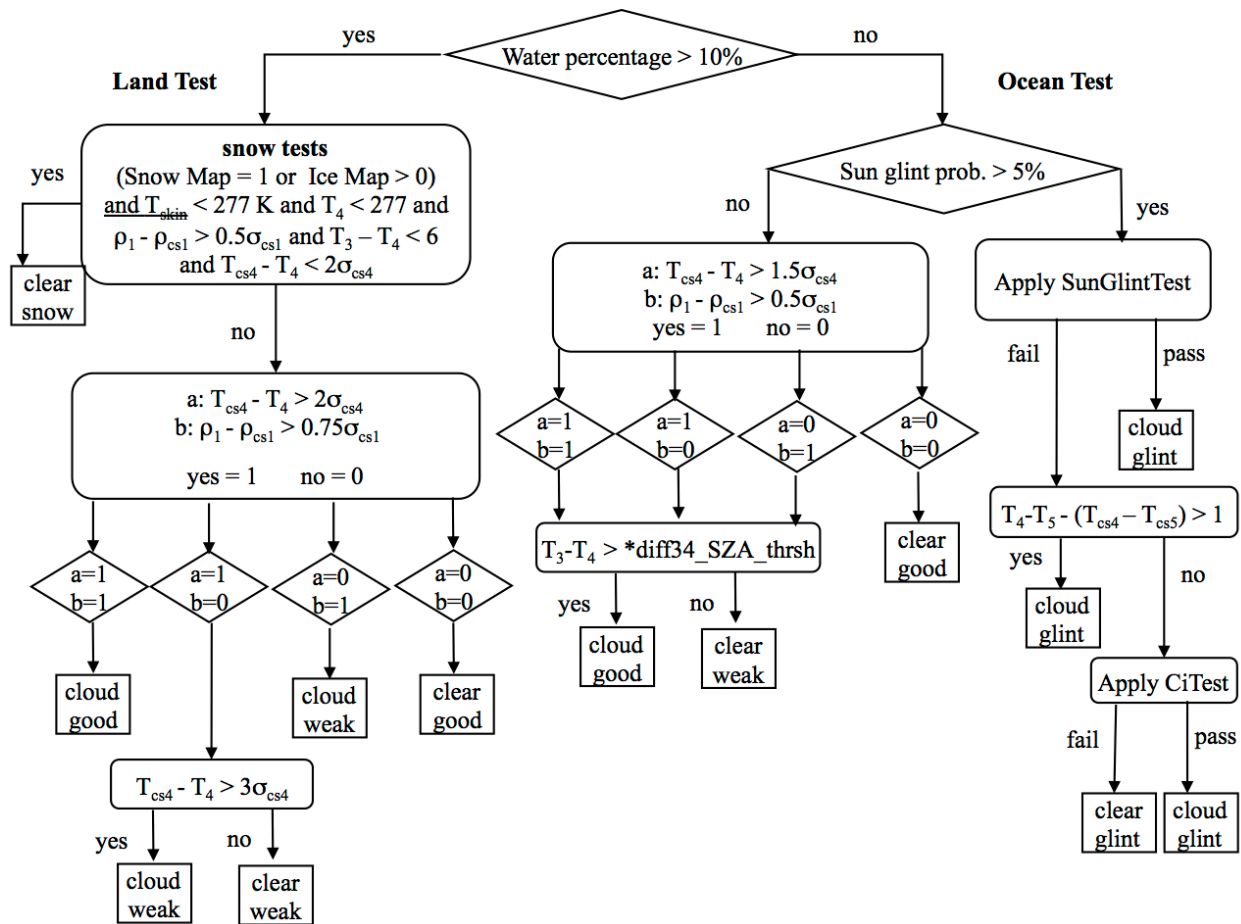**Figure C.4. Schematic of SatCORPS-A1/3 C4 tests.**
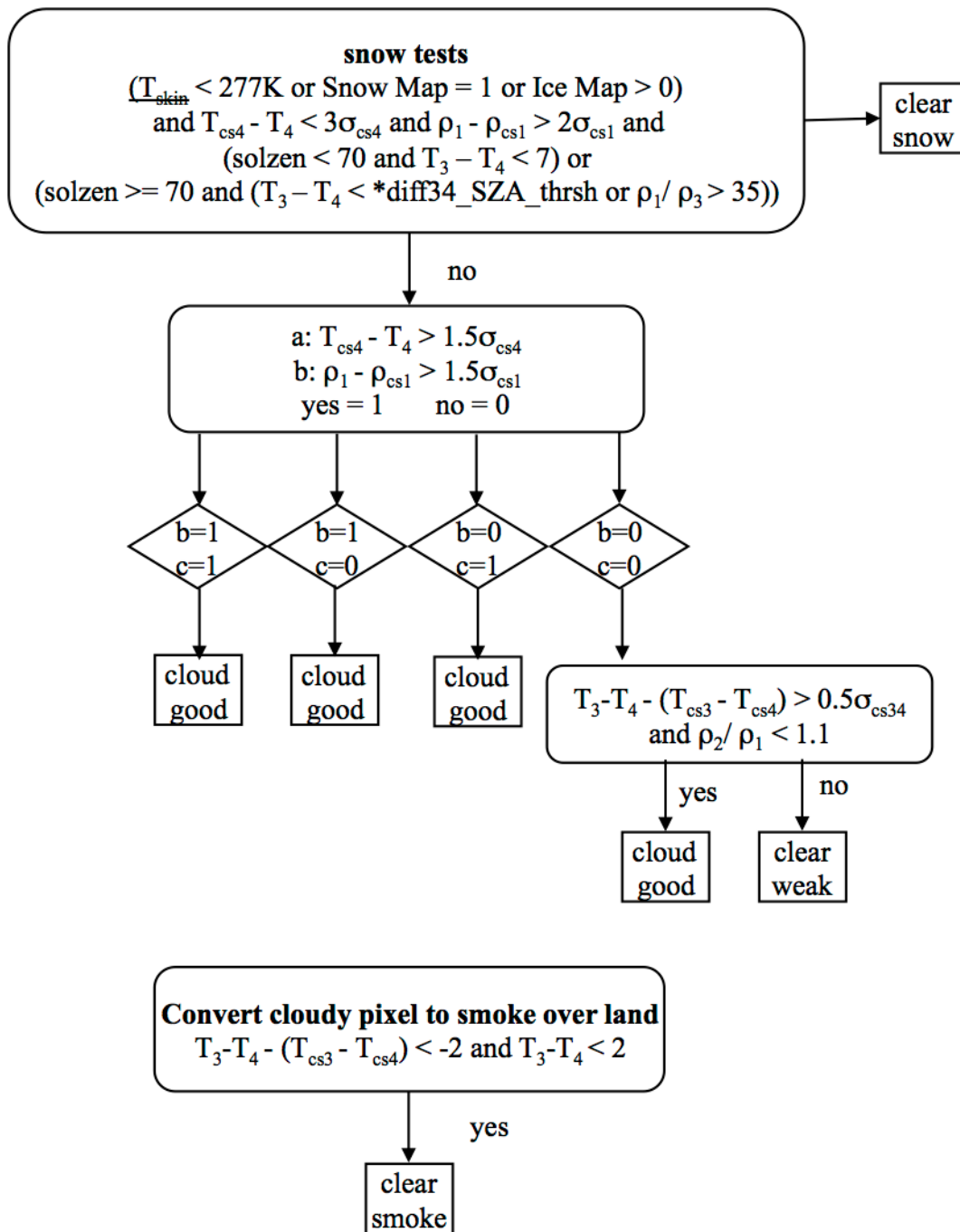
Figure C.5. Schematic of SatCORPS-A1/3 C5 tests.

snow tests

$(T_{skin} < 277K$ or Snow Map $= 1$ or Ice Map $> 0)$
and $T_{cs4} - T_4 < 3\sigma_{cs4}$ and $\rho_1 - \rho_{cs1} > 2\sigma_{cs1}$ and
(solzen < 70 and $T_3 - T_4 < 7)$ or
(solzen $>= 70$ and $(T_3 - T_4 < $ *diff34_SZA_thrsh or $\rho_1 / \rho_3 > 35))$

→ clear snow

no

a: $T_{cs4} - T_4 > 1.5\sigma_{cs4}$
b: $\rho_1 - \rho_{cs1} > 1.5\sigma_{cs1}$
yes $= 1$ no $= 0$

b=1 c=1 | b=1 c=0 | b=0 c=1 | b=0 c=0

cloud good | cloud good | cloud good | $T_3 - T_4 - (T_{cs3} - T_{cs4}) > 0.5\sigma_{cs34}$ and $\rho_2 / \rho_1 < 1.1$

yes no

cloud good clear weak

Convert cloudy pixel to smoke over land
$T_3 - T_4 - (T_{cs3} - T_{cs4}) < -2$ and $T_3 - T_4 < 2$

yes

clear smoke

Figure C.6. Schematic of SatCORPS-A1/3 C6 tests over land.
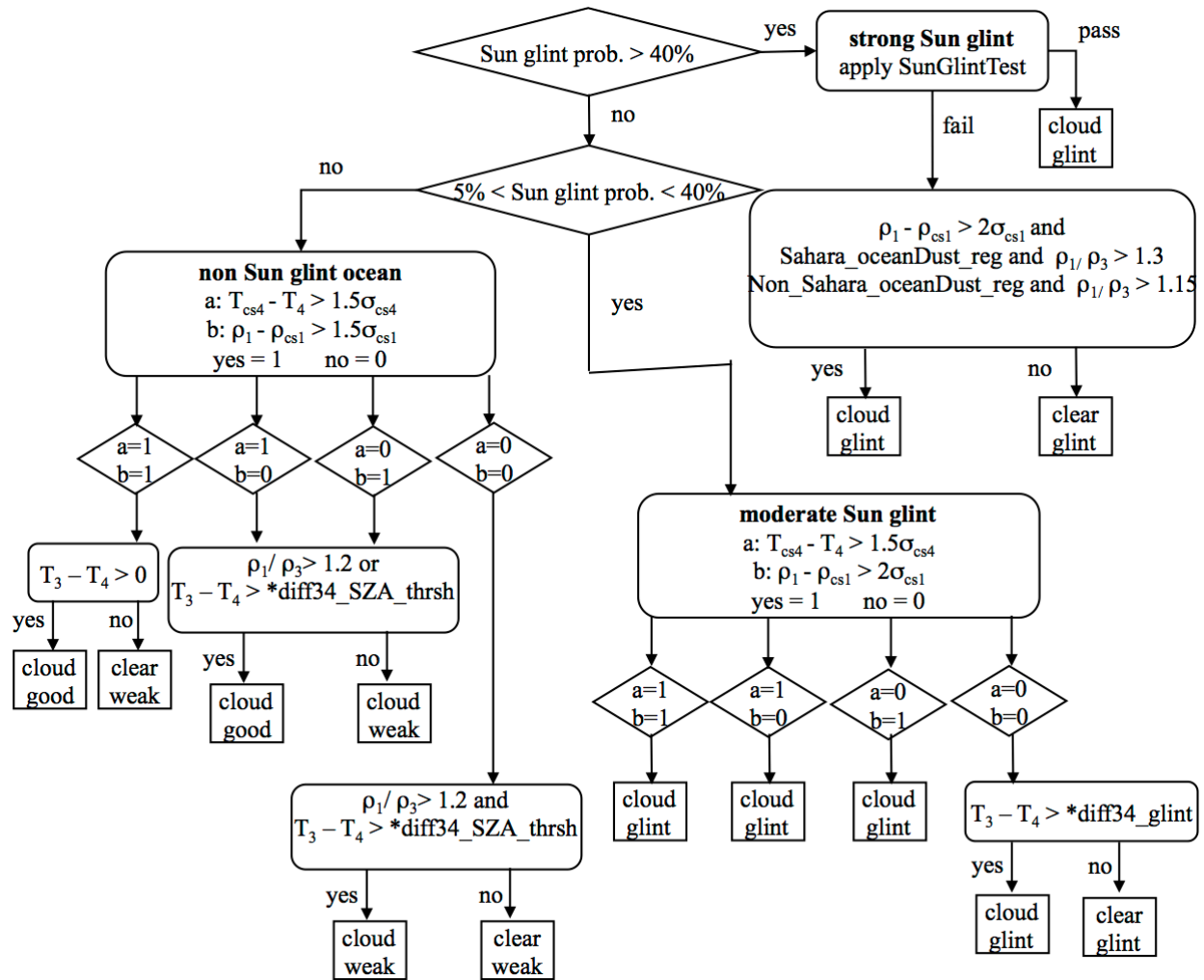
Figure C.7. Schematic of SatCORPS-A1/3 C6 tests over ocean.

C.2 E Tests

The flow chart for the E3 test is given in Figure 10. The remaining E tests are shown in Figure C.8 (E1), Figure C.9 (E2), Figure C.10 (E4), and Figure C.11 (E5).
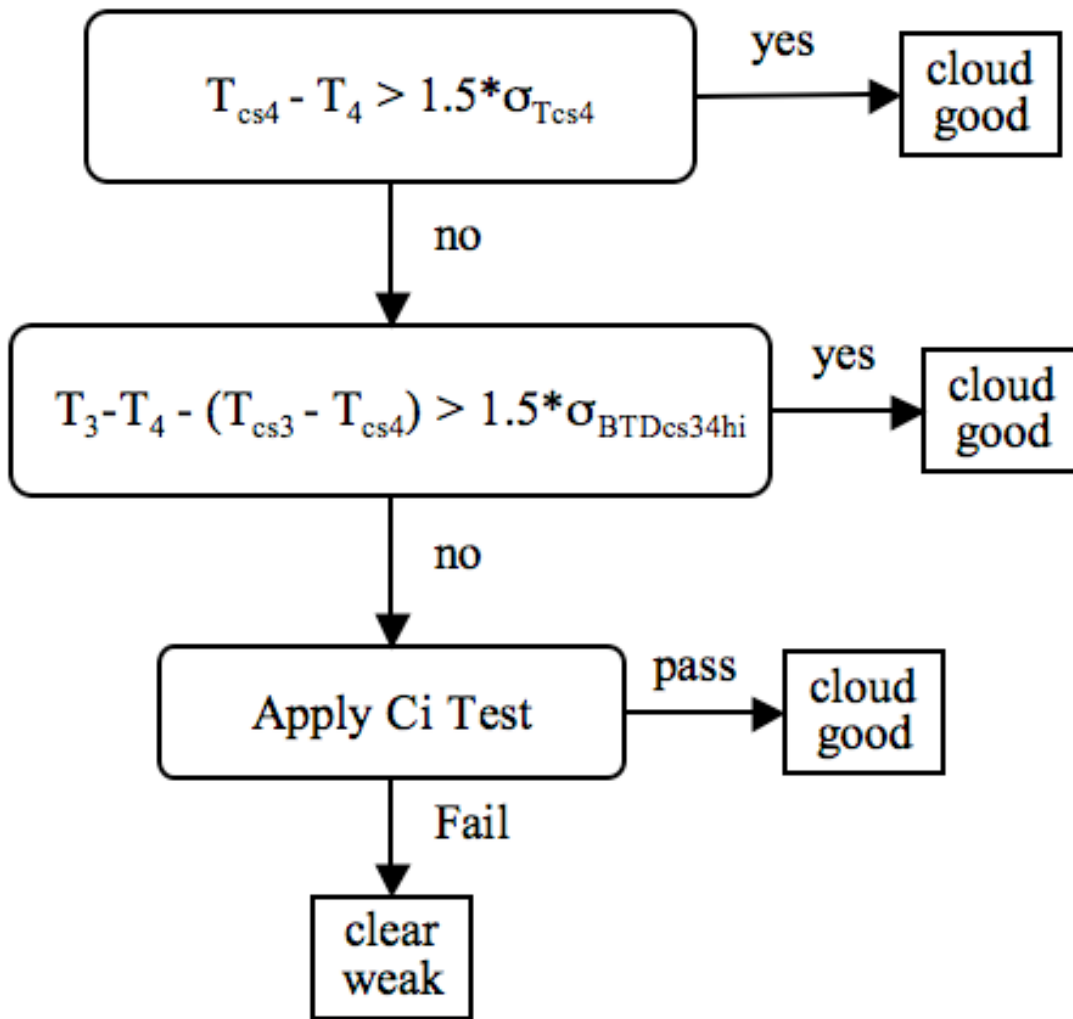
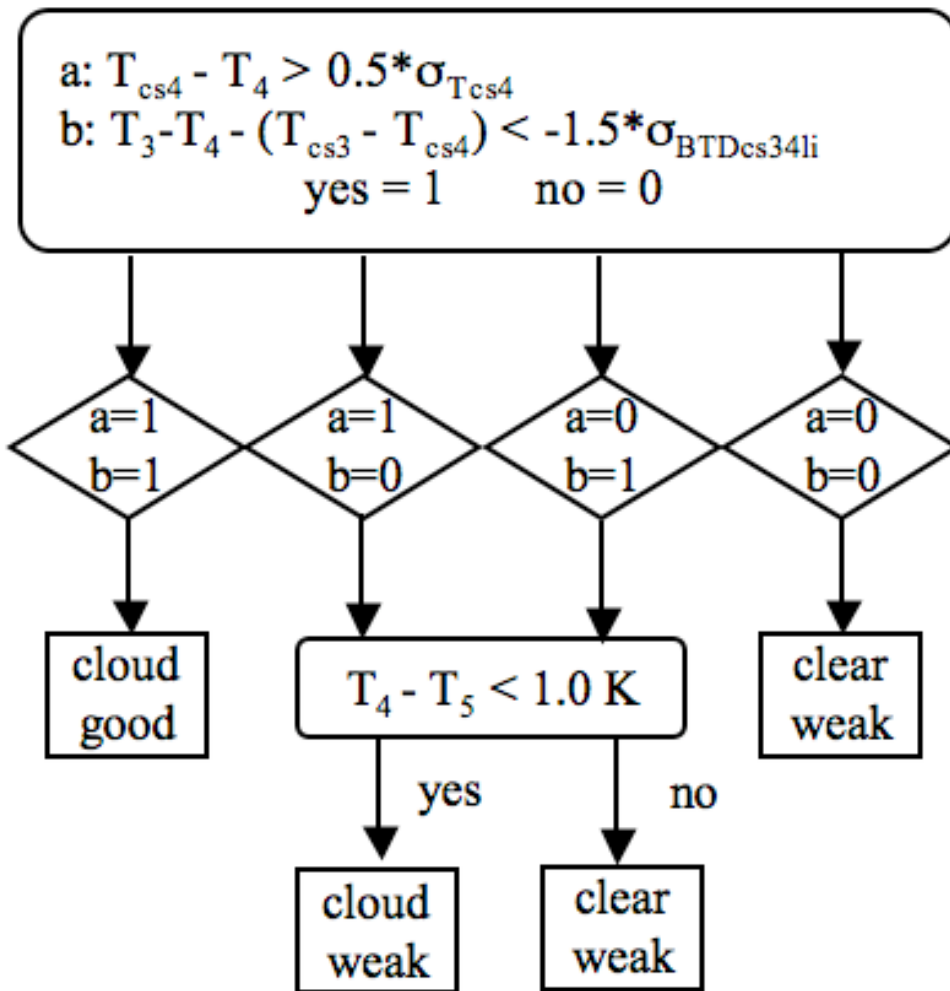**Figure. C.8. Schematic of SatCORPS-A1 E1 tests.**

$$\text{a: } T_{cs4} - T_4 > 0.5 * \sigma_{Tcs4}$$
$$\text{b: } T_3 - T_4 - (T_{cs3} - T_{cs4}) < -1.5 * \sigma_{BTDcs34li}$$
$$\text{yes} = 1 \qquad \text{no} = 0$$

| a=1 b=1 | a=1 b=0 | a=0 b=1 | a=0 b=0 |

cloud good

$$T_4 - T_5 < 1.0 \text{ K}$$

clear weak

yes　　　　　no

cloud weak

clear weak

Figure C.9. Schematic of SatCORPS-A1/2 E2 tests.

$$T_{cs4} - T_4 > 1.5*\sigma_{Tcs4}$$

yes → cloud good

no ↓

$$T_3 - T_4 - (T_{cs3} - T_{cs4}) < -1.5*\sigma_{BTDcs34lo}$$

yes → cloud good

no ↓

cloud weak

Figure C.10. Schematic of SatCORPS-A1/2 E4 tests.

$$T_{cs4} - T_4 > \text{rlx\_fctr} * \sigma_{Tcs4}$$
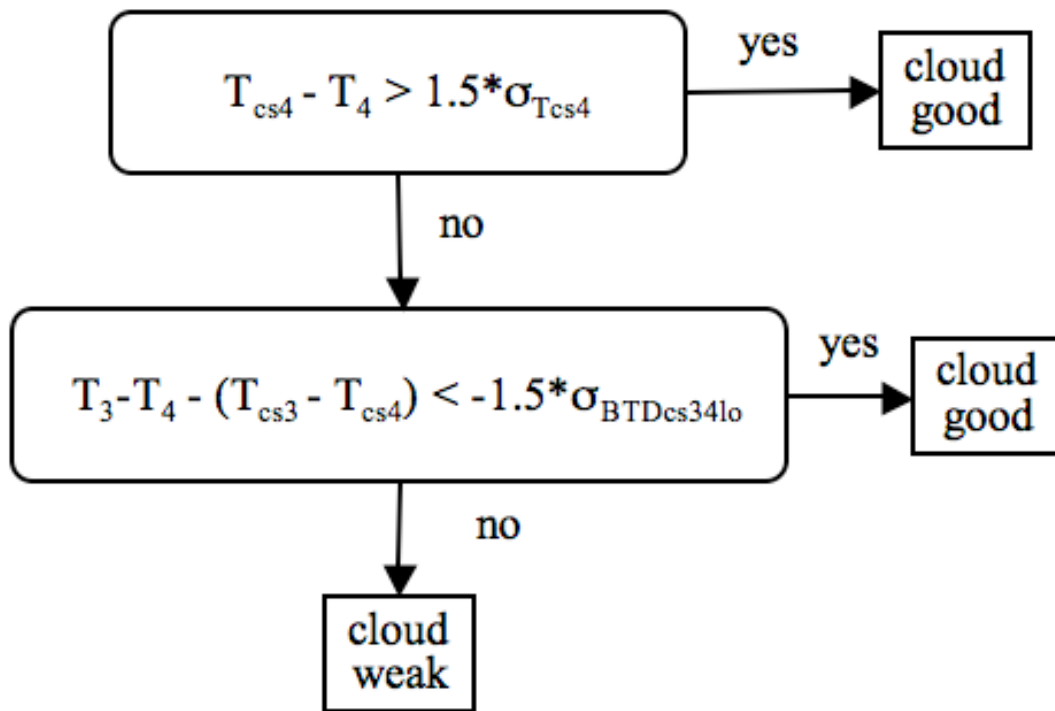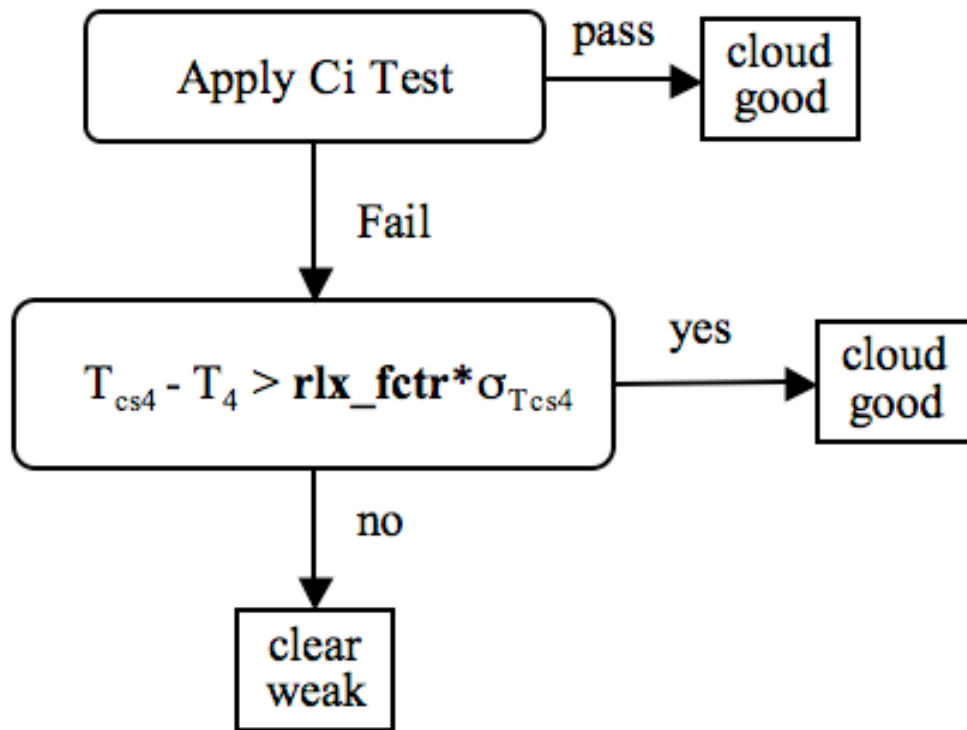
rlx_fctr = 2.0 for light vegetation
rlx_fctr = 1.5 for rest IGBP

Figure C.11. Schematic of SatCORPS-A1/2 E5 tests.